

## Engineering high-quality Fano resonances in open acoustic systems

**Felix Mathias Kronowetter**

Vollständiger Abdruck der von der TUM School of Engineering and Design der Technischen Universität München zur Erlangung eines

**Doktors der Ingenieurwissenschaften (Dr.-Ing.)**

genehmigten Dissertation.

**Vorsitz:**

Prof. Dr.-Ing. Hans-Jakob Kaltenbach

**Prüfende der Dissertation:**

1. Prof. Dr.-Ing. Steffen Marburg
2. Prof. Dr.-Ing. Christian Adams
3. Assoc. Prof. Dr. Sebastian Oberst

Die Dissertation wurde am 25.04.2024 bei der Technischen Universität München eingereicht und durch die TUM School of Engineering and Design am 02.10.2024 angenommen.



# Abstract

As Georg Christoph Lichtenberg said, "Die Erschütterung der Luft wird erst Schall, wo ein Ohr ist", meaning the vibration of air becomes sound only where there is an ear. Vibrations are a part of everyday life. They play an important role in the perception of comfort and, if strong enough, can lead to noise pollution. The question is how the propagation and properties of vibrations can be influenced or even engineered so that our ears perceive only an acceptable amount of sound.

Before engineering, it is necessary to understand the underlying mathematical equations and modeling techniques. Vibrations can propagate almost indefinitely through the air, rather than being confined by fixed boundaries. Steady-state linear acoustics in open systems are described by the Helmholtz equation and are therefore referred to as unbounded Helmholtz problems. In addition to analytical approaches for solving linear acoustic problems, numerical methods are required for complex tasks. Standard numerical methods, such as the finite element method, reach their limits for these problems.

Despite significant technical advances in recent years, solving unbounded Helmholtz problems is still challenging in terms of computational time, memory, and accuracy. Infinite elements are an approach to represent mathematical spaces of infinite extent. In this dissertation, a new spectral stochastic infinite element method is developed that not only solves unbounded problems but also allows efficient computation of solutions with uncertain input parameters. It remains a challenge to determine normal modes of open coupled mechanical-acoustic systems. To solve this problem, contour integral methods are used for fast and accurate solutions.

Acoustic metamaterials are an emerging trend that allows the manipulation of propagating waves in unprecedented ways. The design of metamaterials is usually based on infinite periodic meta-atoms modeled in the reciprocal space. Meta-atoms are acoustic elements with a special set of acoustic properties. The underlying assumptions lack precision when it comes to experimental validation and realistic application being inherently finite. Besides imperfections, diffraction at the edges of finite metamaterials and near-field interactions between meta-atoms are responsible for the deviation from the predicted solution at idealized infinite periodicity. This dissertation addresses this problem by characterizing the metamaterial using normal modes of finite arrays of meta-atoms and identifying those with a high-quality factor. This technique is used to design a metamaterial for an industrial application that outperforms state-of-the-art solutions. Furthermore, inhomogeneous pressure distributions in finite metamaterials demonstrate the need for further insight into the fundamental effects that cause interactions between meta-atoms.

## *Abstract*

In this dissertation, the interaction of degenerate modes in the strong coupling regime is studied, and the near-field coupling is exploited to engineer the sound attenuation properties of coupled meta-atoms.

In this dissertation, another idea to improve sound attenuation makes use of bound states in the continuum. Bound states in the continuum originate in the field of quantum mechanics. When transferred to the field of acoustics, they manifest in modes with a high-quality factor, leading to Fano resonances when coupled into the continuous spectrum. This makes them ideal for application in acoustic devices. However, accurate prediction of bound states is challenging due to realistic losses and missing field data. This dissertation presents a theoretical model based on a non-Hermitian Hamiltonian and a technique for accurately predicting the missing field data. This is a groundbreaking step in facilitating the future application of high-quality factor Fano resonances in acoustics.

This dissertation presents results that advance the state-of-the-art in the analysis of open acoustic systems with application to acoustic metamaterials. The focus is on normal modes, industrial applications of metamaterials, and tuning meta-atoms by coupling. In addition, the research results lead to a breakthrough in the analysis and possible application of high-quality Fano resonances based on bound states coupling into the continuous spectrum. Various measurements validate the numerical predictions to make the results more meaningful. Connecting the results of this work to Lichtenberg's opening statement, seminal findings are presented that can be used to manipulate the propagation and properties of vibrations so that our ears perceive only engineered comfortable sound.

# Zusammenfassung

”Die Erschütterung der Luft wird erst Schall, wo ein Ohr ist”, sagte einst der deutsche Physiker Georg Christoph Lichtenberg. Schwingungen in Form von Vibrationen sind ein alltägliches Phänomen. Sie spielen eine wichtige Rolle für das Wohlbefinden, können beruhigend wirken, aber auch störenden Lärm verursachen. Es stellt sich die Frage, wie die Ausbreitung von Vibrationen und deren Eigenschaften beeinflusst oder gestaltet werden können, damit unser Ohr nur ein akzeptables Maß an Schall wahrnimmt.

Um über die Manipulation von Vibrationen nachdenken zu können, ist es notwendig, die entsprechenden mathematischen Gleichungen und Modellierungsmethoden zu kennen und zu verstehen. In der linearen Akustik beschreibt die Helmholtz-Gleichung, die auf der Wellengleichung basiert, eingeschwungene Systeme im Frequenzbereich. Zur Lösung akustischer Probleme sind neben der analytischen Modellierung auch numerische Methoden erforderlich. Vibrationen können sich in der Luft nahezu ins Unendliche ausbreiten. Konventionelle Finite-Elemente-Methoden stoßen an ihre Grenzen, da die Schallabstrahlung ins Unendliche zu Problemen bei der räumlichen Diskretisierung und damit beim Speicherbedarf führt.

Die Lösung der Helmholtz-Gleichung in unbegrenzten Gebieten bleibt trotz der enormen technischen Fortschritte der letzten Jahre eine Herausforderung hinsichtlich Rechenzeit, Speicherbedarf und Genauigkeit. Es gibt spezielle Methoden, wie z. B. die Infinite-Elemente-Methode, die die unendliche Ausdehnung mathematischer Gebiete modellieren können. Im Rahmen dieser Dissertation wird eine neuartige spektral-stochastische Infinite-Elemente-Methode entwickelt, die nicht nur die Helmholtz-Gleichung in unbegrenzten Gebieten lösen kann, sondern auch eine effiziente Berechnung bei unsicheren Eingangsparametern ermöglicht. Die Berechnung der Eigenfrequenzen von Fluid-Struktur-Kopplungsproblemen stellt eine weitere Herausforderung dar, die mit Hilfe von Konturintegralverfahren angegangen und gelöst wird.

Ein Trend, der die Beeinflussung fortschreitender Wellen in bisher nicht gekanntem Ausmaß ermöglicht, sind akustische Metamaterialien. Akustische Metamaterialien bestehen meist aus periodisch angeordneten Metaatomen. Metaatome sind Grundbausteine, die über definierte akustische Eigenschaften verfügen. Sie werden im reziproken Raum modelliert. Dabei wird angenommen, dass die akustischen Metamaterialien eine unendliche Ausdehnung haben und die Metaatome perfekt periodisch angeordnet sind. Dieser Ansatz weist jedoch einige Ungenauigkeiten bei der Modellierung realistischer, endlicher Systeme und ihrer experimentellen Validierung auf. Neben Imperfektionen sind auch Beugungseffekte an den Rändern sowie lokale Kopplungseffekte zwischen den einzelnen Metaatomen

## *Zusammenfassung*

nicht zu vernachlässigen. Die vorliegende Dissertation befasst sich mit diesen Problemen. Zur Charakterisierung eines Metamaterials werden die Eigenwerte und die zugehörigen Außenraummoden endlicher periodischer Anordnungen von Metaatomen bestimmt. Ein substanzielles Orientierungskriterium sind die Gütefaktoren der Außenraummoden, um diese nach ihrer Relevanz einordnen zu können. Dieser Ansatz wird genutzt, um ein Metamaterial für industrielle Anwendungen zu entwickeln, das den bisher bekannten Lösungen zur Schalldämpfung deutlich überlegen ist. Ein erhebliches Potenzial zur weiteren Verbesserung der Leistungsfähigkeit von Metamaterialien liegt darüber hinaus in der Wechselwirkung zwischen den Metaatomen. Ein Teil der Dissertation ist der Untersuchung der Wechselwirkung stark gekoppelter entarteter Moden gewidmet. Es wird gezeigt, dass die akustischen Eigenschaften zweier Metaatome in hohem Maße durch Nahfeldkopplung manipuliert werden können.

Ein weiteres Potenzial zur Verbesserung der Leistungsfähigkeit von Metamaterialien liegt in der Implementierung von gebundenen Zuständen. Gebundene Zustände haben ihren Ursprung in der Quantenmechanik. Diese Zustände können auch für akustische Wellen nachgewiesen werden, was sich in Form von Fano-Resonanzen äußert. Fano-Resonanzen entstehen, wenn Moden mit hohem Gütefaktor in das kontinuierliche Spektrum einkoppeln. Moden mit solch hohen Gütefaktoren wären zum Beispiel für den Einsatz in akustischen Filtern prädestiniert. Eine genaue Vorhersagetechnik fehlt jedoch noch, da die aus den Moden resultierenden Fano-Resonanzen sehr empfindlich auf Störungen und Verluste reagieren. In dieser Dissertation wird ein theoretisches Vorhersagemodell auf der Basis eines nicht-hermiteschen Hamiltonoperators entwickelt. Zusätzlich wird eine Technik vorgestellt, mit der die genauen Schalldruckdaten der gebundenen Zustände ausgewertet werden können. Die Möglichkeit, gebundene Zustände genau zu analysieren, ist ein großer Schritt für die technische Anwendung von akustischen Fano-Resonanzen mit hohem Gütefaktor.

Die Ergebnisse dieser Dissertation erweitern den Stand der Technik bei der Berechnung und Auslegung von akustischen Metamaterialien. Der Schwerpunkt liegt dabei auf der Berechnung von Außenraummoden, der industriellen Umsetzbarkeit von Metamaterial und der Feinabstimmung von Metaatomen durch Nahfeldkopplung. Darüber hinaus führen die Forschungsergebnisse zu einem Durchbruch bei der Analyse und möglichen Anwendung von Fano-Resonanzen, die auf der Wechselwirkung zwischen gebundenen Zuständen und dem kontinuierlichen Spektrum beruhen. Die Ergebnisse der Berechnungen werden durch experimentelle Untersuchungen bestätigt. In Anlehnung an Lichtenbergs einleitende Aussage kann festgestellt werden, dass die Erkenntnisse dieser Dissertation dazu genutzt werden können, die Ausbreitung und Eigenschaften akustischer Wellen so zu beeinflussen, dass nur angenehme Töne unser Ohr erreichen.

# Acknowledgments

There have been many wonderful people who have supported me during my time at TUM. I would like to thank them all from the bottom of my heart.

First of all, a big thank you to Hans-Jakob Kaltenbach for giving the first lecture on acoustics that I have ever attended and, finally, for the supervision of my viva voce. Thanks also to Christian Adams for the nice time we spent meeting in Australia, attending various conferences and workshops together, and for taking on the role of examiner. Another big thank you goes to the people who made my time in Australia unforgettable and helped me in many ways to complete my Ph.D.: Nicole, thank you for having me! I enjoyed our non-scientific discussions and lunch breaks. David Liu... thank you for having me, for spending time with me and my family. I will always remember the time with you and your family and of course the delicious food. Yan Kei and Lujun, thank you for the great time we had together and all the inspiration you gave me. Sebastian, thank you so much for being such a great supervisor and the fastest reviewer ever, for all the great collaboration, inspiration, and ideas, and for being my thesis examiner! David, thank you for introducing me to the subject of bound states. You were always several steps ahead and guided me through all the research. I am grateful to have worked with such a great mind.

The next big thank you goes to the VIB team. It has been a pleasure working with you all and having fun in our off hours. May the coffee business be with me and bring me gold and diamonds! There are a few names that need to be mentioned... Lennart, who helped me get started at VIB. Marcus, for all the great collaboration and help in the lab. Twins, for keeping the business running. Anton for all the fruitful discussions. The girls of the best office - MW1535. Caglar and Martin, for many, many, many science extreme meetings! Thanks also to all the other members of the VIB. Steffen, thank you for a great time, for the great opportunities, and for everything you've done to support me, especially with my family. I have had the chance to travel the world, develop and find my way. I would also like to thank Thomas Wagner. He made it possible for me to combine sport with my studies, always supported me along the way, and thus also contributed significantly to my path to my doctorate.

Allen Freunden danke für die vielen gemeinsamen Jahre und für die Unterstützung. Danke vor allem an meine Familie, Mama, Papa, Magret, Fabi und Lisl, dass ihr immer hinter mir gestanden seid, mir das alles ermöglicht habt und immer für mich da ward. Ohne euch wäre ich nicht so weit gekommen. Fabi, ein RIESEN MERCI für ALLES! Zum Schluss möchte ich meiner Verlobten Coro und meinen beiden Kindern Emma und Lilly danken. Ihr habt mich so sehr unterstützt, an mich geglaubt und alles mit Freude und Elan mitgemacht. Dafür bin ich unendlich dankbar!





## Appended publications

- [AP1] F. Kronowetter, L. Moheit, M. Eser, K. K. Sepahvand, and S. Marburg. Spectral Stochastic Infinite Element Method in Vibroacoustics. In: *Journal of Theoretical and Computational Acoustics*, 2020, **28**(02), p. 2050009.
- [AP2] F. Kronowetter, S. K. Baydoun, M. Eser, L. Moheit, and S. Marburg. A Benchmark Study on Eigenfrequencies of Fluid-Loaded Structures. In: *Journal of Theoretical and Computational Acoustics*, 2020, **28**(02), p. 2050013.
- [AP3] F. Kronowetter, L. Pretsch, Y. K. Chiang, A. Melnikov, S. Sepehrirahnama, S. Oberst, D. A. Powell, and S. Marburg. Sound attenuation enhancement of acoustic meta-atoms via coupling. In: *The Journal of the Acoustical Society of America*, 2023, **154**(2), pp. 842-851.
- [AP4] F. Kronowetter, P. Wagner, J. Kolodi, I. Brabandt, T. Neumeyer, N. Rümmler, and S. Marburg. Novel compound material and metamaterial wheelhouse liners for tire noise reduction. In: *Mechanical Systems and Signal Processing*, 2023, **200**, p. 110548.
- [AP5] F. Kronowetter, M. Maeder, Y. K. Chiang, L. Huang, J. D. Schmid, S. Oberst, D. A. Powell, and S. Marburg. Realistic prediction and engineering of high-Q modes to implement stable Fano resonances in acoustic devices. In: *Nature Communications*, 2023, **14**(1), p. 6847.



# Publications that are not part of this dissertation

- [P1] F. Kronowetter, L. Moheit, K. K. Sepahvand, and S. Marburg. Spektral-stochastische Infinite-Elemente-Methode in der Vibroakustik. In: *Fortschritte der Akustik - DAGA: 45. Jahrestagung für Akustik, 18.-21. März*, 2019.
- [P2] F. Kronowetter, M. Eser, K. K. Sepahvand, and S. Marburg. Uncertain acoustic meta-atoms. In: *Proceedings of the 23rd International Congress on Acoustics*, 2019, pp. 1963-1970.
- [P3] L. Moheit, S. Anthis, J. Heinz, F. Kronowetter, and S. Marburg. Analysis of scattering by finite sonic crystals in free field with infinite elements and normal modes. In: *Journal of Sound and Vibration*, 2020, **476**, p. 115291.
- [P4] F. Kronowetter, E. Martin, S. K. Baydoun. Computation of normal modes based on a coupled finite/infinite element formulation. In: *The Journal of the Acoustical Society of America*, 2021, **149** A67.
- [P5] C. Gurbuz, F. Kronowetter, C. Dietz, M. Eser, J. Schmid, and S. Marburg. Generative adversarial networks for the design of acoustic metamaterials. In: *The Journal of the Acoustical Society of America*, 2021, **149**(2), pp. 1162–1174.
- [P6] C. Gurbuz, F. Kronowetter, C. Dietz, M. Eser, J. M. Schmid, and S. Marburg. Generatives Design von akustischen Metamaterialien. In: *Fortschritte der Akustik - DAGA 2022: 48. Jahrestagung für Akustik, 21.-24. März 2022 in Stuttgart*, 2022.
- [P7] F. Kronowetter and S. Marburg. Interaction of acoustic meta-atoms as additional degrees of freedom for metamaterial tuning. In: *Proceedings of the 24th International Congress on Acoustics*, 2022.
- [P8] F. Kronowetter, L. Pretsch, Y. K. Chiang, A. Melnikov, S. Sepehrirahnama, S. Oberst, D. A. Powell, and S. Marburg. Interaktionsparameter von akustischen Meta-atomen als zusätzliche Freiheitsgrade zum Tuning von Metamaterialien. In: *Fortschritte der Akustik - DAGA 2023, 49. Jahrestagung für Akustik, 06.-09. März 2023, Hamburg*, 2023.
- [P9] D. H. Le, F. Kronowetter, Y. K. Chiang, J. Rao, M. Maeder, S. Marburg, and D. A. Powell. Bistable Origami-Inspired 1-bit Coding Acoustic Metasurfaces for Reconfigurable Beam Scanning. In: *2023 Seventeenth International Congress on Artificial Materials for Novel Wave Phenomena (Metamaterials), Chania, Greece*, 2023, pp. 186-188.

*Publications that are not part of this dissertation*

- [P10] F. Kronowetter. Application of acoustic metamaterial for tire noise reduction. In: *INTER-NOISE and NOISE-CON Congress and Conference Proceedings, Conference Proceeding 1, 5 November, 2023*, pp. 318-321(4).
- [P11] D. H. Le, F. Kronowetter, Y. K. Chiang, J. Rao, M. Maeder, S. Marburg, and D. A. Powell. Bistable origami-inspired acoustics metasurface for dynamic beam scanning. In: *The Journal of the Acoustical Society of America*, 2023, **154**(4), pp. A233-A233.

# Contents

<b>Abstract</b>	<b>iii</b>
<b>Zusammenfassung</b>	<b>v</b>
<b>Acknowledgments</b>	<b>vii</b>
<b>Appended publications</b>	<b>ix</b>
<b>Publications that are not part of this dissertation</b>	<b>xi</b>
<b>List of Figures</b>	<b>xv</b>
<b>Acronyms</b>	<b>xvii</b>
<b>1 Introduction</b>	<b>1</b>
1.1 Problem formulation and motivation . . . . .	1
1.2 State-of-the-art . . . . .	3
1.2.1 Open systems . . . . .	3
1.2.2 Uncertainty quantification . . . . .	5
1.2.3 Acoustic metamaterials . . . . .	6
1.2.4 Bound states in the continuum . . . . .	7
1.3 Contribution of this dissertation . . . . .	9
<b>2 Methods</b>	<b>13</b>
2.1 Governing equations in acoustics . . . . .	13
2.1.1 Wave equation . . . . .	14
2.1.2 Helmholtz equation . . . . .	14
2.1.3 Navier-Lamé equation . . . . .	17
2.2 Numerical methods . . . . .	19
2.2.1 Finite element method . . . . .	19
2.2.2 Infinite element method . . . . .	26
2.2.3 Spectral stochastic infinite element method . . . . .	31
2.3 Normal modes . . . . .	33
2.3.1 Second-order Krylov subspace methods . . . . .	34
2.3.2 Contour integral methods . . . . .	34
2.4 Effective non-Hermitian Hamiltonian for open systems . . . . .	35
2.5 Modeling of acoustically effective materials . . . . .	38
2.5.1 Porous materials . . . . .	38

*Contents*

2.5.2	Microperforated panels . . . . .	39
2.5.3	Composite materials . . . . .	41
2.5.4	Acoustic metamaterials . . . . .	41
2.6	Experimental techniques . . . . .	42
2.6.1	Impedance tube . . . . .	43
2.6.2	Transmission tube . . . . .	44
2.6.3	Laser Doppler Vibrometer . . . . .	46
<b>3</b>	<b>Major Findings of Attached Publications</b>	<b>49</b>
<b>4</b>	<b>Discussion</b>	<b>61</b>
	<b>Bibliography</b>	<b>69</b>
<b>5</b>	<b>Appended Publications</b>	<b>99</b>
5.1	Publication AP1 . . . . .	99
5.2	Publication AP2 . . . . .	119
5.3	Publication AP3 . . . . .	144
5.4	Publication AP4 . . . . .	156
5.5	Publication AP5 . . . . .	173

# List of Figures

2.1	<b>Isoparametric concept.</b> A two-dimensional element with four nodes in the real space and in the parameter space is presented. . . . .	22
2.2	<b>Coupled mechanical-acoustic system.</b> A coupled mechanical-acoustic system is presented, where $\Omega_s$ is the solid domain bounded by the solid-fluid interface $\Gamma$ , $\Omega_f$ is the fluid domain with the outer boundary $\Gamma_f$ . . . . .	24
2.3	<b>Exterior Helmholtz problem.</b> A coupled mechanical-acoustic system is presented, where $\Omega_s$ is the solid domain bounded by the solid-fluid interface $\Gamma$ , $\Omega_f$ is the truncated fluid domain with the outer boundary $\Gamma_c$ , and $\Omega_c$ is the complementary domain with the outer boundary at infinity $\Gamma_\infty$ . . . . .	27
2.4	<b>IFEM mapping.</b> Topology of a two-dimensional infinite element with four radial nodes in the physical space and in the isoparametric space. . . . .	29
2.5	<b>Elliptic domain.</b> Elliptic contour enclosing the complex domain in which the eigenvalues of interest are to be found. . . . .	35
2.6	<b>Duct-cavity system.</b> Schematic drawing of a coupled two-dimensional waveguide-resonator system. . . . .	36
2.7	<b>RLC series circuit.</b> Equivalent circuit for the MPP absorber with air layer. . . . .	40
2.8	<b>Impedance tube.</b> A sketch of an impedance tube with two microphones attached. The system is excited by the loudspeaker, which produces a plane wave $p_i$ . The sample is positioned at the right end of the tube, with its inward-facing surface defining $x = 0$ . The reflected sound pressure is denoted by $p_r$ . . . . .	43
2.9	<b>Transmission tube.</b> A sketch of a transmission tube with four microphones attached. The system is excited by the loudspeaker, which produces a plane wave $p_i$ . The sample of thickness $d$ is positioned in the center of the tube. The surface facing the loudspeaker defines $x = 0$ . The reflected sound pressure is denoted by $p_r$ , the transmitted sound pressure is $p_t$ , and the reflected sound pressure behind the sample is $p_R$ . The two-load method uses two different conditions to determine the transmission loss, such as a sound hard, a sound soft, or an absorbing boundary. . . . .	45
2.10	<b>LDV setup.</b> A sketch of a setup for sound field visualization. The setup consists of an air cavity that can be excited by a loudspeaker. The cavity has two glass sidewalls to ensure viable laser transmission. The laser is reflected from a coated rigid wall. . . . .	46





# Acronyms

AMM	Acoustic Metamaterial
BC	Boundary condition
BEM	Boundary element method
BIC	Bound state in the continuum
block SS	Block Sakurai Sugiura method
CIM	Contour integral method
EVP	Eigenvalue problem
FEM	Finite element method
gPC	Generalized polynomial chaos
IBZ	Irreducible Brillouin zone
IFEM	Infinite element method
JCA	Johnson-Champoux-Allard
LDV	Laser Doppler Vibrometer
MPP	Microperforated panel
NVH	Noise, vibration, and harshness
PML	Perfectly matched layer
Q	Quality
QBIC	Quasi-bound state in the continuum
RLC	Resistor, Inductor, and Capacitor
SOAR	Second-order Arnoldi
SRC	Sommerfeld radiation condition

*Acronyms*

UQ      Uncertainty quantification

# 1 Introduction

## 1.1 Problem formulation and motivation

Sound is a familiar concept. We are constantly exposed to it in our lives, from quiet sounds like chewing and talking, to loud sounds like mowing the lawn or passing traffic, to extremely noisy sounds like explosions. But what is sound? And how is it that we perceive it in so many different ways?

Vibrations in gases, liquids, and solids are converted to sound when they impinge on a receiver, such as the human ear. Mathematically, sound can be described as the wavelike propagation of small perturbations in physical quantities, such as sound pressure, and is part of the field of acoustics. A distinction is made between linear and nonlinear acoustics, where the amplitude of the sound determines the difference. The amplitude depends on the compression of the medium as the sound wave propagates. The upper limit for linear acoustics in air is an amplitude of about 177 dB [1]. In the context of this dissertation, the main focus is on linear acoustics.

The surrounding medium strongly influences the propagation of sound waves. Sound propagation in gases or liquids allows only longitudinal waves due to negligible viscous forces and is governed by the acoustic wave equation. In contrast, solids allow longitudinal and solenoidal or transverse waves that are governed by the Navier-Lamé equation [2]. Mechanical-acoustic interaction is represented by strong or weak coupling [3, 4]. In the first case, the mutual interaction is considered and the governing equations of the fluid and the solid are solved simultaneously. The second case uses the simplification that the fluid loads acting on the structure are negligible, allowing the systems to be solved iteratively.

Another influencing factor is the extent of the domain. Sound waves in closed fluid domains describing a system in a steady-state must satisfy the Helmholtz equation, which can be completely closed by Dirichlet, Neumann, or Robin boundary conditions [5]. Those systems are called interior Helmholtz problems. In contrast, the underlying domains of unbounded or exterior Helmholtz problems are assumed to be so large that the influence of the outer boundaries can be neglected. Therefore, they are modeled by an infinite domain. Thus, sound waves must satisfy the Helmholtz equation and, additionally, the Sommerfeld radiation condition (SRC) [6, 7].

Infinite domains lead to problems with established numerical approaches, i.e. the finite element method (FEM) [5, 8–11]. A popular technique for solving unbounded Helmholtz

## 1 Introduction

problems is the boundary element method (BEM) [12–15]. It is based on the Kirchhoff-Helmholtz integral, where Green’s function is a fundamental solution established to solve the Helmholtz operator and implicitly satisfies the SRC. Nevertheless, a side effect of the BEM for unbounded domains is irregular frequencies [16]. In addition, the BEM leads to frequency-dependent dense system matrices. Another approach to solving unbounded Helmholtz problems is to use the FEM combined with an artificially truncated domain. Because the domain truncation must mimic an infinite domain, special treatment of the outer boundaries is required. Three possible methods are artificial absorbing boundary condition [17–19], perfectly matched layers (PMLs) [20–25], and infinite elements [26–28]. A comprehensive review of all three methods can be found in the literature [29–31].

Unbounded Helmholtz problems are typically modeled with deterministic input data. In reality, however, input data such as geometric parameters and material properties are never deterministic, but follow a statistical distribution depending on manufacturing tolerances, imperfections, etc. Uncertainty quantification (UQ) methods are mathematical tools for incorporating stochastic input data into systems and determining corresponding output data [32].

Sound in fluid domains is composed of incident and scattered pressure. Sound sources, such as a vibrating diaphragm in a loudspeaker, generate incident pressure. The pressure field distribution follows the Helmholtz equation, and therefore, the transfer paths depend on the sources and objects within or bounding the fluid domain. One question remains: how can it be subject to manipulation and even designed engineering?

Acoustic metamaterials (AMMs) are an emerging trend that allows the design of acoustic fields. A comprehensive review can be found in the literature [33–42]. AMMs defy the capabilities of conventional materials by exhibiting material parameters not found in nature. Their design is usually based on the assumption of an arrangement of perfectly periodic meta-atoms and is, therefore, modeled in reciprocal space. However, the uncertainties in the system, the interaction between the meta-atoms, and the diffraction at the corners of the AMM structure cannot be described.

In addition, mechanisms derived from quantum mechanical theorems can be used to enhance field manipulation. Bound states in the continuum are one such mechanism, leading to high-quality (Q) factor modes when slightly perturbed. These modes manifest in the form of Fano resonances upon coupling into the continuous spectrum. However, they are highly sensitive to variations in geometric parameters and highly attenuated by thermo-viscous losses, which poses a challenge in their application to acoustic devices such as acoustic filters and sensors. See the literature for a comprehensive review [43–47].

The development of new techniques for sound field engineering of open systems is the main goal of this dissertation. Therefore, a new method is developed to account for uncertainties in unbounded domains. Normal modes of open systems are further investigated for this purpose. In addition, an acoustic metamaterial for automotive applications is designed

based on these methods. Fundamental effects between meta-atoms and their potential for metamaterial tuning are also investigated. The last and most important part of this dissertation is the engineering of high-Q Fano resonances in open acoustic systems.

## 1.2 State-of-the-art

A comprehensive literature review is provided on the topics of the dissertation.

### 1.2.1 Open systems

Computational solution techniques for exterior Helmholtz problems can be divided into two categories: surface-based methods and domain-based methods. The BEM [12–15] falls in the category of surface-based methods. By discretizing only the surface of the radiator and the surfaces of the scattering objects, the number of degrees of freedom is reduced compared to domain-based methods. However, system matrices are usually neither Hermitian nor positive definite [5]. Domain-based methods such as the FEM [5, 8–11], on the other hand, require artificial truncation of the domain and special treatment of the outer boundary to satisfy the SRC. Absorbing boundary conditions [17–19] and PMLs [20–25] rely on artificial dissipation, while the infinite element method (IFEM) relies on elements whose interpolation functions implicitly satisfy the SRC [6, 7].

#### Infinite element method

Infinite elements for exterior Helmholtz problems were first proposed by Zienkiewicz and Bettess [48]. Since then, either unconjugated or conjugated formulations have been used for infinite elements [49]. The unconjugated formulation is a traditional Bubnov-Galerkin method and is typically used for the Burnett [27], Bettess elements [28], and Bettess elements with adjusted decay rate [50, 51]. The unconjugated formulation results in symmetric system matrices. However, they are frequency-dependent due to the oscillatory term in the radial interpolation function. The conjugated formulation is a Petrov-Galerkin method, where the radial interpolation function is a complex conjugate of the test function and was proposed by Gerdes [52]. The Astley-Leis formulation is based on the wave-envelope element method, which is also a Petrov-Galerkin method with an additional geometric weight [26, 53–56]. Astley-Leis elements fit the general framework proposed by Leis [57]. In general, there are four types of infinite elements: separable-unconjugated, separable-conjugated, mapped-unconjugated, and mapped-conjugated. The underlying truncated finite element domain is either circular/spherical [54, 55] or elliptical/spheroidal [27, 56, 58–61]. The neighboring infinite elements are based on the discretized form of the finite element domain. A comprehensive review of infinite elements can be found in literature [49, 62–64].

Astley and Coyette [60] compare the performance of unconjugated Burnett and conjugated Astley-Leis elements for spheroidal domains. At high frequencies and aspect ratios, both formulations reach their limits. Astley [62] evaluates the accuracy of both

## 1 Introduction

the unconjugated Burnett formulation and the conjugated Astley-Leis formulation. The unconjugated elements outperform the conjugated elements in the near field, while the conjugated elements provide improved performance in the far field, consistent with Gerdes [49] and Shirron [65]. The condition number of the system matrices strongly depends on the radial order of the infinite element. Both formulations become ill-conditioned for large radial orders. Astley et al. [55] also investigate the influence of the radial order on accuracy and matrix conditioning. Accuracy is improved up to a radial order of 11. For an order greater than 10, the ill-conditioning predominates. Astley and Coyette [66] show the influence of the choice of polynomials as radial basis on the condition number of infinite element schemes. The Bettess-Burnett formulation, the conjugated Burnett formulation, and the Astley-Leis formulation are compared. The ill-conditioning of the conjugated formulations can be circumvented by choosing a shifted Legendre radial basis.

Dreyer and von Estorff [67] and von Estorff et al. [68] introduce Jacobi polynomials as radial interpolation functions, leading to low-conditioned system matrices and improved performance with iterative solvers. In addition, Dreyer et al. [69] show that the improved Astley-Leis elements with Jacobi radial basis outperform the traditional wave-envelope elements in almost all simulations. Rui-liang and Hong-zhen [70] present a new ellipsoidal infinite element that is superior in accuracy to other elements in the cases of the dilating sphere and the oscillating sphere. Coyette and Van den Nieuwenhof [71] introduce a conjugated IFEM for half-space acoustic problems. The influence of the distance of infinite elements to a scattering object is investigated by Huang et al. [72]. Infinite elements are also formulated for domains with fluid flow [73, 74] and formulated in the time domain [75–77]. Hardy space infinite elements have been an emerging trend in recent years [78–81]. They are particularly suitable for the calculation of resonances because they preserve the eigenvalue structure of the problem, unlike classical infinite elements and boundary elements [78].

Within the scope of this dissertation, Astley-Leis infinite elements are used. They result in frequency-independent system matrices that are well suited for open-system analysis.

### Normal modes

The modal analysis of an open system solves an eigenvalue problem (EVP) and provides eigenvalues and corresponding modes. In contrast to closed systems, the eigenvalues are mostly complex-valued. The corresponding modes are orthogonal and linearly independent. They represent the distribution of the pressure field corresponding to an eigenvalue and are, thus, the mode shapes of the fluid. Modal methods are more challenging for open systems than for closed ones because the infinite domain assumption can affect the sparsity and symmetry of the system matrices. The frequency independence of the system matrices is a fundamental condition for the calculation of frequency independent normal modes. Conjugated Astley-Leis infinite elements are therefore a suitable method.

Marburg [82] computes the solution to a one-dimensional duct problem with fully absorbing ends. A quadratic EVP is solved based on a state-space formulation. The system response is constructed by superposition of normal modes and its convergence is studied. Another paper by Marburg et al. [83] evaluates the quadratic EVP of two-dimensional open systems using conjugated Astley-Leis infinite elements. The authors propose a formulation to solve the rank deficiency of the hypermatrices. In a third paper by Marburg [84], a mode ranking is established, confirming that only a few modes remain necessary for the determination of sound power based on modal superposition. Tisseur and Meerbergen [85] survey the quadratic EVP. Retka et al. [86] solve a quadratic EVP for a three-dimensional unbounded long slender hollow object. Conjugated Astley-Leis elements are used in combination with an iterative Arnoldi eigenvalue solver. Selected weakly damped normal modes are computed. Retka and Marburg [87] calculate the modes of an open system with flow. They use the Galbrun equation in combination with conjugated Astley-Leis elements. Van Ophem et al. [76] present a novel method enabling model order reduction of a fully-coupled, exterior vibro-acoustic model for time domain simulations. In addition, van Ophem et al. [88] use a Krylov-based model order reduction technique to solve an exterior vibro-acoustic problem. Since the stability of the full model is preserved, a model-based state estimator in the form of a Kalman filter is applied. A finite and infinite element approach is used in both works.

Contour integral methods (CIMs) [89–93] are based on the transformation of a non-linear EVP into a generalized EVP of reduced dimensions. The advantage of these methods is that the most important computations can be performed in parallel. Baydoun et al. [94] investigate the radiation damping in fully coupled sandwich structures by analyzing the eigenvalues of the system. In addition, Baydoun et al. [95] use a subspace iteration eigensolver based on Cauchy integrals to determine the eigenvalues of a musical bell in an unbounded domain. The numerical framework of the two articles by Baydoun et al. is based on a FEM-BEM formulation.

A special feature of the open system is that trapped modes can coexist with the continuous spectrum [96–101]. Hein et al. [100] use Hardy space infinite elements based on the work of Hohage and Nannen [78] and Nannen and Schädle [79] to analyze the eigenfrequencies of an open waveguide.

In this dissertation, normal modes are used to calculate local resonances of meta-atoms.

### 1.2.2 Uncertainty quantification

Probabilistic UQ methods are used to capture the random nature of model parameters or system responses [32]. Thus, input data, such as the excitation of a solid body as an acoustic source, is not represented by a constant value, but by a probability distribution. The type of distribution has to be determined in advance by experiments in order to obtain a realistic representation. The Karhunen-Loève expansion and the Polynomial Chaos expansion are two possible spectral methods for uncertainty quantification [102].

## 1 Introduction

The Karhunen-Loève representation of a stochastic process can be seen as a bi-orthogonal decomposition based on the eigenfunctions obtained by analyzing its correlation function [103, 104]. While the Karhunen-Loève expansion requires the correlation function to be known, polynomial chaos expansions do not depend on the correlation function. They are Fourier-like expansions based on orthogonal polynomials. Stochastic quantities are parameterized and represented by a spectral expansion. There are several approaches to solving the stochastic problem. Galerkin methods, for example, are based on a weighted residual formalism, so they affect the underlying system of equations. Non-intrusive methods are designed to solve the stochastic problem without the need to adjust the infinite element formulation. Compared to orthogonal projection, non-intrusive collocation methods are efficient in terms of computational cost and accuracy [105, 106].

Ghanem and Spanos [107] first introduced the spectral stochastic FEM. Over the past three decades, extensive work has been published on the application of spectral methods to stochastic finite elements [108–112]. There are also several publications on acoustic metamaterials and uncertainty quantification [113–116]. Henneberg et al. [117] demonstrate the need for uncertainty quantification for AMMs in industrial applications. Al Ba’ba’a et al. [118] use polynomial chaos to represent inconsistencies in the unit cell parameters of a metamaterial. The influence on how they change the target band gap width, the frequency range, and the confidence level with which it is guaranteed is investigated. Atzrodt et al. [119] investigate the influence of parameter uncertainties on the stop band behavior of a vibro-acoustic metamaterial plate. Santoro et al. [120] develop a computational framework for uncertain locally resonant metamaterial structures.

As part of this dissertation, polynomial chaos expansions are used in combination with the non-intrusive collocation method to represent uncertain input data in open systems.

### 1.2.3 Acoustic metamaterials

AMMs are artificial structures consisting of an array of meta-atoms [121, 122]. Due to their exotic behavior, they can be used to control or manipulate the propagation of sound and elastic waves [34, 40–42]. Acoustic meta-atoms are mostly based on local resonances. This leads to, for example, a negative effective mass density [123–125], negative bulk modulus [126] or negative refractive index [127].

There are two main approaches to modeling AMMs. The first is to assume perfect periodicity of the meta-atoms. Periodic meta-atoms are called sonic or phononic crystals [128–132]. These periodic structures lead to band gaps, also called stop bands that prohibit wave propagation in particular frequency bands [133–135]. AMMs can be represented in reciprocal space and only a unit cell with periodic Floquet-Bloch boundary conditions needs to be modeled [136, 137]. Furthermore, simply the contours of the irreducible Brillouin zone (IBZ) need to be calculated to obtain the band structures [138]. These band structures are also called dispersion curves. The shape of the Brillouin zone depends on the group symmetry of the structure. Maurin et al. [139] investigate the



probability that the band gap extremum is located on the contour of the IBZ. Nojima and Kamakura [140] introduce spatial anisotropy into the unit cell. Due to the asymmetry of the atomic configurations, the entire first Brillouin zone must be rendered. King and Cox [141] study acoustic band gaps in periodically and quasiperiodically modulated waveguides. Laude et al. [142] show the existence of evanescent Bloch waves in phononic crystals. Romero-García et al. [143] show the existence of evanescent Bloch waves in phononic crystals with point defects. Furthermore Romero-García et al. [144] demonstrate evanescent modes in sonic crystals with point defects. The second approach is to fully model the AMM structure. For example, aperiodic arrays and edge diffraction can be represented [145]. Various types of metamaterials exist. Their working principle is based on, for example, space-coiling resonators [146–151], membrane-type or plate-type structures [152–156], honeycomb-like structures [157–159], and porous structures [160]. Among other things, they can be used for acoustic cloaking [161], acoustic lenses [162–165], and acoustic metagratings [166, 167]. Acoustic metamaterials also have applications in the aerospace [168] and automotive industries [169–173].

Thermo-viscous losses, c.f. [174], can significantly affect the performance of metamaterials, particular for structures with narrow geometry features [121, 175, 176] which is why they are extensively studied in this context [177, 178]. Recent advances in artificial intelligence and deep learning algorithms facilitate the design of AMMs [179–181]. Another development in AMMs is the analysis of coupling between meta-atoms. Meta-atoms are typically spaced less than their operating wavelength, so interactions such as longitudinal coupling [182], also known as pressure coupling, and transverse coupling occur [183]. Since it is not only the transmission or reflection spectra that are of interest, Song et al. [184] investigate the gain of the sound pressure level in a metamaterial cavity. Topology protected states are demonstrated and studied [185–187].

An essential feature of AMMs to achieve perfect absorption is impedance matching [188–191]. AMMs based on Fano resonances are an emerging trend [192, 193]. Fano resonances are narrowband features that are based on destructive interference. Although Fano resonances have narrowband characteristics, broadband capabilities can be achieved [194–196]. A comprehensive overview of AMMs can be found in the following literature [35, 39, 168].

This dissertation includes the development of novel AMMs. It also addresses the analysis of the interaction of meta-atoms.

#### 1.2.4 Bound states in the continuum

In linear acoustics, the continuous spectrum of an open system is spanned by propagating waves that radiate to infinity. Propagating waves are solutions corresponding to complex-valued eigenfrequencies greater than or equal to the cut-off frequency of the system. The continuous spectrum and localized solutions to discrete eigenvalues comprise the entire frequency spectrum of the open system. Localized solutions belonging to discrete eigenvalues outside the continuous spectrum are called bounded states, which are

## 1 Introduction

perfectly confined waves. These evanescent waves are completely decoupled from open propagation channels and thus cannot radiate away. Localized solutions in the continuous spectrum are called trapped modes and result, for example, from the evanescent nature of transverse modes in waveguides. They tend to couple to the open propagation channels and become leaky resonances. For a certain configuration of geometrical parameters, the leaky modes become confined states, better known as (embedded) trapped modes or, more commonly, as bound states in the continuum (BICs). BICs are invisible to extended states in the first propagation channel. Therefore, they can't be excited by them. Embedded trapped modes can be found only for a certain configuration of the geometrical parameters of the system. They are a result of modal coupling via a common continuum, i.e., the interaction of modes of the same symmetry. As a consequence of the interaction, avoided crossings are observed. This is a characteristic feature of the strong coupling regime [197–201]. Mathematically, the discrete eigenvalues of the BIC can be described by a purely real-valued eigenfrequency. BICs were first established by Neumann and Wigner [202], whereas the transfer to acoustics was made by Ursell [203]. By variation of geometrical parameters, BICs become quasi-BICs (QBICs). QBICs are high-Q modes that manifest as Fano resonances when coupled into the propagating spectrum. See Miroschnichenko et al. [204] for a detailed review of Fano resonances.

In recent years, groundbreaking work has been done on symmetry-protected BICs [99, 100, 205–207], Fabry-Pérot BICs [101, 208, 209], and Friedrich-Wintgen BICs [101, 210–212]. In addition, extensive studies have been conducted on a variety of BIC configurations and BIC tuning [46, 197, 213–221]. Topologically protected BICs [222] and corner states as BICs [223] are also comprehensively investigated. Topological Fano resonances are investigated by Zangeneh-Nejad and Fleury [224]. A persistent problem is the sensitivity of the Fano resonances, since small perturbations can lead to strong attenuation of the Fano peak. Huang et al. [225] introduce an analytical framework to construct BICs in an open acoustic resonator. The work is based on the approach published by Maksimov et al. [226] and allows to design BICs at the next level. The achievable Q-factor is a major advantage of BICs. It has been pushed to new limits in recent years [227, 228] and lays the foundation for the future design of high-performance acoustic sensors. Huang et al. [229] demonstrate a Friedrich-Wintgen QBIC that leads to an emission enhancement of a sound source by nearly two orders of magnitude. Recent studies have suggested that acoustodynamic devices can be used for quantum computing [230–233]. The application of mechanical BIC-induced high-Q Fano resonances (e.g., Yu et al. [234]) open a new way of phonon trapping in micromechanical structures. Deriy et al. [235] demonstrate a BIC in a compact solid resonator with a rotational symmetry placed in a gas or nonviscous fluid.

For a comprehensive review of BICs, see Hsu et al. [43], Pagneux [44], Joseph [45], Sadreev [46], and Huang et al. [47].

A technique for the design and accurate prediction of stable high-Q Fano resonances is developed in this dissertation.

## 1.3 Contribution of this dissertation

The following research questions arise from the current state-of-the-art. They form the basis of this dissertation:

1. How to model uncertainties in unbounded domains?
2. How to compute normal modes of mechanical-acoustic coupled problems in unbounded domains?
3. How to tune acoustic metamaterials using coupling?
4. How to reduce tire noise by applying acoustic metamaterials?
5. How to accurately predict high-Q Fano resonances?

These questions are the subject of five publications that form the basis of this dissertation. Reprints of these peer-reviewed publications are included in the appendix. This dissertation contributes to the ongoing research in the field of numerical analysis of exterior Helmholtz problems and in the field of noise control using AMMs. Furthermore, this dissertation allows a significant advancement in the state-of-the-art application of high-Q Fano resonances.

### Publication AP1

F. Kronowetter, L. Moheit, M. Eser, K. K. Sepahvand, and S. Marburg. Spectral Stochastic Infinite Element Method in Vibroacoustics. In: *Journal of Theoretical and Computational Acoustics*, 2020, **28**(02), p. 2050009.

Imperfections, inhomogeneities, and manufacturing tolerances are examples of uncertain input data and have become an integral part of today's numerical models. Uncertainty quantification is a tool for representing uncertain input data in a system. A novel method based on stochastic finite elements is demonstrated that solves exterior Helmholtz problems in the case of multipole excitation and uncertain input data. A spectral stochastic infinite element formulation is obtained from the probabilistic generalized polynomial chaos expansion of the uncertain data. The non-intrusive collocation method is chosen as the solution technique. The performance of the method is demonstrated for two two-dimensional examples. First, an open convertible is analyzed in the half-space domain. The sound propagation from a vibrating windshield as the sound source to the driver's ear is simulated for uncertain impedance data. Second, the normal modes of a single meta-atom are computed. The influence of uncertain geometry parameters on the cavity modes is shown. In addition, the influence of uncertain input data on the dispersion curves of AMMs is investigated. Thus, the spectral stochastic IFEM is well suited for modeling parameter uncertainties in unbounded domains.

## Publication AP2

F. Kronowetter, S. K. Baydoun, M. Eser, L. Moheit, and S. Marburg. A Benchmark Study on Eigenfrequencies of Fluid-Loaded Structures. In: *Journal of Theoretical and Computational Acoustics*, 2020, **28**(02), p. 2050013.

The determination of normal modes of open systems for Helmholtz problems can be accurately solved using a state-space formulation despite the rank deficiency of the hypermatrices. However, if a solid is added to the fluid domain and strong coupling is assumed, the matrix condition will cause the normal mode prediction to fail. A contour integral method based on resolvent moment is demonstrated to solve the quadratic EVP of an unbounded vibro-acoustic problem. Finite elements are used for the solid and fluid domain, whereas conjugated Astley-Leis elements are applied for the complementary domain. Normal modes of a hollow sphere submerged in water are calculated. The numerical results are compared with an analytical solution, with those obtained by boundary element discretizations, and with those obtained by finite element discretizations in conjunction with perfectly matched layers. Extensive parameter studies are performed to evaluate the performance of the method. Additionally, a Rayleigh-Ritz procedure with second-order Krylov subspaces is used to compute the normal modes. The contour integral method achieves significantly smaller residuals of the computed eigenpairs. It is found, that a coupled FEM-IFEM formulation combined with contour integral methods based on resolvent moments is an adequate tool for predicting normal modes of coupled mechanical-acoustic problems in unbounded domains.

## Publication AP3

F. Kronowetter, L. Pretsch, Y. K. Chiang, A. Melnikov, S. Sepehrirahnama, S. Oberst, D. A. Powell, and S. Marburg. Sound attenuation enhancement of acoustic meta-atoms via coupling. In: *The Journal of the Acoustical Society of America*, 2023, **154**(2), pp. 842-851.

Acoustic metamaterials are often modeled in reciprocal space, which allows for computationally efficient and accurate band gap predictions. Under realistic conditions, however, the assumption of a perfect and infinitely periodic assembly of meta-atoms does not hold. Diffraction at the edges of a finite periodic AMM and interactions between acoustic meta-atoms are neglected in this approach. Their influence on the performance of the AMM proved to be particularly important. A new approach is introduced to demonstrate the importance of coupling between acoustic meta-atoms. Extensive numerical studies of different configurations of a pair of resonators show that the coupling can lead to degenerate modes at periodic distances between the resonators. Furthermore, the influence of parameters like distance and relative orientation of the resonators on the coupling is analyzed. It is shown how coupling can be used to tune the sound attenuation properties in simulation and experiment. In summary, it is shown that coupling parameters such as distance, orientation, and radiation loss provide additional degrees of freedom for tuning acoustic meta-atoms.

#### Publication AP4

F. Kronowetter, P. Wagner, J. Kolodi, I. Brabandt, T. Neumeyer, N. Rümmler, and S. Marburg. Novel compound material and metamaterial wheelhouse liners for tire noise reduction. In: *Mechanical Systems and Signal Processing*, 2023, **200**, p. 110548.

The European Union has decided to counteract the increase in traffic noise with stricter regulations. This means a reduction of the pass-by noise of vehicles of 4 dB(A) by 2026. The lightweight construction of automobiles worsens the noise, vibration, and harshness (NVH) performance. Thus, new technologies must be developed to meet the regulations. This paper addresses the design of two novel wheelhouse liners to improve the acoustic attenuation properties in the frequency range of interest. One design consists of porous layers and a microperforated panel, and the other is made of AMM. The two designs differ in how they work. The porous liner targets broadband sound attenuation, while the AMM liner targets a specific frequency of interest. The porous liner is the subject of both analytical and numerical modeling. Since the AMM liner is based on local resonances, the normal modes of the system are calculated and the resonances are identified. Simulated results are validated experimentally by impedance tube, Alpha cabin, and full vehicle measurements. Both types of liners are designed for mass production. They exceed the current state-of-the-art. As a result, tire noise can be significantly reduced by installing AMM liners.

#### Publication AP5

F. Kronowetter, M. Maeder, Y. K. Chiang, L. Huang, J. D. Schmid, S. Oberst, D. A. Powell, and S. Marburg. Realistic prediction and engineering of high-Q modes to implement stable Fano resonances in acoustic devices. In: *Nature Communications*, 2023, **14**(1), p. 6847.

QBICs are high-Q modes that are susceptible to geometric perturbations and visco-thermal losses. When coupled into the continuous spectrum, these high-Q modes manifest as Fano resonances, such as in the reflection spectrum. Accurately predicting stable Fano resonances is, therefore, challenging. Furthermore, it is not known where and when the maximum pressure enhancement occurs in real applications. A Friedrich-Wintgen BIC in an open acoustic cavity is demonstrated in theory and experiment. In addition, the pressure field inside the cavity is mapped using laser Doppler vibrometry, providing the missing field enhancement data. This is also the first visual evidence that an acoustic Friedrich-Wintgen BIC exists. Based on the acquired data, a Fourier transform field decomposition allows the design of a symmetry-reduced BIC. An approximately threefold increase in pressure field is achieved compared to the original cavity. This demonstrates a technique for accurately predicting high-Q Fano resonances under realistic conditions.



## 2 Methods

This section introduces the theoretical background of linear acoustics. Fundamental equations, the FEM, and the IFEM for vibro-acoustic problems are explained. In addition, the spectral stochastic IFEM is introduced. After clarifying the equations and methods, EVPs of unbounded Helmholtz domains, i.e. normal modes, are discussed. The effective non-Hermitian Hamiltonian for open systems is also presented. Additionally, modeling of acoustically effective materials and experimental techniques are introduced.

### 2.1 Governing equations in acoustics

There are two spatial reference systems in continuum mechanics, the Lagrangian and the Eulerian. For fluids, in the Lagrangian frame of reference, an observer follows a control volume containing identical fluid particles along a trajectory and measures its physical quantities. However, it has limitations for large deformations. Such deformations are typical for problems in the field of fluid mechanics. The Eulerian frame of reference is based on an observer measuring physical quantities on a control volume at a fixed location and therefore has no problems dealing with large deformations. Reynold's transport theorem defines the rate of change of a scalar or vector quantity represented by  $\bullet(\mathbf{x}, t)$  within a volume  $\Omega(t)$

$$\frac{D}{Dt} \int_{\Omega(t)} \bullet \, d\mathbf{x} = \int_{\Omega(t)} \left( \frac{\partial}{\partial t} \bullet + \bullet \nabla \cdot \mathbf{v} \right) d\mathbf{x} \quad (2.1)$$

It consists of a local derivative and a convective term and is used to derive the balance equations, i.e. the balance of mass and momentum [5, 236–238]

1. balance of mass:

$$\dot{\rho} + \rho \nabla \cdot \mathbf{v} = 0. \quad (2.2)$$

2. balance of momentum:

$$\rho \dot{\mathbf{v}} + \rho (\mathbf{v} \cdot \nabla) \mathbf{v} + \nabla p = 0. \quad (2.3)$$

The pressure is denoted by  $p(\mathbf{x}, t)$ , the density by  $\rho(\mathbf{x}, t)$  and the velocity by  $\mathbf{v}(\mathbf{x}, t)$ . Eqs. (2.2) and (2.3) are nonlinear due to the convective term. The conservation of mass and momentum is an underdetermined system of equations that can be closed by adding a constitutive equation relating pressure and density [5, 236–239]. This system of equations is called the Euler equations. They are a special case of the Navier-Stokes equations assuming compressible, inviscid, adiabatic fluids. Neither heat transfer nor viscous dissipation is possible with these formulations.

### 2.1.1 Wave equation

The Helmholtz decomposition says that the fluid velocity can be described by the superposition of a curl-free scalar potential  $\phi$  and a divergence-free vector potential  $\boldsymbol{\psi}$  [237]

$$\boldsymbol{v} = \nabla\phi + \nabla \times \boldsymbol{\psi}. \quad (2.4)$$

Equation (2.4) consists of an irrotational part and a purely solenoidal part. The irrotational part also describes the compressible part, while the solenoidal part represents the incompressible part. The proof can be found by inserting Eq. (2.4) into Eq. (2.2), where  $\nabla \cdot (\nabla \times \boldsymbol{\psi}) = 0$ , since the divergence of a curl of a vector potential is zero. Since only irrotational vector fields  $\nabla \times \boldsymbol{v} = \nabla \times \nabla\phi = 0$  have a potential, e.g. homogeneous, inviscid flow, the velocity can be described by  $\boldsymbol{v} = \nabla\phi$ . The propagation of longitudinal waves characterizes irrotational vector fields, while transverse waves are forbidden in inviscid fluids. Under the assumption of only small perturbations, we can describe all physical quantities in terms of a static part and an oscillatory term

$$\rho(\boldsymbol{x}, t) = \rho_0(\boldsymbol{x}, t) + \tilde{\rho}(\boldsymbol{x}, t), \quad (2.5)$$

$$p(\boldsymbol{x}, t) = p_0(\boldsymbol{x}, t) + \tilde{p}(\boldsymbol{x}, t), \quad (2.6)$$

$$\boldsymbol{v}(\boldsymbol{x}, t) = \boldsymbol{v}_0(\boldsymbol{x}, t) + \tilde{\boldsymbol{v}}(\boldsymbol{x}, t) = \tilde{\boldsymbol{v}}(\boldsymbol{x}, t), \quad (2.7)$$

where  $\tilde{\rho}$  the density perturbation,  $\tilde{\boldsymbol{v}}$  the sound particle velocity, and  $\tilde{p}(\boldsymbol{x}, t)$  the sound pressure which is a measure of pressure fluctuations around the static pressure  $p_0$ . Since we are talking about static pressure, which means the fluid is at rest, the velocity of the fluid is assumed to be zero  $\boldsymbol{v}_0(\boldsymbol{x}, t) = 0$ . Hence, we can linearize and simplify Eqs. (2.2) and (2.3), add a constitutive relation, e.g.  $\tilde{p}(\boldsymbol{x}, t) = c_f^2 \tilde{\rho}(\boldsymbol{x}, t)$  [237], and summarize them in the homogeneous wave equation

$$\Delta \tilde{p}(\boldsymbol{x}, t) = \frac{1}{c_f^2} \frac{\partial^2 \tilde{p}(\boldsymbol{x}, t)}{\partial t^2} \quad , \quad \boldsymbol{x} \in \Omega_f \subset \mathbb{R}^d \quad , \quad d = 1, 2, 3, \quad (2.8)$$

with  $c_f$  being the speed of sound in the fluid domain  $\Omega_f$ . The wave equation is a hyperbolic partial differential equation. It depends on space and time. Boundary and initial conditions are required to find a unique solution to the partial differential equation.

### 2.1.2 Helmholtz equation

The system response of a forced oscillation consists of a homogeneous and a particular solution. After the transient response subsides, the steady-state is reached. Mathematically, the homogeneous solution tends to zero, or in other words, the initial conditions decay. What remains is a time-harmonic (periodic) oscillation with constant amplitude and frequency. This steady-state is also called the frequency domain. The transformation of the wave equation into the frequency domain will be shown for the one-dimensional case by means of the following steps as an example:



1. perform a Fourier transform with respect to  $x$ :  $\hat{p}(x, t) = \int_{-\infty}^{\infty} \tilde{p}(x, t) e^{-ikx} dx$ , where  $k = \omega/c_f$  is the wavenumber and  $\omega$  is the angular frequency, resulting in a homogeneous second order ordinary differential equation with constant coefficients, since the spatial derivative has vanished,
2. solve the differential equation by using an exponential function and perform an inverse Fourier transform to get the form of d'Alembert's solution to the wave equation (one dimensional)  $p(x, t) = f(x - c_f t) + g(x + c_f t)$  representing perturbations propagating in positive ( $f$ ) and negative ( $g$ )  $x$ -direction with the speed  $c_f$ . This is the general solution to the one-dimensional wave equation.

Since a superposition of propagating perturbations solves the wave equation, propagating waves correspond to a general solution. Plane waves are a simple solution to the wave equation that can be applied to multidimensional problems. They can be described using Euler's identity  $e^{ix} = \cos(x) + i\sin(x)$  and the time convention in a complex manner [5, 236–239]

$$\tilde{p}(\mathbf{x}, t) = p_+ \cos(\pm(\omega t - k\mathbf{x})) = \Re\left\{p_+ e^{\pm i(\omega t - k\mathbf{x})}\right\} = \Re\left\{\bar{p}(\mathbf{x}) e^{\pm i\omega t}\right\}, \quad (2.9)$$

with  $p_+$  being the pressure amplitude of a plane wave propagating in positive  $x$ -direction and  $\bar{p}(\mathbf{x})$  being the complex-valued pressure amplitude. From here on, for simplicity, the complex-valued sound pressure will be denoted by  $p = \bar{p}$ . The negative sign in front of the  $k\mathbf{x}$  term represents wave propagation in positive  $x$ -direction and vice versa. The choice of the sign  $\pm i(\omega t - k\mathbf{x})$  can be chosen arbitrarily, since  $\cos(x) = \cos(-x)$  and  $\Re\{e^{ix}\} = \Re\{e^{-ix}\}$ .

Inserting the formulation in Eq. (2.9) into Eq. (2.8) is a method of separation of variables and leads to a purely space-dependent formulation of the wave equation, which yields the Helmholtz equation. The Helmholtz equation is an elliptic partial differential equation and its homogeneous form reads as

$$\Delta p(\mathbf{x}) + k^2 p(\mathbf{x}) = 0 \quad , \quad \mathbf{x} \in \Omega_f \subset \mathbb{R}^d \quad , \quad d = 1, 2, 3. \quad (2.10)$$

From here on, we consider only time-harmonic problems. Therefore, the complex-valued pressure amplitude is solely space-dependent.

### Interior Helmholtz problems

The size of the fluid domain is a crucial criterion for the complexity of the acoustic problem. We distinguish between interior and exterior Helmholtz problems. For interior Helmholtz problems, the Helmholtz equation can be closed by specific boundary conditions to obtain the solution to acoustic problems within a fully bounded domain of finite extent. For a better understanding of boundary conditions to a bounded acoustic domain, the impedance  $Z(\mathbf{x}) = p(\mathbf{x})/\mathbf{v}(\mathbf{x}) = Y^{-1}(\mathbf{x})$  with  $Y(\mathbf{x})$  being the admittance and  $\mathbf{v}(\mathbf{x}) = \tilde{\mathbf{v}}(\mathbf{x})$  is introduced. Impedance is generally a complex number with a real part called resistance

## 2 Methods

and an imaginary part called reactance. It can be interpreted as the resistance of a fluid element to oscillation due to pressure fluctuations. Three main boundary conditions (BCs) are commonly used for interior Helmholtz problems:

1. Dirichlet BC:

$$p(\mathbf{x}) = p_0(\mathbf{x}) \quad , \quad \mathbf{x} \in \Gamma_f \subset \mathbb{R}^{d-1}, \quad (2.11)$$

2. Neumann BC:

$$\nabla p(\mathbf{x}) \cdot \mathbf{n}(\mathbf{x}) = \frac{\partial p}{\partial \mathbf{n}}(\mathbf{x}) = \pm i\omega\rho_0 \mathbf{v}(\mathbf{x}) \cdot \mathbf{n}(\mathbf{x}) = \pm i\omega\rho_0 \mathbf{v}_f \quad , \quad \mathbf{x} \in \Gamma_f \subset \mathbb{R}^{d-1}, \quad (2.12)$$

3. Robin BC:

$$\mathbf{v}_f(\mathbf{x}) - \mathbf{v}_s(\mathbf{x}) = Y(\mathbf{x})p(\mathbf{x}) \quad , \quad \mathbf{x} \in \Gamma_f \subset \mathbb{R}^{d-1}. \quad (2.13)$$

The Dirichlet BC or essential BC prescribes an explicit value of the sound pressure at the boundary. In contrast, the Neumann BC or natural BC establishes a relation between the complex-valued sound pressure and the particle velocity of the fluid. The Neumann boundary condition can be derived by taking the normal components of the linearized steady-state expression of the Euler equation, i.e. Eq. (2.3). Two special cases are sound hard and sound soft BCs. The sound hard BC describes a boundary where the normal component of the fluid particle velocity  $\mathbf{v}_f(\mathbf{x})$  is equal to the normal component of the structural particle velocity  $\mathbf{v}_s(\mathbf{x})$ , both being zero. Thus, the impedance is infinite, and the admittance is zero at a rigid boundary. There is no phase change with respect to sound hard boundaries. The opposite is true for the sound soft boundary condition, where impedance is zero and admittance is infinite. The phase change is  $\pi$ . Since boundaries are never completely sound hard or sound soft, the Robin BC is a mixed formulation of Dirichlet and Neumann data. This BC type includes phase change and absorption for coupled adjacent structures.

### Exterior Helmholtz problems

Interior Helmholtz problems are limited to completely bounded fluid domains, such as a closed room. But what about an open window? In this case, the surrounding fluid is assumed to be infinite and thus falls into the category of exterior Helmholtz problems. Unbounded fluid domains must satisfy free field conditions, such as no wave reflection from the boundary at infinity, and the pressure must decay to zero at infinity.

In contrast, unbounded or exterior Helmholtz problems are problems with a fluid domain of infinite extension or problems with a negligible influence of the environment. Additional free field conditions must be satisfied, which is ensured by the SRC [7, 238, 240, 241]

$$\lim_{|\mathbf{x}| \rightarrow \infty} |\mathbf{x}|^\alpha \left( \frac{\partial p}{\partial |\mathbf{x}|} \pm ikp \right) = 0, \quad (2.14)$$

where  $|\mathbf{x}|$  is the radial coordinate and  $\alpha = (d - 1)/2$  for two- and three-dimensional problems ( $d = 2, 3$ ). In the one-dimensional case, there is no pressure decay. Depending on the sign of the time convention, the sign before the term  $ikp$  is different. The Sommerfeld radiation condition, written in Bachmann-Landau notation, consists of three parts:

1.  $p(|\mathbf{x}|)$  is a solution to the Helmholtz equation,
2. decay condition:

$$p(|\mathbf{x}|) = \mathcal{O}(|\mathbf{x}|^{-\alpha}) \quad , \quad |\mathbf{x}| \rightarrow \infty, \quad (2.15)$$

3. radiation condition:

$$\left( \frac{\partial p}{\partial |\mathbf{x}|} - ikp \right) = o(|\mathbf{x}|^{-\alpha}) \quad , \quad |\mathbf{x}| \rightarrow \infty. \quad (2.16)$$

The decay condition assures that  $p(|\mathbf{x}|)$  has an asymptotic upper bound  $|\mathbf{x}|^{-\alpha}$ . The radiation condition characterizes the directional character of the stationary solution in the far field. Only outgoing waves, i.e. waves that propagate away from their corresponding source, are allowed, and it is ensured that  $p$  and  $v$  are in phase in the direction of the propagation of the wave in the infinite limit. The decay condition is automatically satisfied by any function that satisfies both the Helmholtz equation and the radiation condition. The radiation condition decays faster than the decay condition. For an exact formulation of the decay rates, see Hubert and Palencia [241].

### 2.1.3 Navier-Lamé equation

Unlike fluids, solids counteract not only changes in volume but also changes in shape due to elastic resistance. The solid domain is denoted by  $\Omega_s$ . Three equations form the basis for the description of elastic solids. The kinematic equation, which relates strain fields to displacements; the balance equation, which requires the stresses and body forces to be in equilibrium; and the constitutive equation, which relates strains to stresses. In the case of a linear elastic material, strains are linearly related to stresses and can be expressed by Hooke's law [242]. Assuming an isotropic material, the stress-strain relationship can be expressed using the Lamé parameters

$$\lambda_L = \frac{\nu E}{(1 + \nu)(1 - \nu)}, \quad (2.17)$$

and

$$\mu_L = G = \frac{E}{2(1 + \nu)}, \quad (2.18)$$

where the Young's modulus is denoted  $E$ , the shear modulus is denoted  $G$ , and  $\nu$  is Poisson's ratio. Thus, the time-dependent Navier-Lamé equation reads as [243]

$$\mu_L \nabla \cdot \nabla \mathbf{u}(\mathbf{x}, t) + (\lambda_L + \mu_L) \nabla (\nabla \cdot \mathbf{u}(\mathbf{x}, t)) + f_V(\mathbf{x}, t) = \rho \frac{\partial^2 \mathbf{u}(\mathbf{x}, t)}{\partial t^2} \quad , \quad \mathbf{x} \in \Omega_s \subset \mathbb{R}^d, \quad (2.19)$$

where  $\mathbf{u}(\mathbf{x}, t)$  is the time-dependent displacement field,  $\rho$  is the material's mass density, and  $f_V(\mathbf{x}, t)$  are the body forces.

### Waves in solid bodies

The displacement field can be decomposed into an irrotational part and a solenoidal part. Applying the Helmholtz decomposition, see Eq. (2.4) yields

$$\mathbf{u}(\mathbf{x}, t) = \nabla\phi(\mathbf{x}, t) + \nabla \times \boldsymbol{\psi}(\mathbf{x}, t). \quad (2.20)$$

Inserting Eq. (2.20) into Eq. (2.19) and omitting body forces results in

$$\nabla \left( \rho \frac{\partial^2 \phi(\mathbf{x}, t)}{\partial t^2} - (\lambda_L + \mu_L) \Delta \phi(\mathbf{x}, t) \right) + \nabla \times \left( \rho \frac{\partial^2 \boldsymbol{\psi}(\mathbf{x}, t)}{\partial t^2} - \mu_L \Delta \boldsymbol{\psi}(\mathbf{x}, t) \right) = 0. \quad (2.21)$$

By setting both brackets to zero and assuming time-harmonic oscillations, the elastodynamic wave equations for longitudinal waves ( $\nabla \times \mathbf{u}(\mathbf{x}, t) = 0$ ) and transversal waves ( $\nabla \cdot \mathbf{u}(\mathbf{x}, t) = 0$ ) with their corresponding wave velocities are obtained [2].

### Time-harmonic elastodynamics

Due to symmetry, the Cauchy stress tensor  $[\boldsymbol{\sigma}]$  can be written in Voigt notation [244]

$$[\boldsymbol{\sigma}] = \begin{bmatrix} \sigma_{xx} & \sigma_{xy} & \sigma_{xz} \\ \sigma_{yx} & \sigma_{yy} & \sigma_{yz} \\ \sigma_{zx} & \sigma_{zy} & \sigma_{zz} \end{bmatrix} = \begin{bmatrix} \sigma_{11} & \sigma_{12} & \sigma_{13} \\ \sigma_{21} & \sigma_{22} & \sigma_{23} \\ \sigma_{31} & \sigma_{32} & \sigma_{33} \end{bmatrix} \rightarrow \begin{pmatrix} \sigma_{11} \\ \sigma_{22} \\ \sigma_{33} \\ \sigma_{23} \\ \sigma_{13} \\ \sigma_{12} \end{pmatrix} = \begin{pmatrix} \sigma_1 \\ \sigma_2 \\ \sigma_3 \\ \sigma_4 \\ \sigma_5 \\ \sigma_6 \end{pmatrix} = \boldsymbol{\sigma}. \quad (2.22)$$

The differential operator  $\mathbf{B}$  has the definition

$$\mathbf{B} = \begin{bmatrix} \frac{\partial}{\partial x} & 0 & 0 & 0 & \frac{\partial}{\partial z} & \frac{\partial}{\partial y} \\ 0 & \frac{\partial}{\partial y} & 0 & \frac{\partial}{\partial z} & 0 & \frac{\partial}{\partial x} \\ 0 & 0 & \frac{\partial}{\partial z} & \frac{\partial}{\partial y} & \frac{\partial}{\partial x} & 0 \end{bmatrix}^T. \quad (2.23)$$

Therefore, the divergence of the Cauchy stress tensor can be written in terms of

$$\nabla \cdot [\boldsymbol{\sigma}] = \mathbf{B}^T \boldsymbol{\sigma}. \quad (2.24)$$

Hooke's law maps the mechanical strain tensor  $[\boldsymbol{\epsilon}]$  to the Cauchy stress tensor via tensor contraction of the fourth order elasticity tensor  $[\mathbf{c}]$

$$[\boldsymbol{\sigma}] = [\mathbf{c}] : [\boldsymbol{\epsilon}]. \quad (2.25)$$

Assuming only small deformations to occur, the linear strain tensor can be written in displacement formulation  $[\boldsymbol{\epsilon}] = \mathbf{B}\mathbf{u}$ . Thus the Navier-Lamé equation can be reformulated

$$\mathbf{B}^T [\mathbf{c}] \mathbf{B} \mathbf{u}(\mathbf{x}, t) - \rho \frac{\partial^2 \mathbf{u}(\mathbf{x}, t)}{\partial t^2} = f_V(\mathbf{x}, t) \quad (2.26)$$

Due to the assumption of time-harmonic oscillations, the displacement can be expressed as  $\mathbf{u}(\mathbf{x}, t) = \Re \left\{ \bar{\mathbf{u}}(\mathbf{x}) e^{\pm i\omega t} \right\}$ . Inserting this approach into Eq. (2.26) results in

$$\mathbf{B}^T [\mathbf{c}] \mathbf{B} \mathbf{u}(\mathbf{x}) + \rho \omega^2 \mathbf{u}(\mathbf{x}) = f_V(\mathbf{x}). \quad (2.27)$$

## 2.2 Numerical methods

In some cases, an analytical solution of the Helmholtz equation exists, but most solutions depend on numerical methods. The numerical solution of partial differential equations is based on a discrete formulation of the problem. In this formulation, the physical quantities are described only at specific discrete points in the entire domain. The most common numerical methods in linear acoustics are the FEM and the BEM. A more detailed insight into the methods can be found in literature [5, 8–11]. In this dissertation, the focus is on the FEM.

### 2.2.1 Finite element method

The continuous domain is divided into a finite number of elements that span a grid or mesh that approximates the continuous shape of the domain. The physical quantities are evaluated at the mesh nodes and interpolated within each element. Each node contains degrees of freedom in the system of equations. To derive the FEM, a variational form of the Helmholtz equation is formulated.

#### Weak formulation

For this purpose, the Helmholtz equation Eq. (2.10) is multiplied by a weight/test function  $\chi(\mathbf{x}) \in C_0^\infty(\Omega_f) \subset \mathbb{H}_0^1$ , which is the space of functions  $C^\infty(\Omega_f)$  with compact support and integrated over the domain  $\Omega_f$

$$\int_{\Omega_f} \chi(\mathbf{x}) [\Delta p(\mathbf{x}) + k^2 p(\mathbf{x})] d\Omega_f(\mathbf{x}) = 0. \quad (2.28)$$

Applying Green's first identity

$$\int_S \theta(\nabla \zeta \cdot \mathbf{n}) dS = \int_V [\theta \Delta \zeta + \nabla \theta \cdot \nabla \zeta] dV \quad (2.29)$$

to the weak formulation of the Helmholtz equation leads to

$$\begin{aligned} & \int_{\Omega_f} \chi(\mathbf{x}) [\Delta p(\mathbf{x}) + k^2 p(\mathbf{x})] d\Omega_f(\mathbf{x}) = \\ & \int_{\Gamma} \chi(\mathbf{x}) (\nabla p(\mathbf{x}) \cdot \mathbf{n}(\mathbf{x})) d\Gamma(\mathbf{x}) - \int_{\Omega_f} \nabla \chi(\mathbf{x}) \cdot \nabla p(\mathbf{x}) d\Omega_f(\mathbf{x}) + \\ & \int_{\Omega_f} k^2 \chi(\mathbf{x}) p(\mathbf{x}) d\Omega_f(\mathbf{x}) = 0. \end{aligned} \quad (2.30)$$

Considering the directional derivative at the boundary  $\Gamma$   $\nabla p(\mathbf{x}) \cdot \mathbf{n}(\mathbf{x}) = \frac{\partial p}{\partial \mathbf{n}}(\mathbf{x})$  results in

$$\int_{\Gamma} \chi(\mathbf{x}) \frac{\partial p(\mathbf{x})}{\partial \mathbf{n}(\mathbf{x})} d\Gamma(\mathbf{x}) - \int_{\Omega_f} \nabla \chi(\mathbf{x}) \cdot \nabla p(\mathbf{x}) d\Omega_f(\mathbf{x}) + \int_{\Omega_f} k^2 \chi(\mathbf{x}) p(\mathbf{x}) d\Omega_f(\mathbf{x}) = 0. \quad (2.31)$$

## 2 Methods

Using  $\frac{\partial p(\mathbf{x})}{\partial n(\mathbf{x})} = a \cdot \mathbf{v}_f(\mathbf{x})$ , with  $a = sk$  and  $s = i\rho_0 c$

$$sk \int_{\Gamma} \chi(\mathbf{x}) \mathbf{v}_f(\mathbf{x}) \, d\Gamma(\mathbf{x}) - \int_{\Omega_f} \nabla \chi(\mathbf{x}) \cdot \nabla p(\mathbf{x}) \, d\Omega_f(\mathbf{x}) + \int_{\Omega_f} k^2 \chi(\mathbf{x}) p(\mathbf{x}) \, d\Omega_f(\mathbf{x}) = 0. \quad (2.32)$$

In a next step, the Robin BC is incorporated replacing  $\mathbf{v}_f(\mathbf{x})$  by  $\mathbf{v}_s(\mathbf{x})$  and  $Y(\mathbf{x})$

$$sk \int_{\Gamma} \chi(\mathbf{x}) \mathbf{v}_s(\mathbf{x}) \, d\Gamma(\mathbf{x}) + sk \int_{\Gamma} \chi(\mathbf{x}) Y(\mathbf{x}) p(\mathbf{x}) \, d\Gamma(\mathbf{x}) - \int_{\Omega_f} \nabla \chi(\mathbf{x}) \cdot \nabla p(\mathbf{x}) \, d\Omega_f(\mathbf{x}) + \int_{\Omega_f} k^2 \chi(\mathbf{x}) p(\mathbf{x}) \, d\Omega_f(\mathbf{x}) = 0. \quad (2.33)$$

This is the weak form of the Helmholtz equation. It is called the weak form because of the reduced continuity requirement for the physical variable, e.g. the sound pressure. The second-order differentiability requirement of the Laplace operator is weakened by shifting a first-order differentiability requirement from the physical quantity to the test function. Equation (2.33) is the basis for the finite element formulation.

### Discretization and matrix form

Since Eq. (2.33) is still formulated in terms of continuous quantities, a discretization procedure for the physical quantities is introduced, the Galerkin scheme. This weighted residual technique is essentially a method of undetermined coefficients with unknown basis coefficients, which generates a system of  $N$  equations. The basis functions  $\underline{\phi}_i$  span the approximation space  $X_0^1 \subset \mathcal{H}_0^1$ . The physical quantities are approximated by

$$p(\mathbf{x}) = \sum_{j=1}^N \phi_j(\mathbf{x}) p_j = \boldsymbol{\phi}^T(\mathbf{x}) \mathbf{p}, \quad (2.34)$$

$$\mathbf{v}_s(\mathbf{x}) = \sum_{k=1}^{\bar{N}} \bar{\phi}_k(\mathbf{x}) v_{sk} = \bar{\boldsymbol{\phi}}^T(\mathbf{x}) \mathbf{v}_s, \quad (2.35)$$

$$Y(\mathbf{x}) = \sum_{l=1}^{\tilde{N}} \tilde{\phi}_l(\mathbf{x}) Y_l = \tilde{\boldsymbol{\phi}}^T(\mathbf{x}) \mathbf{Y}, \quad (2.36)$$

with  $N = \bar{N} = \tilde{N}$  and  $\phi = \bar{\phi} = \tilde{\phi}$ . The physical quantities in Eqs. (2.34) to (2.36) are approximated, discrete values, have no spatial dependence anymore, and are a solution satisfying Eq. (2.33). A Bubnov-Galerkin method is used, which means that the same function is used as the basis and the test function

$$\chi(\mathbf{x}) = \sum_{i=1}^N \underline{\phi}_i(\mathbf{x}), \quad (2.37)$$

with  $\underline{N} = N$  and  $\underline{\phi} = \phi$ . The  $\mathbb{L}_2$  inner product is defined, stating that the residual is orthogonal to the test function

$$\langle \chi(\mathbf{x}), \Delta p(\mathbf{x}) + k^2 p(\mathbf{x}) \rangle = 0. \quad (2.38)$$

The inner product statement is quite powerful since it states that the approximated solution is an  $a$ -orthogonal projection of the real solution onto the approximation space, and thus the best fit in terms of the energy norm. Applying these formulations to Eq. (2.33) leads to the discretized form of the Helmholtz equation's weak form

$$\begin{aligned} & sk \int_{\Gamma} \left[ \sum_{i=1}^N \phi_i(\mathbf{x}) \right] \left\{ \sum_{k=1}^N \phi_k(\mathbf{x}) v_{sk} + \left[ \sum_{l=1}^N \phi_l(\mathbf{x}) Y_l \right] \left[ \sum_{j=1}^N \phi_j(\mathbf{x}) p_j \right] \right\} d\Gamma(\mathbf{x}) \\ & - \int_{\Omega_f} \left\{ \nabla \left[ \sum_{i=1}^N \phi_i(\mathbf{x}) \right] \cdot \nabla \left[ \sum_{j=1}^N \phi_j(\mathbf{x}) p_j \right] - k^2 \left[ \sum_{i=1}^N \phi_i(\mathbf{x}) \right] \left[ \sum_{j=1}^N \phi_j(\mathbf{x}) p_j \right] \right\} d\Omega_f(\mathbf{x}) = 0, \end{aligned} \quad (2.39)$$

with the mass matrix  $\mathbf{M}$ :

$$m_{ij} = \int_{\Omega_f} \phi_i(\mathbf{x}) \phi_j(\mathbf{x}) d\Omega_f(\mathbf{x}), \quad (2.40)$$

the stiffness matrix  $\mathbf{K}$ :

$$k_{ij} = \int_{\Omega_f} \nabla \phi_i(\mathbf{x}) \cdot \nabla \phi_j(\mathbf{x}) d\Omega_f(\mathbf{x}), \quad (2.41)$$

the damping matrix  $\mathbf{D}$ :

$$d_{ij} = \rho_0 c \int_{\Gamma} \phi_i(\mathbf{x}) \left[ \boldsymbol{\phi}^T(\mathbf{x}) \mathbf{Y} \right] \phi_j(\mathbf{x}) d\Gamma(\mathbf{x}), \quad (2.42)$$

and the boundary mass matrix  $\boldsymbol{\Theta}$ :

$$\theta_{ik} = \int_{\Gamma} \phi_i(\mathbf{x}) \phi_k(\mathbf{x}) d\Gamma(\mathbf{x}). \quad (2.43)$$

The system can now be written in matrix form

$$\left( \mathbf{K} - ik\mathbf{D} - k^2\mathbf{M} \right) \mathbf{p} = sk\boldsymbol{\Theta}\mathbf{v}_s = \mathbf{f}. \quad (2.44)$$

Equation (2.44) is a discrete formulation of the continuous weak form. Thus, the physical quantities are approximated by interpolation functions with local support. However, two problems remain to be solved. First, the interpolation functions are space-dependent, and the integration domains are based on finite elements. Therefore, it is quite complicated to perform the integration in the physical space. Second, the integration itself is a continuous-space operation.

### Isoparametric concept

The first problem is solved by introducing the isoparametric concept. According to this concept, a standard element geometry is defined in the parameter space. A mapping between this parameter space and the real space is defined. Thus, the integration takes place in the parameter space  $\xi$ . This is shown in Fig. 2.1 for a two-dimensional quadrilateral element with four nodes. From here on, the matrix computation is explained

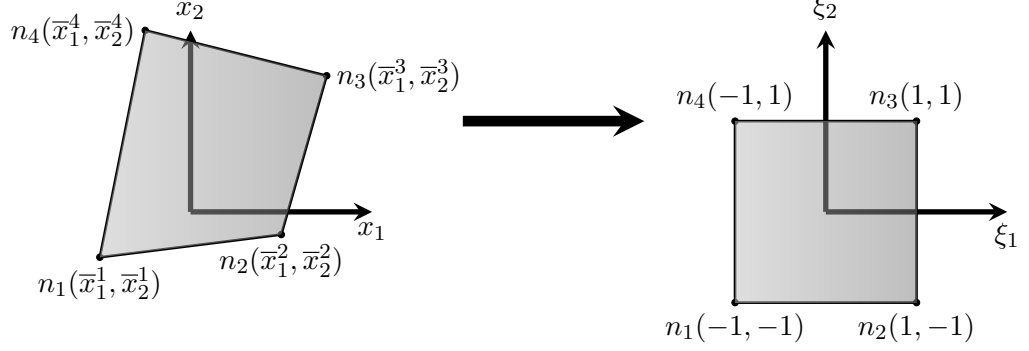


**Figure 2.1: Isoparametric concept.** A two-dimensional element with four nodes in the real space and in the parameter space is presented.

for two-dimensional problems. However, it can easily be extended to the third dimension. The Cartesian nodal coordinates are denoted  $\bar{x}$  and the shape functions in the parameter space are defined by

$$\mathbf{x}(\xi) = \phi^T(\xi)\bar{\mathbf{x}}. \quad (2.45)$$

The nodal discretization for the element shown in Fig. 2.1 reads as

$$\begin{bmatrix} x_1 \\ x_2 \end{bmatrix}_{(\xi)} = \begin{bmatrix} \phi^1 & 0 & \phi^2 & 0 & \phi^3 & 0 & \phi^4 & 0 \\ 0 & \phi^1 & 0 & \phi^2 & 0 & \phi^3 & 0 & \phi^4 \end{bmatrix}_{(\xi)} \begin{bmatrix} \bar{x}_1^1 \\ \bar{x}_2^1 \\ \bar{x}_1^2 \\ \bar{x}_2^2 \\ \vdots \\ \bar{x}_2^4 \end{bmatrix}. \quad (2.46)$$

The nodal coordinates are now defined in the parameter space. Thus, the partial and total derivatives can also be formulated in parameter space. Therefore, the chain rule is applied

$$\frac{\partial \bullet}{\partial x_1} = \frac{\partial \bullet}{\partial \xi_1} \frac{\partial \xi_1}{\partial x_1} + \frac{\partial \bullet}{\partial \xi_2} \frac{\partial \xi_2}{\partial x_1}. \quad (2.47)$$

Equation (2.47) can also be expressed in matrix form

$$\begin{bmatrix} \frac{\partial \bullet}{\partial x_1} \\ \frac{\partial \bullet}{\partial x_2} \end{bmatrix} = \begin{bmatrix} \frac{\partial \xi_1}{\partial x_1} & \frac{\partial \xi_2}{\partial x_1} \\ \frac{\partial \xi_1}{\partial x_2} & \frac{\partial \xi_2}{\partial x_2} \end{bmatrix} \begin{bmatrix} \frac{\partial \bullet}{\partial \xi_1} \\ \frac{\partial \bullet}{\partial \xi_2} \end{bmatrix} \rightarrow \begin{bmatrix} \frac{\partial \bullet}{\partial \xi_1} \\ \frac{\partial \bullet}{\partial \xi_2} \end{bmatrix} = \begin{bmatrix} \frac{\partial x_1}{\partial \xi_1} & \frac{\partial x_2}{\partial \xi_1} \\ \frac{\partial x_1}{\partial \xi_2} & \frac{\partial x_2}{\partial \xi_2} \end{bmatrix} \begin{bmatrix} \frac{\partial \bullet}{\partial x_1} \\ \frac{\partial \bullet}{\partial x_2} \end{bmatrix}. \quad (2.48)$$



Hence, a transformation from real to parameter space is defined. It is called the Jacobian matrix

$$\mathbf{J} = \frac{\partial \mathbf{x}}{\partial \boldsymbol{\xi}} = \begin{bmatrix} \frac{\partial x_1}{\partial \xi_1} & \frac{\partial x_2}{\partial \xi_1} \\ \frac{\partial x_1}{\partial \xi_2} & \frac{\partial x_2}{\partial \xi_2} \end{bmatrix} = \begin{bmatrix} \frac{\partial \phi^1}{\partial \xi_1} & \frac{\partial \phi^2}{\partial \xi_1} & \frac{\partial \phi^3}{\partial \xi_1} & \frac{\partial \phi^4}{\partial \xi_1} \\ \frac{\partial \phi^1}{\partial \xi_2} & \frac{\partial \phi^2}{\partial \xi_2} & \frac{\partial \phi^3}{\partial \xi_2} & \frac{\partial \phi^4}{\partial \xi_2} \end{bmatrix} \begin{bmatrix} \bar{x}_1^1 & \bar{x}_2^1 \\ \bar{x}_1^2 & \bar{x}_2^2 \\ \bar{x}_1^3 & \bar{x}_2^3 \\ \bar{x}_1^4 & \bar{x}_2^4 \end{bmatrix}. \quad (2.49)$$

Equation (2.49) is purely dependent on  $\boldsymbol{\xi}$  with the input of the nodal coordinates in real space. Total derivatives can be expressed as

$$d\mathbf{x}_i = \frac{\partial x_i}{\partial \xi_1} d\xi_1 + \frac{\partial x_i}{\partial \xi_2} d\xi_2. \quad (2.50)$$

Thereupon, the area of a domain is defined by the cross product

$$\begin{aligned} d\Omega &= |d\boldsymbol{\Omega}| = |d\mathbf{x}_1 \times d\mathbf{x}_2| = \left| \left( \frac{\partial x_1}{\partial \xi_1} d\xi_1 + \frac{\partial x_1}{\partial \xi_2} d\xi_2 \right) \times \left( \frac{\partial x_2}{\partial \xi_1} d\xi_1 + \frac{\partial x_2}{\partial \xi_2} d\xi_2 \right) \right| = \\ &= \left( \frac{\partial x_1}{\partial \xi_1} \frac{\partial x_2}{\partial \xi_2} - \frac{\partial x_1}{\partial \xi_2} \frac{\partial x_2}{\partial \xi_1} \right) |d\xi_1 \times d\xi_2| = \det(\mathbf{J}) d\xi_1 d\xi_2. \end{aligned} \quad (2.51)$$

The Jacobian  $\mathcal{J}$  is defined by  $\det(\mathbf{J})$ . It contains information about the transformation behavior. The Jacobian must be greater than zero for FEMs to avoid negative volumes. To determine all the integrands, the interpolation functions are defined. The choice of interpolation functions is critical for matrix conditioning. Since FEMs integrate element-wise, the interpolation function has local support. In this dissertation, the focus is on Lagrangian interpolants. Lagrangian bases must satisfy the orthogonality condition  $\phi_i(\xi_j) = \delta_{ij}$ , which is called the orthogonality condition. The approximation space  $X_0^N \subset \mathbb{P}_N$  is the space of all polynomials of degree  $\leq N$ . Hence, the Lagrange polynomial in the parameter space is defined by

$$L_k^{N-1}(\xi) = \prod_{\substack{j=1 \\ j \neq k}}^N \frac{\xi - \bar{\xi}^j}{\bar{\xi}^k - \bar{\xi}^j}. \quad (2.52)$$

The interpolation function passes through  $n = N$  nodes with coordinates  $\bar{\xi}^j$ ,  $j = 1, \dots, n$  of which node  $k$  evaluates unity. The solution to the first problem is now closed.

## Numerical integration

The continuous integrals need to be discretized to solve the second problem. Therefore, the Gauss-Legendre quadrature is used. It is a method to approximate integrals over a functional multiplied by a weighted summation

$$\int_a^b f(\xi) w(\xi) d\xi \simeq \sum_{i=0}^n \alpha_i f(\xi^i). \quad (2.53)$$

## 2 Methods

In contrast to the normal Gauss quadrature, the Gauss-Legendre quadrature has the advantage that  $w(\xi) = 1$  and the upper and lower bounds are bounded by  $a = -1$  and  $b = 1$ . This makes this method ideal for integration on the unit element in the parameter space. Legendre polynomials are orthogonal in  $[-1, 1]$  regarding the weight  $w(\xi) = 1$

$$\langle P_N(\xi), P_M(\xi) \rangle := \int_{-1}^1 P_N(\xi) P_M(\xi) d\xi = 0 \quad , \quad N \neq M. \quad (2.54)$$

A general polynomial  $P(\xi)$  of order  $\leq 2N + 1$  can be described using long division  $P(\xi) = Q(\xi)P_{N+1}(\xi) + R(\xi)$ , with the order of  $Q(\xi)$  and  $R(\xi)$  being  $\leq N$ . Since  $\langle Q(\xi)P_{N+1}(\xi) \rangle \stackrel{!}{=} 0$ , the Gaussian quadrature estimate of the integral of  $P(\xi)$  of order up to  $2N + 1$  is exact if the nodes are roots of the Legendre polynomial of order  $N + 1$ .

### Coupled mechanical-acoustic system

Let  $\Omega_s$  be a solid body bounded by  $\Gamma$  and surrounded by a fluid domain  $\Omega_f$ , see Fig. 2.2. The kinetic condition and the kinematic condition must be considered at the solid-fluid

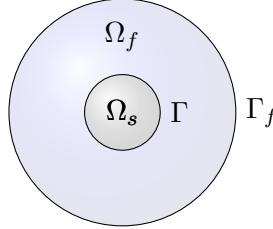


**Figure 2.2: Coupled mechanical-acoustic system.** A coupled mechanical-acoustic system is presented, where  $\Omega_s$  is the solid domain bounded by the solid-fluid interface  $\Gamma$ ,  $\Omega_f$  is the fluid domain with the outer boundary  $\Gamma_f$ .

interface. The first condition relates the Cauchy stress tensor at the interface to the pressure exerted by the fluid

$$\boldsymbol{\sigma}(\mathbf{x}) \cdot \mathbf{n}(\mathbf{x}) = -p(\mathbf{x}) \cdot \mathbf{n}(\mathbf{x}) \quad , \quad \text{on } \Gamma. \quad (2.55)$$

This is the action-reaction principle. It can also be called pressure-force coupling. The second condition ensures that the fluid and solid are in contact without friction

$$\mathbf{n}(\mathbf{x}) \cdot (\mathbf{v}_s(\mathbf{x}) - \mathbf{v}_f(\mathbf{x})) = 0 \quad , \quad \text{on } \Gamma. \quad (2.56)$$

where  $\mathbf{v}_s$  is the velocity of the solid and  $\mathbf{v}_f$  is the acoustic particle velocity. The kinematic condition is also called slippery condition or continuity of velocities. The relationship between the normal components of the acoustic particle velocity and the sound pressure is the linear Euler equation

$$\mathbf{n}(\mathbf{x}) \cdot \rho_0 \frac{\partial \mathbf{v}_f(\mathbf{x}, t)}{\partial t} = -\nabla p(\mathbf{x}, t) \cdot \mathbf{n}(\mathbf{x}). \quad (2.57)$$

This, combined with the assumption  $v_s = \frac{\partial u}{\partial t}$ , and the time-harmonic assumption, leads to a kinematic coupling condition that omits time dependence:

$$\frac{\partial p(\mathbf{x})}{\partial \mathbf{n}(\mathbf{x})} = \rho_0 \omega^2 \mathbf{n}(\mathbf{x}) \cdot \mathbf{u}(\mathbf{x}). \quad (2.58)$$

In a first step, the weak formulation of the Helmholtz equation, see Eq. (2.31), is reformulated using the kinematic coupling condition (Eq. (2.58))

$$\begin{aligned} & \int_{\Gamma} \chi(\mathbf{x}) \frac{\partial p(\mathbf{x})}{\partial \mathbf{n}(\mathbf{x})} d\Gamma(\mathbf{x}) - \int_{\Omega_f} \nabla \chi(\mathbf{x}) \cdot \nabla p(\mathbf{x}) d\Omega_f(\mathbf{x}) + \int_{\Omega_f} k^2 \chi(\mathbf{x}) p(\mathbf{x}) d\Omega_f(\mathbf{x}) = \\ & \int_{\Gamma} \chi(\mathbf{x}) \rho_0 \omega^2 \mathbf{n}(\mathbf{x}) \cdot \mathbf{u}(\mathbf{x}) d\Gamma(\mathbf{x}) - \int_{\Omega_f} \nabla \chi(\mathbf{x}) \cdot \nabla p(\mathbf{x}) d\Omega_f(\mathbf{x}) + \\ & \int_{\Omega_f} k^2 \chi(\mathbf{x}) p(\mathbf{x}) d\Omega_f(\mathbf{x}) = 0. \end{aligned} \quad (2.59)$$

The discretized form of Eq. (2.59) is similar to Eq. (2.39) except for the coupling term

$$\rho_0 \omega^2 \int_{\Gamma} \left[ \sum_{i=1}^N \phi_i(\mathbf{x}) \right] \cdot \mathbf{n}(\mathbf{x}) \cdot \left[ \sum_{n=1}^{N'} \phi_n(\mathbf{x}) u_n \right] d\Gamma(\mathbf{x}). \quad (2.60)$$

In a next step, the weak formulation of the Navier-Lamé equation is derived

$$\begin{aligned} & \int_{\Omega_s} \chi(\mathbf{x}) \cdot \mathbf{B}^T [\mathbf{c}] \mathbf{B} \mathbf{u}(\mathbf{x}) + \rho \omega^2 \mathbf{u}(\mathbf{x}) d\Omega_s(\mathbf{x}) = \\ & \int_{\Omega_s} \chi(\mathbf{x}) \cdot (\rho \omega^2 \mathbf{u}(\mathbf{x})) d\Omega_s(\mathbf{x}) + \int_{\Omega_s} \chi(\mathbf{x}) \cdot [\mathbf{B}^T [\mathbf{c}] \mathbf{B} \mathbf{u}(\mathbf{x})] d\Omega_s(\mathbf{x}) = \\ & \int_{\Omega_s} \chi(\mathbf{x}) \cdot \mathbf{f}_V d\Omega_s(\mathbf{x}). \end{aligned} \quad (2.61)$$

Applying Green's first identity or the general divergence theorem

$$\int_{\Omega} \chi \nabla \cdot \boldsymbol{\sigma} d\Omega = \int_{\Gamma} \chi (\boldsymbol{\sigma} \cdot \mathbf{n}(\mathbf{x})) d\Gamma - \int_{\Omega} \boldsymbol{\sigma} \cdot \nabla \chi d\Omega \quad (2.62)$$

to Eq. (2.61) results in

$$\begin{aligned} & \int_{\Omega_s} \chi(\mathbf{x}) \cdot (\rho \omega^2 \mathbf{u}(\mathbf{x})) d\Omega_s(\mathbf{x}) - \int_{\Omega_s} (\mathbf{B} \chi(\mathbf{x}))^T [\mathbf{c}] \mathbf{B} \mathbf{u}(\mathbf{x}) d\Omega_s(\mathbf{x}) \\ & + \int_{\Gamma} \chi(\mathbf{x}) \cdot (\boldsymbol{\sigma} \cdot \mathbf{n}(\mathbf{x})) d\Gamma(\mathbf{x}) = \int_{\Omega_s} \chi(\mathbf{x}) \cdot \mathbf{f}_V d\Omega_s(\mathbf{x}). \end{aligned} \quad (2.63)$$

Considering  $\boldsymbol{\sigma} \cdot \mathbf{n}(\mathbf{x}) = -p(\mathbf{x}) \cdot \mathbf{n}(\mathbf{x})$ , the kinetic coupling boundary condition can be included

$$\int_{\Gamma} \chi(\mathbf{x}) \cdot (\boldsymbol{\sigma} \cdot \mathbf{n}(\mathbf{x})) d\Gamma(\mathbf{x}) = - \int_{\Gamma} \chi(\mathbf{x}) \cdot \mathbf{n}(\mathbf{x}) \cdot p(\mathbf{x}) d\Gamma(\mathbf{x}). \quad (2.64)$$

## 2 Methods

The discretized form of the Navier-Lamé equation's weak form applying a Bubnov-Galerkin scheme reads as

$$\begin{aligned} & \int_{\Omega_s} \left[ \sum_{m=1}^{N'} \phi_m(\mathbf{x}) \right] \cdot \left\{ \rho \omega^2 \left[ \sum_{n=1}^{N'} \phi_n(\mathbf{x}) u_n \right] \right\} d\Omega_s(\mathbf{x}) - \int_{\Omega_s} \mathbf{B}_m^T[\mathbf{c}] \mathbf{B}_n d\Omega_s(\mathbf{x}) \\ & + \int_{\Gamma} \left[ \sum_{m=1}^{N'} \phi_m(\mathbf{x}) \right] \cdot \mathbf{n}(\mathbf{x}) \cdot \left[ \sum_{j=1}^N \phi_j(\mathbf{x}) p_j \right] d\Gamma(\mathbf{x}) = \int_{\Omega_s} \left[ \sum_{m=1}^{N'} \phi_m(\mathbf{x}) \right] \cdot \mathbf{f}_V d\Omega_s(\mathbf{x}), \end{aligned} \quad (2.65)$$

where the number of degrees of freedom is denoted by  $N'$  and

$$\mathbf{B}_m = \begin{bmatrix} \frac{\partial \phi_m}{\partial x} & 0 & 0 & 0 & \frac{\partial \phi_m}{\partial z} & \frac{\partial \phi_m}{\partial y} \\ 0 & \frac{\partial \phi_m}{\partial y} & 0 & \frac{\partial \phi_m}{\partial z} & 0 & \frac{\partial \phi_m}{\partial x} \\ 0 & 0 & \frac{\partial \phi_m}{\partial z} & \frac{\partial \phi_m}{\partial y} & \frac{\partial \phi_m}{\partial x} & 0 \end{bmatrix}^T. \quad (2.66)$$

The coupled mechanical-acoustic system has the form

$$\left\{ \begin{bmatrix} \mathbf{K}_s & \mathbf{R} \\ \mathbf{0} & \frac{1}{\rho_0} \mathbf{K} \end{bmatrix} - i\omega \begin{bmatrix} \mathbf{D}_s & \mathbf{0} \\ \mathbf{0} & \frac{1}{c_f \rho_0} \mathbf{D} \end{bmatrix} - \omega^2 \begin{bmatrix} \mathbf{M}_s & \mathbf{0} \\ -\mathbf{R}^T & \frac{1}{c_f^2 \rho_0} \mathbf{M} \end{bmatrix} \right\} \begin{pmatrix} \mathbf{u} \\ \mathbf{p} \end{pmatrix} = \begin{pmatrix} \mathbf{f}_s \\ \mathbf{0} \end{pmatrix}, \quad (2.67)$$

with the mass matrix of the solid domain  $\mathbf{M}_s$ :

$$m_{mn,s} = \rho \int_{\Omega_s} \phi_m(\mathbf{x}) \phi_n(\mathbf{x}) d\Omega_s(\mathbf{x}), \quad (2.68)$$

and the stiffness matrix of the solid domain  $\mathbf{K}_s$ :

$$k_{mn,s} = \int_{\Omega_s} \mathbf{B}_m^T[\mathbf{c}] \mathbf{B}_n d\Omega_s(\mathbf{x}). \quad (2.69)$$

The damping matrix depends on the damping model used, e.g. Rayleigh damping. It can be found in the literature [243]. The right hand side is expressed by  $f_s$ :

$$f_{m,s} = \int_{\Omega_s} \phi_m(\mathbf{x}) \cdot \mathbf{f}_V d\Omega_s(\mathbf{x}). \quad (2.70)$$

The coupling at the solid-fluid interface is determined by the following matrix  $\mathbf{R}$

$$\mathbf{R}_{mj} = \int_{\Gamma} \begin{pmatrix} \phi_m \phi_j n_x \\ \phi_m \phi_j n_y \\ \phi_m \phi_j n_z \end{pmatrix} d\Gamma. \quad (2.71)$$

### 2.2.2 Infinite element method

A mapped wave envelope or conjugated Astley-Leis infinite element formulation is used in this dissertation [54, 55]. Finite element discretization is used in the artificially truncated

domain, while infinite elements are used in the complementary domain to mimic the unboundedness of the system. Infinite element basis functions satisfy the SRC through an advanced radial interpolation scheme. These radial interpolation functions have a wave-like characteristic. The conjugated Astley-Leis formulation is based on a Petrov-Galerkin method that uses complex conjugates of the radial interpolation (or basis) functions with an additional geometric factor as the weight functions. Therefore, all wave-like terms in the formulation are eliminated by the use of complex conjugates. All time-harmonic, wave-like terms are eliminated. This results in frequency-independent system matrices in the complementary domain.

### Problem statement

The derivation for two- and three-dimensional infinite elements is similar except for geometric weight and decay factors. The fluid domain is divided into a near-field  $\Omega_f$  and a far-field region  $\Omega_c$ . These regions are separated by  $\Gamma_c$ , see Fig. 2.3. In  $\Omega_f$  and  $\Omega_c$  the

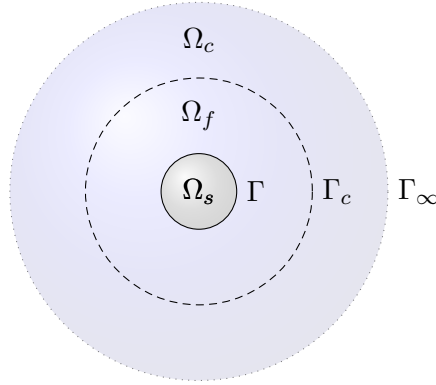


**Figure 2.3: Exterior Helmholtz problem.** A coupled mechanical-acoustic system is presented, where  $\Omega_s$  is the solid domain bounded by the solid-fluid interface  $\Gamma$ ,  $\Omega_f$  is the truncated fluid domain with the outer boundary  $\Gamma_c$ , and  $\Omega_c$  is the complementary domain with the outer boundary at infinity  $\Gamma_\infty$ .

Helmholtz equation must be satisfied. Furthermore, two boundary conditions need to be fulfilled. The continuity of velocities at the solid-fluid interface  $\Gamma$  [3]

$$\mathbf{n}(\mathbf{x}) \cdot \mathbf{a}(\mathbf{x}) + \frac{1}{\rho_0} \nabla p(\mathbf{x}) \cdot \mathbf{n}(\mathbf{x}) = 0, \quad (2.72)$$

and the plane wave damper boundary condition on  $\Gamma_\infty$

$$\nabla p(\mathbf{x}) \cdot \mathbf{n}(\mathbf{x}) + ikp(\mathbf{x}) = 0. \quad (2.73)$$

## 2 Methods

The weak formulation is derived starting from Eq. (2.30) and incorporating the boundary conditions

$$\int_{\Gamma} W(\mathbf{x}, \omega) (\rho_0 \mathbf{n}(\mathbf{x}) \cdot \mathbf{a}(\mathbf{x})) d\Gamma(\mathbf{x}) + \int_{\Gamma_{\infty}} W(\mathbf{x}, \omega) (ikp(\mathbf{x})) d\Gamma(\mathbf{x}) + \int_{\Omega} \nabla W(\mathbf{x}, \omega) \cdot \nabla p(\mathbf{x}) d\Omega(\mathbf{x}) - k^2 \int_{\Omega} W(\mathbf{x}, \omega) p(\mathbf{x}) d\Omega(\mathbf{x}) = 0, \quad (2.74)$$

with  $W(\mathbf{x})$  being the frequency-dependent weight functions.

### Asymptotic form

An infinite number of outwardly propagating solutions exist in unbounded domains. The pressure can thus be expressed as a multipole expansion in spherical coordinates  $(r, \theta, \phi)$  [245] by

$$p(\mathbf{x}, \omega) = e^{-ikr} \sum_{n=1}^{\infty} \frac{G_n(\theta, \phi, \omega)}{r^n}, \quad (2.75)$$

where  $G_n(\theta, \phi, \omega)$  is a directivity function. The Atkinson-Wilcox theorem can be interpreted in terms of near-field and far-field contributions. The far field is dominated by the leading term, while the remaining terms contribute to the near field. The asymptotic form of the far-field contribution is given [246] by

$$p(\mathbf{x}, \omega) = e^{-ikr} \frac{G_1(\theta, \phi, \omega)}{r} + \mathcal{O}\left(\frac{1}{r^2}\right), \quad r \rightarrow \infty. \quad (2.76)$$

Eq. (2.76) is valid for three-dimensional problems. In the case of two-dimensional problems, the decay factor changes from  $1/r$  to  $\sqrt{1/r}$  [247].

### Mapping

For the sake of simplicity, the mapping is explained for two-dimensional problems. Marques and Owen [248] provide the mapping functions for infinite elements. Figure 2.4 shows a two-dimensional infinite element with four radial nodes in the physical and isoparametric space.

Nodes one and two are base nodes that originate from the boundary of the discretized finite element domain  $\Gamma_c$ . The infinite element extends radially, defined by the direction from source points to the corresponding base nodes. It is convenient to define the source points in a single location, such as the center of the fluid domain. The distance from the center to the base nodes is denoted  $r_i = a_i$ . Mapping nodes, nodes one through four, are used to transform the physical element to the parent domain. Furthermore, the nodal degrees of freedom are defined at variable nodes. Often variable nodes coincide with mapping nodes. The mapping is defined by

$$\mathbf{x} = \sum_{i=1}^4 M_i(s, t) \mathbf{x}_i \quad (2.77)$$

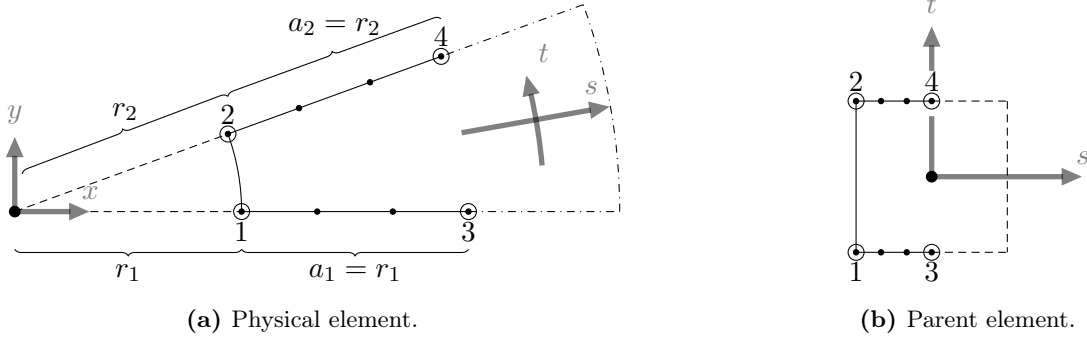


**Figure 2.4: IFEM mapping.** Topology of a two-dimensional infinite element with four radial nodes in the physical space and in the isoparametric space.

where  $M_i(s, t)$  are the mapping functions

$$\begin{aligned}
 M_1(s, t) &= -\frac{(1-t)s}{(s-1)} & , & & M_2(s, t) &= -\frac{(1+t)s}{(s-1)} \\
 M_3(s, t) &= -\frac{(1-t)(1+s)}{2(s-1)} & , & & M_4(s, t) &= -\frac{(1+t)(1+s)}{2(s-1)}.
 \end{aligned} \tag{2.78}$$

The relation between the radial distance  $r$  and the mapped coordinate  $s$  along each side of the element has the form

$$s = 1 - \frac{2a_i}{r} \quad , \quad i = 1, 2. \tag{2.79}$$

Thus, the base nodes with  $r = a_i$  are mapped to  $s = -1$ , the mapping nodes three and four with  $r = 2a_i$  are mapped to  $s = 0$ , and  $s \rightarrow 1$  is mapped to  $r \rightarrow \infty$ . The variable nodes must be chosen carefully to keep the radial expansion of the infinite elements within reasonable limits. The interpolation of  $a_i$  along the inner edge results in

$$a(t) = \sum_i S_i(t) a_j, \tag{2.80}$$

where  $S_i(t)$  are one-dimensional shape functions over the base of the parent element.

### The choice of basis and weight functions

The interpolation functions are described for three-dimensional problems in the  $s - t - v$  coordinate system, where  $s$  is the radial coordinate. The base nodes are repeated  $m$  times in the radial direction, depending on the radial order  $m$ . The radial interpolation functions are based on the Atkinson-Wilcox theorem truncated after  $m$  terms. Thus, the basis function is defined as

$$\psi_l(s, t, v, \omega) = \frac{1-s}{2} S_i(t, v) S_j^m(s) e^{-ik\mu(s, t, v)}. \tag{2.81}$$

## 2 Methods

The phase component reads as  $\mu(s, t, v) = r - a_i = a(t, v) \frac{1+s}{1-s}$ . Based on the mapping point  $i$  and located at the  $j$ -th radial point, it defines the interpolation for node  $l$  on a radial edge.  $S_j^m(s)$  is either a Lagrange polynomial, a Legendre polynomial, or a Jacobian polynomial of order  $m$ . The exponential term represents a radial wave-like factor that equals  $e^{-ik(r-a)}$ . All  $m$  radial nodes are evenly distributed between  $-1$  and  $0$  regarding the parent element. The radial order must be  $m \geq 3$  to avoid improper conditions [55]. Since  $2a_i/r = 1 - s$ , polynomial terms in  $s$  are equivalent to ascending powers in  $a/r$ . Thus, the radial interpolation scheme satisfies the SRC for  $m \geq 1$  and is equivalent to the Atkinson-Wilcox theorem

$$\psi_l(s, t, v, \omega) \sim \left\{ \frac{\alpha_1}{r} + \frac{\alpha_2}{r^2} + \dots + \frac{\alpha_m}{r^m} \right\} e^{-ik(r-a)}. \quad (2.82)$$

The interpolation polynomial is asymptotically correct with the factor  $\frac{a}{r} = \frac{1-s}{2}$  or  $\sqrt{\frac{a}{r}} = \sqrt{\frac{1-s}{2}}$  for two-dimensional problems. Elements of order  $m$  can therefore accurately represent multipole fields of order  $m - 1$ .

The weight functions  $W(\mathbf{s}, \mathbf{t}, \boldsymbol{\omega})$  for the conjugated Astley-Leis formulation are the complex conjugates of the basis function  $\psi_l(s, t, v, \omega)$  with an additional geometric factor  $D(s)$

$$W(s, t, v, \omega) = D(s) \frac{1-s}{2} S_i(t, v) S_j^m(s) e^{ik\mu(s, t, v)}. \quad (2.83)$$

The geometric factor is  $D(s) = ((1-s)/2)^2$  for three-dimensional infinite elements and can be adjusted for two-dimensional problems. Summarizing, both the basis and weight functions behave like a multipole series

$$\psi(r, \omega) \sim \left( \frac{a}{R} \right)^n e^{-ik(r-a)}, \quad W(r, \omega) \sim \left( \frac{a}{R} \right)^{n+2} e^{ik(r-a)}, \quad n = 1, \dots, m. \quad (2.84)$$

### Matrix form

The presence of complex conjugates in the basis and weight functions ensures frequency-independent system matrices. The matrix form can be formulated by rewriting the interpolation functions  $P_l(s, t, v) = \frac{1-s}{2} S_i(t, v) S_j^m(s)$ . The matrix expressions in the infinite element domain are given by the mass matrix  $\mathbf{M}_c$ :

$$m_{ij} = \frac{1}{c_f^2} \int_{\Omega_c} \left\{ DP_i P_j (1 - \nabla \mu \cdot \nabla \mu) \right\} d\Omega_c, \quad (2.85)$$

the stiffness matrix  $\mathbf{K}_c$ :

$$k_{ij} = \int_{\Omega_c} \left\{ (P_i \nabla D + D \nabla P_i) \cdot \nabla P_j \right\} d\Omega_c, \quad (2.86)$$



and the damping matrix  $\mathbf{D}_c$ :

$$c_{ij} = \frac{1}{c_f} \int_{\Omega_c} \left\{ DP_i \nabla \mu \cdot \nabla P_j - P_i P_j \nabla D \cdot \nabla \mu - DP_j \nabla P_i \cdot \nabla \mu \right\} d\Omega_c. \quad (2.87)$$

The fully coupled mechanical-acoustic hypermatrix system reads as

$$\left\{ \begin{bmatrix} \mathbf{K}_s & \mathbf{R} & \mathbf{0} \\ \mathbf{0} & \mathbf{K} & \mathbf{K}_{fc} \\ \mathbf{0} & \mathbf{K}_{cf} & \mathbf{K}_c \end{bmatrix} - i\omega \begin{bmatrix} \mathbf{D}_s & \mathbf{0} & \mathbf{0} \\ \mathbf{0} & \frac{1}{c_f} \mathbf{D} & \mathbf{D}_{fc} \\ \mathbf{0} & \mathbf{D}_{cf} & \mathbf{D}_c \end{bmatrix} - \omega^2 \begin{bmatrix} \mathbf{M}_s & \mathbf{0} & \mathbf{0} \\ -\mathbf{R}^T & \frac{1}{c_f^2} \mathbf{M} & \mathbf{M}_{fc} \\ \mathbf{0} & \mathbf{M}_{cf} & \mathbf{M}_c \end{bmatrix} \right\} \begin{pmatrix} \mathbf{u} \\ \mathbf{p} \\ \mathbf{p}_c \end{pmatrix} = \begin{pmatrix} \mathbf{f}_s \\ \mathbf{0} \\ \mathbf{0} \end{pmatrix}. \quad (2.88)$$

The coupling matrices containing shared nodes at  $\Gamma_c$  are denoted by  $\bullet_{fc}$  and  $\bullet_{cf}$ , respectively. All matrices specified with  $\underline{\bullet}$  are normalized to the fluid density  $\rho_0$ .

### 2.2.3 Spectral stochastic infinite element method

Simulations typically deal with deterministic input data that correspond to a reference or mean value. Under realistic conditions, however, the input data is subject to uncertainties. The uncertain input data can be parameterized by a set of independent random variables  $\boldsymbol{\xi} = \{\xi_1, \dots, \xi_N\}$ , where  $\xi_i(\theta)$  are vectorial quantities in the size of the number of elements in the sample space  $i = 1, \dots, N_s$ . One method for solving problems with uncertain input data is the Monte Carlo method. This method provides an exact solution, but the problem must be solved for each realization of the input data. Therefore, the method requires considerable computational power [249].

### Spectral expansions

Spectral methods, on the other hand, are more efficient and advanced, but more complicated to use. Spectral expansions are based on Fourier-like expansions of a random process in  $\mathbb{L}_2$ , which are convergent with respect to the norm associated with the corresponding inner product. The polynomial chaos expansion, first introduced by Wiener [250], is restricted to Hermite polynomials spanning the orthogonal basis. The choice of polynomials for the expansion depends on the nature of the distribution of the uncertain input data [102]. A more sophisticated model is generalized polynomial chaos (gPC) [251], which is not restricted to Hermite polynomials or Gaussian distributed input data. The gPC allows all kinds of orthogonal polynomials from the Askey scheme [252]. The gPC is accurate to the mean of the data. For numerical calculations, the infinite series representation of a uncertain variable  $X$  must be truncated

$$X(\boldsymbol{\xi}) = \sum_{i=0}^{\infty} x_i \Phi_i(\boldsymbol{\xi}) = \sum_{i=0}^P x_i \Phi_i(\boldsymbol{\xi}) + \epsilon(N, p), \quad (2.89)$$

## 2 Methods

with the approximation error  $\epsilon(N, p)$ . Depending on the number of random variables  $N$  and the highest order  $p$  of the polynomials  $\Phi$ , the number of deterministic coefficients  $x_i$  in the truncated expansion (Eq. (2.89)) is defined as follows

$$P + 1 = \frac{(N + p)!}{N!p!}. \quad (2.90)$$

### Collocation method

A system of equations with spectral expansions of the uncertain input data can be solved using either intrusive or non-intrusive methods. In this dissertation, only the non-intrusive methods are studied, where the system of equations can be treated as a black box. The collocation method is a non-intrusive method that requires solving the system of equations only at certain specially selected collocation points [253–255]. The collocation points are defined by the roots of the polynomial of order  $p + 1$ , sorted by the region with the highest probability, and the required number of points is determined [106]. The deterministic spectral modes are denoted  $x_i$  and the particular solutions of the system of equations  $X^p(\mathbf{cp}^i)$  for the corresponding collocation points  $\mathbf{cp}^i$ .

$$\begin{bmatrix} \Phi_0(\mathbf{cp}^0) & \Phi_1(\mathbf{cp}^0) & \cdots & \Phi_P(\mathbf{cp}^0) \\ \Phi_0(\mathbf{cp}^1) & \Phi_1(\mathbf{cp}^1) & \cdots & \Phi_P(\mathbf{cp}^1) \\ \vdots & \vdots & \ddots & \vdots \\ \Phi_0(\mathbf{cp}^Q) & \Phi_1(\mathbf{cp}^Q) & \cdots & \Phi_P(\mathbf{cp}^Q) \end{bmatrix} \begin{Bmatrix} x_0 \\ x_1 \\ \vdots \\ x_P \end{Bmatrix} = \begin{Bmatrix} X^p(\mathbf{cp}^0) \\ X^p(\mathbf{cp}^1) \\ \vdots \\ X^p(\mathbf{cp}^Q) \end{Bmatrix} \quad (2.91)$$

In the case of multiple random variables  $\xi$ , there are many possible combinations of roots. Thus, the number of collocation points is higher than required  $Q > P$  and the system of equations (Eq. (2.91)) is overdetermined. Optimal points are selected points that capture regions of high probability [256]. In the case of standard normally distributed variables, the origin is the region with the highest probability. If the roots do not contain the value zero, it must be added. Thus, the collocation points are sorted according to the  $\mathbb{L}_2$  criterion. The mean value represents the region with the highest probability. Collocation points in the outer region do not contribute significantly to the solution. For other types of distributions, least squares minimization can be applied and the region of the highest probability is adjusted to the mean of the distribution.

### Matrix form

The matrix form of an open system, c.f. Eq. (2.88), depending on random variables  $\xi$  can be written as follows

$$\left\{ \mathbf{K}(\xi) - i\omega \mathbf{D}(\xi) - \omega^2 \mathbf{M}(\xi) \right\} \mathbf{p}(\xi) = \mathbf{f}(\xi). \quad (2.92)$$

The hypermatrices of Eq. (2.88) are the matrices  $\mathbf{K}$ ,  $\mathbf{D}$  and  $\mathbf{M}$ . The uncertain hypermatrices can then be represented via gPC expansions, such as the uncertain stiffness hypermatrix

$$\mathbf{K}(\xi) \approx \sum_{i=0}^P \mathbf{k}_i \Phi_i(\xi) = \overline{\mathbf{K}}^T \Phi(\xi). \quad (2.93)$$

The deterministic matrix coefficients are denoted by  $\mathbf{k}_i$ . Using gPC expansions to represent the uncertain hypermatrices results in the spectral stochastic IFEM

$$\left\{ \overline{\mathbf{K}}^T \boldsymbol{\Phi}(\boldsymbol{\xi}) - i\omega \overline{\mathbf{D}}^T \boldsymbol{\Phi}(\boldsymbol{\xi}) - \omega^2 \overline{\mathbf{M}}^T \boldsymbol{\Phi}(\boldsymbol{\xi}) \right\} \overline{\mathbf{p}}^T \boldsymbol{\Phi}(\boldsymbol{\xi}) = \overline{\mathbf{f}}^T \boldsymbol{\Phi}(\boldsymbol{\xi}). \quad (2.94)$$

All gPC expansions are assumed to have the same orthogonal basis type  $\boldsymbol{\Phi}(\boldsymbol{\xi})$  for simplicity. The solution of Eq. (2.94) gives an estimate of the unknown deterministic coefficient vector  $\overline{\mathbf{p}}^T$ , where the entries are called spectral modes of the sound pressure. The realizations at the collocation points can be treated as deterministic inputs to the system of equations to generate partial solutions

$$\mathbf{p}_i^p(\mathbf{c}\mathbf{p}_i) = \frac{\overline{\mathbf{f}}^T \boldsymbol{\Phi}(\mathbf{c}\mathbf{p}_i)}{\overline{\mathbf{K}}^T \boldsymbol{\Phi}(\mathbf{c}\mathbf{p}_i) - i\omega \overline{\mathbf{D}}^T \boldsymbol{\Phi}(\mathbf{c}\mathbf{p}_i) - \omega^2 \overline{\mathbf{M}}^T \boldsymbol{\Phi}(\mathbf{c}\mathbf{p}_i)}. \quad (2.95)$$

Similar to Eq. (2.91), the spectral modes can then be calculated from the partial solutions and the coefficient matrix

$$\overline{\mathbf{p}} = \boldsymbol{\Phi}^{-1}(\mathbf{c}\mathbf{p}_i) \mathbf{p}_i^p(\mathbf{c}\mathbf{p}_i). \quad (2.96)$$

With the final solution

$$\mathbf{p}(\boldsymbol{\xi}) = \overline{\mathbf{p}}^T \boldsymbol{\Phi}(\boldsymbol{\xi}). \quad (2.97)$$

Setting the right hand side of Eq. (2.94) to zero leads to a spectral stochastic formulation of the quadratic EVP

$$\overline{\mathbf{Q}}^T(\lambda) \boldsymbol{\Phi}(\boldsymbol{\xi}) = \left\{ \overline{\mathbf{K}}^T \boldsymbol{\Phi}(\boldsymbol{\xi}) + \left[ \overline{\boldsymbol{\lambda}}^T \boldsymbol{\Phi}(\boldsymbol{\xi}) \right] \overline{\mathbf{D}}^T \boldsymbol{\Phi}(\boldsymbol{\xi}) + \left[ \overline{\boldsymbol{\lambda}}^T \boldsymbol{\Phi}(\boldsymbol{\xi}) \right]^2 \overline{\mathbf{M}}^T \boldsymbol{\Phi}(\boldsymbol{\xi}) \right\} \left[ \overline{\mathbf{v}}^T \boldsymbol{\Phi}(\boldsymbol{\xi}) \right]. \quad (2.98)$$

The uncertain complex-valued eigenvalues  $\bar{\omega}(\boldsymbol{\xi})$  are represented by  $\lambda(\boldsymbol{\xi}) = -i\bar{\omega}(\boldsymbol{\xi})$ , with the corresponding gPC expansion  $\lambda(\boldsymbol{\xi}) = \overline{\boldsymbol{\lambda}}^T \boldsymbol{\Phi}(\boldsymbol{\xi})$ . The uncertain fluid-loaded structural modes are represented by  $\mathbf{v}(\boldsymbol{\xi}) = \overline{\mathbf{v}}^T \boldsymbol{\Phi}(\boldsymbol{\xi})$ .

## 2.3 Normal modes

The mechanical-acoustic EVP is obtained by setting the right-hand side of Eq. (2.88) to zero

$$(\mathbf{K} - i\bar{\omega}\mathbf{D} - \bar{\omega}^2\mathbf{M})\mathbf{v} = (\mathbf{K} + \lambda\mathbf{D} + \lambda^2\mathbf{M})\mathbf{v} = \mathbf{0}. \quad (2.99)$$

The matrices  $\mathbf{K}$ ,  $\mathbf{D}$ , and  $\mathbf{M}$  represent the hypermatrices of Eq. (2.88). The complex-valued eigenvalues are denoted by  $\bar{\omega}$  or their corresponding substitutes  $\lambda = -i\bar{\omega}$ . The fluid-loaded structural modes are represented by  $\mathbf{v}$ . Marburg et al. [83] introduce the concept of normal modes to unbounded problems in linear acoustics. The approach is based on the state-space linearization proposed by Ruge [257]. The linearized EVP is defined by the hypermatrix system

$$\left\{ \begin{bmatrix} \mathbf{M} & \mathbf{0} \\ \mathbf{0} & -\mathbf{K} \end{bmatrix} + ik \begin{bmatrix} \mathbf{0} & \mathbf{M} \\ \mathbf{M} & \mathbf{D} \end{bmatrix} \right\} \begin{bmatrix} -ik\mathbf{p} \\ \mathbf{p} \end{bmatrix} = \begin{bmatrix} \mathbf{0} \\ \mathbf{0} \end{bmatrix}. \quad (2.100)$$

This approach results in a generalized EVP that is twice as large.

### 2.3.1 Second-order Krylov subspace methods

The FEM-IFEM formulation given in Eq. (2.99) explicitly depends quadratically on the complex eigenfrequency  $\bar{\omega}$  and hence poses a quadratic EVP. The quadratic EVP can be projected onto a second-order Krylov subspace using a stable model order reduction scheme, see van Ophem et al. [76]. The reduced EVP is transformed into a general EVP. The general EVP is then solved using conventional methods. The orthonormal basis of the projection subspace is generated using a second-order Arnoldi (SOAR) algorithm [258]. The Ritz eigenpairs of a reduced-order quadratic EVP are good approximations of the eigenpairs of the original quadratic EVP [259]. An unsplit orthonormal projection basis  $\mathbf{V}$  is generated using the SOAR algorithm. An arbitrary initialization vector with random values between 0 and 1 is chosen to generate the projection basis. The EVP of reduced dimension  $q$  then reads as [259]

$$(\mathbf{K}_q - i\bar{\omega}\mathbf{D}_q - \bar{\omega}^2\mathbf{M}_q)\mathbf{v}_q = \mathbf{0}, \quad (2.101)$$

with the reduced system matrices given as

$$\mathbf{K}_q = \mathbf{V}^T \mathbf{K} \mathbf{V} \quad , \quad \mathbf{D}_q = \mathbf{V}^T \mathbf{D} \mathbf{V} \quad , \quad \mathbf{M}_q = \mathbf{V}_1^T \mathbf{M} \mathbf{V}_1 \quad , \quad \mathbf{v}_q = \mathbf{V}^T \mathbf{v}. \quad (2.102)$$

Only a part of the unsplit projection basis with entries corresponding to the degrees of freedom of the structural and the acoustic finite element domain ( $\mathbf{V}_1$ ) is considered for the projection of the mass matrix. Thus, the actual zero-block of the mass matrix of the complementary domain  $\underline{\mathbf{M}}_c$  is taken into account, as suggested by van Ophem et al. [76]. Fully populated, dense system matrices of the reduced system result from the projection process. Thus, the reduced quadratic EVP can be solved efficiently, and the resulting eigenvectors of reduced dimensions can be re-projected to the original size to evaluate the relative residuals of the approximate eigenpair solution.

### 2.3.2 Contour integral methods

Typically, CIMs are used to solve nonlinear EVPs. For example, the nonlinear EVP posed by an unbounded mechanical-acoustic problem using a FEM-BEM formulation. However, quadratic EVPs can also be solved with CIMs. CIMs essentially work by transforming a nonlinear EVP into a generalized EVP of reduced dimension. The latter has identical eigenvalues within a predefined region in the complex plane, see Fig. 2.5.

The advantage of CIMs is that key computations can be performed on distributed parallel computers. The block Sakurai Sugiura method (block SS) [89] can be used for solving mechanical-acoustic EVPs. The block SS is a contour integral method based on resolvent moments. It essentially transforms the nonlinear EVP into a generalized EVP with block Hankel matrices containing moments of the resolvent of the system matrix. Using an ellipse defined by a predefined frequency range and aspect ratio as the contour for the CIM is often useful. The contour is also divided into contour points for integration. Since slightly damped complex-valued eigenfrequencies are usually associated with small imaginary parts, this choice of parameters allows a more accurate projection via the CIM than a circular contour. The number of source vectors and the order of the moment

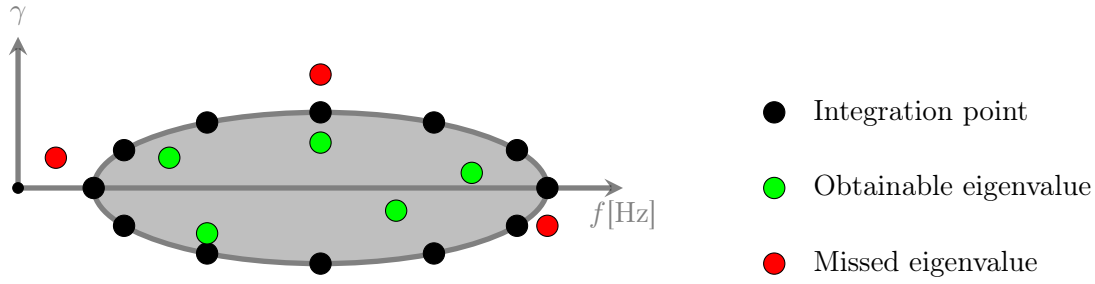


**Figure 2.5: Elliptic domain.** Elliptic contour enclosing the complex domain in which the eigenvalues of interest are to be found.

matrices are the parameters used for block SS. Since the contour of the ellipse and both parameters are critical to the accuracy of the block SS, they must be chosen carefully. Sakurai et al. [260] recommend an appropriate choice of parameters.

## 2.4 Effective non-Hermitian Hamiltonian for open systems

The Hamiltonian goes back to Hamiltonian mechanics [261] and is typically used in classical physics and quantum physics. One of the key postulates of quantum mechanics is the hermiticity of a Hamiltonian [262]. This postulate, which leads to theoretical formulations based on Hermitian Hamiltonians, requires that a closed system has real eigenenergies [263]. In many situations, only a limited subspace of a system is of interest. Energy can be exchanged between the subsystem and its environment. A theoretical framework for the description of open systems is the non-Hermitian theory [264]. The entire Hilbert space is divided into subspaces. One subspace is formed by the eigenfunctions of the localized solutions and another subspace is spanned by the eigenfunctions of the scattering channels. Thus, matching the wave functions of discrete and continuous spectra is a problem in the exact description of open systems. Feshbach's [265] solution was to project the entire Hilbert space onto the discrete eigenstates of the system. This leads to the approach of the effective non-Hermitian Hamiltonian [266–270]

$$\mathbf{H}_{eff} = \mathbf{H}_R - \sum_{p=1}^{\infty} \sum_C i k_p \mathbf{W}_{Cp} \mathbf{W}_{Cp}^\dagger. \quad (2.103)$$

The Hermitian Hamiltonian of the closed system is denoted by  $\mathbf{H}_R$ . The coupling of the localized states to the scattering channel  $C$  is described by the coupling matrix  $\mathbf{W}_{Cp}$  and the symbol  $\dagger$  stands for Hermitian transpose. This simple form is widely used in scattering theory. The real parts of the complex-valued eigenfrequencies of  $\mathbf{H}_{eff}$  correspond to the resonance frequencies, while their imaginary parts correspond to the half-resonant line widths [266,267]. Maksimov et al. [226] state that the effective non-Hermitian Hamiltonian method is analogous to the coupled-mode theory [271,272], except that it neglects the radiation shifts caused by a finite lower band edge and the dispersive properties of the waveguides. Therefore, the effective non-Hermitian Hamiltonian approach can be

## 2 Methods

described as an advanced form of coupled-mode theory. The effective non-Hermitian Hamiltonian application to open acoustic resonators with Neumann boundary conditions has been extensively studied and developed in recent years [46, 213, 225, 226].

### Open duct-cavity system

Steady-state solutions for closed cavities and waveguides with Neumann boundary conditions can be derived analytically [273–276]. For convenience, we describe an open two-dimensional duct-cavity system, shown in Fig. 2.6. The eigenfrequencies of a closed

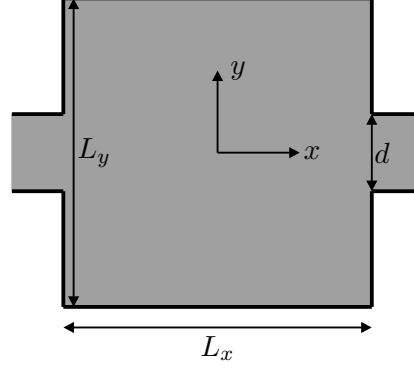


**Figure 2.6: Duct-cavity system.** Schematic drawing of a coupled two-dimensional waveguide-resonator system.

rectangular cavity with Neumann boundary conditions are given by

$$\lambda_{m,n} = \frac{c_f}{2\pi} \sqrt{\left(\frac{(m-1)}{L_x}\right)^2 + \left(\frac{(n-1)}{L_y}\right)^2}, \quad m, n = 1, 2, 3, \dots, \quad (2.104)$$

where the resonant frequency is  $\lambda_{m,n}$ , the speed of sound in air is  $c_f$ , and  $L_x$  and  $L_y$  are the width and the height of the cavity, respectively. The corresponding modes  $\psi$  are defined by

$$\psi_{m,n} = \sqrt{\frac{(2 - \delta_m^1)(2 - \delta_n^1)}{L_x L_y}} \cos\left(\frac{\pi(m-1)(2x + L_x)}{2L_x}\right) \cos\left(\frac{\pi(n-1)(2y + L_y)}{2L_y}\right), \quad (2.105)$$

where  $\delta_n^1$  and  $\delta_m^1$  are the Kronecker deltas. The Neumann waveguide can be decomposed into symmetric and anti-symmetric modes. Symmetric modes are symmetric about the  $x$ -axis, i.e. plane waves can always propagate. The possible wavenumbers for transverse or anti-symmetric modes are defined by

$$k_y = \frac{(p-1)\pi}{h}, \quad p = 1, 2, 3, \dots \quad (2.106)$$

To make the conclusion as general as possible, the height of the waveguide is set to  $h = 1$  (unitless). Thus, all dimensions are measured in terms of the height of the waveguide.

## 2.4 Effective non-Hermitian Hamiltonian for open systems

The resonator's center is set as the origin, and the left and right waveguides are attached along the  $x$ -axis. Thus, the waveguide spans from  $y = -1/2$  to  $y = +1/2$ . The transverse modes  $\phi$  have the form

$$\phi_p(y) = \sqrt{(2 - \delta_p^1)} \cos\left(\frac{\pi(p-1)(2y+1)}{2}\right). \quad (2.107)$$

The propagating solutions in the waveguide are given by

$$\psi_p(x, y) = \frac{1}{\sqrt{4\pi k_p}} e^{\pm i k_p x} \phi_p(y). \quad (2.108)$$

The wavenumber of the  $p$ th channel of the waveguide is denoted by  $k_p$ . Thus the dispersion relation is defined by

$$k_p^2 = k^2 - \left(\frac{(p-1)\pi}{h}\right)^2. \quad (2.109)$$

Transverse modes are propagating modes if  $k_y > ((p-1)\pi)/h$ , i.e. the anti-symmetric threshold is at  $k = \pi/h$ . Thus, transverse modes are evanescent waves if the wavenumber is below the threshold [44].

The entries for the coupling matrix are evaluated as overlapping integrals between transverse waveguide modes and the cavity modes on the waveguide-cavity interface [213, 226, 268]

$$W_{m,n;p} = \int_{-\frac{1}{2}}^{\frac{1}{2}} \psi_{m,n}(x = -\frac{L_x}{2}, y) \phi_p(y) dy. \quad (2.110)$$

The eigenvalues of the effective Hamiltonian can be computed knowing the coupling matrix. The BIC manifests itself as a purely real-valued eigenvalue. The eigenfunction of any BIC can be decomposed as

$$\psi_{BIC} = \sum_{m,n} a_{m,n} \psi_{m,n}(x, y). \quad (2.111)$$

The unknown constants  $a_{m,n}$  can be obtained by solving the effective Hamiltonian's EVP [213, 226]. The BIC is perfectly decoupled from the continuum. Therefore, its eigenfunction must follow

$$\int_{-\frac{1}{2}}^{\frac{1}{2}} \psi_{BIC}(x = \pm \frac{L_x}{2}, y) dy = 0. \quad (2.112)$$

Since mainly two modes interact in the vicinity of a BIC, it is reasonable to truncate the effective Hamiltonian to a 2x2 matrix. Two strongly coupled degenerate modes forming a Friedrich-Wintgen BIC are thus well explained by the two-level effective non-Hermitian Hamiltonian [46, 209, 225, 277]

$$\mathbf{H}_{eff} = \begin{bmatrix} \lambda_{m,n} & 0 \\ 0 & \lambda_{n,m} \end{bmatrix} - i k_p \begin{bmatrix} W_{m,n}^2 & W_{m,n} W_{n,m} \\ W_{n,m} W_{m,n} & W_{n,m}^2 \end{bmatrix}. \quad (2.113)$$

## 2 Methods

The two-level Hamiltonian depends on the wavenumber  $k_p$  and is therefore linked to the eigenvalue via the dispersion relation, see Eq. (2.109). Possible solution techniques are presented by Sadreev [277] as well as by Wiersig and Jörg [278]. Equation (2.113) has a real-valued eigenvalue at the point of degeneracy by varying a control parameter, where the eigenvector contains only two non-zero entries. Thus, the BIC solution can be written as a linear superposition in a two-level approximation at the point of degeneracy. The lowest case of degenerate modes symmetric about the  $x$ -axis in a closed cavity corresponds to  $m = 1, n = 3$  and  $m = 3, n = 1$ . Only the first scattering channel with the wavenumber  $k_1$  is open at the frequency of interest. Propagation channels with  $p > 1$  are further assumed to be closed. The entries of the coupling matrix then read as

$$W_{1,3;p=1} = \sum_{C=L,R} W_{1,3;p=1}^C = \frac{1}{\pi} \sqrt{\frac{2L_y}{L_x}} \left[ \sin\left(\frac{\pi(Ly+1)}{L_y}\right) - \sin\left(\frac{\pi(Ly-1)}{L_y}\right) \right], \quad (2.114)$$

$$W_{3,1;p=1} = \sum_{C=L,R} W_{3,1;p=1}^C = 2\sqrt{\frac{2}{L_x L_y}}. \quad (2.115)$$

The eigenfunction of this Friedrich-Wintgen BIC can be approximated by a superposition of the two eigenmodes of the closed resonator fulfilling Eq. (2.112)

$$\psi_{BIC} \approx a_{1,3}\psi_{1,3}(x, y) + a_{3,1}\psi_{3,1}(x, y). \quad (2.116)$$

The coefficients are defined by [213]

$$a_{1,3} = \frac{W_{3,1;p=1}}{\sqrt{W_{1,3;p=1}^2 + W_{3,1;p=1}^2}}, \quad (2.117)$$

$$a_{3,1} = -\frac{W_{1,3;p=1}}{\sqrt{W_{1,3;p=1}^2 + W_{3,1;p=1}^2}}. \quad (2.118)$$

## 2.5 Modeling of acoustically effective materials

The NVH performance of a system is primarily a function of the mass and stiffness of the materials used. Noise reduction techniques that rely on increased mass and stiffness are not always a viable option. This is especially true when lightweight design criteria are targeted.

### 2.5.1 Porous materials

Porous materials are lightweight and increase sound attenuation. However, their sound attenuation properties are related to their thickness. Therefore, they are effective sound absorbers at higher frequencies. They can be modeled using semi-empirical models. Among other models, the five-parameter Johnson-Champoux-Allard (JCA) model [279–281]



effectively describes the characteristics of acoustic propagation in porous materials. The equivalent dynamic density is given by the following equation

$$\rho_p = \frac{\rho_0 \alpha_\infty}{\phi} \left( 1 + \frac{\phi \sigma}{i \omega \rho_0 \alpha_\infty} \left( 1 + i \frac{4 \omega \rho_0 \eta \alpha_\infty^2}{(\sigma \phi \Lambda)^2} \right)^{\frac{1}{2}} \right) \quad (2.119)$$

and the equivalent bulk modulus by

$$K_p = \frac{\gamma p_0}{\phi} \left( \gamma - (\gamma - 1) \left( 1 + \frac{8 \eta}{i \omega \text{Pr} \Lambda'^2 \rho_0} \left( 1 + i \frac{\omega \text{Pr} \rho_0 \Lambda'^2}{16 \eta} \right)^{\frac{1}{2}} \right)^{-1} \right)^{-1}. \quad (2.120)$$

We define  $\phi$ ,  $\alpha_\infty$ ,  $\sigma$ ,  $\Lambda$ ,  $\Lambda'$ ,  $\text{Pr}$ ,  $\gamma$ , and  $p_0$  as open porosity, high-frequency limit of the tortuosity, static air-flow resistivity, viscous characteristic length, thermal characteristic length, Prandtl number, specific heat ratio of air at room temperature, and ambient pressure, respectively. The characteristic impedance and wavenumber of the equivalent fluid modeling the porous material depend on the square root of the dynamic density and bulk modulus

$$Z_c = \sqrt{\rho_p K_p} \quad , \quad k_p = \omega \sqrt{\frac{\rho_p}{K_p}}. \quad (2.121)$$

### 2.5.2 Microperforated panels

Microperforated panels (MPPs) are another approach to increasing sound attenuation. An MPP can be thought of as an assembly of small tubes connected to a cavity. Each tube and enclosed air cavity acts as an individual Helmholtz resonator. Thus, an MPP can be viewed as a large number of Helmholtz resonators with a common air volume. The advantage of MPPs is that they can be connected in a variety of ways. This makes them adaptable to a wide range of acoustic problems [282–285]. However, MPPs have limitations. These include narrowband absorption, aperture size, and the quarter-wavelength dependence of the cavity required for maximum absorption. One way to overcome these limitations is to combine MPPs and porous materials. In comparison to conventional porous materials, the composite structure has a broadband absorption shifted to a lower frequency [286–291].

The viscous boundary layer thickness is approximately that of the orifices, resulting in high viscous losses and absorption. The oscillating air in the neck acts as a mass and the cavity as a spring, making the resonator a harmonic oscillator. An analytical model is proposed by Maa [292–294]

$$Z_{\text{MPP}} = r + i \omega m. \quad (2.122)$$

The acoustic resistance is denoted by  $r$  and the acoustic mass reactance is denoted by  $m$

$$\begin{aligned} r &= \frac{32 \eta t}{\rho_0 c_0 \sigma d^2} k_r \quad , \quad k_r = \left( 1 + \frac{k_n^2}{32} \right)^{\frac{1}{2}} + \frac{\sqrt{2}}{8} k_n \frac{d}{t} \quad , \quad k_n = \frac{d}{2} \sqrt{\frac{\omega \rho}{\eta}} = \frac{d}{2} \sqrt{\frac{\omega}{\mu}}, \\ m &= \frac{t \rho k_m}{\sigma} \quad , \quad k_m = 1 + \left( 9 + \frac{k^2}{2} \right)^{-\frac{1}{2}} + 0.85 \frac{d}{t}, \end{aligned} \quad (2.123)$$

## 2 Methods

with  $\eta, \sigma, \rho, \omega, d, t$  being the dynamic viscosity of air, perforation ratio, density of air, angular frequency, diameter of the orifice and thickness of the MPP layer, respectively. Using the standing wave approach, the acoustic impedance of the cavity of length  $x$  can be derived as

$$Z_D = -i\rho c_f \cot(kx), \quad (2.124)$$

where  $c_f$  is the speed of sound in air and  $k$  is the wavenumber. The collective impedance is then given by the following equation, which consists of a resistance term  $R = r$  and a reactance term  $X$

$$Z = Z_{\text{MPP}} + Z_D = R + X = r + i(\omega m - \rho c_f \cot(k_0 x)). \quad (2.125)$$

Long-wavelength sound waves in small structures can be approximated by assuming uniform pressure throughout the structures. Thus, small acoustic structures can be analyzed using lumped components [295]. Acoustic elements have mechanical and electrical analogues [296]. Therefore, acoustic elements can be analyzed based on equivalent electric circuits, i.e. an electric circuit consisting of a resistor, an inductor, and a capacitor (RLC). The equivalent RLC series circuit is shown in Fig. 2.7 for a better understanding of the terminology. The reactance term consists of an inductive part  $X_L$  that dominates at

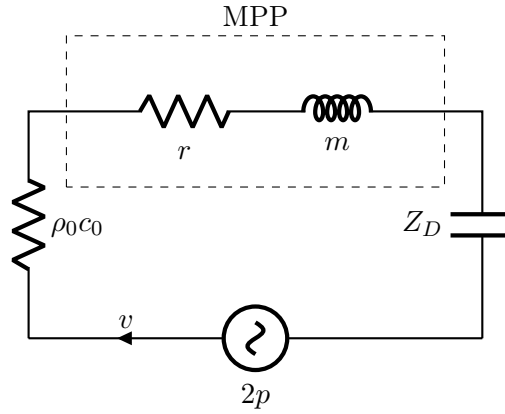


**Figure 2.7: RLC series circuit.** Equivalent circuit for the MPP absorber with air layer.

higher frequencies and a capacitive part  $X_C$  that dominates at lower frequencies

$$X = X_L + X_C = i\omega L + \frac{1}{i\omega C}. \quad (2.126)$$

Regarding a series circuit the resonance corresponds to a minimized impedance. Therefore, the reactance is set to zero  $\omega L - 1/\omega C = 0$ . The resonant frequency of the system can then be extracted from the circuit formulation [293, 297, 298]. Sound absorption under a normal incident wave is defined by [284, 299]

$$\alpha = 1 - \left| \frac{Z - 1}{Z + 1} \right|^2 = \frac{4\text{Re}(Z)}{(1 + \text{Re}(Z))^2 + (\text{Im}(Z))^2}. \quad (2.127)$$

### 2.5.3 Composite materials

The absorption of a single-layer MPP supported by an air-filled cavity is dominated by its resonant frequency. The system can be tuned by filling the hollow space with a porous material. Thus, the surface impedance is obtained by using the transfer matrix method [300, 301]

$$\mathbf{T}_{\text{MPP}} = \begin{bmatrix} 1 & Z_{\text{MPP}} \\ 0 & 1 \end{bmatrix}, \quad \mathbf{T}_p = \begin{bmatrix} \cos(k_p x_p) & iZ_c \sin(k_p x_p) \\ i \sin(k_p x_p)/Z_c & \cos(k_p x_p) \end{bmatrix} \quad (2.128)$$

leading to

$$\mathbf{T} = \mathbf{T}_{\text{MPP}} \mathbf{T}_p = \begin{bmatrix} T_{11} & T_{12} \\ T_{21} & T_{22} \end{bmatrix}, \quad \begin{bmatrix} p_s \\ v_s \end{bmatrix} = \begin{bmatrix} T_{11} & T_{12} \\ T_{21} & T_{22} \end{bmatrix} \begin{bmatrix} p_w \\ v_w \end{bmatrix} \quad (2.129)$$

$$Z_s = \frac{T_{11}}{T_{21}} = Z_{\text{MPP}} - iZ_c \cot(k_p x_p).$$

The individual transfer matrix for a porous layer is denoted by  $\mathbf{T}_p$ , the thickness of the porous layer is denoted by  $x_p$ , the pressure and velocity at the impinged surface of the MPP are denoted by  $p_s, v_s$ , and the pressure and velocity at the rigid wall behind the porous layer are denoted by  $p_w, v_w = 0$ . The transfer matrix method can also be used to calculate an MPP with air cavity. Therefore,  $Z_{\text{MPP}}$  must be multiplied by the impedance of air, and all porous material properties must be replaced by those of air. The absorption coefficient is therefore similar to Eq. (2.127) [299, 302]

$$\alpha = \frac{4 \frac{\text{Re}(Z_s)}{\rho_0 c_0}}{\left(1 + \frac{\text{Re}(Z_s)}{\rho_0 c_0}\right)^2 + \left(\frac{\text{Im}(Z_s)}{\rho_0 c_0}\right)^2}. \quad (2.130)$$

### 2.5.4 Acoustic metamaterials

Scattering from a spherical particle is described by Mie theory [303] in electromagnetism, which is transferred to Rayleigh scattering in acoustics [304]. Bragg scattering [303, 305] describes the scattering of multiple periodic particles. AMMs are typically periodic structures smaller than the wavelength of their operating frequency.

Periodic structures can be classified into space groups, Bravais lattices, and crystal systems [306, 307]. An infinite number of lattice points with corresponding lattice translation vectors can represent a periodic structure. The lattice translation vectors connect two points in the lattice and depend on the basis vectors of the corresponding Bravais lattices and hence on symmetry groups [139]. The translation vectors of the direct lattice span a unit. The smallest units spanned by the lattice vectors are called unit cells. The Wigner-Seitz cell is a special primitive unit cell with a lattice point in the center [138]. Each direct lattice has a unique reciprocal lattice, where the reciprocal lattice vectors are perpendicular to a surface spanned by two direct lattice vectors [308].

A lattice associated with the crystal in Fourier space is called a reciprocal lattice. The magnitude of a reciprocal lattice vector is proportional to  $2\pi$  divided by the spacing

## 2 Methods

between the sides of the unit cell. Therefore, a reciprocal lattice vector is a grating vector, and thus, the diffraction pattern of a periodic structure is a map of its reciprocal lattice [138]. The underlying mathematical model is called the Bloch theorem, which describes the solution of the Schrödinger equation over a periodic structure [137]. In acoustics, the Bloch theorem reads as

$$p(\mathbf{x} + \mathbf{t}) = p(\mathbf{x})e^{i\mathbf{k}\mathbf{t}}, \quad (2.131)$$

where  $p(\mathbf{x})$  has the period of the lattice. The plane wave-like term can be interpreted as changes in the phase of a wave between a plane and its neighboring plane along the direction of translation. Bragg's law states that constructive interference occurs when the path difference is an integer multiple  $n$  of the wavelength  $\lambda$  [138]

$$2d \sin \beta = n\lambda. \quad (2.132)$$

The spacing between two lattice planes is denoted by  $d$  and the glancing angle is denoted by  $\beta$ . The Bragg condition is equivalent to the Laue condition in the reciprocal space

$$|\mathbf{k}| \sin \phi = \frac{\pi n}{d}, \quad (2.133)$$

with the Bloch wave vector  $|\mathbf{k}| = 2\pi/\lambda$ . A Wigner-Seitz cell constructed in the reciprocal lattice is called a Brillouin zone. Due to reciprocity and the fact that a reciprocal lattice uniquely defines a direct lattice, knowing the solution of the Helmholtz equation within the first Brillouin zone also defines the solutions in the entire lattice. Using the symmetry of the lattice, the Brillouin zone can be further reduced to the IBZ. The contour of the IBZ plays a major role in the computation of dispersion curves or band diagrams, which show the eigenvalues of the system in dependence on the Bloch wave vector. Thus, the reciprocal space is also called  $k$ -space. Band diagrams represent eigenvalues evaluated around the perimeter of the IBZ. The reciprocal lattice vectors cover all possible directions of wave propagation in the system, carry spatial information, and show dispersion information due to the interaction between the wave and the periodic structure. However, we lack information about the points inside the IBZ, but since the extremes always occur at the key points of symmetry, it is sufficient to compute the perimeters.

Lattice asymmetry, finite-periodicity, aperiodic arrangements, and edge diffraction distort the results of a perfectly infinite-periodic  $k$ -space approach. Another approach is to compute the normal modes of the entire structure. This way, all effects can be mathematically reproduced, and more realistic results can be obtained.

## 2.6 Experimental techniques

In addition to theoretical and numerical modeling, the experimental validation of mathematical models is an essential part of the scientific process. Because it is difficult to accurately model an experimental setup, ISO standards exist to characterize a system within certain limits. Specific quantities are used to describe a system. These quantities are then used to compare the mathematical prediction with the experimental results.

Two important acoustic quantities are the intensity  $\mathbf{I}(\mathbf{x})$  and the sound power  $P$ . The intensity of the time-harmonic waves is defined by [237, 274]

$$\mathbf{I}(\mathbf{x}) = \frac{1}{2} \Re \left\{ p(\mathbf{x}) \mathbf{v}(\mathbf{x}) \right\}. \quad (2.134)$$

Eq. (2.134) is simplified for plane waves and thus in phase propagation of pressure and particle velocity  $p(\mathbf{x}) = \rho_0 c \mathbf{v}(\mathbf{x})$  as

$$\mathbf{I}(\mathbf{x}) = \frac{1}{2\rho_0 c} \Re \left\{ p(\mathbf{x}) p^*(\mathbf{x}) \right\}. \quad (2.135)$$

Sound power is defined as the intensity integrated over a surface

$$P = \int_S \mathbf{I}(\mathbf{x}) \, d\mathbf{S}. \quad (2.136)$$

### 2.6.1 Impedance tube

Normal incidence material characterization can be performed using a Kundt's tube. Kundt's tube is better known as an impedance tube, which only allows plane wave propagation within a certain frequency range. The complex-valued reflection coefficient  $r$ , the absorption  $\alpha$ , and the complex-valued surface impedance  $Z_s$  of a material or structure under normal incidence can be determined using the standard ISO 10534-2:2023 [309]. A sketch of an impedance tube is shown in Fig. 2.8.

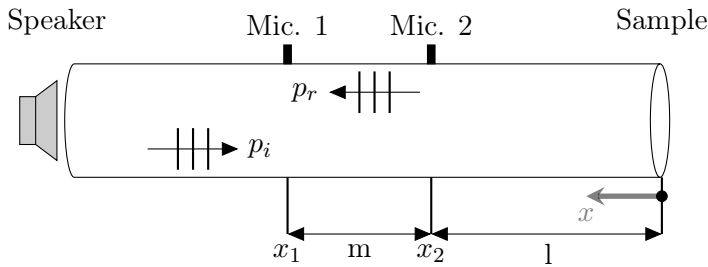


**Figure 2.8: Impedance tube.** A sketch of an impedance tube with two microphones attached. The system is excited by the loudspeaker, which produces a plane wave  $p_i$ . The sample is positioned at the right end of the tube, with its inward-facing surface defining  $x = 0$ . The reflected sound pressure is denoted by  $p_r$ .

A loudspeaker is used to generate a plane wave and the sound pressure is measured with two microphones at the locations  $x_1$  and  $x_2$ . The coordinates  $x_1$  and  $x_2$  are defined by  $x = l + m$  and  $x = l$ , respectively. The cut-on frequencies are defined by the geometry of the tube [274]. The upper and lower frequency limits are defined by the distance of the microphones [309]. The complex-valued sound pressures at the microphone positions are then given by

$$p_1(\omega) = p_i(x_1, \omega) + p_r(x_1, \omega) = p_i(0, \omega) e^{ikx_1} + p_r(0, \omega) e^{-ikx_1} \quad (2.137)$$

## 2 Methods

and

$$p_2(\omega) = p_i(x_2, \omega) + p_r(x_2, \omega) = p_i(0, \omega)e^{ikx_2} + p_r(0, \omega)e^{-ikx_2}. \quad (2.138)$$

The reflected sound pressure can also be expressed as  $p_r(x, \omega) = p_i(x, \omega)r$  [237, 274]. The transfer function between microphone one and microphone two can then be formulated as

$$H_{12} = \frac{p_2(\omega)}{p_1(\omega)} = \frac{e^{-ikx_2} + re^{-ikx_2}}{e^{ikx_1} + re^{ikx_1}}. \quad (2.139)$$

In addition, the transfer functions of the incident and reflected waves between microphone one and microphone two are given by

$$H_i = \frac{p_i(x_2, \omega)}{p_i(x_1, \omega)} = e^{-ikm} \quad (2.140)$$

and

$$H_r = \frac{p_r(x_2, \omega)}{p_i(x_1, \omega)} = e^{ikm}. \quad (2.141)$$

Consequently, the complex-valued reflection coefficient  $r$  can be calculated

$$r = \frac{p_r(0, \omega)e^{-ikx_1}}{p_i(0, \omega)e^{ikx_1}} = \frac{H_{12} - H_i}{H_r - H_{12}} \cdot e^{i2k(m+l)}. \quad (2.142)$$

Based on  $r$ , the complex-valued impedance of the surface can be determined as

$$Z_s = Z_0 \frac{1+r}{1-r}, \quad (2.143)$$

where  $Z_0 = \rho_0 c_0$  is the characteristic acoustic impedance of the fluid medium. The absorption then reads as

$$\alpha = 1 - |r|^2. \quad (2.144)$$

### 2.6.2 Transmission tube

In addition to the reflected spectrum, the transmission of a system is of interest. Therefore, normal incidence transmission loss measurements can be performed. A perfectly anechoic termination is required to accurately determine the transmission loss. Since this is difficult to achieve, the sample must be measured under two different conditions. The most common method is the two-load method [310–314]. It is standardized in ASTM E2611-19 [315]. Figure 2.9 shows a sketch of a transmission tube. The four microphones in combination with the transfer matrix method are used to obtain the complex-valued transmission coefficient  $t$ . A detailed discussion of the methods used can be found in the literature [316–320]. The wave decomposition yields

$$p_i = i \frac{p(x_1)e^{ikx_2} - p(x_2)e^{ikx_1}}{2 \sin k(x_1 - x_2)}, \quad (2.145)$$

$$p_r = i \frac{p(x_2)e^{-ikx_2} - p(x_1)e^{-ikx_1}}{2 \sin k(x_1 - x_2)}, \quad (2.146)$$

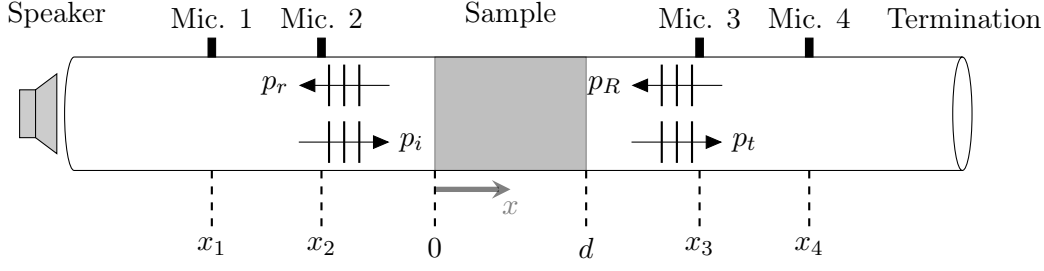


**Figure 2.9: Transmission tube.** A sketch of a transmission tube with four microphones attached. The system is excited by the loudspeaker, which produces a plane wave  $p_i$ . The sample of thickness  $d$  is positioned in the center of the tube. The surface facing the loudspeaker defines  $x = 0$ . The reflected sound pressure is denoted by  $p_r$ , the transmitted sound pressure is  $p_t$ , and the reflected sound pressure behind the sample is  $p_R$ . The two-load method uses two different conditions to determine the transmission loss, such as a sound hard, a sound soft, or an absorbing boundary.

$$p_t = i \frac{p(x_3)e^{ikx_4} - p(x_4)e^{ikx_3}}{2 \sin k(x_3 - x_4)}, \quad (2.147)$$

$$p_R = i \frac{p(x_4)e^{-ikx_3} - p(x_3)e^{-ikx_4}}{2 \sin k(x_3 - x_4)}. \quad (2.148)$$

The evaluation of the pressure and velocity at the surface of the sample leads to the following results [321]

$$p(0) = p_i + p_r \quad , \quad v(0) = \frac{p_i - p_r}{\rho_0 c_0}, \quad (2.149)$$

$$p(d) = p_t e^{-ikd} + p_R e^{ikd} \quad , \quad v(d) = \frac{p_t e^{-ikd} - p_R e^{ikd}}{\rho_0 c_0}. \quad (2.150)$$

The two-port approach, derived from the theory of electrical circuits [322], relates the pressures and velocities at  $x = 0$  and  $x = d$  using the transfer matrix method. The two-load method, with terminations  $a$  and  $b$ , results in a four-pole matrix [323–325]

$$\begin{bmatrix} p_a(0)p_b(0) \\ v_a(0)v_b(0) \end{bmatrix} = \begin{bmatrix} T_{11}T_{12} \\ T_{21}T_{22} \end{bmatrix} \begin{bmatrix} p_a(d)p_b(d) \\ v_a(d)v_b(d) \end{bmatrix}, \quad \mathbf{T} = \begin{bmatrix} T_{11}T_{12} \\ T_{21}T_{22} \end{bmatrix}. \quad (2.151)$$

Reciprocity requires that  $\det \mathbf{T} = 1$  and  $T_{11} = T_{22}$  holds for symmetric samples. The matrix entries are defined as

$$\begin{aligned} T_{11} &= \frac{p(d)v(d) + p(0)v(0)}{p(0)v(d) + p(d)v(0)} \quad , \quad T_{12} = \frac{p(0)^2 - p(d)^2}{p(0)v(d) + p(d)v(0)}, \\ T_{21} &= \frac{v(0)^2 - v(d)^2}{p(0)v(d) + p(d)v(0)} \quad , \quad T_{22} = \frac{p(d)v(d) + p(0)v(0)}{p(0)v(d) + p(d)v(0)}. \end{aligned} \quad (2.152)$$

For an anechoic termination the transmission coefficient  $t$  is calculated by inserting  $p(0) = 1 - r$ ,  $v(0) = (1 - r)/(\rho_0 c_0)$ ,  $p(d) = t e^{-ikd}$ , and  $v(d) = t e^{-ikd}/(\rho_0 c_0)$  into

## 2 Methods

Eq. (2.151) for  $a = b$

$$t = \frac{p_t}{p_i} = \frac{2e^{ikd}}{T_{11} + \frac{T_{12}}{\rho_0 c_0} + \rho_0 c_0 T_{21} + T_{22}}. \quad (2.153)$$

The transmission loss  $L_P$  in dB can be calculated by [326]

$$\begin{aligned} L_P &= 10 \log_{10} \left( \frac{|p_i|^2}{|p_t|^2} \right) = 10 \log_{10} \left( \frac{1}{|t|^2} \right) = \\ &= 20 \log_{10} \left( \frac{1}{|t|} \right) = 10 \log_{10} \left( \frac{P_i}{P_T} \right) = 10 \log_{10} \left( \frac{1}{T} \right), \end{aligned} \quad (2.154)$$

where  $P_i$  is the incident sound power,  $P_T$  is the transmitted sound power, and  $T = |t|^2$  is the transmission.

### 2.6.3 Laser Doppler Vibrometer

Laser Doppler vibrometry is classically used to measure the surface velocity of a vibrating body. The mechanism of operation is based on the Doppler shift of the laser. This is caused by an oscillating reflector. However, Laser Doppler Vibrometer (LDV) measurements can also be used to detect changes in the refractive index of air [327]. This is called refracto-vibrometry and is used to visualize the sound pressure fields. Figure 2.10 shows the setup for a sound field visualization inside a cavity.

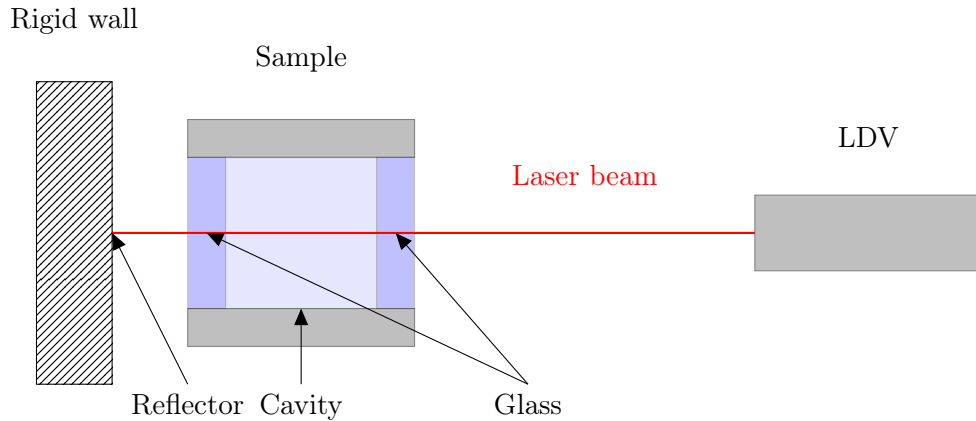


**Figure 2.10: LDV setup.** A sketch of a setup for sound field visualization. The setup consists of an air cavity that can be excited by a loudspeaker. The cavity has two glass sidewalls to ensure viable laser transmission. The laser is reflected from a coated rigid wall.

The laser beam of the scanning LDV passes through a transparent sample and is reflected by a rigid wall. The wall is coated with a highly reflective film. The surface vibration of the rigid wall must also be measured to ensure the required stiffness. It is necessary to ensure that the surface velocities are much smaller than the signal from the scanning LDV. This means that sound pressure changes will dominate the measurement.



The glass walls of the sample should be made of highly transmissive glass to reduce reflections. The thickness of the glass must be such that the glass walls can be considered rigid. Thus, the resonances of the cavity will not interfere with the resonances of the glass. The glass is bonded to the sample and the sample is hermetically sealed. The density variation slightly shifts the phase of the emitted monochromatic laser light due to the propagation of sound waves inside the cavity. The superposition of the reflected and emitted laser light produces a speckle pattern on the photodetector. This allows measurement of the corresponding pressure wave frequency and refractive index change.

Gladstone and Dale [328] established a relation between the refractive index  $n$  and the density  $\rho$  for several fluids. The relationship can be expressed in terms of the refractive index  $n$  and total pressure  $p = p_0 + \tilde{p}$  in the case of air using  $p/p_0 = (\rho/\rho_0)^\gamma$ , where  $\gamma$  is the ratio of specific heats, and a first-order Taylor series approximation as follows

$$n = (n_0 - 1) \left( 1 + \frac{\tilde{p}}{p_0} \right)^{\frac{1}{\gamma}} \cong n_0 + \frac{n_0 - 1}{\gamma p_0} \tilde{p}. \quad (2.155)$$

For simplification,  $\tilde{p}$  is expressed as  $p$ . The refractive index of air determines the phase of light passing through a sound field [329]. The phase depends on the refractive index  $n$ , which can be related to the sound pressure. Therefore, the phase of light can also be related to the sound pressure. The velocity of the LDV being proportional to the dynamic phase of the light can hence be expressed as [330–334]

$$v(\omega) = \omega \frac{1}{\gamma p_0} \frac{n_0 - 1}{n_0} \int_L p(l, \omega) dl. \quad (2.156)$$

The sound pressure field inside the cavity can be reconstructed without perturbing the pressure field using Eq. (2.156).



### 3 Major Findings of Attached Publications

The main results and novelty of the attached publications are summarized with respect to the state-of-the-art and the research questions.

## Publication AP1

F. Kronowetter, L. Moheit, M. Eser, K. K. Sepahvand, and S. Marburg. Spectral Stochastic Infinite Element Method in Vibroacoustics. In: *Journal of Theoretical and Computational Acoustics*, 2020, **28**(02), p. 2050009.

**How can we model uncertainties in unbounded domains?** The first research question arose from previous works in Steffen Marburg’s group [335–337]. In [AP1], a FEM-IFEM framework has been developed to solve unbounded Helmholtz problems. The infinite elements in the complementary domain are based on the conjugated Astley-Leis formulation [54, 55]. The underlying Petrov-Galerkin method uses complex conjugates of the radial interpolation functions with an additional geometric factor as weight functions, resulting in frequency-independent system matrices. The performance of the code has been investigated for two-dimensional problems. It has also been extended to half-space problems [71, 338, 339]. The code has been validated against an analytical solution to a radiation problem with multipole excitations [340].

Furthermore, a UQ framework has been implemented to address the influence of uncertain input data on the system response. Using the non-intrusive collocation method, the matrix system is a black-box model, while the UQ is modeled within a stochastic framework. There are several publications on probabilistic UQ using stochastic finite elements [108, 109, 111]. Previous works in Steffen Marburg’s group deal with UQ in acoustics [110, 112]. [AP1] presents the spectral stochastic IFEM for discretizing the complementary domain.

The example of an open convertible with uncertain parameters is investigated. The structural particle velocity at the window-fluid interface is assumed to be uncertain. A log-normal distribution is chosen. To cover the effects of reflections in the cabin, the seat cushion admittance is assumed to depend on a standard normally distributed random variable. It is shown that the influence of the polynomial order, as well as the size of the sample space, have a significant impact on the performance of the method. The results of the gPC expansions with a polynomial of order 9 are in agreement with the Monte Carlo simulations.

A second example presents uncertain dispersion curves of infinite-periodic C-shaped meta-atoms based on gPC expansions of the uncertain input data. The radius and aperture width are chosen as uncertain input data. The standard deviation corresponds to the manufacturing tolerances of the additive manufacturing technique used. It is shown that the first band gap is slightly affected by uncertain input data, while the second band gap almost disappears. Thus, the attenuation characteristics of sonic crystals are significantly affected by uncertain input data such as manufacturing tolerances.

In a third example the influence of uncertain input data on normal modes of a single C-shaped meta-atom is studied. Since the C-shaped meta-atom does not meet the strict symmetry requirements of the IBZ, the eigenvalues evaluated around the perimeter of the IBZ may lack information. Thus, normal modes give accurate results of local resonances while neglecting Bragg scattering, i.e. in the case of a single meta-atom. Local resonances typically dominate the transmission loss curve over Bragg band gaps [129]. This supports the normal mode approach. The results of [AP1] show that small deviations in radius and aperture width from the optimal configuration have a large effect on the frequency shift of the resonances.

How to solve time-harmonic problems and compute normal modes of exterior Helmholtz problems with uncertain input data has not been shown before this work. The accuracy of the UQ framework and the importance of considering uncertain data in the modeling of AMMs are discussed. This work lays the mathematical foundation for the design and analysis of future acoustic meta-atoms.

**Author contributions.** Felix Kronowetter, Lennart Moheit, Kian K. Sepahvand, and Steffen Marburg conceived the project. Felix Kronowetter and Lennart Moheit implemented and validated the code. Felix Kronowetter performed the analysis. All authors discussed the results. Felix Kronowetter prepared the paper with contributions from all authors. Lennart Moheit, Martin Eser, Kian K. Sepahvand, and Steffen Marburg edited the paper.

## Publication AP2

F. Kronowetter, S. K. Baydoun, M. Eser, L. Moheit, and S. Marburg. A Benchmark Study on Eigenfrequencies of Fluid-Loaded Structures. In: *Journal of Theoretical and Computational Acoustics*, 2020, **28**(02), p. 2050013.

**How to compute normal modes of mechanical-acoustic coupled problems in unbounded domains?** The second research question arose based on the results of [AP1] using state-space linearization, see Ruge [257], to compute the normal modes of the system. A well-known reference problem with an existing analytical solution, i.e. a vibrating submerged spherical shell [341], is chosen for the study. Strong coupling conditions are assumed. This problem has been included in preliminary studies using boundary elements [342–344]. In AP2, as a first attempt, a state space linearization proposed in previous works of the group [83,84,86,336] is applied to solve the FEM-IFEM based EVP of the reference problem. The quadratic EVP is linearized and solved in a state-space. The result is a generalized EVP that is twice as large. The problem with this approach is that the solver leads to incorrect eigenfrequencies.

Thereupon, [AP2] addresses this problem. Two additional remedial techniques are compared. First, a stable model order reduction technique is used. The stability of the original system is preserved and accurate results are obtained, while only a fraction of the original system’s degrees of freedom are required. Therefore, the quadratic EVP is projected onto a second-order Krylov subspace. The reduced EVP is then transformed into a general EVP. The orthonormal basis of the projection subspace is generated by means of a SOAR algorithm [258]. A second-order Krylov subspace approach is used in this paper for the generation of a state-of-the-art reference solution.

Second, the Cauchy integral formula is used. CIMs have recently been used to solve FEM-BEM based nonlinear EVPs [89–91] and mechanical-acoustic EVPs [343,345]. Based on the work of Baydoun and Marburg [94], the block SS [89] is used to solve FEM-IFEM and FEM-BEM based mechanical-acoustic EVPs. The choice of parameters for the method is in accordance with the recommendations of Sakurai et al. [260].

In [AP2], the time-harmonic solutions as well as the solutions to the EVP of a submerged spherical shell are computed using FEM-PML, FEM-BEM, and FEM-IFEM. Their accuracy and performance is compared. In particular, the accuracy of CIM is compared to the solution of the same FEM-IFEM EVP by a Rayleigh-Ritz procedure with second-order Krylov subspaces. The CIM requires a similar numerical effort. However, the CIM achieves relative residuals that are several orders of magnitude smaller. In addition, the eigenfrequencies obtained by FEM-IFEM, FEM-PML and FEM-BEM are compared with each other and it is found that they agree well.

[AP2] demonstrates the accuracy of CIMs for solving quadratic EVPs of mechanical-acoustic coupled unbounded Helmholtz problems based on FEM-IFEM discretization.

The ability to limit the scope of the problem to a predefined region in the complex plane is the advantage of CIMs. CIMs also allow problem parallelization at multiple levels. For example, the evaluation of matrix-vector products, the computation of each contour point, and even the evaluation of multiple elliptical contours over a large frequency range can be performed in parallel. As a result, CIMs are accurate and recommended for the solution of mechanical-acoustic coupled problems with FEM-IFEM discretization.

**Author contributions.** Felix Kronowetter, Martin Eser, Suhaib Koji Baydoun, and Steffen Marburg conceived the project. Felix Kronowetter, Martin Eser, and Suhaib Koji Baydoun implemented the code, performed the analysis, and discussed the results. Felix Kronowetter prepared the paper with contributions from all authors. Lennart Moheit, Martin Eser, Suhaib Koji Baydoun, and Steffen Marburg edited the paper.

## Publication AP3

F. Kronowetter, L. Pretsch, Y. K. Chiang, A. Melnikov, S. Sepehrirahnama, S. Oberst, D. A. Powell, and S. Marburg. Sound attenuation enhancement of acoustic meta-atoms via coupling. In: *The Journal of the Acoustical Society of America*, 2023, **154**(2), pp. 842-851.

The results of [AP1] and [AP2] form the basis for a more detailed study of the normal modes of meta-atoms in unbounded domains. In addition, the works of Elford et al. [129] and Moheit et al. [337] suggest that there is some interaction between meta-atoms. The distance between meta-atoms is typically smaller than their operating wavelength. Therefore, interactions such as longitudinal near-field coupling [182] and transverse coupling occur [183]. In the case of fluid acoustics, there is only pressure coupling. Since the interaction could be used to further improve, e.g., sound attenuation, the question arises: **How to tune acoustic metamaterials using coupling?**

In [AP3], the cavity resonant modes of two C-shaped resonators are analyzed in an unbounded domain as a function of variable geometrical parameters. The cavity resonant modes are those with the highest Q-factor.

First, the distance between the resonators is studied. It is shown that symmetric and antisymmetric modes cross at periodic distances equal to half the resonant wavelength. The crossing points of the real and imaginary parts are shifted with respect to each other by about a quarter wavelength. Based on modal analysis, the highest attenuation of a normal incident sound wave is expected at the points of degenerate modes. The time-harmonic analyses show that at every other degeneracy point with the dominant symmetric mode, there are dips in the transmitted sound power. It is found that modal degeneracy is a prerequisite for particularly high transmission minima and thus for increased local energy trapping.

Second, the relative orientation of the C-shapes' apertures is studied. Coupling introduces the possibility of tuning via the relative arrangement of the resonators, i.e. distance and orientation. The degeneracy of the modes can be shifted to arbitrary distances by changing their orientation. In addition, the relative orientation affects the width of the degeneracy regions. Thus, the coupling strength depends on the relative orientation and the distance. Transmission dips occur at modal crossings, but only where the symmetric mode dominates. Good agreement with the numerical data is obtained from experiments performed in a two-dimensional parallel plate waveguide. Accordingly, these two parameters provide additional degrees of freedom to tune the response of the metamaterial without changing the components. Surprisingly, the attenuation maxima do not occur at the apertures facing the normal incident wave. Instead, they occur at a particular orientation. For example, the configuration used in [AP3] leads to an attenuation maximum at a twist angle of 70 deg.

Third, the influence of a detuned resonator is analyzed. The modes no longer cross



in the real part but in the imaginary part. The state of degenerate modes is not realizable except for the first crossing. Thus, it is found that detuning weakens the coupling of modes and leads to poorer sound attenuation compared to identical resonators. In addition, the aperture size of the detuned resonator is increased, resulting in increased radiation loss. As a result, modal crossings are restored and degenerate modes are obtained. The increased radiation loss counteracts the anti-crossings. The increased radiation loss also stabilizes the system against detuning and increases coupling.

The influence of the relative arrangement of the resonators on the interaction and, thus, on the AMM response provides additional degrees of freedom for tuning AMMs. The transmission efficiency of the coupled meta-atoms can be significantly manipulated by changing the twist angle. Thus, the results obtained in [AP3] open up new possibilities for more efficient and versatile AMMs for noise control. In addition, increased aperture widths and distances corresponding to modal degeneracy can be used to achieve stronger coupling and, for example, mitigate the effects of manufacturing inaccuracies. In summary, the results of [AP3] contribute to the advancement of the design and tuning of advanced and high-performance AMMs.

**Author contributions.** Felix Kronowetter, Steffen Marburg, Sebastian Oberst, and David A. Powell conceived the project. Felix Kronowetter and Lisa Pretsch performed the analysis and discussed the results. Yan Kei Chiang designed the experiment and performed measurements to obtain the transmission coefficients. Felix Kronowetter and Yan Kei Chiang evaluated the experimental data. All authors discussed the results. Felix Kronowetter prepared the paper with contributions from all authors. Anton Melnikov, Shahrokh Sepehrihahnama, Steffen Marburg, Sebastian Oberst, and David A. Powell edited the paper.

## Publication AP4

F. Kronowetter, P. Wagner, J. Kolodi, I. Brabandt, T. Neumeyer, N. Rümmler, and S. Marburg. Novel compound material and metamaterial wheelhouse liners for tire noise reduction. In: *Mechanical Systems and Signal Processing*, 2023, **200**, p. 110548.

[AP1], [AP2], and [AP3] show the numerical framework, the design procedure, and the adjusting screws for performance tuning in the design of AMMs. The next step is to apply AMMs in a real-world environment and demonstrate their superiority over state-of-the-art NVH solutions through standardized measurements. Since the European Union has decided to address the increasing exposure to traffic noise by strengthening United Nations Economic Commission for Europe (UN/ECE) Regulations Nos. 51 and 117, the pass-by noise of vehicles in the lowest power class must be reduced by 4 dB(A) by 2026. In the future, there will be a growing interest in electric vehicles. Engine noise will decrease and tires will become a more dominant noise source regarding pass-by noise and cabin noise. A project has therefore been launched in cooperation with the industry to find an answer to the question: **How to reduce tire noise by applying acoustic metamaterials?**

In [AP4], the focus is on composites and AMMs. As possible approaches to noise reduction are discussed, one question remains: Where to place the materials? The wheelhouse of a vehicle provides a large area for installing acoustic liners. Since modern wheelhouse liners are made of compressed nonwovens or even plastics, there is a huge potential to improve sound absorption and take advantage of surfaces with untapped acoustic potential. Therefore, the influence of a composite wheelhouse liner and an AMM wheelhouse liner on both the pass-by noise and the cabin noise is investigated in AP4. The pass-by noise of a reference car is measured and the frequencies leading to noise maxima are identified. In a first step, a completely new process for manufacturing sound-absorbing nonwoven components is developed. The composite liner consists of a fiberglass polyester bi-component material with an integrated MPP layer. The acoustic properties of the composite liner are measured in an Alpha Cabin and are in good agreement with the predictions of the mathematical model. The composite liner is measured and compared to a currently installed liner, called the reference liner. The sound pressure level is measured in relation to the pass-by standard. In addition, microphones are installed at the driver's seat and at the rear seat. The composite liner slightly outperforms the reference liner in almost all frequency bands, with the main effect being on interior noise.

The next step is to perform frequency response measurements with special volume sources. In this way, the effect of the liner can be studied in more detail. Based on the previous findings of the panel contributions, a new AMM is designed to mitigate the main frequencies affected by the liner. The absorption of the AMM liner is validated via Alpha Cabin measurements. Full-vehicle measurements show that the AMM liner outperforms the composite liner over the whole frequency range.

[AP4] examines the use of composite liners and AMM wheelhouse liners to reduce pass-by noise and cabin noise. Although the AMM liner clearly outperforms both the state-of-the-art liner and the composite liner, the effect of the liner on overall vehicle noise is dominated by other components. Thus, AMMs provide noise reduction but must be applied on a larger scale to have a significant effect on pass-by noise.

**Author contributions.** Felix Kronowetter, Steffen Marburg, Thomas Neumeyer, Ines Brabandt, and Norbert Rümmler conceived the project. Felix Kronowetter designed the geometries and performed the analysis. Juri Kolodi fabricated the porous materials and the composite liner. Felix Kronowetter, Juri Kolodi, Ines Brabandt, and Philipp Wagner conducted the experiments and evaluated the experimental data. All authors discussed the results. Felix Kronowetter prepared the paper with contributions from all authors. Steffen Marburg, Juri Kolodi, Thomas Neumeyer, Philipp Wagner, and Norbert Rümmler edited the paper.

## Publication AP5

F. Kronowetter, M. Maeder, Y. K. Chiang, L. Huang, J. D. Schmid, S. Oberst, D. A. Powell, and S. Marburg. Realistic prediction and engineering of high-Q modes to implement stable Fano resonances in acoustic devices. In: *Nature Communications*, 2023, **14**(1), p. 6847.

[AP3] successfully demonstrates tunable meta-atoms. The working principle of acoustic meta-atoms is usually based on local resonances whose energy localization properties are characterized by the Q-factor. Theoretically, BICs have an infinite Q-factor. Small changes in the geometric parameters degrade the BICs into QBICs, which couple into extended states and manifest themselves in the form of high-Q Fano resonances. These high-Q Fano resonances are significantly affected by thermo-viscous losses. This results in attenuated Fano peaks and an extreme reduction of the Q-factor. In addition, the geometry must be manufactured accurately. Even small deviations have a significant effect on the Fano peak, which can even collapse [346]. Designing a BIC-induced mode with a high Q-factor remains a challenge [227, 228]. This poses the research question: **How to accurately predict high-Q Fano resonances?**

In [AP5] a BIC associated with the Friedrich-Wintgen full destructive interference of degenerate modes of the same symmetry in an open channel-cavity system is demonstrated in theory and experiment. The BIC formation is well explained by the two-level effective non-Hermitian Hamiltonian [46, 213, 225, 226], that can be described as an advanced form of coupled-mode theory [271, 272]. The BIC configuration is obtained by evaluating the natural frequencies of the system as a function of the geometric parameters. Since BICs are localized solutions they cannot be excited by extended states in the first propagation channel.

Three cavities with different cavity lengths are designed. They represent the BIC and two QBICs. Transmission tube measurements are performed to obtain the transmission spectra. The measurement results are compared with numerical simulations that accurately predict the ghost of the Fano resonance, see Guevara et al. [346], which corresponds to the BIC. The Fano peaks induced by the QBICs are also accurately predicted. The transmission spectra are significantly affected by thermo-viscous losses, resulting in attenuated Fano peaks and an extreme reduction of the Q-factor, as expected.

This raises the question: What is the pressure field of a QBIC under realistic conditions? LDV measurements are performed on specially designed samples that allow laser transmission, suppress additional reflections from the glass, and are rigid with respect to structural vibrations. This technique allows the cavity pressure field to be visualized without disturbing it. In [AP5] a high-Q mode induced by an acoustic QBIC is visualized for the first time. As a result, this work provides direct evidence for an acoustic BIC. The measured pressure field data provides information on the pressure field amplification.

This raises another question: Where and when does the maximum field enhancement

occur? For a given QBIC configuration, the pressure fields are measured at multiple frequencies and the configuration with the peak pressure enhancement is identified. For further analysis of the excited mode, the pressure field is decomposed using a Fast Fourier Transform. Higher-order modes that are excited simultaneously as the BIC mode are identified. In order to suppress these modes, the concept of a symmetry-reduced cavity proposed by Huang et al. [225,228] is applied. Therefore, the cavity is gradually reduced by the use of each of the symmetry axes. Numerical predictions of the cavity reflection spectra are verified by impedance tube measurements. The configuration with the maximum pressure enhancement is determined by mapping the pressure fields of the fully reduced cavity with different lengths. The fully reduced cavity results in the highest pressure increase of the Friedrich-Wintgen BICs studied, by a factor of about three compared to the full cavity.

When large field enhancement occurs in real acoustic devices, taking into account thermo-viscous losses, has not been shown before this work. LDV measurements are a promising technique for obtaining the missing field enhancement data. [AP5] is a fundamental contribution to the study of BICs. This study enables the design of high-Q Fano resonances under realistic conditions. The results open up completely new possibilities in this field of research, such as the application of BICs to high-intensity sound sources, acoustic devices, and nonlinear acoustics.

**Author contributions.** Felix Kronowetter, Steffen Marburg, Sebastian Oberst, and David A. Powell conceived the project. Felix Kronowetter, Yan Kei Chiang, Lujun Huang, and David A. Powell designed the geometry and modeled the physics behind it. Felix Kronowetter and Marcus Maeder made samples and performed measurements to obtain the transmission spectra and the visualization of the BIC. David Anthony Powell and Yan Kei Chiang advised the modeling and experimental process. Johannes D. Schmid implemented and uploaded the BIC application. All authors discussed the results. Felix Kronowetter prepared the paper with contributions from all authors. Marcus Maeder, Steffen Marburg, Sebastian Oberst, and David A. Powell edited the paper.



## 4 Discussion

The novelty of the dissertation's findings with respect to the state-of-the-art is discussed. The scientific impact is outlined by addressing the research questions posed.

This dissertation presents results that advance the state-of-the-art in analyzing open acoustic systems. The choice of discretization method for open systems is critical to accuracy and solvability. Harari and Hughes [347] examine the cost-effectiveness of the BEM and FEM with Dirichlet-to-Neumann conditions for interior and exterior Helmholtz problems. In terms of general applicability, robustness and mathematical structure, and overall flexibility, they find the FEM to be quite attractive for further development. Shirron and Babuška [247] study the performance of approximate BCs and infinite elements for plane wave scattering. The accuracy of the approximate BCs decreases with increasing frequency. At higher frequencies, their accuracy is several orders of magnitude lower than that of the IFEM. In [AP1], a FEM-IFEM formulation is used which has proven to be quite efficient and accurate in solving time-harmonic problems and computing normal modes for a variety of open acoustic systems [335–337].

However, it has not been shown how to model open systems with uncertain input data using the IFEM. Probabilistic UQ with stochastic finite elements is the subject of several publications [108, 109, 111]. UQ in acoustics has also been addressed in previous works in Steffen Marburg’s group [110, 112]. [AP1] is a follow-up to other recent publications on open acoustic systems with uncertain input data. A new method for open acoustic systems with epistemic uncertainties using BEM is proposed by Chen et al. [348]. A hybrid perturbation approach with both random and interval variables for open acoustic systems is discussed in another paper by Chen et al. [349]. Two new interval analysis methods for open acoustic systems are proposed by Wang and Qiu [350].

Research on AMMs and UQ are combined in some publications. He et al. [113] demonstrate an uncertainty model based on the change of variable perturbation stochastic FEM to predict the probability density functions of physical responses of AMMs with random parameters. Pan et al. [114] evaluate uncertainty effects on band gap behavior of circuitry-integrated piezoelectric metamaterial using order-reduced analysis. Henneberg et al. [117] show the need to consider uncertainties in phononic crystals. This statement begs the question: How are the dispersion curves of infinite-periodic sonic crystals affected by uncertain input data? [AP1] addresses this question by presenting uncertain dispersion curves of infinite-periodic C-shaped meta-atoms based on gPC expansions of the uncertain parameters.

Moheit et al. [337] analyze normal modes of finite periodic sonic crystals and their influence on the transmission. This work led to a second question: How are normal modes affected by manufacturing tolerances? [AP1] answers this question by studying the influence of uncertain input data on normal modes of a single C-shaped meta-atom. The results of [AP1] show that small deviations in radius and aperture width from the optimal configuration have a large effect on the frequency shift of the resonances.

However, the spectral stochastic IFEM has certain limitations. The radial order of the infinite elements must be adapted to the characteristics of the scattering object according to the Atkinson-Wilcox theorem [245]. At higher radial orders the system



matrices become ill-conditioned [62]. Furthermore, [AP1] shows that the influence of the polynomial order of the gPC has a significant impact on the performance of the spectral stochastic IFEM. So does the size of the sample space. Another point of discussion is the normal mode approach to AMM modeling. Comparing the calculation of normal modes for the characterization of AMMs with the  $k$ -space approach using periodic boundary conditions reveals several drawbacks. While the normal mode approach provides a more realistic prediction, it takes longer to compute. In addition, the size of the system matrices depends on the degrees of freedom of the system and, thus, on the order of the interpolation polynomials and the size of the mesh. So does the number of modes. Spurious modes are an artifact of the complementary domain discretization. Therefore, an additional criterion is needed to classify and sort the modes.

In [AP2] state-space linearization [83, 84, 86, 257, 336] is used to compute the normal modes of an FEM-IFEM discretized open system. The quadratic EVP is linearized and solved in a state-space. The result is a generalized EVP that is twice as large. However, for mechanical-acoustic problems in open systems, this method leads to incorrect eigenfrequencies.

Another method for solving unbounded vibroacoustic problems in the time domain is presented by Van Ophem et al. [76]. Conjugated Astley-Leis infinite elements are also used to account for the SRC. The quadratic EVP is projected onto a second-order Krylov subspace, resulting in a reduced EVP, which is then transformed into a general EVP. A SOAR algorithm [258] generates the orthonormal basis of the projection subspace. Bai and Su [259] have shown, that the Ritz eigenpairs of a reduced-order quadratic EVP are good approximations of the eigenpairs of the original quadratic EVP. Thus, by solving an EVP of significantly reduced dimension, the eigenpairs of the original system can be obtained. The proposed method uses only a fraction of the degrees of freedom of the original system. Thus, the stability of the original system is maintained and accurate results are obtained.

Several publications deal with nonlinear mechanical-acoustic EVPs based on a boundary element discretization. In a series of papers, Peters et al. [342, 351] used a frequency approximation of the BEM matrices. The resulting polynomial EVP was solved by symmetric linearization. The Krylov subspace model order reduction addresses the computational complexity associated with EVP inflation. Polynomial frequency approximations quickly deteriorate when dealing with complex eigenvalues other than those on the real axis. El-Guide et al. [352] approximate the boundary element system matrices within a contour in the complex plane by a highly accurate rational approximation using the Cauchy integral formula. CIMs are also used by many researchers to derive subspace projection methods for nonlinear EVPs [89–91] and in particular for mechanical-acoustic EVPs [343, 345].

[AP2] solves a mechanical-acoustic EVP based on a FEM-IFEM formulation using a Rayleigh-Ritz procedure with second-order Krylov subspaces as well as a CIM based

on resolvent moments. The numerical results are compared with the known analytical solution of the problem. Both methods require a similar numerical effort. However, the CIM achieves relative residuals that are several orders of magnitude smaller. An appropriate choice of the contour is crucial to obtain small relative residuals. The degree of the resolvent moments should be large enough so that the dimension of the resulting subspace is greater than the number of expected eigenvalues. In addition, a sufficiently accurate radial discretization of the infinite elements is critical to capture the modes of interest.

The numerical results are also compared with those of a FEM-BEM formulation and a FEM-PML formulation, showing good agreement throughout. The CIM is suitable for computing normal modes of FEM-IFEM based mechanical-acoustic problems. However, approximate prior knowledge of the eigenvalues of interest is required to define a tight contour that encloses them. This allows an accurate projection with only a few contour points. A larger contour will result in less accurate results and increased computation time.

[AP1] and [AP2] demonstrate numerical methods for solving EVPs of open acoustic systems. The works of Moheit et al. [337] and Elford et al. [129] indicate inhomogeneous pressure distributions within a finite-periodic array of meta-atoms. This leads to the two questions: How do meta-atoms interact? What parameters affect the interaction?

Acoustic coupling plays an important role in analyzing organ pipes [353–355]. Strutt [356] shows that two pipes sound in unison when they are close together, even if their eigenfrequencies differ slightly. Johansson and Kleiner [357] study the coupling effects of two Helmholtz resonators and argue that the coupling mechanisms of organ pipes and Helmholtz resonators are similar. Thus, Helmholtz resonators provide a good approximation for more complex organ pipes, despite their different operating principles. The local resonances of Helmholtz resonators can be coupled by bringing them close together. The coupling of organ pipes and the transfer to local resonances of Helmholtz resonators raise the question: Do these results hold for meta-atoms?

In recent years, several publications have addressed the coupling of acoustic resonators in waveguides [182, 358–360]. In addition, the interaction of local resonances within an AMM unit cell in the subwavelength regime has been demonstrated [361–364]. Yang et al. [365] demonstrate how strong coupling can affect the performance of an AMM superlens. Dong et al. [366] study the application of multiple coupled Helmholtz resonators to acoustic gratings.

Coupling and near-field interaction in electromagnetic metamaterials have also been investigated [367–370]. Liu et al. [371] note that the coupling between electromagnetic metamaterial elements can have a significant impact on the behavior of the material as a whole. Keiser et al. [372] and Liu et al. [371] conclude that near-field interactions must be considered, especially for closely spaced arrays. Powell et al. [373] demonstrate that relative orientation and separation affect the near-field interaction between split-ring res-

onators and that the metamaterial response can be tuned. In a subsequent paper, Powell et al. [374] analyze the (anti-) crossing behavior of the symmetric and antisymmetric modes of a pair of split-ring resonators based on the model proposed by Yakovlev and Hanson [375]. A similar study on split-ring resonators is conducted by Liu et al [376]. Thus, the tunable coupling of split-ring resonators leads to metamaterial tuning. As they are the electromagnetic counterparts of Helmholtz resonators [377], the following question arises: How can the results be applied to AMMs?

In [AP3] all the above questions are answered by analyzing the interaction between two meta-atoms in an open system. Geometrical parameters are identified that influence the interaction between two cavity resonant modes and, thus, the coupling between the two meta-atoms. It is found that the coupling parameters provide additional degrees of freedom for tuning AMMs. The analysis of systems with more than three or four meta-atoms is certainly difficult since the identification of the relevant modes and their identification through the parameter space requires additional algorithms. The results found in [AP3] incidentally provide the basis for the future design of exceptional points in an open acoustic system [264, 378, 379].

Since the numerical modeling of open systems and its application to the study of AMMs is demonstrated in [AP1], [AP2], and [AP3], a new question arises: Is it possible to translate academic research into a manufacturable, low-cost AMM product that meets industry standards?

The European Union has decided to reduce the pass-by noise of vehicles in the lowest power class by 4dB(A) by 2026. In the future, there will be an increased interest in noise propagation in electric vehicles [380–382]. Electrification of the powertrain reduces engine noise. As a result, tires become a more dominant noise source. Tire noise contributes to pass-by noise and also contributes to interior noise as it propagates through the structure of the vehicle. That’s why a project has been launched in cooperation with the industry. The aim is to reduce tire noise.

Tire noise consists of texture impact, tread impact, air pumping, tube resonance, Helmholtz resonance, horn effect, and tire cavity resonance [383]. The low frequency cavity resonances have been intensively studied by the scientific community in recent years [384–390]. As well as the overall performance of the tire and its optimization as an acoustic source [383, 391–393]. Lafont et al. [394] perform a numerical study of the tire radiation and identify the contact patch as the main contributor in the 800 Hz to 2000 Hz range. The main noise source is identified, but how can it be attenuated?

Traditional NVH manipulation techniques rely on increasing mass or stiffness. They are, therefore, inapplicable as they contradict the lightweight design of the vehicle. Another well-known approach to increasing sound attenuation is the installation of sound-absorbing materials. Porous materials are broadband absorbers for higher frequencies, while MPPs are narrowband absorbers. By combining these two absorbers into a composite absorber,

broadband absorption shifted to a lower frequency range can be achieved. In recent years, various composite structures have been intensively studied [286–291]. Recent innovative approaches propose the application of AMMs in vehicles, e.g. for structural noise mitigation [169, 171, 172] or rubber resonant metamaterials in tires [170]. All of the above approaches use solid structures. When activated, these structures convert energy at their natural frequencies.

[AP4] links to the question of reducing both pass-by and cabin noise with an AMM wheelhouse liner. The designed liner outperforms state-of-the-art solutions. This statement is supported by several measurements. Two problems remain. First, the AMM liner, although simple in design, is more expensive to manufacture than the state-of-the-art integrated compressed nonwoven liners. Second, the AMM liner is subject to contamination. This results in reduced sound attenuation. Applying a membrane layer over the AMM could be a possible remedy. The future goal is to develop a commercially viable process to begin manufacturing.

This dissertation introduces numerical methods in [AP1] and [AP2], demonstrates tunable meta-atoms in [AP3], and presents AMMs in an industrial application in [AP4]. AMMs usually rely on energy localization, e.g. local resonances in acoustics. Local resonances are characterized by the Q-factor. The higher the Q-factor the higher the energy localization. BICs have a theoretically infinite Q-factor, are perfectly localized modes, and are thus predestined for energy localization. Liu et al. [395] demonstrate high-Q QBICs with Q-factors up to 18511 in all-dielectric metasurfaces. Duan et al. [396] obtain a QBIC with an ultra-high Q-factor of about  $4.1 \times 10^7$  in a one-dimensional photonic crystal nanobeam.

In contrast to the two optical systems mentioned above, thermal and viscous boundary layers in acoustic systems induce relatively large intrinsic losses. This prevents ultra-high Q-factors in experiments. As a result, increasing the Q-factor based on QBICs has been a hot topic in the field of acoustics in recent years [228, 229]. Q-factors of up to 1041 with a pressure amplification ratio of 50 have been obtained [227]. QBICs couple into the continuous spectrum leading to high-Q Fano resonances in the reflection and transmission spectra. The higher the Q-factor, the more dominant the losses and the more unpredictable the Fano resonances. Two questions remain: How to predict stable high-Q Fano resonances? When does the maximum pressure enhancement occur? [AP5] answers both of these questions by providing direct access to the pressure values of a Friedrich-Wintgen BIC.

A new technique is presented to map the sound pressure field of a QBIC. This technique uses an LDV to ensure that measuring does not interfere with the pressurized field. This is the first visual proof of an acoustic QBIC. Accurate mapping of the pressure field gives us a better understanding of real QBICs, including losses of all types and field enhancement data that allow further analysis of the excited modes. It also shows how to analyze the pressure field using overlap integrals, which allows for a design with improved field enhancement properties.

[AP5] demonstrates how to accurately predict the large field enhancement when thermo-viscous losses are accounted for in real acoustic devices. This research helps facilitate the use of BICs in acoustic lasers [397] or ultra-narrow band filtering, for example. The presented mapping method is time-consuming compared to impedance tube measurements that provide reflection and transmission spectra. Accurate sizing of the sample is required. In order not to interfere with the laser beam, it is also necessary to know the natural frequencies of the sample and transparent walls. The whole setup can be quite costly.

Summarizing the results of the dissertation, the numerical tools to simulate open acoustic systems are developed, AMMs are analyzed and designed using normal modes, coupling turns out to be a parameter for AMM tuning, and BICs are studied to allow engineering of high-Q Fano resonances in open acoustic systems. By again connecting the results to Lichtenberg's opening statement, groundbreaking findings are presented that can be used to manipulate the propagation of sound in unprecedented ways.



# Bibliography

- [1] J. E. Greenspon. Acoustics, linear. In R. A. Meyers, editor, *Encyclopedia of Physical Science and Technology (Third Edition)*, pages 129–167. Academic Press, New York, third edition edition, 2003.
- [2] R. Lerch, W. Dietrich, and S. Gerhard. *Akustische Wellen in festen Körpern*, pages 93–132. Springer Berlin Heidelberg, Berlin, Heidelberg, 2009.
- [3] M. Kaltenbacher. *Coupled Mechanical-Acoustic Systems*, pages 297–308. Springer Berlin Heidelberg, Berlin, Heidelberg, 2015.
- [4] A. Bermúdez, P. Gamallo, L. Hervella-Nieto, R. Rodríguez, and D. Santamarina. *Fluid–Structure Acoustic Interaction*, pages 253–286. Springer Berlin Heidelberg, Berlin, Heidelberg, 2008.
- [5] S. Marburg. *A Unified Approach to Finite and Boundary Element Discretization in Linear Time–Harmonic Acoustics*, pages 1–34. Springer Berlin Heidelberg, Berlin, Heidelberg, 2008.
- [6] A. Sommerfeld. Die greensche funktion der schwingungsgleichung. *Jahresbericht der Deutschen Mathematiker-Vereinigung*, 21:309–352, 1912.
- [7] S. H. Schot. Eighty years of sommerfeld’s radiation condition. *Historia Mathematica*, 19(4):385–401, 1992.
- [8] R. Lerch, W. Dietrich, and S. Gerhard. *Numerische Verfahren der Akustik - Computational Acoustics*, pages 757–820. Springer Berlin Heidelberg, Berlin, Heidelberg, 2009.
- [9] M. Kaltenbacher. *The Finite Element (FE) Method*, pages 7–91. Springer Berlin Heidelberg, Berlin, Heidelberg, 2015.
- [10] M. Ochmann, S. Lippert, and O. von Estorff. *Numerische Methoden der Technischen Akustik*, pages 1–37. Springer Berlin Heidelberg, Berlin, Heidelberg, 2016.
- [11] M. Petyt. *Finite Element Techniques for Acoustics*, pages 51–103. Springer Vienna, Vienna, 1983.
- [12] O. von Estorff. Boundary elements in acoustics : Advances and applications. 2000.
- [13] T. W. Wu and M. Ochmann. Boundary Element Acoustics Fundamentals and Computer Codes. *The Journal of the Acoustical Society of America*, 111(4):1507–1508, 04 2002.

## Bibliography

- [14] S. Kirkup. The boundary element method in acoustics: A survey. *Applied Sciences*, 9(8), 2019.
- [15] S. Preuss, M. Paltorp, A. Blanc, V. C. Henríquez, and S. Marburg. Revising the boundary element method for thermoviscous acoustics: An iterative approach via schur complement. *Journal of Theoretical and Computational Acoustics*, 31(04):2350015, 2023.
- [16] S. Marburg and T.-W. Wu. *Treating the Phenomenon of Irregular Frequencies*, pages 411–434. Springer Berlin Heidelberg, Berlin, Heidelberg, 2008.
- [17] B. Engquist and A. Majda. Absorbing boundary conditions for the numerical simulation of waves. *Mathematics of Computation*, 31(139):629–651, 1977.
- [18] D. Givoli, I. Patlashenko, and J. B. Keller. High-order boundary conditions and finite elements for infinite domains. *Computer Methods in Applied Mechanics and Engineering*, 143(1):13–39, 1997.
- [19] D. Givoli. *Computational Absorbing Boundaries*, pages 145–166. Springer Berlin Heidelberg, Berlin, Heidelberg, 2008.
- [20] E. Turkel and A. Yefet. Absorbing pml boundary layers for wave-like equations. *Applied Numerical Mathematics*, 27(4):533–557, 1998. Special Issue on Absorbing Boundary Conditions.
- [21] A. Bermúdez, L. Hervella-Nieto, A. Prieto, and R. Rodríguez. *Perfectly Matched Layers*, pages 167–196. Springer Berlin Heidelberg, Berlin, Heidelberg, 2008.
- [22] I. Harari, E. Turkel, and M. Slavutin. Analytical and numerical studies of a finite element pml for the helmholtz equation. *Journal of Computational Acoustics*, 8:121–137, 03 2000.
- [23] G. Bunting, A. Prakash, T. Walsh, and C. Dohrmann. Parallel ellipsoidal perfectly matched layers for acoustic helmholtz problems on exterior domains. *Journal of Theoretical and Computational Acoustics*, 26:1850015, 06 2018.
- [24] F. L. Teixeira and W. C. Chew. Complex space approach to perfectly matched layers: a review and some new developments. *International Journal of Numerical Modelling: Electronic Networks, Devices and Fields*, 13(5):441–455, 2000.
- [25] A. Bermúdez, L. Hervella-Nieto, A. Prieto, and R. Rodríguez. Perfectly matched layers for time-harmonic second order elliptic problems. *Archives of Computational Methods in Engineering*, 17:77–107, 03 2010.
- [26] R. J. Astley. *Infinite Elements*, pages 197–230. Springer Berlin Heidelberg, Berlin, Heidelberg, 2008.



- [27] D. S. Burnett. A three-dimensional acoustic infinite element based on a prolate spheroidal multipole expansion. *The Journal of the Acoustical Society of America*, 96(5):2798–2816, 11 1994.
- [28] P. Bettess. Infinite elements. *International Journal for Numerical Methods in Engineering*, 11(1):53–64, 1977.
- [29] F. Ihlenburg, editor. *Discretization Methods for Exterior Helmholtz Problems*, pages 61–99. Springer New York, New York, NY, 1998.
- [30] S. V. Tsynkov. Numerical solution of problems on unbounded domains. a review. *Applied Numerical Mathematics*, 27(4):465–532, 1998. Special Issue on Absorbing Boundary Conditions.
- [31] L. L. Thompson. A review of finite-element methods for time-harmonic acoustics. *The Journal of the Acoustical Society of America*, 119(3):1315–1330, 03 2006.
- [32] O. P. Le Maître and O. M. Knio. *Introduction: Uncertainty Quantification and Propagation*, pages 1–13. Springer Netherlands, Dordrecht, 2010.
- [33] G. Liao, C. Luan, Z. Wang, J. Liu, X. Yao, and J. Fu. Acoustic metamaterials: A review of theories, structures, fabrication approaches, and applications. *Advanced Materials Technologies*, 6(5):2000787, 2021.
- [34] S. Cummer, J. Christensen, and A. Alù. Controlling sound with acoustic metamaterials. *Nature Reviews Materials*, 1:16001, 02 2016.
- [35] J. Liu, H. Guo, and T. Wang. A review of acoustic metamaterials and phononic crystals. *Crystals*, 10:305, 04 2020.
- [36] J. Zhang, B. Hu, and S. Wang. Review and perspective on acoustic metamaterials: From fundamentals to applications. *Applied Physics Letters*, 123(1):010502, 07 2023.
- [37] G. Ji and J. Huber. Recent progress in acoustic metamaterials and active piezoelectric acoustic metamaterials - a review. *Applied Materials Today*, 26:101260, 2022.
- [38] H. Dai, X. Zhang, Y. Zheng, W. Pei, R. Zhou, R. Liu, and Y. Gong. Review and prospects of metamaterials used to control elastic waves and vibrations. *Frontiers in Physics*, 10, 2022.
- [39] N. Gao, Z. Zhang, J. Deng, X. Guo, B. Cheng, and H. Hou. Acoustic metamaterials for noise reduction: A review. *Advanced Materials Technologies*, 7:2100698, 01 2022.
- [40] P. A. Deymier. *Introduction to Phononic Crystals and Acoustic Metamaterials*, pages 1–12. Springer Berlin Heidelberg, Berlin, Heidelberg, 2013.
- [41] F. Zangeneh-Nejad and R. Fleury. Active times for acoustic metamaterials. *Reviews in Physics*, 4:100031, 2019.

## Bibliography

- [42] G. Ma and P. Sheng. Acoustic metamaterials: From local resonances to broad horizons. *Science Advances*, 2(2):e1501595, 2016.
- [43] C. W. Hsu, B. Zhen, A. D. Stone, J. Joannopoulos, and M. Soljačić. Bound states in the continuum. *Nature Reviews Materials*, 1:16048, 07 2016.
- [44] V. Pagneux. *Trapped Modes and Edge Resonances in Acoustics and Elasticity*, pages 181–223. Springer Vienna, Vienna, 2013.
- [45] S. Joseph, S. Pandey, S. Sarkar, and J. Joseph. Bound states in the continuum in resonant nanostructures: an overview of engineered materials for tailored applications. *Nanophotonics*, 10(17):4175–4207, 2021.
- [46] A. Sadreev. Interference traps waves in open system: Bound states in the continuum. *Reports on Progress in Physics*, 84, 03 2021.
- [47] L. Huang, S. Huang, C. Shen, S. Yves, A. S. Pilipchuk, X. Ni, S. Kim, Y. K. Chiang, D. A. Powell, J. Zhu, Y. Cheng, Y. Li, A. F. Sadreev, A. Alù, and A. E. Miroshnichenko. Acoustic resonances in non-hermitian open systems. *Nature Reviews Physics*, 6(1):11–27, Jan 2024.
- [48] P. Bettess and O. C. Zienkiewicz. Diffraction and refraction of surface waves using finite and infinite elements. *International Journal for Numerical Methods in Engineering*, 11(8):1271–1290, 1977.
- [49] K. Gerdes. The conjugated vs. the unconjugated infinite element method for the helmholtz equation in exterior domains. *Computer Methods in Applied Mechanics and Engineering*, 152(1):125–145, 1998. Containing papers presented at the Symposium on Advances in Computational Mechanics.
- [50] O. C. Zienkiewicz, K. Bando, P. Bettess, C. Emson, and T. C. Chiam. Mapped infinite elements for exterior wave problems. *International Journal for Numerical Methods in Engineering*, 21(7):1229–1251, 1985.
- [51] J. Goransson and C. Davidsson. A three dimensional infinite element for wave propagation. *Journal of Sound and Vibration*, 115(3):556–559, 1987.
- [52] K. Gerdes and L. Demkowicz. Solution of 3d-laplace and helmholtz equations in exterior domains using hp-infinite elements. *Computer Methods in Applied Mechanics and Engineering*, 137(3):239–273, 1996.
- [53] R. Astley and W. Eversman. Finite element formulations for acoustical radiation. *Journal of Sound and Vibration*, 88(1):47–64, 1983.
- [54] R. Astley, G. Macaulay, and J. Coyette. Mapped wave envelope elements for acoustical radiation and scattering. *Journal of Sound and Vibration*, 170(1):97–118, 1994.

- [55] R. J. Astley, G. J. Macaulay, J.-P. Coyette, and L. Cremers. Three-dimensional wave-envelope elements of variable order for acoustic radiation and scattering. Part I. Formulation in the frequency domain. *The Journal of the Acoustical Society of America*, 103(1):49–63, 01 1998.
- [56] R. J. Astley. Mapped spheroidal wave-envelope elements for unbounded wave problems. *International Journal for Numerical Methods in Engineering*, 41(7):1235–1254, 1998.
- [57] R. Leis. *Initial boundary value problems in mathematical physics*. Courier Corporation, 2013.
- [58] D. S. Burnett and R. L. Holford. An ellipsoidal acoustic infinite element. *Computer Methods in Applied Mechanics and Engineering*, 164(1):49–76, 1998. Exterior Problems of Wave Propagation.
- [59] D. S. Burnett and R. L. Holford. Prolate and oblate spheroidal acoustic infinite elements. *Computer Methods in Applied Mechanics and Engineering*, 158(1):117–141, 1998.
- [60] R. J. Astley and J.-P. Coyette. The performance of spheroidal infinite elements. *International Journal for Numerical Methods in Engineering*, 52(12):1379–1396, 2001.
- [61] J. J. Shirron and S. Dey. Acoustic infinite elements for non-separable geometries. *Computer Methods in Applied Mechanics and Engineering*, 191(37):4123–4139, 2002.
- [62] R. J. Astley. Infinite elements for wave problems: a review of current formulations and an assessment of accuracy. *International Journal for Numerical Methods in Engineering*, 49(7):951–976, 2000.
- [63] K. Gerdes. A summary of infinite element formulations for exterior helmholtz problems. *Computer Methods in Applied Mechanics and Engineering*, 164(1):95–105, 1998. Exterior Problems of Wave Propagation.
- [64] K. Gerdes. A review of infinite element methods for exterior helmholtz problems. *Journal of Computational Acoustics*, 08(01):43–62, 2000.
- [65] J. J. Shirron. *Solution of Exterior Helmholtz Problems Using Finite and Infinite Elements*. PhD thesis, University of Maryland, College Park, January 1995.
- [66] R. J. Astley and J.-P. Coyette. Conditioning of infinite element schemes for wave problems. *Communications in Numerical Methods in Engineering*, 17(1):31–41, 2001.
- [67] D. Dreyer and O. von Estorff. Improved conditioning of infinite elements for exterior acoustics. *International Journal for Numerical Methods in Engineering*, 58(6):933–953, 2003.

## Bibliography

- [68] O. von Estorff, S. Petersen, and D. Dreyer. *Efficient Infinite Elements based on Jacobi Polynomials*, pages 231–250. Springer Berlin Heidelberg, Berlin, Heidelberg, 2008.
- [69] D. Dreyer, S. Petersen, and O. von Estorff. Effectiveness and robustness of improved infinite elements for exterior acoustics. *Computer Methods in Applied Mechanics and Engineering*, 195(29):3591–3607, 2006. Absorbing Boundary Conditions.
- [70] Y. Rui-liang and W. Hong-zhen. A novel ellipsoidal acoustic infinite element. *Applied Mathematics and Mechanics*, 26(2):261–268, Feb 2005.
- [71] J.-P. Coyette and B. Nieuwenhof. A conjugated infinite element method for half-space acoustic problems. *The Journal of the Acoustical Society of America*, 108:1464–73, 11 2000.
- [72] Z. Huang, H. Zheng, L. Guo, and D. Mo. Influence of the position of artificial boundary on computation accuracy of conjugated infinite element for a finite length cylindrical shell. *Acoustics Australia*, 48, 04 2020.
- [73] W. Eversman. Mapped infinite wave envelope elements for acoustic radiation in a uniformly moving medium. *Journal of Sound and Vibration*, 224(4):665–687, 1999.
- [74] J. A. Hamilton and R. J. Astley. Acoustic propagation on irrotational mean flows using transient finite and infinite elements. *AIAA Journal*, 43(1):124–134, 2005.
- [75] R. Astley, J.-P. Coyette, and L. Cremers. Three-dimensional wave-envelope elements of variable order for acoustic radiation and scattering. part ii. formulation in the time domain. *Journal of The Acoustical Society of America - J ACOUST SOC AMER*, 103:64–72, 01 1998.
- [76] S. van Ophem, O. Atak, E. Deckers, and W. Desmet. Stable model order reduction for time-domain exterior vibro-acoustic finite element simulations. *Computer Methods in Applied Mechanics and Engineering*, 325:240–264, 2017.
- [77] R. Astley and J. Hamilton. The stability of infinite element schemes for transient wave problems. *Computer Methods in Applied Mechanics and Engineering*, 195(29):3553–3571, 2006. Absorbing Boundary Conditions.
- [78] T. Hohage and L. Nannen. Hardy space infinite elements for scattering and resonance problems. *SIAM Journal on Numerical Analysis*, 47(2):972–996, 2009.
- [79] L. Nannen and A. Schädle. Hardy space infinite elements for helmholtz-type problems with unbounded inhomogeneities. *Wave Motion*, 48, 04 2010.
- [80] M. Halla. Convergence of hardy space infinite elements for helmholtz scattering and resonance problems. *SIAM Journal on Numerical Analysis*, 54(3):1385–1400, 2016.
- [81] M. Halla and L. Nannen. Two scale hardy space infinite elements for scalar waveguide problems. *Advances in Computational Mathematics*, 44(3):611–643, Jun 2018.

- [82] S. Marburg. Normal modes in external acoustics. part i: Investigation of the one-dimensional duct problem. *Acta Acustica united with Acustica*, 91:1063–1078, 11 2005.
- [83] S. Marburg, F. Dienerowitz, T. Horst, and S. Schneider. Normal modes in external acoustics. part ii: Eigenvalues and eigenvectors in 2d. *Acta Acustica united with Acustica*, 92:97–111, 01 2006.
- [84] S. Marburg. Normal modes in external acoustics. part iii: Sound power evaluation based on superposition of frequency-independent modes. *Acta Acustica united with Acustica*, 92:296–311, 03 2006.
- [85] F. Tisseur and K. Meerbergen. The quadratic eigenvalue problem. *SIAM Review*, 43:235–286, 08 2001.
- [86] S. Retka, S. Hawkins, and S. Marburg. An eigenvalue search algorithm for modal analysis of a resonator in free space. *Journal of Computational Acoustics*, 19:95–109, 11 2011.
- [87] S. Retka and S. Marburg. An infinite element for the solution of galbrun equation. *ZAMM - Journal of Applied Mathematics and Mechanics / Zeitschrift für Angewandte Mathematik und Mechanik*, 93(2-3):154–162, 2013.
- [88] S. van Ophem, E. Deckers, and W. Desmet. Model based virtual intensity measurements for exterior vibro-acoustic radiation. *Mechanical Systems and Signal Processing*, 134:106315, 2019.
- [89] J. Asakura, T. Sakurai, H. Tadano, T. Ikegami, and K. Kimura. A numerical method for nonlinear eigenvalue problems using contour integrals. *JSIAM Letters*, 1:52–55, 2009.
- [90] S. Yokota and T. Sakurai. A projection method for nonlinear eigenvalue problems using contour integrals. *JSIAM Letters*, 5:41–44, 2013.
- [91] W.-J. Beyn. An integral method for solving nonlinear eigenvalue problems. *Linear Algebra and its Applications*, 436(10):3839–3863, 2012. Special Issue dedicated to Heinrich Voss’s 65th birthday.
- [92] T. Sakurai and H. Sugiura. A projection method for generalized eigenvalue problems using numerical integration. *Journal of Computational and Applied Mathematics*, 159(1):119–128, 2003. 6th Japan-China Joint Seminar on Numerical Mathematics; In Search for the Frontier of Computational and Applied Mathematics toward the 21st Century.
- [93] B. Gavin, A. Miedlar, and E. Polizzi. Feast eigensolver for nonlinear eigenvalue problems. *Journal of Computational Science*, 27:107–117, 2018.

## Bibliography

- [94] S. K. Baydoun and S. Marburg. Investigation of radiation damping in sandwich structures using finite and boundary element methods and a nonlinear eigensolver. *The Journal of the Acoustical Society of America*, 147:2020–2034, 03 2020.
- [95] S. K. Baydoun, M. Voigt, B. Goderbauer, C. Jelich, and S. Marburg. A subspace iteration eigensolver based on cauchy integrals for vibroacoustic problems in unbounded domains. *International Journal for Numerical Methods in Engineering*, 122(16):4250–4269, 2021.
- [96] S. Hein, T. Hohage, and W. Koch. On resonances in open systems. *Journal of Fluid Mechanics*, 506:255–284, 2004.
- [97] W. Koch. Acoustic resonances in rectangular open cavities. *AIAA Journal*, 43(11):2342–2349, 2005.
- [98] W. Koch. Acoustic resonances and trapped modes in annular plate cascades. *Journal of Fluid Mechanics*, 628:155–180, 2009.
- [99] S. Hein and W. Koch. Acoustic resonances and trapped modes in pipes and tunnels. *Journal of Fluid Mechanics*, 605:401–428, 06 2008.
- [100] S. Hein, W. Koch, and L. Nannen. Fano resonances in acoustics. *Journal of Fluid Mechanics*, Vol. 664:238–264, 12 2010.
- [101] S. Hein, W. Koch, and L. Nannen. Trapped modes and fano resonances in two-dimensional acoustical duct-cavity systems. *Journal of Fluid Mechanics*, Vol. 692:257–287, 02 2012.
- [102] O. P. Le Maître and O. M. Knio. *Spectral Expansions*, pages 17–44. Springer Netherlands, Dordrecht, 2010.
- [103] K. Karhunen. Über lineare methoden in der wahrscheinlichkeitsrechnung. 1947.
- [104] M. Loève. *Probability Concepts*, pages 151–176. Springer New York, New York, NY, 1977.
- [105] O. P. Le Maître and O. M. Knio. *Non-intrusive Methods*, pages 45–72. Springer Netherlands, Dordrecht, 2010.
- [106] S. Hosder, R. Walters, and M. Balch. *Efficient Sampling for Non-Intrusive Polynomial Chaos Applications with Multiple Uncertain Input Variables*. 2007.
- [107] R. G. Ghanem and P. D. Spanos. *Stochastic Finite Element Method: Response Representation*, pages 67–99. Springer New York, New York, NY, 1991.
- [108] R. G. Ghanem and R. M. Kruger. Numerical solution of spectral stochastic finite element systems. *Computer Methods in Applied Mechanics and Engineering*, 129(3):289–303, 1996.

- [109] M. Ngah and A. Young. Application of the spectral stochastic finite element method for performance prediction of composite structures. *Composite Structures*, 78(3):447–456, 2007.
- [110] K. Sepahvand, S. Marburg, and H.-J. Hardtke. Numerical solution of one-dimensional wave equation with stochastic parameters using generalized polynomial chaos expansion. *Journal of Computational Acoustics*, 15(04):579–593, 2007.
- [111] K. Sepahvand, S. Marburg, and H.-J. Hardtke. Uncertainty quantification in stochastic systems using polynomial chaos expansion. *International Journal of Applied Mechanics*, 02(02):305–353, 2010.
- [112] K. Sepahvand, M. Scheffler, and S. Marburg. Uncertainty quantification in natural frequencies and radiated acoustic power of composite plates: Analytical and experimental investigation. *Applied Acoustics*, 87:23–29, 2015.
- [113] Z. C. He, J. Y. Hu, and E. Li. An uncertainty model of acoustic metamaterials with random parameters. *Computational Mechanics*, 62(5):1023–1036, Nov 2018.
- [114] W. Pan, G. Tang, and J. Tang. Evaluation of uncertainty effects to band gap behavior of circuitry-integrated piezoelectric metamaterial using order-reduced analysis. *Journal of Intelligent Material Systems and Structures*, 29:1045389X1877835, 05 2018.
- [115] B. Xia, Y. Qin, N. Chen, D. Yu, and C. Jiang. Optimization of uncertain acoustic metamaterial with helmholtz resonators based on interval model. *Science China Technological Sciences*, 60(3):385–398, Mar 2017.
- [116] J. Chen, B. Xia, and J. Liu. A sparse polynomial surrogate model for phononic crystals with uncertain parameters. *Computer Methods in Applied Mechanics and Engineering*, 339:681–703, 2018.
- [117] J. Henneberg, J. Gomez Nieto, K. Sepahvand, A. Gerlach, H. Cebulla, and S. Marburg. Periodically arranged acoustic metamaterial in industrial applications: The need for uncertainty quantification. *Applied Acoustics*, 157:107026, 2020.
- [118] H. Al Ba’ba’a, S. Nandi, T. Singh, and M. Nouh. Uncertainty quantification of tunable elastic metamaterials using polynomial chaos. *Journal of Applied Physics*, 127(1):015102, 01 2020.
- [119] H. Atzrodt, A. Maniam, M. Droste, S. Rieß, and M. Hülsebrock. A power-based framework for quantifying parameter uncertainties in finite vibroacoustic metamaterial plates. *Materials*, 16(14), 2023.
- [120] R. Santoro, M. Mazzeo, and G. Failla. A computational framework for uncertain locally resonant metamaterial structures. *Mechanical Systems and Signal Processing*, 190:110094, 2023.

## Bibliography

- [121] L. Quan, Y. Ra'di, D. L. Sounas, and A. Alù. Maximum willis coupling in acoustic scatterers. *Phys. Rev. Lett.*, 120:254301, 06 2018.
- [122] A. Melnikov, Y. K. Chiang, L. Quan, S. Oberst, A. Alù, S. Marburg, and D. Powell. Acoustic meta-atom with experimentally verified maximum willis coupling. *Nature Communications*, 10(1):3148, Jul 2019.
- [123] G. W. Milton and J. R. Willis. On modifications of Newton's second law and linear continuum elastodynamics. *Proceedings of the Royal Society A: Mathematical, Physical and Engineering Sciences*, 463(2079):855–880, 2007.
- [124] S. Yao, X. Zhou, and G. Hu. Experimental study on negative effective mass in a 1D mass-spring system. *New Journal of Physics*, 10(4):43020, 2008.
- [125] Z. Liu, X. Zhang, Y. Mao, Y. Y. Zhu, Z. Yang, C. T. Chan, and P. Sheng. Locally Resonant Sonic Materials. *Science*, 289(5485):1734 LP – 1736, 2000.
- [126] N. Fang, D. Xi, J. Xu, M. Ambati, W. Srituravanich, C. Sun, and X. Zhang. Ultrasonic metamaterials with negative modulus. *Nature Materials*, 5(6):452–456, 2006.
- [127] J. B. Pendry. Negative Refraction Makes a Perfect Lens. *Phys. Rev. Lett.*, 85(18):3966–3969, 2000.
- [128] C. C. Claeys, K. Vergote, P. Sas, and W. Desmet. On the potential of tuned resonators to obtain low-frequency vibrational stop bands in periodic panels. *Journal of Sound and Vibration*, 332(6):1418–1436, 2013.
- [129] D. P. Elford, L. Chalmers, F. Kusmartsev, and G. Swallowe. Matryoshka locally resonant sonic crystal. *The Journal of the Acoustical Society of America*, 130:2746–55, 11 2011.
- [130] D. P. Elford, L. chalmers, F. Kusmartsev, and G. Swallowe. Acoustic band gap formation in metamaterials. *International Journal of Modern Physics B*, 24(25n26):4935–4945, 2010.
- [131] A. Gupta. A review on sonic crystal, its applications and numerical analysis techniques. *Acoustical Physics*, 60:223–234, 03 2014.
- [132] T. Miyashita. Sonic crystals and sonic wave-guides. *Measurement Science and Technology*, 16(5):R47, apr 2005.
- [133] Y. Lai, X. Zhang, and Z.-Q. Zhang. Engineering acoustic band gaps. *Applied Physics Letters*, 79(20):3224–3226, 11 2001.
- [134] A. Melnikov, M. Maeder, N. Friedrich, Y. Pozhanka, A. Wollmann, M. Scheffler, S. Oberst, D. Powell, and S. Marburg. Acoustic metamaterial capsule for reduction of stage machinery noise. *The Journal of the Acoustical Society of America*, 147(3):1491–1503, 03 2020.



- [135] C. Claeys, N. G. Rocha de Melo Filho, L. Van Belle, E. Deckers, and W. Desmet. Design and validation of metamaterials for multiple structural stop bands in waveguides. *Extreme Mechanics Letters*, 12:7–22, 2017. Frontiers in Mechanical Metamaterials.
- [136] G. Floquet. Sur les équations différentielles linéaires à coefficients périodiques. *Annales scientifiques de l'École Normale Supérieure*, 2e série, 12:47–88, 1883.
- [137] F. Bloch. Über die quantenmechanik der elektronen in kristallgittern. *Zeitschrift für physik*, 52(7-8):555–600, 1929.
- [138] C. Kittel. *Introduction to solid state physics*. John Wiley & Sons, Inc., 2005.
- [139] F. Maurin, C. Claeys, E. Deckers, and W. Desmet. Probability that a band-gap extremum is located on the irreducible brillouin-zone contour for the 17 different plane crystallographic lattices. *International Journal of Solids and Structures*, 135:26–36, 2018.
- [140] S. Nojima and Y. Kamakura. Irreducible first brillouin-zone for two-dimensional binary-compound photonic crystals. *Journal of The Physical Society of Japan - J PHYS SOC JPN*, 77, 03 2008.
- [141] P. King and T. Cox. Acoustic band gaps in periodically and quasiperiodically modulated waveguides. *Journal of Applied Physics*, 102:014902–014902, 07 2007.
- [142] V. Laude, Y. Achaoui, S. Benchabane, and A. Khelif. Evanescent bloch waves and the complex band structure of phononic crystals. *Phys. Rev. B*, 80:092301, Sep 2009.
- [143] V. Romero-García, J. V. Sánchez-Pérez, S. Castiñeira-Ibáñez, and L. M. Garcia-Raffi. Evidences of evanescent Bloch waves in phononic crystals. *Applied Physics Letters*, 96(12):124102, 03 2010.
- [144] V. Romero-García, J. V. Sánchez-Pérez, and L. M. García-Raffi. Evanescent modes in sonic crystals: Complex relation dispersion and supercell approximation. *Journal of Applied Physics*, 108, 01 2010.
- [145] Q. Yang, X. Chen, Y. Li, X. Zhang, Y. Xu, Z. Tian, C. Ouyang, J. Gu, J. Han, and W. Zhang. Aperiodic-metamaterial-based absorber. *APL Materials*, 5(9):096107, 09 2017.
- [146] I. Prasetyo, E. Wongso, and J. Sarwono. Developing sub-wavelength sound absorber based on coiled up tube resonator. *Journal of Engineering and Technological Sciences*, 51:323, 06 2019.
- [147] X. Wang, Y. Zhou, J. Sang, and W. Zhu. A generalized model for space-coiling resonators. *Applied Acoustics*, 158:107045, 2020.
- [148] Z. Liang and J. Li. Extreme acoustic metamaterial by coiling up space. *Physical review letters*, 108:114301, 03 2012.

## Bibliography

- [149] J. Guo, X. Zhang, Y. Fang, and Z. Jiang. A compact low-frequency sound-absorbing metasurface constructed by resonator with embedded spiral neck. *Applied Physics Letters*, 117:221902, 11 2020.
- [150] C. Zhang and X. Hu. Three-dimensional single-port labyrinthine acoustic metamaterial: Perfect absorption with large bandwidth and tunability. *Physical Review Applied*, 6, 12 2016.
- [151] X. Wu, K. Y. Au Yeung, X. Li, R. Roberts, T. Jingxuan, H. Chuandeng, Y. Huang, S. Wang, Z. Yang, and W. Wen. High-efficiency ventilated metamaterial absorber at low frequency. *Applied Physics Letters*, 112:103505, 03 2018.
- [152] T.-Y. Huang, C. Shen, and Y. Jing. Membrane- and plate-type acoustic metamaterials. *The Journal of the Acoustical Society of America*, 139(6):3240–3250, 06 2016.
- [153] Y. Gu, Y. Cheng, J. Wang, and X. Liu. Controlling sound transmission with density-near-zero acoustic membrane network. *Journal of Applied Physics*, 118(2):024505, 07 2015.
- [154] Z. Yang, J. Mei, M. Yang, N. H. Chan, and P. Sheng. Membrane-type acoustic metamaterial with negative dynamic mass. *Phys. Rev. Lett.*, 101:204301, Nov 2008.
- [155] F. Langfeldt and W. Gleine. Plate-type acoustic metamaterials with strip masses. *The Journal of the Acoustical Society of America*, 149(6):3727–3738, 06 2021.
- [156] F. Langfeldt and W. Gleine. Membrane- and plate-type acoustic metamaterials with elastic unit cell edges. *Journal of Sound and Vibration*, 453:65–86, 2019.
- [157] C. Claeys, E. Deckers, B. Pluymers, and W. Desmet. A lightweight vibro-acoustic metamaterial demonstrator: Numerical and experimental investigation. *Mechanical Systems and Signal Processing*, 70-71:853–880, 2016.
- [158] X.-L. Gai, X.-W. Guan, Z.-N. Cai, X.-H. Li, W.-C. Hu, T. Xing, and F. Wang. Acoustic properties of honeycomb like sandwich acoustic metamaterials. *Applied Acoustics*, 199:109016, 2022.
- [159] M. Xu, Z. Zhao, P. Wang, S. Duan, H. Lei, and D. Fang. Mechanical performance of bio-inspired hierarchical honeycomb metamaterials. *International Journal of Solids and Structures*, 254-255:111866, 2022.
- [160] A. Elliott, R. Venegas, J. Groby, and O. Umnova. Omnidirectional acoustic absorber with a porous core and a metamaterial matching layer. *Journal of Applied Physics*, 115:204902–204902, 05 2014.
- [161] H. Chen and C. T. Chan. Acoustic cloaking in three dimensions using acoustic metamaterials. *Applied Physics Letters*, 91(18):183518, 11 2007.

- [162] L. Zigoneanu, B.-I. Popa, and S. A. Cummer. Design and measurements of a broadband two-dimensional acoustic lens. *Phys. Rev. B*, 84:024305, Jul 2011.
- [163] X. Li, J. Li, and X. Huang. Reconfigurable coding acoustic meta-lens based on helical metamaterials. *Applied Acoustics*, 211:109538, 2023.
- [164] R. Ghaffarivardavagh, J. Nikolajczyk, R. Glynn Holt, S. Anderson, and X. Zhang. Horn-like space-coiling metamaterials toward simultaneous phase and amplitude modulation. *Nature Communications*, 9(1):1349, Apr 2018.
- [165] J. Lan, Y. Li, Y. Xu, and X. Liu. Manipulation of acoustic wavefront by gradient metasurface based on helmholtz resonators. *Scientific Reports*, 7(1):10587, Sep 2017.
- [166] Y. K. Chiang, S. Oberst, A. Melnikov, L. Quan, S. Marburg, A. Alù, and D. A. Powell. Reconfigurable acoustic metagrating for high-efficiency anomalous reflection. *Phys. Rev. Appl.*, 13:064067, Jun 2020.
- [167] A. Melnikov, S. Köble, S. Schweiger, Y. K. Chiang, S. Marburg, and D. A. Powell. Microacoustic metagratings at ultra-high frequencies fabricated by two-photon lithography. *Advanced Science*, 9(20):2200990, 2022.
- [168] G. Palma, H. Mao, L. Burghignoli, P. Göransson, and U. Iemma. Acoustic metamaterials in aeronautics. *Applied Sciences*, 8:971, 06 2018.
- [169] L. Sangiuliano, B. Reff, J. Palandri, F. Wolf-Monheim, B. Pluymers, E. Deckers, W. Desmet, and C. C. Claeys. Low frequency tyre noise mitigation in a vehicle using metal 3d printed resonant metamaterials. *Mechanical Systems and Signal Processing*, 179:109335, 2022.
- [170] L. Sangiuliano, R. Boukadia, E. Deckers, W. Desmet, and C. Claeys. Reduction of structure-borne tyre/road noise through rubber resonant metamaterials in tyres. In *12th International Styrian Noise, Vibration & Harshness Congress: The European Automotive Noise Conference*. SAE International, 06 2022.
- [171] K.-J. Chang, J. Jung, H.-G. Kim, D. Choi, and S. Wang. An application of acoustic metamaterial for reducing noise transfer through car body panels. *SAE Technical Papers*, 06 2018.
- [172] Y. Liao, H. Huang, G. Chang, D. Luo, C. Xu, Y. Wu, and J. Tang. Research on low-frequency noise control of automobiles based on acoustic metamaterial. *Materials*, 15(9), 2022.
- [173] J. Jung, H.-G. Kim, S. Goo, K.-J. Chang, and S. Wang. Realisation of a locally resonant metamaterial on the automobile panel structure to reduce noise radiation. *Mechanical Systems and Signal Processing*, 122:206–231, 2019.
- [174] A. S. Dukhin and P. J. Goetz, editors. *Chapter 4. Acoustic theory for particulates*, volume 15 of *Studies in Interface Science*, pages 101–152. Elsevier, 2002.

## Bibliography

- [175] X. Jiang, Y. Li, and L. Zhang. Thermoviscous effects on sound transmission through a metasurface of hybrid resonances. *The Journal of the Acoustical Society of America*, 141(4):EL363–EL368, 2017.
- [176] J. Jordaan, S. Punzet, A. Melnikov, A. Sanches, S. Oberst, S. Marburg, and D. A. Powell. Measuring monopole and dipole polarizability of acoustic meta-atoms. *Applied Physics Letters*, 113(22):224102, 2018.
- [177] V. C. Henríquez, P. R. Andersen, J. S. Jensen, P. M. Juhl, and J. Sánchez-Dehesa. A numerical model of an acoustic metamaterial using the boundary element method including viscous and thermal losses. *Journal of Computational Acoustics*, 25(04):1750006, 2017.
- [178] V. C. Henríquez, V. M. García-Chocano, and J. Sánchez-Dehesa. Viscothermal losses in double-negative acoustic metamaterials. *Phys. Rev. Applied*, 8:014029, 07 2017.
- [179] C. Gurbuz, F. Kronowetter, C. Dietz, M. Eser, J. Schmid, and S. Marburg. Generative adversarial networks for the design of acoustic metamaterials. *The Journal of the Acoustical Society of America*, 149(2):1162–1174, 02 2021.
- [180] L. He, Y. Li, D. Torrent, X. Zhuang, T. Rabczuk, and Y. Jin. Machine learning assisted intelligent design of meta structures: a review. *Microstructures*, 3, 08 2023.
- [181] C.-X. Liu and G.-L. Yu. Deep learning for the design of phononic crystals and elastic metamaterials. *Journal of Computational Design and Engineering*, 10, 02 2023.
- [182] Y.-F. Wang and V. Laude. Longitudinal near-field coupling between acoustic resonators grafted onto a waveguide. *Crystals*, 7, 01 2017.
- [183] Y. H. Fu, A. Q. Liu, W. M. Zhu, X. M. Zhang, D. P. Tsai, J. B. Zhang, T. Mei, J. F. Tao, H. C. Guo, X. H. Zhang, J. H. Teng, N. I. Zheludev, G. Q. Lo, and D. L. Kwong. A micromachined reconfigurable metamaterial via reconfiguration of asymmetric split-ring resonators. *Advanced Functional Materials*, 21(18):3589–3594, 2011.
- [184] K. Song, K. Kim, S. Hur, J.-H. Kwak, J. Park, J. R. Yoon, and J. Kim. Sound pressure level gain in an acoustic metamaterial cavity. *Scientific Reports*, 4(1):7421, Dec 2014.
- [185] J. Mei, Z. Chen, and Y. Wu. Pseudo-time-reversal symmetry and topological edge states in two-dimensional acoustic crystals. *Scientific Reports*, 6(1):32752, Sep 2016.
- [186] J. Lu, C. Qiu, L. Ye, X. Fan, M. Ke, F. Zhang, and Z. Liu. Observation of topological valley transport of sound in sonic crystals. *Nature Physics*, 13(4):369–374, Apr 2017.

- [187] C. He, X. Ni, H. Ge, X.-C. Sun, Y.-B. Chen, M.-H. Lu, X.-P. Liu, and Y.-F. Chen. Acoustic topological insulator and robust one-way sound transport. *Nature Physics*, 12(12):1124–1129, Dec 2016.
- [188] Y. Xie, A. Konneker, B.-I. Popa, and S. A. Cummer. Tapered labyrinthine acoustic metamaterials for broadband impedance matching. *Applied Physics Letters*, 103(20):201906, 11 2013.
- [189] J. Mei and Y. Wu. Controllable transmission and total reflection through an impedance-matched acoustic metasurface. *New Journal of Physics*, 16(12):123007, dec 2014.
- [190] Y. Ding, E. C. Statharas, K. Yao, and M. Hong. A broadband acoustic metamaterial with impedance matching layer of gradient index. *Applied Physics Letters*, 110(24):241903, 06 2017.
- [191] M. Duan, C. Yu, Z. Xu, F. Xin, and T. J. Lu. Acoustic impedance regulation of Helmholtz resonators for perfect sound absorption via roughened embedded necks. *Applied Physics Letters*, 117(15):151904, 10 2020.
- [192] A. Elayouch, M. Addouche, M. Farhat, M. Amin, H. Bağcı, and A. Khelif. Density-near-zero using the acoustically induced transparency of a fano acoustic resonator. *Europhysics Letters*, 116(4):46004, jan 2017.
- [193] R. Ghaffarivardavagh, J. Nikolajczyk, S. Anderson, and X. Zhang. Ultra-open acoustic metamaterial silencer based on fano-like interference. *Physical Review B*, 99:024302, 01 2019.
- [194] M. Sun, X. Fang, D. Mao, X. Wang, and Y. Li. Broadband acoustic ventilation barriers. *Phys. Rev. Appl.*, 13:044028, Apr 2020.
- [195] H. Nguyen, Q. Wu, X. Xu, H. Chen, S. Tracy, and G. Huang. Broadband acoustic silencer with ventilation based on slit-type Helmholtz resonators. *Applied Physics Letters*, 117(13):134103, 09 2020.
- [196] H. Q. Nguyen, Q. Wu, H. Chen, J. J. Chen, Y. K. Yu, S. Tracy, and G. L. Huang. A fano-based acoustic metamaterial for ultra-broadband sound barriers. *Proceedings of the Royal Society A: Mathematical, Physical and Engineering Sciences*, 477(2248):20210024, 2021.
- [197] A. Bogdanov, K. Koshelev, P. Kapitanova, M. Rybin, S. Gladyshev, Z. Sadrieva, K. Samusev, Y. Kivshar, and M. Limonov. Bound states in the continuum and fano resonances in the strong mode coupling regime. *Advanced Photonics*, 1:1, 01 2019.
- [198] N. Solodovchenko, K. Samusev, D. Bocek, and M. Limonov. Bound states in the continuum in strong-coupling and weak-coupling regimes under the cylinder – ring transition. *Nanophotonics*, 10(17):4347–4355, 2021.

## Bibliography

- [199] G. Khitrova, H. M. Gibbs, M. Kira, S. W. Koch, and A. Scherer. Vacuum rabi splitting in semiconductors. *Nature Physics*, 2(2):81–90, Feb 2006.
- [200] M. A. Miropoliubov, A. K. Samusev, I. D. Toftul, and M. I. Petrov. Spectral characteristics and time dynamics of tunable acoustic resonators in the strong coupling regime. *JETP Letters*, 113(8):547–553, Apr 2021.
- [201] M. Günay, A. Biçer, N. Korozlu, and A. Cicek. Tunable acoustic resonances: From weak to strong coupling regime. *Applied Physics Letters*, 123(9):092201, 08 2023.
- [202] J. von Neumann and E. P. Wigner. *Über merkwürdige diskrete Eigenwerte*, pages 291–293. Springer Berlin Heidelberg, Berlin, Heidelberg, 1993.
- [203] F. Ursell. Trapping modes in the theory of surface waves. *Mathematical Proceedings of the Cambridge Philosophical Society*, 47(2):347–358, 1951.
- [204] A. E. Miroschnichenko, S. Flach, and Y. S. Kivshar. Fano resonances in nanoscale structures. *Rev. Mod. Phys.*, 82:2257–2298, 08 2010.
- [205] D. Evans and C. Linton. Trapped modes in open channels. *Journal of Fluid Mechanics*, 225:153 – 175, 04 1991.
- [206] D. V. Evans, M. Levitin, and D. Vassiliev. Existence theorems for trapped modes. *Journal of Fluid Mechanics*, 261:21–31, 1994.
- [207] N. Sugimoto and H. Imahori. Localized mode of sound in a waveguide with helmholtz resonators. *Journal of Fluid Mechanics*, 546:89–111, 2006.
- [208] E. H. E. Boudouti, T. Mrabti, H. Al-Wahsh, B. Djafari-Rouhani, A. Akjouj, and L. Dobrzynski. Transmission gaps and fano resonances in an acoustic waveguide: analytical model. *Journal of Physics: Condensed Matter*, 20(25):255212, 05 2008.
- [209] L. Huang, B. Jia, Y. K. Chiang, S. Huang, C. Shen, F. Deng, T. Yang, D. A. Powell, Y. Li, and A. E. Miroschnichenko. Topological supercavity resonances in the finite system. *Advanced Science*, 9(20):2200257, 2022.
- [210] H. Friedrich and D. Wintgen. Interfering resonances and bound states in the continuum. *Phys. Rev. A*, 32:3231–3242, 12 1985.
- [211] C. M. Linton and P. McIver. Embedded trapped modes in water waves and acoustics. *Wave Motion*, 45(1):16 – 29, 2007. Special Issue on Localization of Wave Motion.
- [212] Y. Duan, W. Koch, C. M. Linton, and M. McIver. Complex resonances and trapped modes in ducted domains. *Journal of Fluid Mechanics*, 571:119–147, 01 2007.
- [213] A. A. Lyapina, D. Maksimov, A. Pilipchuk, and A. Sadreev. Bound states in the continuum in open acoustic resonators. *Journal of Fluid Mechanics*, 780, 06 2015.

- [214] A. A. Lyapina, A. Pilipchuk, and A. Sadreev. Bound states with orbital angular momentum in the continuum of cylindrical non-axisymmetric waveguide. *Annals of Physics*, 396, 07 2018.
- [215] A. A. Lyapina, A. Pilipchuk, and A. Sadreev. Trapped modes in a non-axisymmetric cylindrical waveguide. *Journal of Sound and Vibration*, 421:48–60, 05 2018.
- [216] L. Xiong, W. Bi, and Y. Aurégan. Fano resonance scatterings in waveguides with impedance boundary conditions. *The Journal of the Acoustical Society of America*, 139(2):764–772, 2016.
- [217] A. A. Maznev and A. G. Every. Bound acoustic modes in the radiation continuum in isotropic layered systems without periodic structures. *Phys. Rev. B*, 97:014108, 01 2018.
- [218] K. Koshelev, S. Lepeshov, M. Liu, A. Bogdanov, and Y. Kivshar. Asymmetric metasurfaces with high- $q$  resonances governed by bound states in the continuum. *Phys. Rev. Lett.*, 121:193903, Nov 2018.
- [219] O. Haq and S. Shabanov. Bound states in the continuum in elasticity. *Wave Motion*, 103:102718, 2021.
- [220] A. Sadreev, E. Bulgakov, A. Pilipchuk, A. Miroshnichenko, and L. Huang. Degenerate bound states in the continuum in square and triangular open acoustic resonators. *Phys. Rev. B*, 106:085404, Aug 2022.
- [221] B. Jia, L. Huang, A. S. Pilipchuk, S. Huang, C. Shen, A. F. Sadreev, Y. Li, and A. E. Miroshnichenko. Bound states in the continuum protected by reduced symmetry of three-dimensional open acoustic resonators. *Phys. Rev. Appl.*, 19:054001, May 2023.
- [222] Y.-G. Peng, Z.-G. Geng, and X.-F. Zhu. Topologically protected bound states in one-dimensional floquet acoustic waveguide systems. *Journal of Applied Physics*, 123(9):091716, 2018.
- [223] Z.-G. Chen, C. Xu, R. Al Jahdali, J. Mei, and Y. Wu. Corner states in a second-order acoustic topological insulator as bound states in the continuum. *Phys. Rev. B*, 100:075120, 08 2019.
- [224] F. Zangeneh-Nejad and R. Fleury. Topological fano resonances. *Phys. Rev. Lett.*, 122:014301, Jan 2019.
- [225] L. Huang, B. Jia, A. S. Pilipchuk, Y. K. Chiang, S. Huang, J. Li, C. Shen, E. N. Bulgakov, F. Deng, D. A. Powell, S. A. Cummer, Y. Li, A. F. Sadreev, and A. E. Miroshnichenko. General framework of bound states in the continuum in an open acoustic resonator. *Phys. Rev. Applied*, 18:054021, 11 2022.
- [226] D. Maksimov, A. Sadreev, A. A. Lyapina, and A. Pilipchuk. Coupled mode theory for acoustic resonators. *Wave Motion*, 56:52–66, 02 2015.

## Bibliography

- [227] S. Huang, T. Liu, Z. Zhou, X. Wang, J. Zhu, and Y. Li. Extreme sound confinement from quasibound states in the continuum. *Physical Review Applied*, 14, 08 2020.
- [228] L. Huang, Y. K. Chiang, S. Huang, C. Shen, F. Deng, Y. Cheng, B. Jia, Y. Li, D. A. Powell, and A. E. Miroshnichenko. Sound trapping in an open resonator. *Nature Communications*, 12, 08 2021.
- [229] S. Huang, S. Xie, H. Gao, S. Hao, T. and Zhang, T. Liu, Y. Li, and J. Zhu. Acoustic purcell effect induced by quasibound state in the continuum. *Fundamental Research*, 2022.
- [230] R. Manenti, A. Frisk Kockum, A. Patterson, T. Behrle, J. Rahamim, G. Tancredi, F. Nori, and P. Leek. Circuit quantum acoustodynamics with surface acoustic waves. *Nature Communications*, 8, 10 2017.
- [231] U. von Lüpke, Y. Yang, M. Bild, L. Michaud, M. Fadel, and Y. Chu. Parity measurement in the strong dispersive regime of circuit quantum acoustodynamics. *Nature Physics*, 18:1–6, 07 2022.
- [232] A. Navarathna and W. Bowen. Good vibrations for quantum computing. *Nature Physics*, 18:1–2, 05 2022.
- [233] E. A. Wollack, A. Y. Cleland, R. G. Gruenke, Z. Wang, P. Arrangoiz-Arriola, and A. Safavi-Naeini. Quantum state preparation and tomography of entangled mechanical resonators. *Nature*, 604:463–467, 04 2022.
- [234] Y. Yu, X. Xi, and X. Sun. Observation of mechanical bound states in the continuum in an optomechanical microresonator. *Light: Science & Applications*, 11:328, 11 2022.
- [235] I. Deriy, I. Toftul, M. Petrov, and A. Bogdanov. Bound states in the continuum in compact acoustic resonators. *Phys. Rev. Lett.*, 128:084301, 02 2022.
- [236] M. Kaltenbacher. *Fundamental Equations of Acoustics*, pages 1–33. Springer International Publishing, Cham, 2018.
- [237] R. Lerch, W. Dietrich, and S. Gerhard. *Schall in Gasen und Flüssigkeiten*, pages 7–53. Springer Berlin Heidelberg, Berlin, Heidelberg, 2009.
- [238] F. Ihlenburg, editor. *The Governing Equations of Time-Harmonic Wave Propagation*, pages 1–20. Springer New York, New York, NY, 1998.
- [239] M. Möser. *Grundbegriffe der Wellenausbreitung*, pages 19–75. Springer Berlin Heidelberg, Berlin, Heidelberg, 2015.
- [240] F. Atkinson. Lxi. on sommerfeld’s “radiation condition.”. *The London, Edinburgh, and Dublin Philosophical Magazine and Journal of Science*, 40(305):645–651, 1949.



- [241] J. S. Hubert and E. S. Palencia. *The Helmholtz Equation in Unbounded Domains*, pages 322–375. Springer Berlin Heidelberg, Berlin, Heidelberg, 1989.
- [242] F. Ziegler. *Constitutive Equations*, pages 183–224. Springer New York, New York, NY, 1995.
- [243] M. Kaltenbacher. *Mechanical Field*, pages 93–135. Springer Berlin Heidelberg, Berlin, Heidelberg, 2015.
- [244] T. Belytschko, W. Liu, B. Moran, and K. Elkhodary. *Nonlinear Finite Elements for Continua and Structures*. No Longer used. Wiley, 2013.
- [245] C. H. Wilcox. A generalization of theorems of Rellich and Atkinson. *Proceedings of the American Mathematical Society*, 7(2):271–276, 1956.
- [246] G. Dassios. The Atkinson–Wilcox theorem in ellipsoidal geometry. *Journal of Mathematical Analysis and Applications*, 274(2):828–845, 2002.
- [247] J. J. Shirron and I. Babuška. A comparison of approximate boundary conditions and infinite element methods for exterior Helmholtz problems. *Computer Methods in Applied Mechanics and Engineering*, 164(1):121–139, 1998. Exterior Problems of Wave Propagation.
- [248] J. Marques and D. Owen. Infinite elements in quasi-static materially nonlinear problems. *Computers & Structures*, 18(4):739–751, 1984.
- [249] G. Stefanou. The stochastic finite element method: Past, present and future. *Computer Methods in Applied Mechanics and Engineering*, 198(9):1031–1051, 2009.
- [250] N. Wiener. The homogeneous chaos. *American Journal of Mathematics*, 60(4):897–936, 1938.
- [251] D. Xiu and G. E. Karniadakis. The Wiener–Askey polynomial chaos for stochastic differential equations. *SIAM Journal on Scientific Computing*, 24(2):619–644, 2002.
- [252] R. A. Askey and J. A. Wilson. Some basic hypergeometric orthogonal polynomials that generalize Jacobi polynomials. *Memoirs of the American Mathematical Society*, 54:0–0, 1985.
- [253] J. Villadsen and M. Michelsen. *Solution of Differential Equation Models by Polynomial Approximation*. Prentice-Hall international series in the physical and chemical engineering sciences. Prentice-Hall, 1978.
- [254] L. Lefèvre, D. Dochain, S. Feye de Azevedo, and A. Magnus. Optimal selection of orthogonal polynomials applied to the integration of chemical reactor equations by collocation methods. *Computers & Chemical Engineering*, 24(12):2571–2588, 2000.
- [255] S. S. Isukapalli, A. Roy, and P. G. Georgopoulos. Stochastic response surface methods (srsms) for uncertainty propagation: Application to environmental and biological systems. *Risk Analysis*, 18(3):351–363, 1998.

## Bibliography

- [256] M. Tatang, W. Pan, R. Prinn, and G. McRae. An efficient method for parametric uncertainty analysis of numerical geophysical model. *Journal of Geophysical Research*, 102:21925–21932, 09 1997.
- [257] P. Ruge. Eigenvalues of damped structures: Vectoriteration in the original space of dof. *Computational Mechanics*, 22(2):167–173, Aug 1998.
- [258] Z. Bai and Y. Su. Dimension reduction of large-scale second-order dynamical systems via a second-order arnoldi method. *SIAM J. Scientific Computing*, 26:1692–1709, 01 2005.
- [259] Z. Bai and Y. Su. Soar: A second-order arnoldi method for the solution of the quadratic eigenvalue problem. *SIAM Journal on Matrix Analysis and Applications*, 26(3):640–659, 2005.
- [260] T. Sakurai, Y. Futamura, and H. Tadano. Efficient parameter estimation and implementation of a contour integral-based eigensolver. *Journal of Algorithms & Computational Technology*, 7(3):249–269, 2013.
- [261] V. I. Arnold. *Variational principles*, pages 55–74. Springer New York, New York, NY, 1978.
- [262] Y. Ashida, Z. Gong, and M. Ueda. Non-hermitian physics. *Advances in Physics*, 69(3):249–435, 2020.
- [263] R. El-Ganainy, K. G. Makris, M. Khajavikhan, Z. H. Musslimani, S. Rotter, and D. N. Christodoulides. Non-hermitian physics and pt symmetry. *Nature Physics*, 14(1):11–19, Jan 2018.
- [264] K. Ding, C. Fang, and G. Ma. Non-hermitian topology and exceptional-point geometries. *Nature Reviews Physics*, 4(12):745–760, Dec 2022.
- [265] H. Feshbach. Unified theory of nuclear reactions. *Annals of Physics*, 5(4):357–390, 1958.
- [266] F.-M. Dittes. The decay of quantum systems with a small number of open channels. *Physics Reports*, 339:215–316, 12 2000.
- [267] J. Okolowicz, M. Płoszajczak, and I. Rotter. Dynamics of quantum systems embedded in a continuum. *Physics Reports*, 374:271–383, 02 2003.
- [268] K. Pichugin, H. Schanz, and P. Šeba. Effective coupling for open billiards. *Phys. Rev. E*, 64:056227, Oct 2001.
- [269] I. Rotter. A continuum shell model for the open quantum mechanical nuclear system. *Reports on Progress in Physics*, 54(4):635, apr 1991.
- [270] A. Sadreev and I. Rotter. S-matrix theory for transmission through billiards in tight-binding approach. *Journal of Physics A General Physics*, 36, 04 2003.

- [271] H. A. Haus and W. Huang. Coupled-mode theory. *Proceedings of the IEEE*, 79(10):1505–1518, 1991.
- [272] T. Lee, X. Li, Z. Yu, T. Nomura, E. M. Dede, and H. Iizuka. Coupled acoustic resonance for wave control and sensing. *Frontiers in Physics*, 10, 2022.
- [273] R. Lerch, W. Dietrich, and S. Gerhard. *Raumakustik*, pages 215–239. Springer Berlin Heidelberg, Berlin, Heidelberg, 2009.
- [274] M. Möser. *Schallabsorption*, pages 183–232. Springer Berlin Heidelberg, Berlin, Heidelberg, 2015.
- [275] H. Lin, T. Bengisu, and Z. P. Mourelatos. *Acoustic Waveguides*, pages 197–226. Springer International Publishing, Cham, 2021.
- [276] M. A. Langthjem and M. Nakano. On the acoustic trapped modes and their symmetry properties in a circular cylindrical waveguide with a cavity. *Journal of Engineering Mathematics*, 128(1):14, May 2021.
- [277] A. F. Sadreev, E. N. Bulgakov, and I. Rotter. Bound states in the continuum in open quantum billiards with a variable shape. *Phys. Rev. B*, 73:235342, Jun 2006.
- [278] J. Wiersig and J. Main. Fractal weyl law for chaotic microcavities: Fresnel’s laws imply multifractal scattering. *Phys. Rev. E*, 77:036205, Mar 2008.
- [279] J. Allard and Y. Champoux. New empirical equations for sound propagation in rigid frame fibrous materials. *The Journal of the Acoustical Society of America*, 91(6):3346–3353, 1992.
- [280] Y. Champoux and J. Allard. Dynamic tortuosity and bulk modulus in air-saturated porous media. *Journal of Applied Physics*, 70(4):1975–1979, 1991.
- [281] D. L. Johnson, J. Koplik, and R. Dashen. Theory of dynamic permeability and tortuosity in fluid-saturated porous media. *Journal of Fluid Mechanics*, 176:379–402, 1987.
- [282] X. Zhao and X. Fan. Enhancing low frequency sound absorption of micro-perforated panel absorbers by using mechanical impedance plates. *Applied Acoustics*, 88:123–128, 2015.
- [283] A. Mosa, A. Putra, R. Ramlan, and E. Al-Ameri. Micro-perforated panel absorber arrangement technique: A review. *Journal of Advanced Research in Dynamical and Control Systems*, 10:372–381, 01 2018.
- [284] Y. Qian, K. Cui, S. M. Liu, Z. B. Li, D. S. Shao, D. Y. Kong, and S. M. Sun. Optimization of multi-size micro-perforated panel absorbers using multi-population genetic algorithm. *Noise Control Engineering Journal*, 62, 01 2014.

## Bibliography

- [285] B. Dong, D. Xie, F. He, and L. Huang. Noise attenuation and performance study of a small-sized contra-rotating fan with microperforated casing treatments. *Mechanical Systems and Signal Processing*, 147:107086, 2021.
- [286] W. Sun, B. Pan, X. Song, H. Xiao, J. Zhou, and D. Sui. A novel sound absorber design of nanofibrous composite porous material. *Materials & Design*, 214:110418, 2022.
- [287] N. Atalla and F. Sgard. Modeling of perforated plates and screens using rigid frame porous models. *Journal of Sound and Vibration*, 303:195–208, 06 2007.
- [288] P. Bai, X. Yang, X. Shen, X. Zhang, Z. Li, Q. Yin, G. Jiang, and F. Yang. Sound absorption performance of the acoustic absorber fabricated by compression and microperforation of the porous metal. *Materials & Design*, 167:107637, 02 2019.
- [289] Q. Zhang. Sound transmission through micro-perforated double-walled cylindrical shells lined with porous material. *Journal of Sound and Vibration*, 485:115539, 2020.
- [290] Z. Liu, J. Zhan, M. Fard, and J. L. Davy. Acoustic measurement of a 3d printed micro-perforated panel combined with a porous material. *Measurement*, 104:233–236, 2017.
- [291] K. Sakagami, S. Kobatake, K. Kano, M. Morimoto, and M. Yairi. Sound absorption characteristics of a single microperforated panel absorber backed by a porous absorbent layer. *Acoustics Australia*, 39, 12 2011.
- [292] D.-Y. Maa. Theory and design of microperforated panel sound-absorbing constructions. *Scientia sinica*, XVIII:55–71, 01 1975.
- [293] D.-Y. Maa. Microperforated-panel wideband absorbers. *Noise control engineering journal*, 29(3):77–84, 1987.
- [294] D.-Y. Maa. Potential of microperforated panel absorber. *The Journal of the Acoustical Society of America*, 104(5):2861–2866, 1998.
- [295] N. H. Fletcher and T. D. Rossing. *Pipes, Horns and Cavities*, pages 190–235. Springer New York, New York, NY, 1998.
- [296] L. Kinsler, A. Frey, A. Coppens, and J. Sanders. *Fundamentals of Acoustics*. Wiley, 1982.
- [297] C. Rui Liu, J. Hui Wu, Z. Yang, and F. Ma. Ultra-broadband acoustic absorption of a thin microperforated panel metamaterial with multi-order resonance. *Composite Structures*, 246:112366, 2020.
- [298] H. V. Fuchs. *Platten-Resonatoren*, pages 51–70. Springer Berlin Heidelberg, Berlin, Heidelberg, 2017.

- [299] F. Rafique, J. H. Wu, M. Waqas, X. Lushuai, and F. Ma. A thin double-layer multiple parallel-arranged inhomogeneous microperforated panel absorber for wideband low-frequency sound absorption. *Journal of the Brazilian Society of Mechanical Sciences and Engineering*, 44(1):31, Dec 2021.
- [300] B. H. Song and J. S. Bolton. A transfer-matrix approach for estimating the characteristic impedance and wave numbers of limp and rigid porous materials. *The Journal of the Acoustical Society of America*, 107(3):1131–1152, 2000.
- [301] L. Sun, H. Hou, L.-Y. Dong, and F.-R. Wan. Measurement of characteristic impedance and wave number of porous material using pulse-tube and transfer-matrix methods. *The Journal of the Acoustical Society of America*, 126(6):3049–3056, 2009.
- [302] F. Asdrubali and G. Pispola. Properties of transparent sound-absorbing panels for use in noise barriers. *The Journal of the Acoustical Society of America*, 121:214–221, 01 2007.
- [303] D. R. H. Craig F. Bohren. *Introduction*, chapter 1, pages 1–11. John Wiley & Sons, Ltd, 1998.
- [304] J. Rayleigh and R. Lindsay. *The Theory of Sound*. Number Bd. 2 in Dover Books on Physics. Dover Publications, 1945.
- [305] M. Rybin, A. Khanikaev, M. Inoue, K. Samusev, M. Steel, G. Yushin, and M. Limonov. Fano resonance between mie and bragg scattering in photonic crystals. *Physical review letters*, 103:023901, 08 2009.
- [306] D. Hestenes and J. Holt. Crystallographic space groups in geometric algebra. *Journal of Mathematical Physics*, 48:023514–023514, 02 2007.
- [307] C. Bradley and A. Cracknell. *The Mathematical Theory of Symmetry in Solids: Representation Theory for Point Groups and Space Groups*. EBSCO ebook academic collection. OUP Oxford, 2010.
- [308] U. Shmueli. *Reciprocal space in crystallography*, pages 2–9. Springer Netherlands, Dordrecht, 2001.
- [309] ISO 10534-2:2023. Acoustics – determination of acoustic properties in impedance tubes – part 2: Two-microphone technique for normal sound absorption coefficient and normal surface impedance. Standard ISO 10534-2:2023, International Organization for Standardization, Geneva, CH, 2023.
- [310] M. Munjal. *Acoustics of Ducts and Mufflers*. Wiley, 2014.
- [311] C. To and A. Doige. A transient testing technique for the determination of matrix parameters of acoustic systems, i: Theory and principles. *Journal of Sound and Vibration*, 62(2):207–222, 1979.

## Bibliography

- [312] C. To and A. Doige. A transient testing technique for the determination of matrix parameters of acoustic systems, ii: Experimental procedures and results. *Journal of Sound and Vibration*, 62(2):223–233, 1979.
- [313] M. Munjal and A. Doige. Theory of a two source-location method for direct experimental evaluation of the four-pole parameters of an aeroacoustic element. *Journal of Sound and Vibration*, 141(2):323–333, 1990.
- [314] T. Y. Lung and A. G. Doige. A time-averaging transient testing method for acoustic properties of piping systems and mufflers with flow. *The Journal of the Acoustical Society of America*, 73(3):867–876, 03 1983.
- [315] ASTM E2611-19. Standard test method for normal incidence determination of porous material acoustical properties based on the transfer matrix method. Standard ASTM E2611-19, American Society for Testing and Materials, 2019.
- [316] J. S. Bolton, R. J. Yun, J. Pope, and D. Apfel. Development of a new sound transmission test for automotive sealant materials. In *SAE Noise and Vibration Conference and Exposition*. SAE International, may 1997.
- [317] B. Song and J. S. Bolton. A transfer-matrix approach for estimating the characteristic impedance and wave numbers of limp and rigid porous materials. *The Journal of the Acoustical Society of America*, 107:1131–52, 04 2000.
- [318] K. Hou and J. S. Bolton. A transfer matrix method for estimating the dispersion and attenuation of plane waves in the standing wave tube. *The Journal of the Acoustical Society of America*, 125:2596, 05 2009.
- [319] Y. Salissou and R. Panneton. A general wave decomposition formula for the measurement of normal incidence sound transmission loss in impedance tube. *The Journal of the Acoustical Society of America*, 125:2083–90, 05 2009.
- [320] X. Hua and D. Herrin. Practical considerations when using the two-load method to determine the transmission loss of mufflers and silencers. *SAE International Journal of Passenger Cars - Mechanical Systems*, 6:1094–1101, 05 2013.
- [321] R. Lerch, W. Dietrich, and S. Gerhard. *Reflexion, Brechung, Beugung von Schall*, pages 55–76. Springer Berlin Heidelberg, Berlin, Heidelberg, 2009.
- [322] H. Skilling. *Electrical Engineering Circuits*. Wiley, 1957.
- [323] A. D. Pierce. *Low-Frequency Models of Sound Transmission*, pages 361–426. Springer International Publishing, Cham, 2019.
- [324] W. P. Mason. A study of the regular combination of acoustic elements, with applications to recurrent acoustic filters, tapered acoustic filters, and horns. *Bell System Technical Journal*, 6:258–294, 1927.

- [325] M. Åbom. Measurement of the scattering-matrix of acoustical two-ports. *Mechanical Systems and Signal Processing*, 5(2):89–104, 1991.
- [326] M. Möser. *Schalldämpfer*, pages 283–327. Springer Berlin Heidelberg, Berlin, Heidelberg, 2015.
- [327] L. Zipser and H. H. Franke. Refracto-vibrometry - a novel method for visualizing sound waves in transparent media. *The Journal of the Acoustical Society of America*, 123(5):3314–3314, 05 2008.
- [328] J. H. Gladstone and T. P. Dale. Researches on the refraction, dispersion, and sensitiveness of liquids. *Philosophical Transactions of the Royal Society of London*, 153:317–343, 1863.
- [329] K. Ishikawa, K. Yatabe, N. Chitanont, Y. Ikeda, Y. Oikawa, T. Onuma, H. Niwa, and M. Yoshii. High-speed imaging of sound using parallel phase-shifting interferometry. *Opt. Express*, 24(12):12922–12932, Jun 2016.
- [330] F. Mbailassem, Q. Leclère, E. Redon, and E. Gourdon. Experimental analysis of acoustical properties of irregular cavities using laser refracto-vibrometry. *Applied Acoustics*, 130:177–187, 2018.
- [331] R. Malkin, T. Todd, and D. Robert. A simple method for quantitative imaging of 2d acoustic fields using refracto-vibrometry. *Journal of Sound and Vibration*, 333(19):4473–4482, 2014.
- [332] R. Jackett, B. Piper, and R. J. Hughes. Characterization of acoustic diffusion using refracto-vibrometry. *Journal of Sound and Vibration*, 392:70–76, 2017.
- [333] H. Dong, Z. Yu, K. T. V. Grattan, T. Sun, and T. Li. Acoustic standing wave field measurement using a laser doppler vibrometer based on the hankel fourier algorithm. *IEEE Access*, 7:139013–139020, 2019.
- [334] Y. Oikawa, M. Goto, Y. Ikeda, T. Takizawa, and Y. Yamasaki. Sound field measurements based on reconstruction from laser projections. In *Proceedings. (ICASSP '05). IEEE International Conference on Acoustics, Speech, and Signal Processing, 2005.*, volume 4, pages iv/661–iv/664 Vol. 4, 2005.
- [335] L. Moheit and S. Marburg. Infinite elements and their influence on normal and radiation modes in exterior acoustics. *Journal of Computational Acoustics*, 25(04):1650020, 2017.
- [336] L. Moheit and S. Marburg. Normal modes and modal reduction in exterior acoustics. *Journal of Theoretical and Computational Acoustics*, 26:1850029, 07 2018.
- [337] L. Moheit, S. Anthis, J. Heinz, F. Kronowetter, and S. Marburg. Analysis of scattering by finite sonic crystals in free field with infinite elements and normal modes. *Journal of Sound and Vibration*, 476:115291, 03 2020.

## Bibliography

- [338] M. A. Nobile and S. I. Hayek. Acoustic propagation over an impedance plane. *The Journal of the Acoustical Society of America*, 78(4):1325–1336, 10 1985.
- [339] M. Ochmann and H. Brick. *Acoustical Radiation and Scattering above an Impedance Plane*, pages 459–494. Springer Berlin Heidelberg, Berlin, Heidelberg, 2008.
- [340] M. Möser and G. Müller. *Grundlagen der Technischen Akustik*, pages 1–29. Springer Berlin Heidelberg, Berlin, Heidelberg, 2018.
- [341] M. C. Junger, D. Feit, and J. E. Greenspon. Sound, Structures, and Their Interaction, 2nd edition by Miguel C. Junger and David Feit. *The Journal of the Acoustical Society of America*, 82(4):1466–1466, 10 1987.
- [342] H. Peters, N. Kessissoglou, and S. Marburg. Modal decomposition of exterior acoustic-structure interaction. *The Journal of the Acoustical Society of America*, 133(5):2668–2677, 05 2013.
- [343] C.-J. Zheng, C.-X. Bi, C. Zhang, H.-F. Gao, and H.-B. Chen. Free vibration analysis of elastic structures submerged in an infinite or semi-infinite fluid domain by means of a coupled fe–be solver. *Journal of Computational Physics*, 359:183–198, 2018.
- [344] S. K. Baydoun, M. Voigt, C. Jelich, and S. Marburg. A greedy reduced basis scheme for multifrequency solution of structural acoustic systems. *International Journal for Numerical Methods in Engineering*, 121(2):187–200, 2020.
- [345] T. Liang, J. Wang, J. Xiao, and L. Wen. Coupled be–fe based vibroacoustic modal analysis and frequency sweep using a generalized resolvent sampling method. *Computer Methods in Applied Mechanics and Engineering*, 345:518–538, 2019.
- [346] M. L. L. d. Guevara, F. Claro, and P. A. Orellana. Ghost fano resonance in a double quantum dot molecule attached to leads. *Phys. Rev. B*, 67:195335, May 2003.
- [347] I. Harari and T. J. Hughes. A cost comparison of boundary element and finite element methods for problems of time-harmonic acoustics. *Computer Methods in Applied Mechanics and Engineering*, 97(1):77–102, 1992.
- [348] N. Chen, D. Yu, and B. Xia. Hybrid uncertain analysis for the prediction of exterior acoustic field with interval and random parameters. *Computers & Structures*, 141:9–18, 2014.
- [349] N. Chen, D. Yu, and B. Xia. Evidence-theory-based analysis for the prediction of exterior acoustic field with epistemic uncertainties. *Engineering Analysis with Boundary Elements*, 50:402–411, 2015.
- [350] C. Wang and Z. Qiu. An interval perturbation method for exterior acoustic field prediction with uncertain-but-bounded parameters. *Journal of Fluids and Structures*, 49:441–449, 2014.



- [351] H. Peters, N. Kessissoglou, and S. Marburg. Modal decomposition of exterior acoustic-structure interaction problems with model order reduction. *The Journal of the Acoustical Society of America*, 135(5):2706–2717, 05 2014.
- [352] M. El-Guide, A. Międlar, and Y. Saad. A rational approximation method for solving acoustic nonlinear eigenvalue problems. *Engineering Analysis with Boundary Elements*, 111:44–54, 2020.
- [353] J. L. Fischer, R. Bader, and M. Abel. Aeroacoustical coupling and synchronization of organ pipes. *The Journal of the Acoustical Society of America*, 140(4):2344–2351, 2016.
- [354] J. L. Fischer and R. Bader. Switch of synchronization states of aeroacoustical coupled organ pipes. *The Journal of the Acoustical Society of America*, 143(3):1908, 2018.
- [355] A. Pikovsky, M. Rosenblum, and J. Kurths. *Synchronization*. Cambridge University Press, 2001.
- [356] J. W. Strutt. *The Theory of Sound*, volume 1 of *Cambridge Library Collection - Physical Sciences*. Cambridge University Press, 2011.
- [357] T. A. Johansson and M. Kleiner. Theory and experiments on the coupling of two Helmholtz resonators. *The Journal of the Acoustical Society of America*, 110(3):1315–1328, 2001.
- [358] R. Al Jahdali and Y. Wu. Coupled resonators for sound trapping and absorption. *Scientific Reports*, 8(1):13855, Sep 2018.
- [359] Y. Zhou, X. Fang, D. Li, T. Hao, and Y. Li. Acoustic multiband double negativity from coupled single-negative resonators. *Phys. Rev. Applied*, 10:044006, 10 2018.
- [360] I. Herrero-Durá, A. Cebrecos, R. Picó, V. Romero-García, L. M. García-Raffi, and V. J. Sánchez-Morcillo. Sound absorption and diffusion by 2d arrays of helmholtz resonators. *Applied Sciences*, 10(5), 2020.
- [361] T. Cavalieri, A. Cebrecos, J.-P. Groby, C. Chaufour, and V. Romero-García. Three-dimensional multiresonant lossy sonic crystal for broadband acoustic attenuation: Application to train noise reduction. *Applied Acoustics*, 146:1–8, 03 2019.
- [362] T. Lee and H. Iizuka. Bragg scattering based acoustic topological transition controlled by local resonance. *Physical Review B*, 99:064305, 02 2019.
- [363] M. Krasikova, S. Krasikov, A. Melnikov, Y. Baloshin, S. Marburg, D. A. Powell, and A. Bogdanov. Metahouse: Noise-insulating chamber based on periodic structures. *Advanced Materials Technologies*, page 2200711, 2022.

## Bibliography

- [364] M. Krasikova, S. Krasikov, A. Melnikov, Y. Baloshin, S. Marburg, D. A. Powell, and A. Bogdanov. Metahouse: Noise-insulating chamber based on periodic structures. *Advanced Materials Technologies*, 8(1):2200711, 2023.
- [365] X. Yang, J. Yin, G. Yu, L. Peng, and N. Wang. Acoustic superlens using Helmholtz-resonator-based metamaterials. *Applied Physics Letters*, 107(19):193505, 11 2015.
- [366] Y. Dong, G. Yu, X. Wang, X. Niu, K. Wu, and N. Wang. Broadband and wide-angle blazed acoustic gratings using multiple coupled Helmholtz resonators. *Applied Physics Express*, 10(9):097201, September 2017.
- [367] J. B. Pendry, D. Schurig, and D. R. Smith. Controlling Electromagnetic Fields. *Science*, 312(5781):1780–1782, 2006.
- [368] D. Schurig, J. J. Mock, B. J. Justice, S. A. Cummer, J. B. Pendry, A. F. Starr, and D. R. Smith. Metamaterial Electromagnetic Cloak at Microwave Frequencies. *Science*, 314(5801):977–980, 2006.
- [369] J. Valentine, J. Li, T. Zentgraf, G. Bartal, and X. Zhang. An optical cloak made of dielectrics. *Nature Materials*, 8(7):568–571, 2009.
- [370] F. Hesmer, E. Tatartschuk, O. Zhuromskyy, A. Radkovskaya, M. Shamonin, T. Hao, C. Stevens, G. Faulkner, D. Edwards, and E. Shamonina. Coupling mechanisms for split ring resonators: Theory and experiment. *physica status solidi (b)*, 244:1170–1175, 2007.
- [371] H. Liu, Y. M. Liu, T. Li, S. M. Wang, S. N. Zhu, and X. Zhang. Coupled magnetic plasmons in metamaterials. *Phys. Status Solidi B*, 246(7):1397–1406, 2009.
- [372] G. R. Keiser, K. Fan, X. Zhang, and R. D. Averitt. Towards dynamic, tunable, nonlinear metamaterials via near field interactions: A review. *Journal of Infrared, Millimeter, and Terahertz Waves*, 34(11):709–723, 2013.
- [373] D. A. Powell, M. Lapine, M. V. Gorkunov, I. V. Shadrivov, and Y. S. Kivshar. Metamaterial tuning by manipulation of near-field interaction. *Phys. Rev. B*, 82(15):155128, 2010.
- [374] D. A. Powell, K. Hannam, I. V. Shadrivov, and Y. S. Kivshar. Near-field interaction of twisted split-ring resonators. *Phys. Rev. B*, 83(23):235420, 2011.
- [375] A. B. Yakovlev and G. Hanson. Mode-transformation and mode-continuation regimes on waveguiding structures. *IEEE Transactions on Microwave Theory and Techniques*, 48:67–75, 2000.
- [376] N. Liu, H. Liu, S. Zhu, and H. Giessen. Stereometamaterials. *Nature Photonics*, 3(3):157–162, 2009.
- [377] A. B. Movchan and S. Guenneau. Split-ring resonators and localized modes. *Phys. Rev. B*, 70(12):125116, 2004.

- [378] M.-A. Miri and A. Alù. Exceptional points in optics and photonics. *Science*, 363(6422):eaar7709, 2019.
- [379] V. Igoshin, M. Tsimokha, A. Nikitina, M. Petrov, I. Toftul, and K. Frizyuk. Exceptional points in single open acoustic resonator due to symmetry breaking. *Phys. Rev. B*, 109:144102, Apr 2024.
- [380] H. B. Huang, J. H. Wu, X. R. Huang, M. L. Yang, and W. P. Ding. The development of a deep neural network and its application to evaluating the interior sound quality of pure electric vehicles. *Mechanical Systems and Signal Processing*, 120:98–116, 2019.
- [381] H. B. Huang, J. H. Wu, X. R. Huang, W. P. Ding, and M. L. Yang. A novel interval analysis method to identify and reduce pure electric vehicle structure-borne noise. *Journal of Sound and Vibration*, 475:115258, 2020.
- [382] Y. Qin, X. Tang, T. Jia, Z. Duan, J. Zhang, Y. Li, and L. Zheng. Noise and vibration suppression in hybrid electric vehicles: State of the art and challenges. *Renewable and Sustainable Energy Reviews*, 124:109782, 2020.
- [383] S. Mohammadi and A. Ohadi. A novel approach to design quiet tires, based on multi-objective minimization of generated noise. *Applied Acoustics*, 175:107825, 2021.
- [384] X. Hu, X. Liu, X. Wan, Y. Shan, and J. Yi. Experimental analysis of sound field in the tire cavity arising from the acoustic cavity resonance. *Applied Acoustics*, 161:107172, 2020.
- [385] X. Hu, X. Liu, Y. Shan, and T. He. Simulation and experimental validation of sound field in a rotating tire cavity arising from acoustic cavity resonance. *Applied Sciences*, 11(3), 2021.
- [386] C. Wan, C.-J. Zheng, C.-X. Bi, and Y.-B. Zhang. An approach for assessing the effects of porous materials on controlling the tire cavity resonance noise. *Engineering Analysis with Boundary Elements*, 143:418–427, 2022.
- [387] J. Yi, X. Liu, Y. Shan, and H. Dong. Characteristics of sound pressure in the tire cavity arising from acoustic cavity resonance excited by road roughness. *Applied Acoustics*, 146:218–226, 2019.
- [388] Z. Mohamed and X. Wang. A study of tyre cavity resonance and noise reduction using inner trim. *Mechanical Systems and Signal Processing*, 50-51:498–509, 2015.
- [389] Z. Mohamed, X. Wang, and R. Jazar. Structural-acoustic coupling study of tyre-cavity resonance. *Journal of Vibration and Control*, 22(2):513–529, 2016.
- [390] T. Sakata, H. Morimura, and H. Ide. Effects of Tire Cavity Resonance on Vehicle Road Noise. *Tire Science and Technology*, 18(2):68–79, 04 1990.

## Bibliography

- [391] D. de Klerk and A. Ossipov. Operational transfer path analysis: Theory, guidelines and tire noise application. *Mechanical Systems and Signal Processing*, 24(7):1950–1962, 2010. Special Issue: ISMA 2010.
- [392] D. Wang, J. Guo, X. Xiao, and X. Sheng. Csa-based acoustic beamforming for the contribution analysis of air-borne tyre noise. *Mechanical Systems and Signal Processing*, 166:108409, 2022.
- [393] H. Huang, X. Huang, W. Ding, M. Yang, D. Fan, and J. Pang. Uncertainty optimization of pure electric vehicle interior tire/road noise comfort based on data-driven. *Mechanical Systems and Signal Processing*, 165:108300, 2022.
- [394] T. Lafont, R. Stelzer, R. D’Amico, W. Kropp, and C. Bertolini. Modelling tyre noise in finite element simulations for pass-by noise predictions. *Proceedings of the Institution of Mechanical Engineers, Part C: Journal of Mechanical Engineering Science*, 233(18):6398–6408, 2019.
- [395] Z. Liu, Y. Xu, Y. Lin, J. Xiang, T. Feng, Q. Cao, J. Li, S. Lan, and J. Liu. High- $q$  quasibound states in the continuum for nonlinear metasurfaces. *Phys. Rev. Lett.*, 123:253901, Dec 2019.
- [396] B. Duan, S. Liu, X. Liu, X. chong Yu, C. Wang, and D. Yang. High- $q$  quasi-bic in photonic crystal nanobeam for ultrahigh sensitivity refractive index sensing. *Results in Physics*, 47:106304, 2023.
- [397] X. Fan, Q. Jin, H. Xiao, Y. Kang, X. Huang, C. Li, N. Li, and C. Weng. Broadband acoustic metalaser for continuous sine waves and pulses. *Phys. Rev. Appl.*, 20:064026, Dec 2023.

# 5 Appended Publications

## 5.1 Publication AP1

## Spectral Stochastic Infinite Element Method in Vibroacoustics

Felix Kronowetter\*, Lennart Moheit, Martin Eser,  
Kian K. Sepahvand and Steffen Marburg

*Chair of Vibroacoustics of Vehicles and Machines  
Department of Mechanical Engineering  
Technical University of Munich  
Garching 85748, Germany  
\*felix.kronowetter@tum.de*

Received 11 December 2019

Accepted 4 May 2020

Published 4 September 2020

A novel method to solve exterior Helmholtz problems in the case of multipole excitation and random input data is developed. The infinite element method is applied to compute the sound pressure field in the exterior fluid domain. The consideration of random input data leads to a stochastic infinite element formulation. The generalized polynomial chaos expansion of the random data results in the spectral stochastic infinite element method. As a solution technique, the non-intrusive collocation method is chosen. The performance of the spectral stochastic infinite element method is demonstrated for a time-harmonic problem and an eigenfrequency study.

*Keywords:* Infinite element method; random input data; exterior Helmholtz problems.

### 1. Introduction

The Helmholtz equation describes wave propagation in linear time-harmonic acoustics. The sound pressure acts as the major field variable. Many problems of acoustics deal with radiation or scattering into an infinite domain. Such cases are denoted an unbounded problem or an exterior Helmholtz problem. To assure the correct decay of the sound pressure at infinity, the non-reflecting Sommerfeld radiation condition has to be fulfilled. Numerous computational solution techniques have been developed for exterior Helmholtz problems over the last decades. They may be categorized into surface and domain-based methods.

---

\*Corresponding author.

This is an Open Access article published by World Scientific Publishing Company. It is distributed under the terms of the Creative Commons Attribution 4.0 (CC BY) License which permits use, distribution and reproduction in any medium, provided the original work is properly cited.

Surface-based numerical schemes, e.g. the boundary element method (BEM),<sup>1–3</sup> solve the problem just by a surface representation in combination with analytical solutions of the Helmholtz equation, inherently incorporating the Sommerfeld radiation condition. Hence, only the surface of the radiator has to be discretized. This results in fewer degrees of freedom compared to a fully discretized domain. However, BEM system matrices are usually neither Hermitian nor positive definite.<sup>2</sup>

Among the domain-based methods, the finite element method (FEM) is very popular.<sup>4–6</sup> However, FEM requires special treatments to fulfill the Sommerfeld condition. Well-studied approaches are known as absorbing or non-reflecting boundary conditions, either locally formulated<sup>7</sup> or globally,<sup>8</sup> and the so-called perfectly matched layer (PML) approaches.<sup>9</sup>

Yet another approach is utilizing the so-called infinite elements. In the infinite finite element method (IFEM), the exterior domain is discretized by elements approximating the wave decay at infinity according to the Sommerfeld condition. Among the different methods, it has become popular to distinguish between either the conjugated or the unconjugated approaches in combination with either the Bettess–Burnett or the Astley–Leis elements.<sup>10,11</sup> Unconjugated formulations are usually applied to the Bettess–Burnett elements.<sup>12,13</sup> They utilize a standard Bubnov–Galerkin discretization scheme leading to a symmetric coefficient matrix and spatially oscillatory terms in the integral formulation. Conjugated formulations are usually applied to Astley–Leis elements.<sup>14</sup> They use a Petrov–Galerkin discretization scheme in which the test functions appear to be the conjugate complex basis functions of the radial approximation. This results in a cancellation of oscillatory terms and thus, in static system matrices but comes at the cost of unsymmetric coefficient matrices.

It is one advantage of conjugated Astley–Leis elements that a quadratic eigenvalue problem can be formulated, linearized and solved.<sup>16–18</sup> By utilizing the orthogonality of the modes, modal superposition techniques can be applied for the solution of the harmonic problem.<sup>19,20</sup> The accuracy and the possibility to determine frequency independent normal modes account for the main motivation of the authors to use infinite elements for this study. The IFE formulation is combined with a probabilistic uncertainty quantification (UQ) method.

Such probabilistic UQ methods are used to capture randomness in model parameters. They are based on the parameterization of random input data using a set of independent random variables. The set of random variables follows a probability law, that is not necessarily the same as that of the random input data itself. Sampling techniques, e.g. the Monte Carlo (MC) method, rely on solving the system of equations for any realization of the input data leading to unique solutions of the model. The accuracy of the estimated solution depends on the number of samples. The convergence rate of MC methods which is usually measured with respect to the standard deviation behaves as  $\sim M^{-\frac{1}{2}}$ , where  $M$  is the number of realizations.<sup>21</sup> In particular for complex finite element models, such a low convergence rate does hardly allow an efficient UQ if a couple of uncertain parameters or even random fields are taken into account. In contrast to MC methods, spectral decomposition methods are more complicated to implement but often much more efficient.

Spectral methods are chosen in this paper to represent the uncertainties. Possible spectral methods are the Karhunen–Loève expansion and Polynomial Chaos (PC) expansions. The Karhunen–Loève representation of a stochastic process can be understood as a bi-orthogonal decomposition based on the eigenfunctions obtained through the analysis of its correlation function.<sup>22</sup> Whereas the correlation function has to be known for the Karhunen–Loève expansion, PC expansions do not depend on the correlation function. PC expansions are Fourier-like expansions using orthogonal polynomials as basis. Stochastic quantities are thus parametrized and represented by a spectral expansion. Multiple approaches exist to solve the stochastic problem. Among them, there are intrusive methods, e.g. Galerkin methods, which are based on a weighted residual formalism. Hence, they modify the IFE system of equations and the code needs to be adapted. Non-intrusive methods are designed to solve the stochastic problem without the need of an adaptation of the infinite element formulation. Compared to the orthogonal projection, non-intrusive collocation methods are efficient with respect to the computational costs and they come with a good accuracy.<sup>23</sup> In this paper, a non-intrusive, spectral approach of stochastic quantities is applied and the infinite element system is extended to a spectral stochastic infinite element method. The procedure is similar to the derivation of stochastic finite elements (SFEs), first introduced by Ghanem and Spanos.<sup>24</sup> Extensive papers on the application of spectral methods to SFEs were published over the last three decades, see for example Ghanem and Kruger,<sup>25</sup> Ngha and Young,<sup>26</sup> Sepahvand *et al.*<sup>27</sup> In a non-intrusive approach, the infinite element system serves as a black-box model, while the UQ is modeled within a stochastic framework.

While the authors are aware of much literature on probabilistic UQ using stochastic finite elements in structural mechanics and fluid dynamics, applications to the wave equation and acoustics seems rather limited so far. Among the latter, two papers were published by the authors.<sup>28,29</sup>

A special remark is given to the actual works on uncertainties in metamaterials, since a test case in this paper deals with uncertain meta-atoms — the term meta-atom will be explained throughout the paper — used for an uncertain eigenfrequency study. A study on the influence of uncertainties due to manufacturing tolerances and material defects on the performance of metamaterials are found in Ref. 30. A particular version of the stochastic finite element method (SFEM) is applied for the stochastic treatment. The influence of uncertain material parameters on band-gaps, eigenfrequencies and transfer functions of a formation of meta-atoms is analyzed. Similar studies were conducted in Refs. 31 and 32, whereby ideal periodicity in the formation of the meta-atoms is assumed in the three papers previously mentioned papers on metamaterials. Pan *et al.*<sup>33</sup> discuss the effects of uncertainties in the geometry on the formation of band-gaps of piezoelectric-acoustic metamaterials. Another piece of work on the influence of uncertain stiffness and damping parameters on the properties of acoustic metamaterials was published by Sepahvand and Marburg.<sup>34</sup> They use the spectral stochastic finite element method (SSFEM) in combination with the non-intrusive collocation method as a solution technique for the stochastic problem. A non-intrusive approach similar to the one herein was recently published in the work of Henneberg *et al.*,<sup>35</sup> where the effect of uncertainties on dispersion curves was investigated.



In the remainder of this paper, the theory of infinite elements and spectral methods including the non-intrusive collocation method are combined and the spectral stochastic infinite element method (SSIFEM) is established. Further on, the method is validated by numerical examples for time-harmonic problems and applied to test cases.

## 2. Mathematical Models

### 2.1. Infinite element method

Time-harmonic problems describe the state of a system when the initial conditions have decayed. In linear acoustics, steady state problems with a time-harmonic excitation are covered by the Helmholtz equation (1).

$$\Delta p(\mathbf{x}) + k^2 p(\mathbf{x}) = 0, \quad \mathbf{x} \in \Omega_F \subset \mathbb{R}^d, \quad d = 2. \quad (1)$$

The steady solution is formulated as  $\tilde{p}(\mathbf{x}, t) = \Re\{p(\mathbf{x})e^{-i\omega t}\}$ , with  $\tilde{p}(\mathbf{x}, t)$  being the sound pressure and  $p$  the time-harmonic sound pressure. The wavenumber is denoted by  $k = \frac{\omega}{c_f}$ , the speed of sound  $c_f$  and the circular frequency  $\omega = 2\pi f$ . In this paper, just two-dimensional problems are considered. Exterior or unbounded Helmholtz problems are defined by a fluid domain of infinite extension. The unbounded fluid domain  $\Omega_F$  is divided by the interface  $\Gamma_c$  into a finite element domain  $\Omega_f$  and an exterior domain  $\Omega_e$ . The finite element domain is of circular shape and the exterior domain is represented by elements of infinite extension. Similar to the finite element method, the infinite element method is used to solve the Helmholtz equation and leads to frequency independent system matrices. The concept of infinite elements is based on a special radial interpolation scheme. The value of unity of the radial coordinate in the isoparametric space represents infinity in the real space. All formulations in this chapter are given for two-dimensional infinite elements, but can easily be extended to the third dimension and be looked up in Refs. 11, 14 and 15. The discretization of the infinite domain is based on a Petrov–Galerkin scheme. Basis functions  $\psi_t(\mathbf{x}, \omega)$  are chosen such that the Sommerfeld radiation condition<sup>36</sup> is implicitly fulfilled. The asymptotic decay of the sound pressure to zero with an increasing distance from a source is assured by  $\psi_t(\mathbf{x}, \omega) \sim \frac{1}{\sqrt{r}}$ .

The hypermatrix system for a coupled FE-IFE problem reads as

$$\left\{ \begin{bmatrix} \mathbf{K}_f & \mathbf{K}_{fe} \\ \mathbf{K}_{ef} & \mathbf{K}_e \end{bmatrix} - i\omega \begin{bmatrix} \mathbf{D}_f & \mathbf{D}_{fe} \\ \mathbf{D}_{ef} & \mathbf{D}_e \end{bmatrix} - \omega^2 \begin{bmatrix} \mathbf{M}_f & \mathbf{M}_{fe} \\ \mathbf{M}_{ef} & \mathbf{M}_e \end{bmatrix} \right\} \begin{pmatrix} \mathbf{p} \\ \mathbf{p}_e \end{pmatrix} = \mathbf{f}. \quad (2)$$

The index  $e$  symbolizes quantities of the infinite element domain. The matrices  $\mathbf{K}_f, \mathbf{C}_f, \mathbf{M}_f$  are finite element matrices of the fluid domain with contributions of the exterior domain due to the coupling nodes. Degrees of freedom of the coupling nodes are shared by the finite element matrices and the infinite element matrices. The corresponding coupling matrices are denoted by  $\mathbf{K}_{fe}, \mathbf{C}_{fe}, \mathbf{M}_{fe}$  and switched indices vice versa. The sound pressure of the infinite domain is described as  $\mathbf{p}_e$ .

Additionally to full-space exterior Helmholtz problems, we deal with half-space problems. Half-space exterior Helmholtz problems are more common in boundary element formulations.<sup>37–39</sup> An advantageous property of the half-space representation is the reduction of degrees of freedom, hence less computational power is needed. Coyette and Van den Nieuwenhof<sup>40</sup> study the behavior of conjugated infinite elements for half-space domains bounded by an admittance plane. Results of their studies are the influence of the span of the admittance boundary condition — the span of the admittance plane — and the size of the finite element domain surrounding the acoustic source. Interpreting the results leads to the following conclusions. First, a specific admittance has to be constrained not only along the finite element boundary but also on the infinite element boundary. Second, the extension of the inner finite element domain and the resolution of the mesh have a significant influence on the quality of the solution. The same holds for the radial order of the infinite elements. Third, an impedance plane with a zero admittance boundary condition shows an excellent agreement of the simulated solution with the exact solution.

## 2.2. Uncertainty quantification

Spectral random expansions are an optimal representation of random variables, fields or processes in the sense of  $L_2$ -norm, where the functional dependence of the solution on the set of random variables  $\boldsymbol{\xi} = \{\xi_1, \dots, \xi_N\}$  is constructed. The random variable  $\xi_i(\theta)$  denotes a vectorial quantity in the size of the number of elements  $\theta$  in the sample space. The PC expansion<sup>41</sup> is a functional representation of uncertain parameters to span the orthogonal basis having finite variance. A more generalized form of the PC expansion, the so-called as the Wiener–Askey PC or generalized Polynomial Chaos (gPC), was introduced to cover all types of data distributions. Here, the vector of random variables ( $\boldsymbol{\xi}$ ) can be arbitrary and the variables do not need to be Gaussian. Instead of being restricted to Hermite polynomials, the gPC allows different kinds of orthogonal polynomials from the Askey-scheme, cf. Ref. 42 for more details. For computational applications, the number of random variables  $\boldsymbol{\xi} = \{\xi_1, \dots, \xi_N\}$  has to be finite as well as the spectral expansion itself. Hence, the infinite series for the representation of a random variable  $X$  is truncated as

$$X(\cdot, \boldsymbol{\xi}) = \sum_{i=0}^P x_i(\cdot) \Phi_i(\boldsymbol{\xi}) + \epsilon(N, p), \quad P = \frac{(N+p)!}{N!p!} - 1. \quad (3)$$

The number of deterministic coefficients  $x_i$  of the truncated expansion depends on the number of random variables  $N$  and the highest order  $p$  of the polynomials  $\{\Phi\}$ . The error  $\epsilon(N, p)$  vanishes for  $\lim_{p \rightarrow \infty} \langle \epsilon^2(N, p) \rangle$ . Accordingly, the gPC functionals of the output depend on all random input variables and are sorted in the order of the functionals.

For the identification of the deterministic coefficients in the gPC, two types of methods are common, i.e. intrusive and non-intrusive methods. Intrusive methods, mostly Galerkin methods, are based on a weighted residual formalism leading to systems of governing equations for the spectral coefficients of the solution. The deterministic solver has to be adapted,

hence they are called intrusive. On the other side, non-intrusive methods work without any modification of the original deterministic code. They rely on a certain set of realizations of the random input to construct the random output. Thus, the code can be treated as black-box. Non-intrusive methods are for example the non-intrusive Spectral Projection (NISP), that is based on a projection of the random output onto a stochastic finite-dimensional Lebesgue subspace. Computational solution techniques employ sampling-based methods where deterministic integration approaches using quadrature schemes, sparse grid methods and least squares minimization are used. In this paper, the collocation method based on an interpolation scheme is applied. In contrast to the NISP method, the approximation space is not pre-defined by a certain subspace, but its size depends on the number of collocation points ( $\mathbf{cp}$ ) used. The system of equations is solved at the selected collocation points leading to partial solutions  $X^*$  of the problem, i.e.

$$\begin{bmatrix} \Phi_0(\mathbf{cp}^0) & \Phi_1(\mathbf{cp}^0) & \cdots & \Phi_P(\mathbf{cp}^0) \\ \Phi_0(\mathbf{cp}^1) & \Phi_1(\mathbf{cp}^1) & \cdots & \Phi_P(\mathbf{cp}^1) \\ \vdots & \vdots & \ddots & \vdots \\ \Phi_0(\mathbf{cp}^P) & \Phi_1(\mathbf{cp}^P) & \cdots & \Phi_P(\mathbf{cp}^P) \end{bmatrix} \begin{Bmatrix} x_0(\cdot) \\ x_1(\cdot) \\ \vdots \\ x_P(\cdot) \end{Bmatrix} = \begin{Bmatrix} X^*(\cdot, \mathbf{cp}^0) \\ X^*(\cdot, \mathbf{cp}^1) \\ \vdots \\ X^*(\cdot, \mathbf{cp}^P) \end{Bmatrix}. \quad (4)$$

As shown, the size of  $\mathbf{cp}$  equals at least the number of spectral modes  $N_{\mathbf{cp}} = 0, 1, \dots, P$ . This restriction is chosen such that the coefficient matrix is at least square.<sup>43</sup> In general, collocation methods show an oscillatory convergence behavior for randomly chosen collocation points.<sup>23</sup> It has been proven that the right choice of collocation points can achieve approximately the same accuracy as Galerkin methods. This is obtained, when the collocation points are chosen as the roots of a polynomial of one order higher  $p + 1$  than the order of the polynomial expansion  $p$ .<sup>44–47</sup> This procedure is similar to the Gaussian quadrature for the numerical evaluation of integrals. The requirement is imposed such that the residual at the collocation points is equal to zero. Thereby, the residual in the random dimension is minimized. Since there are many possible combination of the roots in case of multiple random variables  $\boldsymbol{\xi}$ , the number of collocation points is higher than required and leads to an over-determined system of equations (4). This means an extension of the number of collocation points from  $\mathbf{cp}^P$  to  $\mathbf{cp}^{P^*}$ , with  $P < P^*$ , whereas the number of spectral modes remains constant. Therefore, a selection of optimal points is needed. Optimal points are selected points that capture regions of high probability.<sup>48</sup> Hosder *et al.*<sup>23</sup> studied the influence of the number of collocation points and the polynomial order on the accuracy of the solution and on the computational power. According to that, it can be computationally more efficient to double the number of collocation points, i.e.  $\tilde{N}_{\mathbf{cp}} = 2N_{\mathbf{cp}}$ , than to increase the polynomial order. The accuracy of the solution is hereby sustained. A further increase of collocation points does not give a significant improvement in accuracy though. The over-determined system is then solved by the least squares method. By solving Eq. (4), the spectral modes are obtained. They are the deterministic coefficients for the gPC of the random output.

### 2.3. Spectral stochastic infinite element method

FEM as well as infinite element methods are designed to solve deterministic problems. Adding random variables to the finite element method is an extension of the deterministic finite element approach to the stochastic framework. This leads to the stochastic finite element method. Considering exterior Helmholtz problems combined with the infinite element formulation and adding a dependency on random variables results in the stochastic infinite element method (SIFEM). This is shown for the hypermatrix system equation (2), in the compact form of

$$\{\mathbf{K} - i\omega\mathbf{C} - \omega^2\mathbf{M}\}\mathbf{p} = \mathbf{f}, \quad (5)$$

in which  $\mathbf{K}$ ,  $\mathbf{C}$ ,  $\mathbf{M}$  denote the hypermatrices for stiffness, damping and mass,  $\mathbf{p}$  the solution vector and  $\mathbf{f}$  is the loading term. The stochastic infinite element formulation of the system is then represented as

$$\{\mathbf{K}(\cdot, \boldsymbol{\xi}) - i\omega\mathbf{C}(\cdot, \boldsymbol{\xi}) - \omega^2\mathbf{M}(\cdot, \boldsymbol{\xi})\}\mathbf{p}(\cdot, \boldsymbol{\xi}) = \mathbf{f}(\cdot, \boldsymbol{\xi}). \quad (6)$$

System matrices and vectors in this form depend on the vector of random variables. Multiple methods and approaches are known to solve the system of equations. For further information see Stefanou.<sup>21</sup> Pseudo random methods like the MC simulation are the most accurate methods, but the whole system of equations has to be solved for each realization which may end up in high computational costs. Applying spectral approaches to the stochastic infinite element system results in the spectral stochastic infinite element method, in analogy to the spectral stochastic finite element method introduced in the publication by Ghanem and Spanos.<sup>24</sup> Random quantities are thus represented by the gPC expansions, e.g. for the stiffness hypermatrix, one can write

$$\mathbf{K}(\cdot, \boldsymbol{\xi}) \approx \sum_{i=0}^P \mathbf{k}_i(\cdot)\Phi_i(\boldsymbol{\xi}) = \overline{\mathbf{K}}^T(\cdot)\boldsymbol{\Phi}(\boldsymbol{\xi}), \quad (7)$$

with  $\mathbf{k}_i$  being deterministic matrix coefficients. The same procedure is applied for all random matrices and responses. Substituting the gPC expansions into Eq. (6) leads to the spectral stochastic infinite element formulation of the system as

$$\{\overline{\mathbf{K}}^T(\cdot)\boldsymbol{\Phi}(\boldsymbol{\xi}) - i\omega\overline{\mathbf{C}}^T(\cdot)\boldsymbol{\Phi}(\boldsymbol{\xi}) - \omega^2\overline{\mathbf{M}}^T(\cdot)\boldsymbol{\Phi}(\boldsymbol{\xi})\}\overline{\mathbf{p}}^T(\cdot)\boldsymbol{\Phi}(\boldsymbol{\xi}) = \overline{\mathbf{f}}^T(\cdot)\boldsymbol{\Phi}(\boldsymbol{\xi}). \quad (8)$$

For the sake of simplification, it is assumed that all gPC expansions have the same orthogonal basis type  $\boldsymbol{\Phi}(\boldsymbol{\xi})$ . The solution of the spectral stochastic infinite element system of equations in Eq. (8) gives an estimation of the unknown deterministic coefficient vector  $\overline{\mathbf{p}}^T(\cdot)$ . The entries of this vector are denoted spectral modes of the sound pressure. The realizations at the collocation points can be treated as deterministic input data to the system of equations to generate partial solutions

$$\mathbf{p}_i^*(\cdot, \mathbf{cp}_i) = \frac{\overline{\mathbf{f}}^T(\cdot)\boldsymbol{\Phi}(\mathbf{cp}_i)}{\overline{\mathbf{K}}^T(\cdot)\boldsymbol{\Phi}(\mathbf{cp}_i) - i\omega\overline{\mathbf{C}}^T(\cdot)\boldsymbol{\Phi}(\mathbf{cp}_i) - \omega^2\overline{\mathbf{M}}^T(\cdot)\boldsymbol{\Phi}(\mathbf{cp}_i)}. \quad (9)$$

For the calculation of the partial solution, the infinite element hypermatrix system of equations in Eq. (2) is not modified but just evaluated for variable input data. All system matrices and vectors are deterministic. The spectral modes can subsequently be calculated using the partial solutions and the coefficient matrix, similar to Eq. (4)

$$\bar{\mathbf{p}}(\cdot) = \mathbf{\Phi}^{-1}(\mathbf{cp}_i)\mathbf{p}_i^*(\cdot, \mathbf{cp}_i). \quad (10)$$

Thus, the final solution is given as

$$\mathbf{p}(\cdot, \boldsymbol{\xi}) = \bar{\mathbf{p}}^T(\cdot)\mathbf{\Phi}(\boldsymbol{\xi}). \quad (11)$$

Clearly, the solution can be evaluated at specific spatial points, e.g.  $\mathbf{x}_e$ , i.e.

$$\mathbf{p}_i^*(\mathbf{x}_e, \mathbf{cp}_i) = \frac{\bar{\mathbf{f}}^T(\mathbf{x}_e)\mathbf{\Phi}(\mathbf{cp}_i)}{\bar{\mathbf{K}}^T(\mathbf{x}_e)\mathbf{\Phi}(\mathbf{cp}_i) - i\omega\bar{\mathbf{C}}^T(\mathbf{x}_e)\mathbf{\Phi}(\mathbf{cp}_i) - \omega^2\bar{\mathbf{M}}^T(\mathbf{x}_e)\mathbf{\Phi}(\mathbf{cp}_i)}, \quad (12)$$

with the spectral modes given by

$$\bar{\mathbf{p}}_e(\mathbf{x}_e) = \mathbf{\Phi}^{-1}(\mathbf{cp}_i)\mathbf{p}_{ie}^*(\mathbf{x}_e, \mathbf{cp}_i). \quad (13)$$

This contribution subsequently follows other recent publications on exterior acoustic problems with uncertainties. Chen *et al.*<sup>49</sup> proposed a new method for exterior acoustic problems with epistemic uncertainties using the BEM. A further publication by Chen *et al.*<sup>50</sup> discussed a hybrid perturbation approach with both random and interval variables for exterior acoustic problems. Wang *et al.*<sup>51</sup> suggested two new interval analysis methods for unbounded problems. In contrast, the SSIFEM uses infinite elements for the exterior domain and covers aleatoric uncertainties. Hence, the method offers a broad application area and efficient computation of the uncertain model. Moheit *et al.*<sup>52</sup> used infinite elements for the analysis of finite periodic sonic crystals. The authors computed the normal modes as well as the insertion losses of different geometries. Furthermore, Melnikov *et al.*<sup>53</sup> applied finite periodic meta-atoms for the noise reduction of machines. Since the noise excited by the machine is based on process parameters and underlies certain fluctuations, uncertainties should be considered for a more accurate analysis. Consecutive studies on both topics could imply the identification of random input parameters and the application of the SSIFEM.

### 3. Results

#### 3.1. Validation

An infinite element formulation is self-implemented and validated against an analytical solution to a radiation problem in order to assure convergence and stability of the simulations. A pulsating two-dimensional sphere represents the acoustic source. The analytical solution is given by Eq. (14) and provided by Möser<sup>54</sup>

$$p(r, \phi) = -i\rho_0c \sum_{n=0}^N V_n \frac{H_n^{(2)}(k_0r)}{H_n^{(2)'}(k_0b)} \cos(n\phi). \quad (14)$$

A radial velocity or structural particle velocity is preset at the surface of a cylindrical body. It is assumed that the emitted waves are not effected by any kind of reflection. Hence, the propagation of the waves is not disturbed and the Hankel function of the second kind can be applied, i.e. The code is validated for full-space and half-space problems with multipole excitations. A mesh study is also conducted to evaluate the quality and performance of the mathematical grid. Results of the validation and mesh study are not shown in this paper, but the most efficient combination of the parameters are used subsequently.

### 3.2. Convertible

The SSIFEM is applied to a two-dimensional convertible with an open roof in the first test case. The car can be considered as a complex system, consisting of mass-spring-damper subsystems, with corresponding eigenfrequencies. Vibrations are generated for example by the engine or can be introduced in the system by the unevenness of the road and thus non-constant values. The frequency range of the vibrations is chosen such that it matches the eigenfrequencies of the interior of the car and of the front window. The influence of the vibrating front window on the sound pressure at the ear of the driver is simulated for frequencies from  $f = 20$  [Hz] to  $f = 500$  [Hz] in steps of 1 [Hz]. This frequency range is chosen referring to Pfeffer and Harrer.<sup>55</sup> Therefore, the structural particle velocity at the window-fluid interface is considered to be random. Rather arbitrarily, a log-normal distribution is chosen. Hence, the random structural particle velocity depends on the standard normal distributed random variable  $\xi_1$  resulting in  $v_s(\xi_1)$ . To cover the effects of the reflections in the interior on the acoustic sound pressure field, a frequency dependent admittance boundary condition is defined at the interior. The values of the admittance boundary conditions of the interior and of the seat cushion are calculated from measured absorption coefficients  $\alpha = 1 - |r|^2$ . The complex reflection coefficient  $r$  is defined as<sup>56</sup>

$$r = \frac{Z_s - Z_f}{Z_s + Z_f}, \quad (15)$$

with  $Z_s$  being the impedance of the solid and  $Z_f = \rho_f c_f$  being the impedance of the fluid. Reformulating Eq. (15) leads to the dimensionless admittance of the solid

$$|\tilde{Y}_s| = \frac{1 - r}{1 + r} = \frac{1 - \sqrt{(1 - \alpha)}}{1 + \sqrt{(1 + \alpha)}}. \quad (16)$$

This formulation lacks information about the phase angle.<sup>57</sup> Additionally, the admittance of the seat cushion is assumed to be random and approximated by a normal distribution. The random admittance of the seat cushion depends on the standard normally distributed random variable  $\xi_2$  resulting in  $Y(\xi_2)$ , with  $Y = \frac{1}{Z_f} |\tilde{Y}_s|$ . Absorption coefficients are frequency dependent, so are the corresponding admittances. An interpolation scheme is implemented. It approximates the absorption coefficients throughout the whole frequency range based on the measured data. A preceding sensitivity analysis by the authors has shown, that the structural particle velocity as well as the seat cushion are the dominant

parameters. Modest changes in the air density or in the speed of sound lead to slight changes of the output of the system compared to the dominant parameters. The complexity of the model and the computational power needed increase considerably with additional random input parameters. Hence, we focus on the dominant parameters and assume all others to be deterministic. A realistic representation of the sound pressure field of an open convertible is assured using the infinite element method.

For simplification, the road underneath the car is represented by a fully reflecting boundary. Thus, it can be considered as a half-space problem. The geometry of the convertible car is simplified to keep the computational costs low. The mesh is chosen considering the results of the previous mesh study. A quadratic, triangular mesh is used in the finite element domain. The finite element domain is defined by a semicircle enclosing the convertible. To minimize the computational costs, the radius of the semicircle of the finite element domain is kept small. For a convertible of an approximate total length of 5 meters, the radius is set to  $r = 3$  [m]. The mesh size in the FE-domain is defined by  $N_e = 10$  elements per wavelength. For the infinite element domain, Lagrange polynomials are selected for the radial discretization with a radial order of  $m = 6$ .

In the case of the convertible, 2000 identical realizations of the random variables  $\xi_1$  and  $\xi_2$  for the input of the MC simulations and for the spectral expansion of the output are used. The random input data and the corresponding distributions are shown in Fig. 1. The probability density functions (PDFs) are displayed for a better understanding and the actual data are shown by the red points. The choice of identical realizations enables the comparison of the results of both simulation techniques and the evaluation of the error at the exact same points. The system responses are evaluated at an assumed position of the driver's ear and shown for  $f = 500$  [Hz].

The results from the MC simulations with 2000 samples and the gPC expansion are shown in Fig. 2. The highest accuracy is achieved in the region of the highest probability for both, the gPC expansion using polynomials of order 3 and 9. Whereas the gPC of order

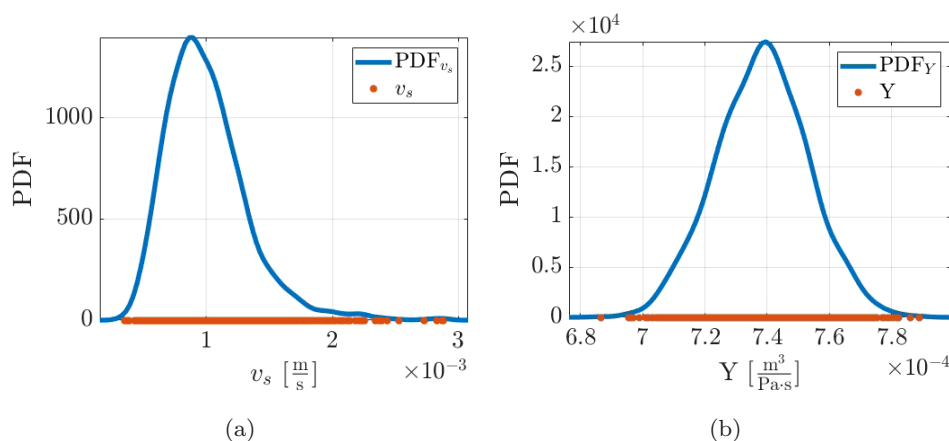


Fig. 1. Distributions of the random input data of the convertible. (a) Random structural particle velocity and (b) random boundary admittance.

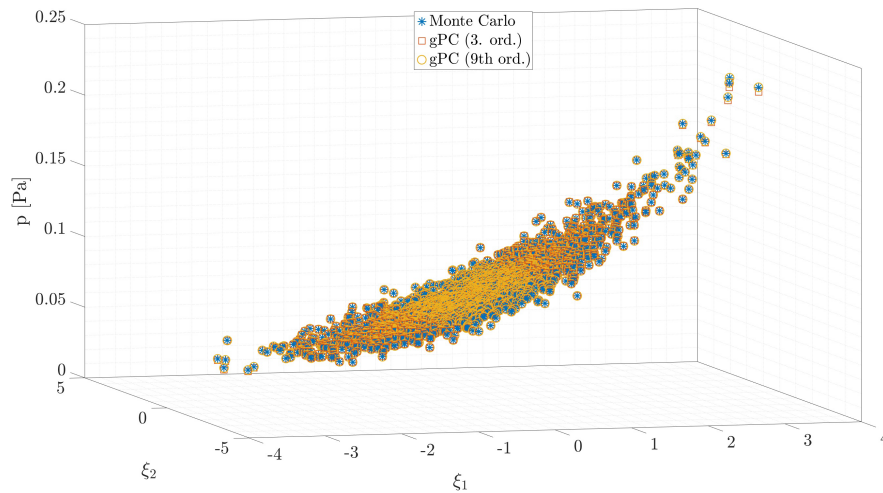


Fig. 2. System response for MC and gPC (3rd and 9th-order) at  $f = 500$  [Hz].

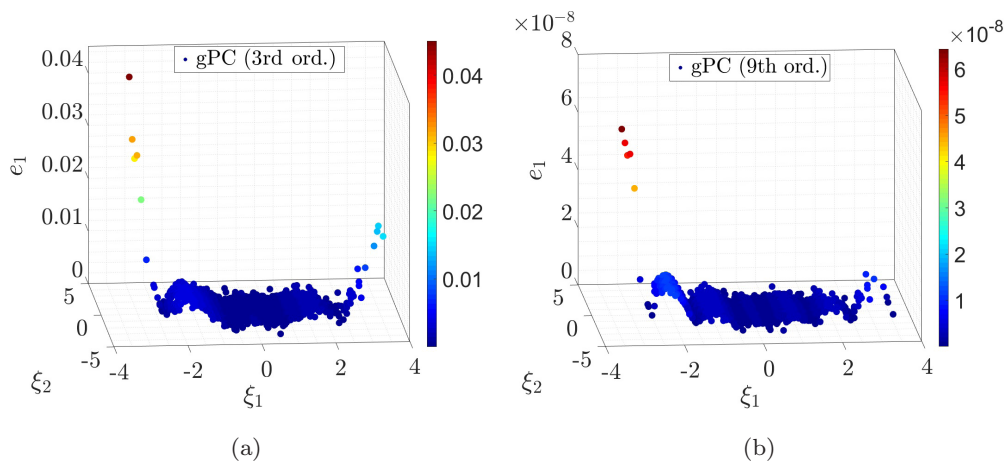


Fig. 3. Pointwise relative error evaluated at  $f = 500$  [Hz]. (a) Pointwise relative error of the 3rd-order gPC and (b) pointwise relative error of the 9th-order gPC.

3 produces higher deviations from the MC reference solutions with an increasing sample space, the gPC of order 9 is stable. A corresponding pointwise relative error is defined by  $e_1 = \|\varepsilon\|_{L_2} = \frac{|P_{MC} - P_{gPC}|}{|P_{MC}|}$  and shown in Fig. 3 for  $f = 500$  [Hz], to explain the behavior of the expansions. By using 20 collocation points, the gPC of order 3 produces a maximum error of  $e_1 = 0.0450$ . The gPC of order 9 leads to a maximum error of  $e_1 = 6.4 \cdot 10^{-8}$ . Since the higher-order expansion needs 110 collocation points, the computational time more than quintupled. Depending on the requirements of the simulation, the polynomial order has to be chosen with care, in particular with respect to the dimension of the sample space. The further results of the convertible are all produced by applying the gPC of order 9 with 100 000 realizations for the random variables. One important feature of the gPC consists in its mean value accuracy. This is presented in Fig. 4(a). The mean values  $\mu$  of the system responses using the gPC and MC methods are identical. The gPC expansion converges in the



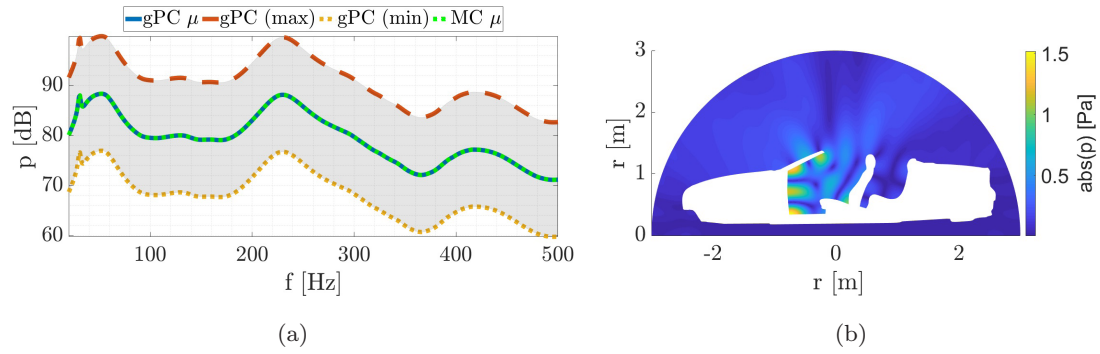


Fig. 4. System response — sound pressure field — for  $f = 20$  [Hz] to  $f = 500$  [Hz] evaluated at the ear of the driver and the sound pressure field for  $f = 500$  [Hz]. (a) System response for MC and gPC (3rd and 9th-order) and (b) sound pressure field of the convertible.

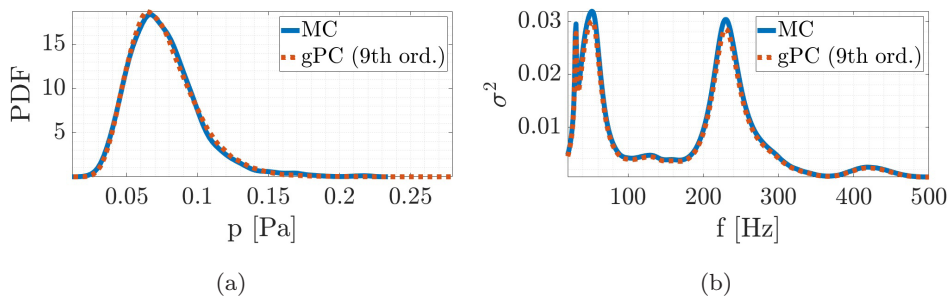


Fig. 5. PDF and variance of the sound pressure evaluated at the ear of the driver at  $f = 500$  [Hz]. (a) Probability density function of the 9th-order gPC and of the MC method and (b) variance of the 9th-order gPC and of the MC method.

mean-square sense with respect to its truncation. Hence, the mean value represents a deterministic value for the system response function. Furthermore, the first spectral mode exactly fits the deterministic solution. The gray area represents all possible outcomes, bounded by the maximum and minimum values of the system response. The deterministic sound pressure field of the convertible for  $f = 500$  [Hz] is shown in Fig. 4(b). The PDF of the system response for  $f = 500$  [Hz] is displayed in Fig. 5(a). The PDF shows good accordance to the reference solution, so does the variance, with some deviations at certain frequencies though. An explanation lies in the mathematical formulation of the spectral expansions. They are mean value accurate but lose accuracy for higher-order stochastic moments. It should be mentioned, that both the PDF and variance reference solutions are based on 2000 realizations. The reference solutions converge for a larger number of realizations. Since this becomes quite time consuming and the mean value accuracy is yet proven, it is not presented in this paper.

### 3.3. Meta-atom

The second test case deals with an uncertain modal analysis of an acoustic meta-atom. Let us denote an acoustic meta-atom as the body inside a unit cell of a periodic structure.

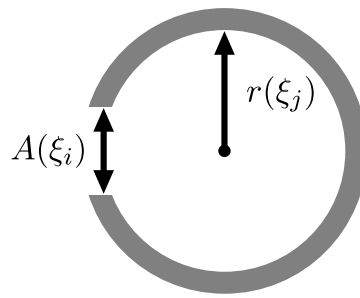


Fig. 6. C-shaped sonic crystal with random radius  $r(\xi_j)$  and size of the aperture  $A(\xi_i)$ .

Since the eigenfrequencies of the unit cell are of importance for the behavior of the acoustic metamaterial, they have to be identified accurately. Several solution techniques exist and are common in current literature. However, they include several assumptions, restrictions and problems, e.g. infinite periodicity and symmetry restrictions depending on the space group. In contrast, the meta-atom is analyzed completely decoupled from its surroundings in this paper. The geometry of the meta-atom is extracted from Melnikov *et al.*<sup>58</sup> and Elford *et al.*<sup>59</sup> and shown in Fig. 6.

This kind of meta-atom, also called *c*-shaped meta-atom, does not fulfill the strict symmetry requirements in the unit cell as, for example, sonic crystals do. As a consequence, the irreducible Brillouin zone and the corresponding reduced wave vectors combined with Floquet–Bloch boundary conditions, which are applied for the computation of dispersion curves, change. Thus, the eigenfrequency study is of more complex nature. Therefore, the SSIFEM is chosen here. The specific properties of the meta-atom are highly sensitive to a slight change in geometry or material parameters. Hence, the deviations from the ideal computer model due to manufacturing tolerances or material inhomogeneities are of interest. This is why UQ is applied. Here, we assume the radius of the cavity and the size of the aperture to be random quantities. For simplification, both random input variables are supposed to be normally distributed. Since normally distributed data do not have a lower or upper limit by definition, we define artificial limitation criteria. Hence, the random input data follow a pseudo normal distribution. The random input data is shown in Fig. 7. The eigenvalue problem

$$\tilde{Q}^T(\lambda, \cdot)\Phi(\xi) = \lambda^2 \tilde{M}^T(\cdot)\Phi(\xi) + \lambda \tilde{C}^T(\cdot)\Phi(\xi) + \tilde{K}^T(\cdot)\Phi(\xi), \quad (17)$$

has to be solved, in order to obtain the eigenfrequencies. The relevant eigenfrequencies can be identified by looking at its mode shapes. The frequencies of interest are those, for which the acoustic energy is focused in the cavity. For simplification and to meet the requirements of the definition of the quality factor, the eigenfrequencies are transferred from the imaginary part to the real part. Similarly, the damping constants are treated in a reciprocal way. The imaginary part of the corresponding eigenfrequencies is extremely small, leading to a high dissipative quality factor  $q = \frac{\Re\{f_{\text{eig}}\}}{2\Im\{f_{\text{eig}}\}}$ .<sup>60</sup> The corresponding modes are also known as cavity modes.

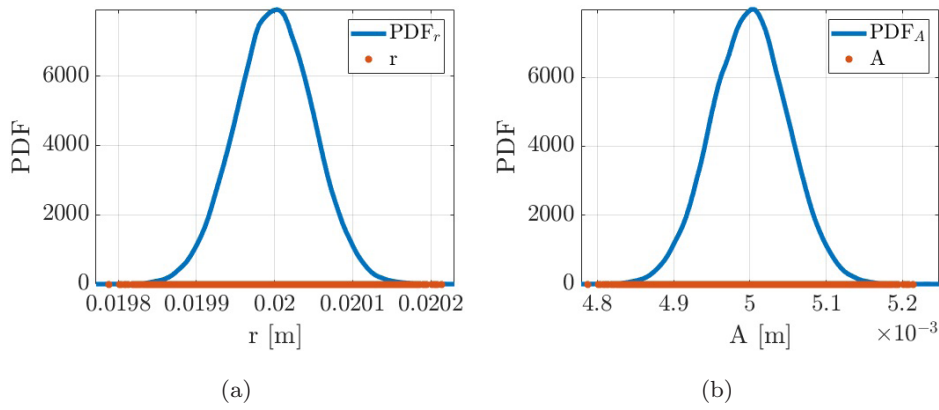


Fig. 7. Random input data of the meta-atom test case. (a) Random radius of the  $c$ -shaped sonic crystal and (b) random size of the aperture of the  $c$ -shaped sonic crystal.

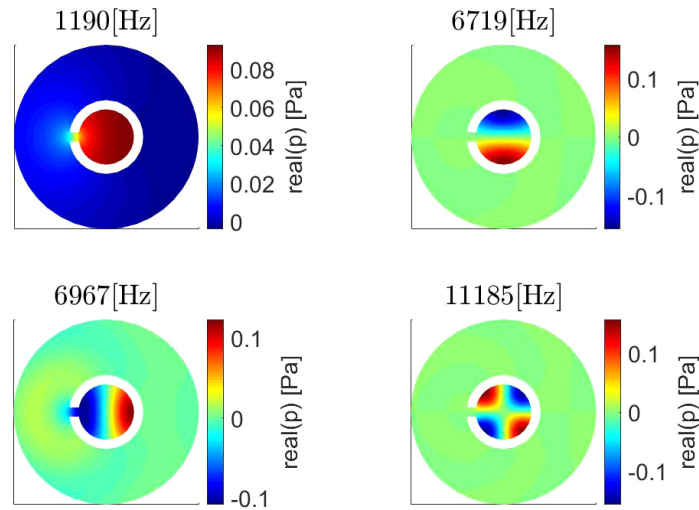


Fig. 8. The first four cavity modes of the  $c$ -shaped sonic crystal.

The first four cavity modes are displayed in Fig. 8. The random eigenfrequencies for the first and fourth cavity modes are presented in Fig. 9. For the first cavity mode, the maximum eigenfrequency is  $f_{\max}^{(1)} = 1.2109 \cdot 10^3$  [Hz] and the minimum eigenfrequency  $f_{\min}^{(1)} = 1.1659 \cdot 10^3$  [Hz]. This leads to a variation in the region of  $\Delta f^{(1)} \approx 50$  [Hz]. The maximum frequency of the fourth cavity mode is  $f_{\max}^{(4)} = 1.1341 \cdot 10^4$  [Hz] and the minimum frequency  $f_{\min}^{(4)} = 1.1027 \cdot 10^4$  [Hz], with a  $\Delta f^{(4)} \approx 314$  [Hz]. Considering the high sensitivity of the design, small variations of the input radius and the size of the aperture lead to significant changes in the effective area of the meta-atom.

Additionally, the band-gaps of an infinite periodic  $c$ -shaped configuration are presented in Fig. 10 to show the effects of uncertainties on band-gaps. The lattice constant is chosen as 0.015 [m] and the standard deviation of the random radius and aperture are selected according to the common tolerances of 3D printing techniques of approximately  $\pm 0.2$  [mm]. The minimal, mean and maximum values of the stochastic analysis are represented by blue, black

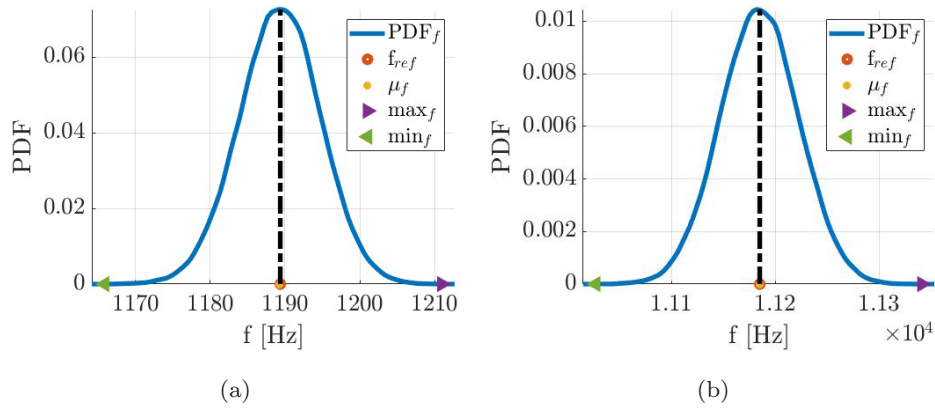


Fig. 9. Random output data of the meta-atom test case. (a) Random eigenfrequency belonging to the first cavity mode and (b) random eigenfrequency belonging to the fourth cavity mode.

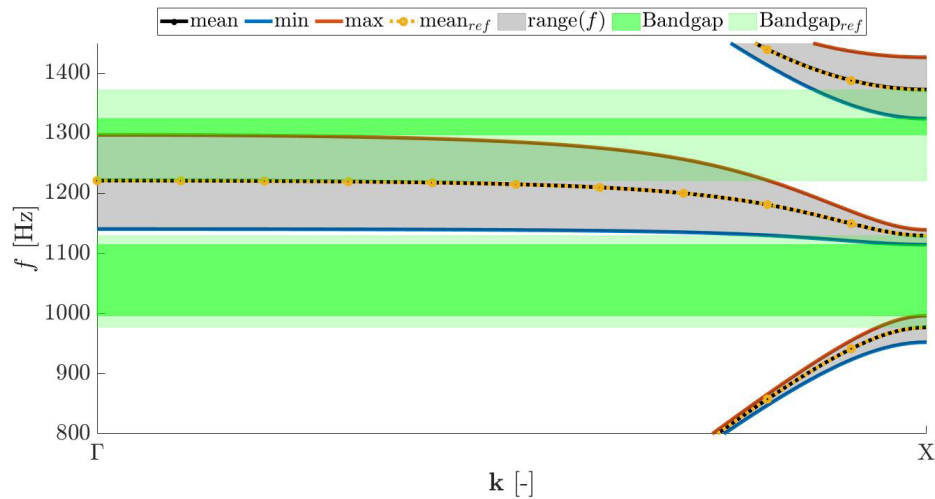


Fig. 10. Uncertain dispersion curves shown for the  $\Gamma \rightarrow X$  direction of the reduced wave vector with highlighted first and second band-gap. The reference band-gaps are the solutions of a deterministic configuration.

and red lines. Furthermore, the area representing the possible outcome of eigenfrequencies is colored in gray. The deterministic configuration of  $c$ -shaped meta-atoms with physical parameters based on the mean values of the random data is plotted as a reference solution. The random parameters show significant influence on the first band-gap. The influence on the second band-gap is even stronger since it is tremendously narrowed. Thus, uncertain input parameters should be considered when simulating periodic structures, since in certain parameter configurations band-gaps can vanish. It has to be mentioned, that the contour of the irreducible Brillouin zone might not lead to a global maximum in the eigenvalues of the system. Hence, the dispersion curves shall not be discussed in more detail. In future application, a combination of infinite elements and Floquet–Bloch boundary conditions with random input parameters features a more realistic method for the analysis of finite periodic structures with negligible boundary effects.

#### 4. Conclusion and Outlook

The spectral stochastic infinite element method turns out to be a profound approach for unbounded Helmholtz problems with uncertain input data. It is shown, that the influence of the polynomial order as well as the size of the sample space have a significant influence on the performance of the method using the test case of an open convertible. A future application of the SSIFEM is the modeling of metamaterials, which might be used in periodically structured sound barriers. Since metamaterials are predominantly produced via 3D printing, the imprecision of the manufacturing process leads to a high deviation of the real model from the computer model. Fortunately, the SSIFEM method covers all physical effects without any simplifications. In particular, it models accurately the manufacturing tolerances and other sources of uncertainties. Both, half-space and full-space formulations are accessible and can be combined with Floquet–Bloch conditions, if boundary effects of the structure can be neglected. In the scope of this contribution, the importance of the incorporation of uncertainties in this case is emphasized. In summary, the SSIFEM has a high potential in the calculation and prediction of the behavior of metamaterials.

#### References

1. T. W. Wu (ed.), *Boundary Element in Acoustics: Fundamentals and Computer Codes* (WIT Press, Southampton, 2000).
2. S. Marburg and B. Nolte (eds.), *Computational Acoustics of Noise Propagation in Fluids - Finite and Boundary Element Methods* (Springer-Verlag, Berlin, Heidelberg, Germany, 2008), <https://doi.org/10.1007/978-3-540-77448-8>.
3. S. Kirkup, The boundary element method in acoustics: A survey, *Appl. Sci.* **9**(8) (2019) 1642, <https://doi.org/10.3390/app9081642>.
4. F. Ihlenburg, *Finite Element Analysis of Acoustic Scattering* (Springer-Verlag, New York, 1998), <https://doi.org/10.1007/b98828>.
5. I. Harari, A survey of finite element methods for time-harmonic acoustics, *Comput. Methods Appl. Mech. Eng.* **195**(13–16) (2006) 1594–1607, <https://doi.org/10.1016/j.cma.2005.05.030>.
6. L. L. Thompson, A review of finite element methods for time-harmonic acoustics, *J. Acoust. Soc. Am.* **119**(3) (2006) 1315–1330, <https://doi.org/10.1121/1.2164987>.
7. A. Bayliss and E. Turkel, Radiation boundary condition for wave-like equations, *Commun. Pure Appl. Math.* **33** (1980) 707–725, <https://doi.org/10.1002/cpa.3160330603>.
8. D. Givoli, Non-reflecting boundary conditions, *J. Comput. Phys.* **94**(1) (1991) 1–29, [https://doi.org/10.1016/0021-9991\(91\)90135-8](https://doi.org/10.1016/0021-9991(91)90135-8).
9. J.-P. Berenger, A perfectly matched layer for the absorption of electromagnetic waves, *J. Comput. Phys.* **114**(2) (1994) 185–200, <https://doi.org/10.1006/jcph.1994.1159>.
10. K. Gerdes, The conjugated vs. the unconjugated infinite element method for the Helmholtz equation in exterior domains, *Comput. Methods Appl. Mech. Eng.* **152**(1–2) (1998) 125–145, [https://doi.org/10.1016/S0045-7825\(97\)00186-2](https://doi.org/10.1016/S0045-7825(97)00186-2).
11. R. J. Astley, Infinite elements for wave problems: A review of current formulations and an assessment of accuracy, *Int. J. Numer. Methods Eng.* **49** (2000) 951–976, [https://doi.org/10.1002/1097-0207\(20001110\)49:7<951::AID-NME989>3.0.CO;2-T](https://doi.org/10.1002/1097-0207(20001110)49:7<951::AID-NME989>3.0.CO;2-T).
12. O. C. Zienkiewicz, K. Bando, P. Bettess, C. Emson and T. C. Chiam, Mapped infinite elements for exterior wave problems, *Int. J. Numer. Methods Eng.* **21**(7) (1985) 1229–1251, <https://doi.org/10.1002/nme.1620210705>.

13. D. S. Burnett, A threedimensional acoustic infinite element based on a prolate spheroidal multipole expansion, *J. Acoust. Soc. Am.* **96**(5) (1994) 2798–2816, <https://doi.org/10.1121/1.411286>.
14. R. J. Astley, G. J. Macaulay, J.-P. Coyette and L. Cremers, Three-dimensional wave-envelope elements of variable order for acoustic radiation and scattering. Part I. Formulation in the frequency domain, *J. Acoust. Soc. Am.* **103** (1998) 49–63, <https://doi.org/10.1121/1.421106>.
15. R. J. Astley, Infinite Elements, in *Computational Acoustics of Noise Propagation in Fluids — Finite and Boundary Element Methods*, Chapter 7, eds. S. Marburg and B. Nolte (Springer-Verlag, Berlin, Heidelberg (Germany, 2008)), pp. 197–230, <https://doi.org/10.1007/978-3-540-77448-8>.
16. S. Marburg, F. Dienerowitz, T. Horst and S. Schneider, Normal modes in external acoustics. Part II: Eigenvalues and Eigenvectors in 2d, *Acta Acust. United Acust.* **92**(1) (2006) 97–111.
17. S. Fuß, S. C. Hawkins and S. Marburg, An eigenvalue search algorithm for modal analysis of a resonator in free space, *J. Comput. Acoust.* **19**(1) (2011) 95–109, <https://doi.org/10.1142/S0218396X11004304>.
18. L. Moheit and S. Marburg, Infinite elements and their influence on normal and radiation modes in exterior acoustics, *J. Comput. Acoust.* **25**(4) (2017) 1650020, <https://doi.org/10.1142/S0218396X1650020X>.
19. S. Marburg, Normal modes in external acoustics. Part III: Sound power evaluation based on frequency-independent superposition of modes, *Acta Acust. United Acust.* **92** (2006) 296–311.
20. L. Moheit and S. Marburg, Normal modes and modal reduction in exterior acoustics, *J. Theoret. Comput. Acoust.* **26**(3) (2018) 1850029, <https://doi.org/10.1142/S2591728518500299>.
21. G. Stefanou, The stochastic finite element method: Past, present and future, *Comput. Methods Appl. Mech. Eng.* **198**(9–12) (2009) 1031–1051, <https://doi.org/10.1016/j.cma.2008.11.007>.
22. O. Le Maître and O. M. Knio, *Spectral Methods for Uncertainty Quantification* (Springer, Netherlands, 2010), <https://doi.org/10.1007/978-90-481-3520-2>.
23. S. Hosder, R. Walters and M. Balch, Efficient sampling for non-intrusive polynomial Chaos applications with multiple uncertain input variables, *Proc. 9th AIAA Non-Deterministic Approaches Conference*, Vol. 125, American Institute of Aeronautics and Astronautics (AIAA), 2007, pp. 1–16, <https://doi.org/10.2514/6.2007-1939>.
24. R. G. Ghanem and P. Spanos, *Stochastic Finite Elements: A Spectral Approach*, edn. (Springer-Verlag, New York, 1991), <https://doi.org/10.1007/978-1-4612-3094-6>.
25. R. G. Ghanem and R. M. Kruger, Numerical solution of spectral stochastic finite element systems, *Comput. Methods Appl. Mech. Eng.* **129**(3) (1996) 289–303, [https://doi.org/10.1016/0045-7825\(95\)00909-4](https://doi.org/10.1016/0045-7825(95)00909-4).
26. M. F. Ngah and A. Young, Application of the spectral stochastic finite element method for performance prediction of composite structures, *Composite Struct.* **78**(3) (2007) 447–456, <https://doi.org/10.1016/j.compstruct.2005.11.009>.
27. K. Sepahvand, S. Marburg and H.-J. Hardtke, Uncertainty quantification in stochastic systems using polynomial Chaos expansion, *Int. J. Appl. Mech.* **2** (2010) 305–353, <https://doi.org/10.1142/S1758825110000524>.
28. K. Sepahvand, S. Marburg and H.-J. Hardtke, Numerical solution of one-dimensional wave equation with stochastic parameters using generalized polynomial chaos expansion, *J. Comput. Acoust.* **15** (2007) 579–593, <https://doi.org/10.1142/S0218396X07003524>.
29. S. Sepahvand, M. Scheffler and S. Marburg, Uncertainty quantification in natural frequencies and radiated acoustic power of composite plates: Analytical and experimental investigation, *Appl. Acoust.* **87** (2015) 23–29, <https://doi.org/10.1016/j.apacoust.2014.06.008>.
30. Z. C. He, J. Y. Hu and E. Li, An uncertainty model of acoustic metamaterials with random parameters, *Comput. Mech.* **62**(5) (2018) 1023–1036, <https://doi.org/10.1007/s00466-018-1548-y>.

31. J. Chen B. Xia and J. Liu, A sparse polynomial surrogate model for phononic crystals with uncertain parameters, *Comput. Methods Appl. Mech. Eng.* **339** (2018) 681–703, <https://doi.org/10.1016/j.cma.2018.05.001>.
32. B. Xia, Y. Qin, N. Chen, D. Yu and C. Jiang, Optimization of uncertain acoustic metamaterial with Helmholtz resonators based on interval model, *Sci. Chin Technol. Sci.* **60**(3) (2017) 385–398, <https://doi.org/10.1007/s11431-016-0562-1>.
33. W. Pan, G. Tang and J. Tang, Evaluation of uncertainty effects to band gap behavior of circuitry-integrated piezoelectric metamaterial using order-reduced analysis, *J. Intell. Mater. Syst. Struct.* **29**(12) (2018) 2677–2692, <https://doi.org/10.1177/1045389X18778359>.
34. K. Sepahvand and S. Marburg, Random acoustic metamaterials, *25th Int. Congress on Sound and Vibration (ICSV25)* (Hiroshima, Japan, 2018), pp. 1–6.
35. J. Henneberg, Gomez J. S. Nieto, K. Sepahvand, A. Gerlach, H. Cebulla and S. Marburg, Periodically arranged acoustic metamaterial in industrial applications: The need for uncertainty quantification, *Appl. Acoust.* **157** (2020) 107026, <https://doi.org/10.1016/j.apacoust.2019.107026>.
36. S. H. Schot, Eighty years of Sommerfeld's radiation condition, *Hist. Math.* **19**(4) (1992) 385–401, [https://doi.org/10.1016/0315-0860\(92\)90004-U](https://doi.org/10.1016/0315-0860(92)90004-U).
37. Gao, X.-W. and T. G. Davies, 3-D infinite boundary elements for half-space problems, *Eng. Anal. Bound. Elem.* **21**(3) (1998) 207–213, [https://doi.org/10.1016/S0955-7997\(97\)00111-2](https://doi.org/10.1016/S0955-7997(97)00111-2).
38. T. G. Davies and S. Bu, Infinite boundary elements for the analysis of halfspace problems, *Comput. Geotech.* **19**(2) (1996) 137–151, [https://doi.org/10.1016/0266-352X\(95\)00039-D](https://doi.org/10.1016/0266-352X(95)00039-D).
39. J. Liang and K. M. Liew, Boundary elements for half-space problems via fundamental solutions: A three-dimensional analysis, *Int. J. Numer. Methods Eng.* **52**(11) (2001) 1189–1202, <https://doi.org/10.1002/nme.235>.
40. J.-P. Coyette and B. Van den Nieuwenhof, A conjugated infinite element method for half-space acoustic problems, *J. Acoust. Soc. Am.* **108**(4) (2000) 1464–1473, <https://doi.org/10.1121/1.1289921>.
41. N. Wiener, The homogeneous chaos, *Am. J. Math.* **60**(4) (1938) 897–936, <http://dx.doi.org/10.2307/2371268>.
42. R. Askey and J. A. Wilson, *Some Basic Hypergeometric Orthogonal Polynomials that Generalize Jacobi Polynomials*, Vol. 319 (American Mathematical Society, 1985).
43. S. Huang, S. Mahadevan and R. Rebba, Collocation-based stochastic finite element analysis for random field problems, *Probabilis. Eng. Mech.* **22**(2) (2007) 194–205, <https://doi.org/10.1016/j.pro bengmech.2006.11.004>.
44. J. Villadsen and M. L. Michelsen, *Solution of Differential Equation Models by Polynomial Approximation* (Prentice-Hall, Englewood Cliffs, New Jersey 1978).
45. B. Fornberg, *Practical Guide to Pseudospectral Methods* (Cambridge University Press, 1996), [doi:10.1017/CBO9780511626357](https://doi.org/10.1017/CBO9780511626357).
46. L. Lefèvre, D. Dochain, S. Feye de Azevedo and A. Magnus, Optimal selection of orthogonal polynomials applied to the integration of chemical reactor equations by collocation methods, *Comput. Chem. Eng.* **24**(12) (2000) 2571–2588, [https://doi.org/10.1016/S0098-1354\(00\)00597-4](https://doi.org/10.1016/S0098-1354(00)00597-4).
47. S. S. Isukapalli, A. Roy and P. G. Georgopoulos, Stochastic response surface methods (SRSMs) for uncertainty propagation: Application to environmental and biological systems, *Risk Anal.* **18**(3) (1998) 351–363, <https://doi.org/10.1111/j.1539-6924.1998.tb01301.x>.
48. M. A. Tatang, W. Pan, R. G. Prinn and G. J. McRae, An efficient method for parametric uncertainty analysis of numerical geophysical models, *J. Geophys. Res. Atmos.* **102**(D18) (1997) 21925–21932, <https://doi.org/10.1029/97JD01654>.
49. N. Chen, Y. Dejie and X. Baizhan, Hybrid uncertain analysis for the prediction of exterior acoustic field with interval and random parameters, *Comput. Struct.* **141** (2014) 9–18, <https://doi.org/10.1016/j.compstruc.2014.05.004>.

50. N. Chen, Y. Dejie and X. Baizhan, Evidence-theory-based analysis for the prediction of exterior acoustic field with epistemic uncertainties, *Eng. Anal. Bound. Elem.* **50** (2015) 402–411, <https://doi.org/10.1016/j.enganabound.2014.09.014>.
51. C. Wang and Z. Qiu, An interval perturbation method for exterior acoustic field prediction with uncertain-but-bounded parameters, *J. Fluids Struct.* **49** (2014) 441–449, <https://doi.org/10.1016/j.jfluidstructs.2014.05.005>.
52. L. Moheit, S. Anthis, J. Heinz, F. Kronowetter and S. Marburg, Analysis of scattering by finite sonic crystals in free field with infinite elements and normal modes, *J. Sound Vib.* **476** (2020) 115291, <https://doi.org/10.1016/j.jsv.2020.115291>.
53. A. Melnikov, M. Maeder, N. Friedrich, Y. Pozhanka, A. Wollmann, M. Scheffler, S. Oberst, D. Powell and S. Marburg, Acoustic metamaterial capsule for reduction of stage machinery noise, *J. Acoust. Soc. Am.* **147**(3) (2020) 1491–1503, <https://doi.org/10.1121/10.0000857>.
54. M. Möser, *Technische Akustik* (Springer-Verlag, Berlin, Heidelberg (Germany), 2005) <https://doi.org/10.1007/b137595>.
55. P. Pfeffer and M. Harrer, *Lenkungshandbuch: Lenksysteme, Lenkgefühl, Fahrdynamik von Kraftfahrzeugen* (Vieweg+Teubner, Wiesbaden, 2011), [https://doi.org/10.1007/978-3-8348-8167-0\\_6](https://doi.org/10.1007/978-3-8348-8167-0_6).
56. R. Lerch, G. Sessler and D. Wolf, *Technische Akustik* (Springer, Berlin, Heidelberg, 2009), <https://doi.org/10.1007/978-3-540-49833-9>.
57. S. Marburg and H.-J. Hardtke, A study on the acoustic boundary admittance. Determination, results and consequences, *Eng. Anal. Bound. Elem.* **23**(9) (1999) 737–744, [https://doi.org/10.1016/S0955-7997\(99\)00024-7](https://doi.org/10.1016/S0955-7997(99)00024-7).
58. A. Melnikov, Y. K. Chiang, L. Quan, S. Oberst, A. Alù, S. Marburg and D. Powell, Acoustic meta-atom with experimentally verified maximum Willis coupling, *Nature Commun.* **10**(1) (2019) 3148, <https://doi.org/10.1038/s41467-019-10915-5>.
59. D. P. Elford, L. Chalmers, F. V. Kusmartsev and G. M. Swallowe, Matryoshka locally resonant sonic crystal, *J. Acoust. Soc. Am.* **130**(5) (2011) 2746–2755, <https://doi.org/10.1121/1.3643818>.
60. J. Jordaan, S. Punzet, A. Melnikov, A. Sanches, S. Oberst, S. Marburg and D. A. Powell, Measuring monopole and dipole polarizability of acoustic meta-atoms, *Appl. Phys. Lett.* **113**(22) (2018) 224102, <https://doi.org/10.1063/1.5052661>.



## 5.2 **Publication AP2**

## A Benchmark Study on Eigenfrequencies of Fluid-Loaded Structures

Felix Kronowetter\*, Suhaib Koji Baydoun, Martin Eser,  
Lennart Moheit and Steffen Marburg

*Chair of Vibroacoustics of Vehicles and Machines  
Department of Mechanical Engineering  
Technical University of Munich  
Garching 85748, Germany  
\*felix.kronowetter@tum.de*

Received 13 January 2020

Accepted 19 May 2020

Published 4 September 2020

In this paper, a coupled finite/infinite element method is applied for computing eigenfrequencies of structures in exterior acoustic domains. The underlying quadratic eigenvalue problem is addressed by a contour integral method based on resolvent moments. The numerical framework is applied to an academic example of a hollow sphere submerged in water. Comparisons of the computed eigenfrequencies to those obtained by boundary element discretizations as well as finite element discretizations in conjunction with perfectly matched layers verify the proposed numerical framework. Furthermore, extensive parameter studies are carried out illustrating the performance of the method with regard to both projection and discretization parameters. Finally, we point out that the proposed method achieves significantly smaller residuals of the computed eigenpairs than the Rayleigh Ritz procedure with second-order Krylov subspaces.

*Keywords:* Infinite element method (IFEM); nonlinear eigenvalue problems (NLEVPs); fluid-structure interaction (FSI).

### 1. Introduction

Frequency-wise response analyses of large-scale vibro-acoustic problems are associated with a significant computational effort and hence, several numerical techniques have been developed in this regard. Projective model order reduction techniques have been successfully applied to accelerate the solution of frequency dependent structural-acoustic systems

---

\*Corresponding author.

This is an Open Access article published by World Scientific Publishing Company. It is distributed under the terms of the Creative Commons Attribution 4.0 (CC BY) License which permits use, distribution and reproduction in any medium, provided the original work is properly cited.

using perfectly matched layers (PML),<sup>1</sup> infinite element methods (IFEM)<sup>2,3</sup> and boundary element methods (BEM).<sup>4</sup> Typically, the respective projectors are computed by an *a priori* sampling of the frequency range. More recently, a strategy for an optimal choice of frequency samples has been developed based on a greedy algorithm.<sup>5</sup>

Alternatively, when the basis vectors for the projection are chosen as the (orthogonal) modes of the system, this procedure is known as modal superposition technique. Modal superposition has been well established for purely structural and interior acoustic problems for decades. However, in the case of vibro-acoustic problems in unbounded domains, modal analysis requires the solution of the underlying nonlinear eigenvalue problem (EVP). While the solution of nonlinear EVPs arising from FEM-BEM discretizations has attracted growing attention in recent years,<sup>4,6,7</sup> to the best of our knowledge, there are just a few publications, e.g. van Ophem,<sup>3</sup> available that address structural-acoustic discretizations with FEM and IFEM. Purely acoustic problems utilizing modal methods and FEM-IFEM formulations have been developed by the author (SM) in recent 15 years, see, for example, Refs. 8–11. Therein, the arising quadratic EVP is linearized and solved in a state-space resulting in a twice as large generalized EVP. Alternative approaches address the direct solution of a quadratic EVP.<sup>12–14</sup> These methods prevent the doubling of degrees of freedom of the state-space representation of the EVP, hence allowing for a computationally more efficient solution of the quadratic EVP. However, for exterior acoustic problems, it is often unclear how to distinguish between relevant and irrelevant eigenvalues — corresponding to so-called spurious modes.<sup>9,11</sup> In the context of large-scale EVP, one is typically interested in a small subset of all eigenvalues and vectors, which precludes application of the aforementioned methods. Therefore, in this paper, we apply a projection method based on contour integration for computing eigenfrequencies of structural-acoustic systems in a predefined region in the complex plane. An adaption of a second-order Krylov subspace method serves as a reference solution scheme. The underlying second-order Krylov subspace method for a fully coupled FEM-IFEM model was initially proposed by van Ophem.<sup>3</sup>

Fluid-loaded structural modes play a decisive role in the design of acoustic metamaterials since they indicate band gap-like behavior.<sup>15</sup> A common numerical method for the calculation of band gaps is based on Floquet–Bloch boundary conditions but limited by the strict definition of symmetry groups and infinite periodic structures.<sup>16</sup> Most applicable metamaterials are designed as finite structures though. Thus, we propose a new technique for the solution of acoustic-structure coupled EVPs, based on an FEM-IFEM approach, that can also be extended via Floquet–Bloch boundary conditions, e.g. for sound barriers. Sound barriers can be treated as infinite structures in longitudinal direction and as exterior problems in transverse direction, see, for example, Refs. 17 and 18.

This paper is organized as follows: In a first step, the mathematical background of the acoustic-structure coupled FEM-IFEM approach is outlined. The acoustic-structure interaction is implemented such that a full coupling in two directions is established. We chose the Astley–Leis formulation for the infinite elements. This formulation results in frequency independent system matrices.<sup>8</sup> In a next step, the steady state solutions of a time-harmonically excited submerged shell are computed and compared to the analytical ones to verify the

coupling scheme. Furthermore, the eigenfrequencies of the shell and their corresponding fluid-loaded structural modes are determined. The accuracy of our numerical results is assessed by comparing them to analytical expressions. Three studies on the performance and accuracy of the contour integration method are conducted. Additionally, the contour integral method is compared to a second-order Krylov subspace method and to COMSOL. In the final step, possible applications are discussed.

## 2. Mathematical Background

### 2.1. Exterior Helmholtz problems

In linear acoustics, we distinguish between interior and exterior problems. The sound pressure field  $p(\mathbf{x})$  for time-harmonic excitation is governed by the Helmholtz equation. Interior Helmholtz problems describe a fluid domain  $\Omega_f$  that is fully closed by boundaries at a finite distance. In contrast, problems with a fluid domain of infinite extension or problems with a negligible influence of their surroundings are denoted as unbounded or exterior Helmholtz problems. An additional radiation criterion has to be fulfilled, i.e. the Sommerfeld radiation condition.<sup>19</sup> This condition applies to the sound pressure field solution and encompasses three parts, i.e.<sup>20</sup>

- (1)  $p(\mathbf{x})$  is a solution of the Helmholtz equation,
- (2)  $p(\mathbf{x})$  decays with the order  $O(r^\alpha)$  with  $\alpha = (d - 1)/2$  where  $d$  represents the spatial dimension being 2 for planar problems and 3 for three-dimensional problems, and
- (3) an additional decay condition often written as

$$\lim_{r \rightarrow \infty} r^\alpha \left( \frac{\partial p}{\partial r} - ikp \right) = 0 \quad (2.1)$$

specifying how the sound pressure is decaying at infinity.

The wavenumber is denoted by  $k$  and the radial co-ordinate for two and three-dimensional problems is denoted by  $r$ . A schematic of an exterior Helmholtz problem is shown in Fig. 1(a). A solid scatterer  $\Omega_s$  is surrounded by a fluid domain  $\Omega_f$  of infinite extension, marked by the outer boundary  $\Gamma_\infty$ . No other sound sources are present. To describe the behavior of the solid body under excitation, the Navier–Lamé equations for linear elasticity<sup>21</sup> as well as an additional damping model are applied. In this paper, we consider a full coupling between the solid and the fluid. Therefore, two coupling conditions are defined at the interface  $\Gamma$  between the solid and the fluid subdomains.<sup>22</sup> The first condition, called the kinetic coupling condition, establishes a relation between the solid stress tensor  $\boldsymbol{\sigma}$  and the sound pressure  $p$  on  $\Gamma$  as

$$\boldsymbol{\sigma} \cdot \mathbf{n} = -p\mathbf{n}, \quad \text{on } \Gamma. \quad (2.2)$$

The second condition known as kinematic coupling condition assures that the normal components of the mechanical surface velocity of the solid body  $\mathbf{v}_s$  and of the acoustic velocity

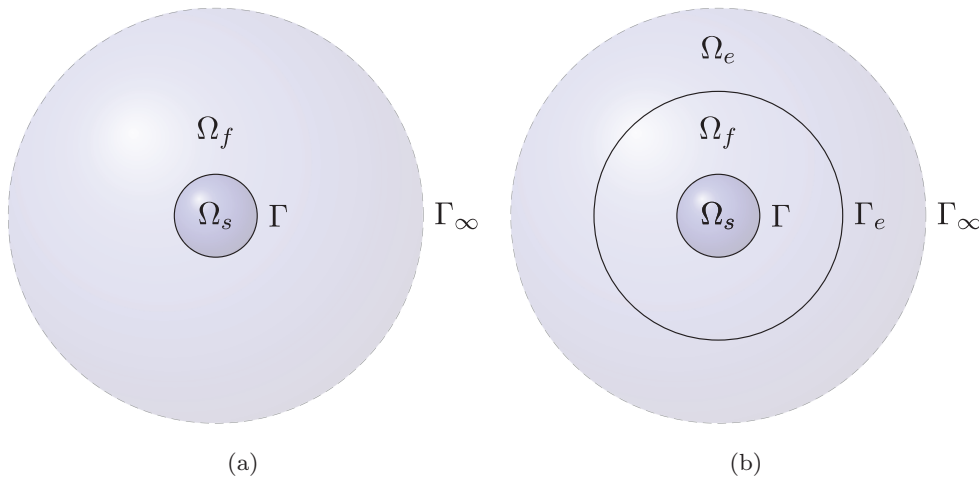


Fig. 1. Exterior Helmholtz problem shown for the general definition and for the infinite element formulation. (a) Exterior Helmholtz problem and (b) exterior Helmholtz problem for the infinite element formulation.

of the fluid  $\mathbf{v}_f$  concur as

$$\mathbf{n} \cdot (\mathbf{v}_s - \mathbf{v}_f) = 0, \quad \text{on } \Gamma. \quad (2.3)$$

In Eqs. (2.2) and (2.3),  $\mathbf{n} = (n_x \ n_y \ n_z)^T$  is the surface normal vector pointing from the surface of the scatterer into the fluid domain. Special numerical solution techniques need to be applied due to the mathematical domain of infinite extension. Here, we focus on domain-based methods and more precisely on the IFEM.

## 2.2. Infinite element method

The infinite element formulation is derived in what follows. For this purpose, recall the schematic in Fig. 1(b). The fluid domain is split up in a domain  $\Omega_f$  that is discretized by a conventional FEM and an (unbounded) exterior domain  $\Omega_e$ . These two subdomains are separated by the interface  $\Gamma_e$ . The exterior domain is discretized by the IFEM, which is an extension of the FEM. The basis functions of infinite elements fulfill the Sommerfeld radiation condition due to an advanced radial interpolation scheme. These elements are characterized by their infinite extent in radial direction. Hence, the exterior domain does not need to be truncated as in other approaches such as approximate boundary conditions (ABCs).<sup>23</sup> The mapped wave-envelope formulation also known as conjugated Astley–Leis formulation<sup>24–26</sup> is implemented in an in-house code. The in-house code is validated for purely fluid time-harmonic problems with multipole excitation.<sup>27</sup> As it will be shown later in the results of the academic example, the numerical results match the analytical ones for fully coupled problems. The conjugated Astley–Leis formulation is based on a Petrov–Galerkin method, which uses complex conjugates of the radial interpolation (or basis) functions as weight functions. These radial interpolation functions  $\phi_j \sim e^{\pm ik\mu(\mathbf{x})}$ , with  $\mu(\mathbf{x})$  being the phase component, have a wavelike characteristic. Hence, the use of complex conjugates

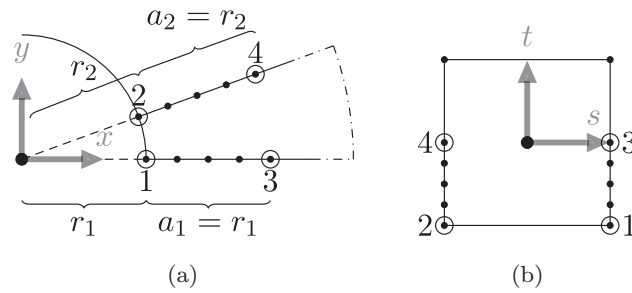


Fig. 2. Topology of a two-dimensional infinite element with five radial nodes —  $m = 5$  — in the physical and isoparametric space. (a) Ten-noded physical element and (b) twelve-noded parent element.

cancels out all wavelike terms in the formulation as  $\phi_i \phi_j \sim e^{-ik\mu(\mathbf{x})} e^{+ik\mu(\mathbf{x})} = 1$ .<sup>28</sup> Since all time-harmonic, wavelike terms are eliminated, frequency independent system matrices are obtained.

Figure 2 shows a two-dimensional, 10-noded infinite element in the physical space and its corresponding 12-noded parent element. The interpolation function for the element depicted in Fig. 2 is given as<sup>25</sup>

$$P_l(s, t) = \frac{1}{2} S_i(s) (1 - t) L_j^m(t) \quad (2.4)$$

with  $(s, t)$  being the co-ordinates in the isoparametric space,  $S_i(s)$  the interpolation function in transversal direction and  $L_j^m$  is a Lagrange polynomial used as interpolation function in radial direction. For example, the interpolation function for node number two, in the case of linear transversal interpolation  $S_2 = \frac{1}{2}(1 - s)$ , can be written as

$$P_2(s, t) = \frac{1}{2}(1 - s) \frac{1}{2}(1 - t) \cdot t(4t + 3)(2t + 1) \frac{1}{3}(4t + 1). \quad (2.5)$$

The influence of the nodes at  $(-1, 1)$  and  $(1, 1)$  in the isoparametric space is covered by the term  $\frac{1}{2}(1 - t)$ . This proves the non-truncating character of the infinite elements. Due to the mapping to the parent element  $t \sim \frac{1}{r}$ , Eq. (2.5) can be re-written as a series of multipole terms similar to the Atkinson–Wilcox theorem.<sup>29</sup> The fifth-order infinite element accurately models radiating sources up to an acoustic hexadecapole.

### 2.3. The structural-acoustic matrix form and eigenvalue problem

The governing equation of an elastic solid is the Navier–Lamé equation. After applying a finite element discretization, the matrix form is written as

$$(\mathbf{K}_s - i\omega \mathbf{D}_s - \omega^2 \mathbf{M}_s) \mathbf{u} = \mathbf{f}_s. \quad (2.6)$$

The terms  $\mathbf{K}_s$  and  $\mathbf{M}_s$  denote the stiffness and mass matrices of the solid domain. The displacement vector is denoted by  $\mathbf{u}$  and the solid is subject to external forces  $\mathbf{f}_s$ . Additionally, Rayleigh damping<sup>30</sup> is considered, resulting in the structural damping matrix  $\mathbf{D}_s$ .

The combined acoustic FEM-IFEM system of equations reads as

$$\left\{ \begin{bmatrix} \mathbf{K}_f & \mathbf{K}_{fe} \\ \mathbf{K}_{ef} & \mathbf{K}_e \end{bmatrix} - i\omega \begin{bmatrix} \mathbf{D}_f & \mathbf{D}_{fe} \\ \mathbf{D}_{ef} & \mathbf{D}_e \end{bmatrix} - \omega^2 \begin{bmatrix} \mathbf{M}_f & \mathbf{M}_{fe} \\ \mathbf{M}_{ef} & \mathbf{M}_e \end{bmatrix} \right\} \begin{pmatrix} \mathbf{p}_f \\ \mathbf{p}_e \end{pmatrix} = \mathbf{f}, \quad (2.7)$$

where we distinguish among the matrices of the finite element domain  $\Omega_f$  denoted by subscript  $\bullet_f$ , the coupling matrices by  $\bullet_{fe}$  or  $\bullet_{ef}$ , and the matrices of the exterior, i.e. infinite element domain  $\Omega_e$  by  $\bullet_e$ . The same applies to the sound pressure. The entries of the coupling matrices relate the degrees of freedom of the nodes that are shared by the conventional and the exterior fluid domain on their interface  $\Gamma_e$  cf. Fig. 1(b). An exact formulation of the FEM-IFEM coupling can be found in the publications by Astley *et al.*<sup>24,25</sup>

The damping matrix  $\mathbf{D}_f$  and the mass matrix  $\mathbf{M}_e$ , are null matrices. The former has zero entries due to the assumption of an inviscid fluid and the latter in consequence of a circular or spherical domain leading to vanishing entries in the exterior domain for  $\mathbf{M}_e$ .<sup>25</sup>

Equations (2.6) and (2.7) are mutually coupled by virtue of the coupling conditions Eqs. (2.2) and (2.3), leading to the fully coupled acoustic-structure system as

$$\left\{ \begin{bmatrix} \mathbf{K}_s & \mathbf{R} & \mathbf{0} \\ \mathbf{0} & \tilde{\mathbf{K}}_f & \tilde{\mathbf{K}}_{fe} \\ \mathbf{0} & \tilde{\mathbf{K}}_{ef} & \tilde{\mathbf{K}}_e \end{bmatrix} - i\omega \begin{bmatrix} \mathbf{D}_s & \mathbf{0} & \mathbf{0} \\ \mathbf{0} & \tilde{\mathbf{D}}_f & \tilde{\mathbf{D}}_{fe} \\ \mathbf{0} & \tilde{\mathbf{D}}_{ef} & \tilde{\mathbf{D}}_e \end{bmatrix} - \omega^2 \begin{bmatrix} \mathbf{M}_s & \mathbf{0} & \mathbf{0} \\ -\mathbf{R}^T & \tilde{\mathbf{M}}_f & \tilde{\mathbf{M}}_{fe} \\ \mathbf{0} & \tilde{\mathbf{M}}_{ef} & \tilde{\mathbf{M}}_e \end{bmatrix} \right\} \begin{pmatrix} \mathbf{u} \\ \mathbf{p}_f \\ \mathbf{p}_e \end{pmatrix} = \begin{pmatrix} \mathbf{f}_s \\ \mathbf{0} \\ \mathbf{0} \end{pmatrix}. \quad (2.8)$$

Matrix  $\mathbf{R}$  — with  $\mathbf{R} = \mathbf{R}_{sf}$  and  $\mathbf{R}^T = \mathbf{R}_{fs}$  — establishes the coupling between the solid and the fluid with contributions from the common nodes at the interface  $\Gamma$ . This matrix is defined as

$$\mathbf{R}_{ij} = \int_{\Gamma} \begin{pmatrix} N_i N_j n_x \\ N_i N_j n_y \\ N_i N_j n_z \end{pmatrix} d\Gamma, \quad (2.9)$$

where  $N_i, N_j$  are the weight and basis functions.

All matrices indicated with  $\tilde{\bullet}$  are normalized by the fluid density, i.e.  $\tilde{\bullet} = \frac{\bullet}{\rho_0}$ . The sparsity pattern of the fully coupled system matrices is shown in Fig. 3. Note that structural damping is neglected in the remainder of the paper, and hence, the corresponding entries vanish in Fig. 3. Only radiation damping<sup>31</sup> is (inherently) considered by fulfilling the Sommerfeld condition.

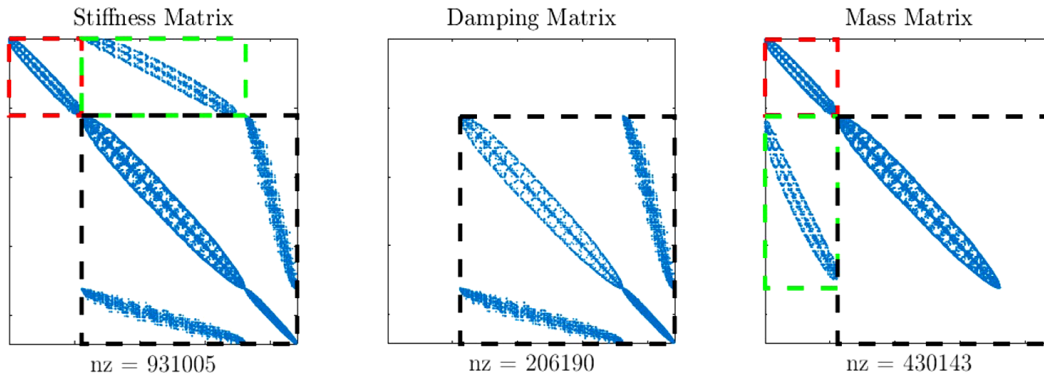


Fig. 3. (Color online) System matrices for the coupled FEM-IFEM formulation. The areas framed by the red lines correspond to the matrices in the solid domain, the ones framed by the green lines indicate the coupling matrices and the matrices of the fluid part are framed by black lines. The number of non-zero entries in each matrix is denoted by  $nz$ .

By setting the right-hand side to zero, we obtain a structural-acoustic EVP based on a FEM-IFEM formulation, that reads as

$$(\mathbf{K} - i\bar{\omega}\mathbf{D} - \bar{\omega}^2\mathbf{M})\mathbf{v} = (\mathbf{K} + \lambda\mathbf{D} + \lambda^2\mathbf{M})\mathbf{v} = \mathbf{0}. \quad (2.10)$$

The fluid-loaded structural modes are denoted by  $\mathbf{v}$  and the complex eigenvalues by  $\bar{\omega}$  or by its corresponding substitutes  $\lambda = -i\bar{\omega}$ . The EVP depends quadratically on the complex eigenfrequency  $\bar{\omega}$ . This EVP is very similar to the one set up and solved in Refs. 8, 10 and 11 and nearly identical to the one analyzed by van Ophem.<sup>3</sup>

#### 2.4. Contour integral methods

Various approaches have been suggested to solve nonlinear structural-acoustic EVPs in the last years. In a series of papers, Peters *et al.*<sup>6,32</sup> employed a frequency approximation of the BEM matrices and solved the resultant polynomial EVP via symmetric linearization. The computational effort associated with the inflation of the EVP has been addressed by means of Krylov subspace model order reduction. However, when dealing with complex eigenvalues, polynomial frequency approximations quickly deteriorate apart from the real axis. As a remedy, El-Guide *et al.*<sup>33</sup> employed a rational approximation method based on Cauchy integral representations of frequency dependent matrices.

Besides, the Cauchy integral formula has also been exploited by many researchers to derive subspace projection methods for nonlinear EVPs. These methods, which are typically termed contour integral methods (CIMs),<sup>34–36</sup> essentially work by transforming a nonlinear EVP to a generalized EVP of reduced dimension. The latter exhibits identical eigenvalues inside a pre-defined region in the complex plane. CIMs are advantageous, because the main computational operations can be executed on distributed parallel computers. Several variations of the contour integral method have been applied for the solution of structural-acoustic EVPs.<sup>4,7</sup>



In this paper, we will use the block Sakurai Sugiura method (block SS)<sup>34</sup> for solving both types of structural-acoustic EVPs — FEM-IFEM and FEM-BEM. The eigensolution with FEM-BEM is obtained by an in-house code that is described in a recent publication of the group.<sup>31</sup> We note that the focus of our contribution is not the further development of contour integral methods but rather its application for computing structural-acoustic modes with IFEM. Regarding the choice of parameters, we follow the recommendations given in the publication by Sakurai *et al.*<sup>37</sup>

## 2.5. Second-order Krylov subspace methods

Compared to the nonlinear EVP from the FEM-BEM formulation, the resulting quadratic EVP from the FEM-IFEM formulation as stated in Eq. (2.10) depends explicitly in quadratic manner on the complex eigenfrequency  $\bar{\omega}$ . The corresponding system matrices are frequency independent and hence constant.

Van Ophem<sup>3</sup> proposed a stable model-order reduction scheme for fully coupled exterior structural-acoustic EVPs using a comparable infinite element formulation as used by the authors of this paper. The reduction scheme is based on projecting the original quadratic EVP to a second-order Krylov subspace. The reduced EVP is transformed into a general EVP and then solved with conventional methods. An efficient second-order Arnoldi (SOAR) algorithm<sup>38</sup> is used to generate the orthonormal basis of the projection subspace. Bai and Su<sup>13</sup> have shown, that the Ritz eigenpairs of a reduced-order quadratic EVP are good approximations of the eigenpairs of the original quadratic EVP. Hence, the eigenpairs of the original system can be obtained by solving a EVP of significantly reduced dimension.

A similar second-order Krylov subspace approach is chosen in this paper in order to generate a state-of-the-art reference solution for the comparison to the proposed CIM. The reduced second-order system of Eq. (2.10) is generated in the same manner as proposed by van Ophem,<sup>3</sup> i.e. using the SOAR algorithm in order to generate an unsplit orthonormal projection basis  $\mathbf{V}$ . An arbitrary initialization vector with random values between 0 and 1 is chosen for the generation of the projection basis. The EVP of reduced dimension  $q$  then states as<sup>13</sup>

$$(\mathbf{K}_q - i\bar{\omega}\mathbf{D}_q - \bar{\omega}^2\mathbf{M}_q)\mathbf{v}_q = \mathbf{0}, \quad (2.11)$$

with the reduced system matrices given as

$$\mathbf{K}_q = \mathbf{V}^T\mathbf{K}\mathbf{V}, \quad \mathbf{D}_q = \mathbf{V}^T\mathbf{D}\mathbf{V}, \quad \mathbf{M}_q = \mathbf{V}_1^T\mathbf{M}\mathbf{V}_1 \quad \text{and} \quad \mathbf{v}_q = \mathbf{V}^T\mathbf{v}. \quad (2.12)$$

Note that only a part of the unsplit projection basis with entries corresponding to the degrees of freedom of the structural and the acoustic FEM domain —  $\mathbf{V}_1$  — are taken into account for the projection of the mass matrix. By this, one accounts for the actual zero-block of the mass matrix of the IFEM domain  $\mathbf{M}_e$ , as proposed by van Ophem.<sup>3</sup> The projection process leads to fully-populated, dense system matrices of the reduced system. The reduced quadratic EVP is solved efficiently with the open-access MATLAB function *quadeig*.<sup>14</sup> This MATLAB function provides the full solution of a dense quadratic EVP. The

resulting eigenvectors of reduced dimension are re-projected to the original size in order to allow for the evaluation of the relative residuals of the approximate eigenpair solution.

### 3. The Benchmark Problem: Spherical Shell in Water

#### 3.1. Problem description

We consider a three-dimensional hollow steel sphere with a vacuum inside. The sphere is submerged in water. A sketch of the sphere is displayed in Fig. 4. The extension of the surrounding water is assumed to be several orders of magnitude larger than the dimensions of the sphere. Hence, the acoustic sub-problem can be regarded as an exterior Helmholtz problem. In the case of a harmonic response analysis, the structure is excited by an external force  $F = 1\text{ N}$  that is applied to the spherical shell. The excitation force leads to vibrations of the sphere that in turn excite the fluid and generate acoustic waves. The wall thickness  $t$  of the hollow sphere is kept small, so membrane stresses dominate over flexural stresses for lower-order modes and hence, we apply the strong coupling conditions in the upcoming simulations. Therefore, the generated acoustic waves result in a surface pressure load on the vibrating structure that is not negligible. Again, structural damping is neglected. The analytical expression for the eigenfrequencies as well as the time-harmonic solutions can be found in the book by Junger and Feit.<sup>39</sup> This problem is particularly well suited for benchmarking, since it has been extensively studied in the past.<sup>5-7</sup> The geometrical parameters of the sphere and the material properties of steel and water are given in Table 1.

#### 3.2. Time-harmonic solution

Before proceeding with the actual modal analysis, the FEM-IFEM formulation is verified in this subsection by comparing the time-harmonic solution to an analytical expression. The time-harmonic solutions of the sound pressure  $p$  and of the normal displacement  $u$  are given as<sup>39</sup>

$$p(r, \alpha) = \frac{F}{4\pi r^2} \sum_{n=0}^{\infty} \frac{(2n+1)z_n}{Z_n + z_n} P_n(\cos(\alpha)), \quad (3.1)$$

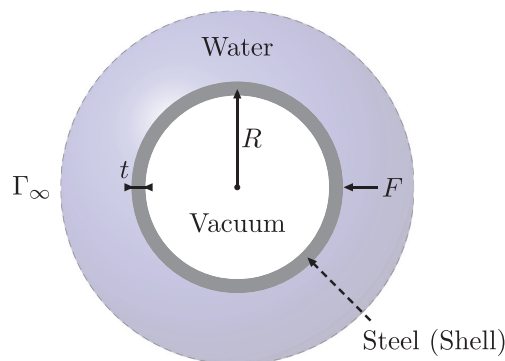


Fig. 4. Two-dimensional cross section of the three-dimensional reference problem.

Table 1. Geometry of the sphere and properties of steel and water.

Radius of the sphere	$R$	5 m
Shell thickness	$t$	0.05 m
Density of steel	$\rho_s$	7860 kg/m <sup>3</sup>
Young's modulus	$E$	210 GPa
Poisson's ratio	$\nu$	0.3
Density of water	$\rho_0$	1000 kg/m <sup>3</sup>
Speed of sound	$c_0$	1500 m/s

and

$$u(r, \alpha) = \frac{1}{i\omega} \frac{F}{4\pi r^2} \sum_{n=0}^{\infty} \frac{2n+1}{Z_n + z_n} P_n(\cos(\alpha)), \quad (3.2)$$

respectively. Both are given as a sum over the mode numbers  $n$  and expressed in terms of the specific acoustic impedance  $z_n$ , the vacuo modal impedance  $Z_n$  and Legendre polynomials  $P_n(\cos(\alpha))$ . The Legendre polynomials are evaluated at the position described by the angle of attack  $\alpha$  with respect to the point of excitation of the shell. For the exact formulation of all terms, the reader is referred to the book by Junger and Feit.<sup>39</sup> The solid domain and the acoustic field are discretized using quadratic shell elements for the former and quadratic tetrahedral elements in combination with infinite elements with the radial order of five for the latter. The outer radius of the fluid domain  $\Gamma_e$  is set to 20 m. This leads to 68529 degrees of freedom for the coupled FEM-IFEM system for six elements per wavelength in the fluid domain at a frequency of 100 Hz. We are interested in solving the system of equations in the frequency range from 1 to 85 Hz with frequency steps of  $\Delta f = 1$  Hz. The absolute displacement and sound pressure values are given in Fig. 5 based on both, the analytical expression and the presented FEM-IFEM formulation. The numerical results show good agreement with the analytical solution.

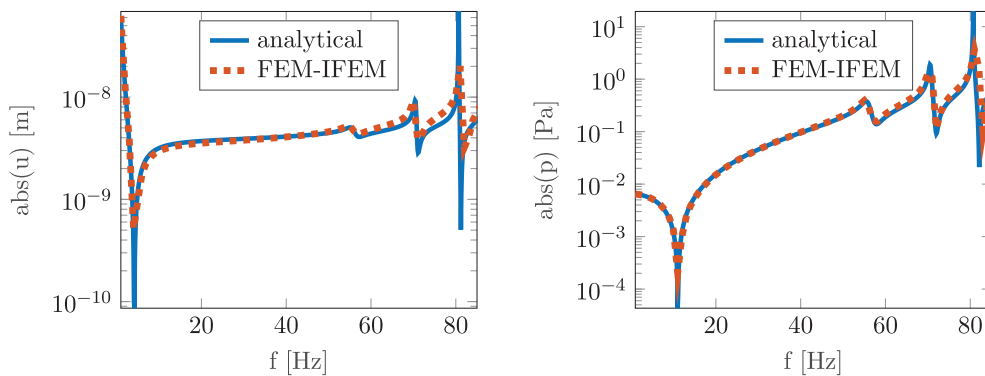


Fig. 5. (Color online) Absolute displacement and sound pressure for the analytical solution (blue line) and the solution obtained by the coupled FEM-IFEM formulation (red dashed line) evaluated at the point of excitation.

### 3.3. Eigenfrequency study

Based on previous analyses,<sup>6</sup> three different eigenfrequencies are expected with multiplicities of 5, 7 and 9, respectively, i.e. five eigenvalues associated with quadrupole modes, seven eigenvalues associated with octupole modes and nine eigenvalues associated with hexadecapole modes. We use an ellipse as contour for the CIM solving the quadratic EVP. The contour of the ellipse is defined by a predefined frequency range and an aspect ratio. Moreover, it is divided into contour points for the integration. Since we expect small imaginary parts of the complex eigenfrequencies, this choice of parameters enables a more accurate projection via the CIM than a circular contour. The parameters used for the block SS are denoted by  $K$  and  $L$ , where the latter stands for the number of source vectors and the former one indicates the order of the moment matrices. As the contour of the ellipse and the parameters  $K$  and  $L$  are crucial concerning the accuracy of the block SS, they have to be chosen with care. The contour points (outlined as blue points) of the ellipses of all three test cases of study one, as well as the computed complex eigenfrequencies (all marked by red points) of the quadratic EVP are shown for 24 contour points in Fig. 6. Infinite elements with a radial order of 5 have been used in order to accurately capture the hexadecapole modes as shown in Eq. (2.5). In a first study, the influence of the shape of the ellipse and the number of contour points on the stability of the eigenfrequencies and on the relative residual — explained later — are investigated for different test cases.

In test case one, the ellipse is divided into 12, 24, 36 and 48 contour points in a frequency range from 50 to 85 Hz and has an aspect ratio of 0.1, with  $K = 5$  and  $L = 16$ . The imaginary part of the first five eigenfrequencies around 55 Hz is quite big compared to the others. Hence, an aspect ratio smaller than 0.1 is not practicable for this frequency range, since the imaginary parts are beyond the contour of the ellipse. Figure 7 shows the real and imaginary parts of the 21 eigenfrequencies found. All four configurations of contour points lead to the same eigenfrequencies, merely minor fluctuations with a maximum relative error

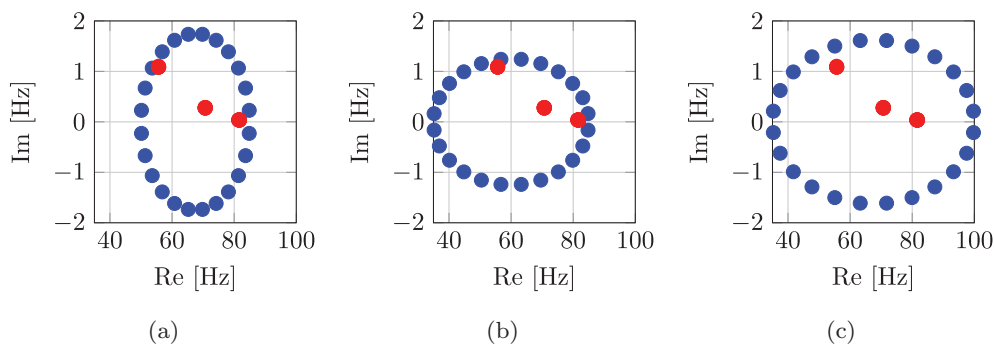


Fig. 6. (Color online) Different elliptical contours in the complex plane for the configurations of all three test cases of the first study are shown. Each ellipse is represented by 24 contour points (blue points), respectively. The eigenfrequencies are represented by the red points. (a) Test Case One ( $f_l = 50$  Hz,  $f_u = 85$  Hz, aspect ratio of 0.1). (b) Test Case Two ( $f_l = 35$  Hz,  $f_u = 85$  Hz, aspect ratio of 0.05). (c) Test Case Three ( $f_l = 35$  Hz,  $f_u = 100$  Hz, aspect ratio of 0.05).

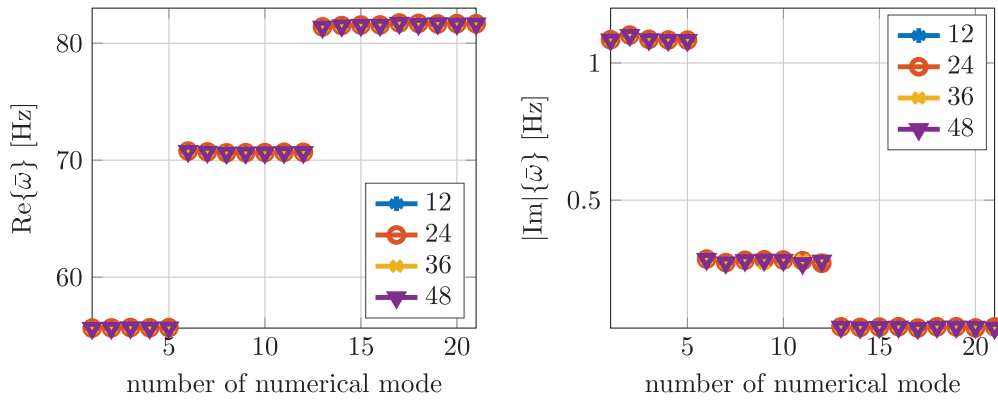


Fig. 7. Real and imaginary parts of the complex eigenfrequencies  $\bar{\omega}$  for test case one ( $f_l = 50$  Hz,  $f_u = 85$  Hz, aspect ratio of 0.1,  $K = 5$ ,  $L = 16$ ). The results are obtained by using 12, 24, 36 and 48 contour points, respectively.

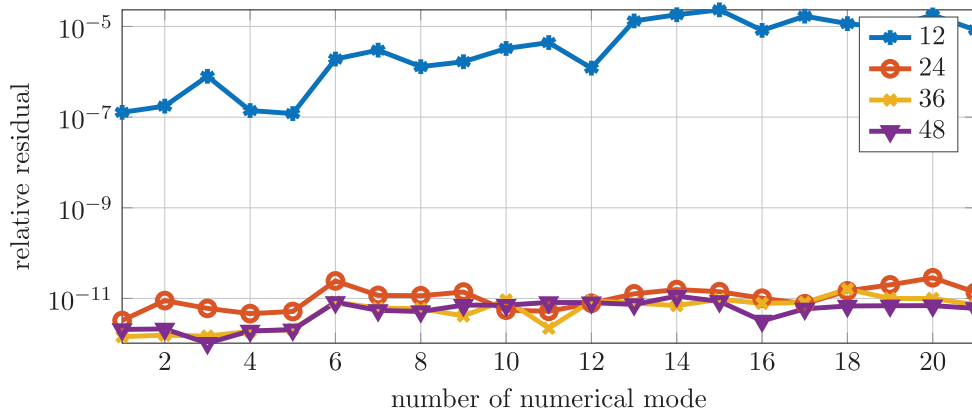


Fig. 8. Relative residuals for test case one ( $f_l = 50$  Hz,  $f_u = 85$  Hz, aspect ratio of 0.1,  $K = 5$ ,  $L = 16$ ), using 12, 24, 36 and 48 contour points, respectively.

of  $\approx 1\%$  at mode number 11 from the analytical solution occur in the imaginary parts. A more significant impact appears in the relative residual shown in Fig. 8. The relative residual of an eigenpair  $(\bar{\omega}, \mathbf{v})$  is defined as

$$\epsilon_{\text{rel}} = \frac{\|(K - i\bar{\omega}D - \bar{\omega}^2M)\mathbf{v}\|_2}{\|\mathbf{v}\|_2}. \quad (3.3)$$

Very accurate results are achieved with 24, 36 and 48 contour points with relative residuals of  $\epsilon_{\text{rel}} \approx 1 \cdot 10^{-11}$ , whereas the numerical results of the 12 point configuration lead to values greater than  $1 \cdot 10^{-7}$ .

In the second test case, the same ellipse and contour points are used. The lower end of the frequency range is changed from 50 to 35 Hz and the aspect ratio is set to 0.05, though. The eigenfrequencies are similar to the ones computed in test case one and shown in Fig. 9.

However, the relative residuals change significantly. This is presented in Fig. 10.

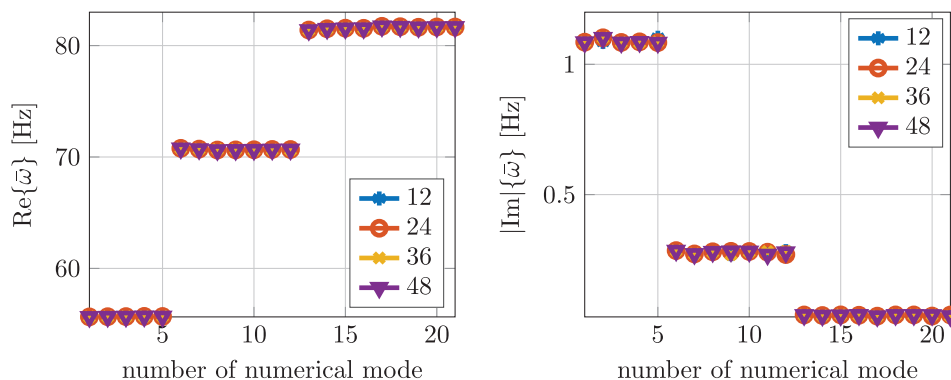


Fig. 9. Real and imaginary parts of the complex eigenfrequencies  $\bar{\omega}$  for test case two ( $f_l = 35$  Hz,  $f_u = 85$  Hz, aspect ratio of 0.05,  $K = 5$ ,  $L = 16$ ). The results are obtained by using 12, 24, 36 and 48 contour points, respectively.

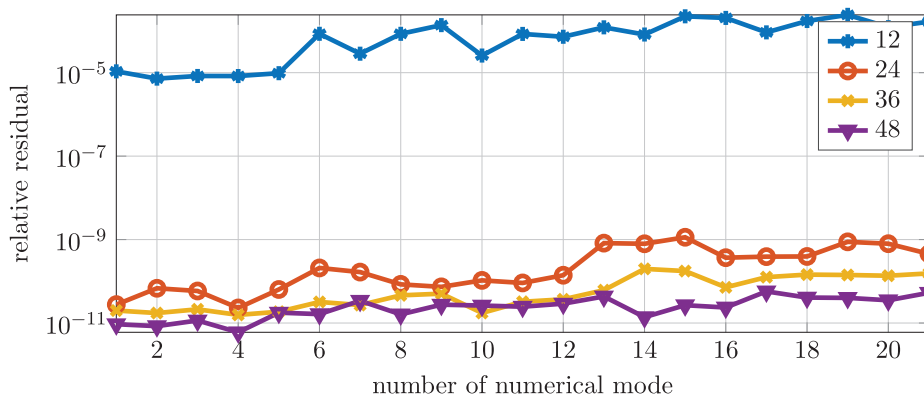


Fig. 10. Relative residuals for test case two ( $f_l = 35$  Hz,  $f_u = 85$  Hz, aspect ratio of 0.05,  $K = 5$ ,  $L = 16$ ), using 12, 24, 36 and 48 contour points, respectively.

The 12 contour point configuration shifts from values greater than  $1 \cdot 10^{-7}$  to values greater than  $\approx 1 \cdot 10^{-5}$ . Furthermore, the relative residuals of the 24 and 36 point configurations increase. Solely, the version with 48 contour points does not change compared to test case one.

In the last test case of the first study, the upper limit of the frequency range is set to 100 Hz. The remaining parameters are similar to the second test case. As it can be seen in Fig. 11, the eigenfrequencies are stable, except mode number 14 and 18 corresponding to hexadecapole modes. Mode number 14 has a maximum error of  $\approx 200\%$ . This fact alone indicates that the choice of 12 contour point for the parameter configuration of test case three is not recommended. Additionally, the corresponding relative residuals displayed in Fig. 12 increase. The residuals corresponding to the 36 and 48 point configurations are generally one order of magnitude larger compared to the other two test cases. An increase of two orders of magnitude compared to test case one occurs for the choice of 12 contour points, while the 24 point residuals even are four orders of magnitude higher.

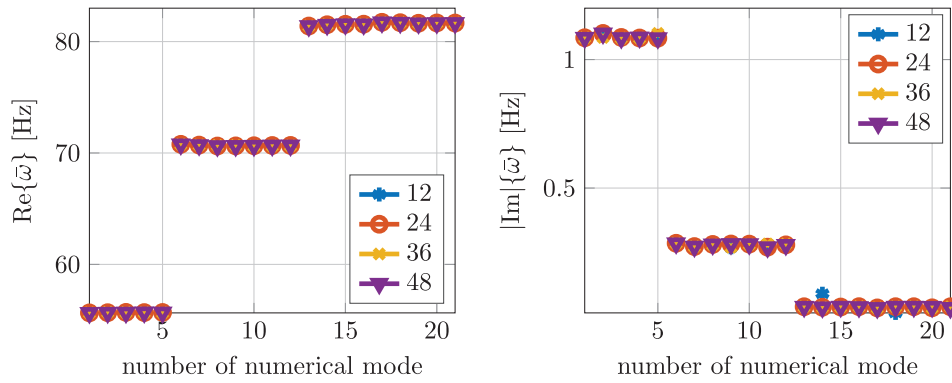


Fig. 11. Real and imaginary parts of the complex eigenfrequencies  $\bar{\omega}$  for the third test case ( $f_l = 35$  Hz,  $f_u = 100$  Hz, aspect ratio of 0.05,  $K = 5$ ,  $L = 16$ ). The results are obtained by using 12, 24, 36 and 48 contour points, respectively.

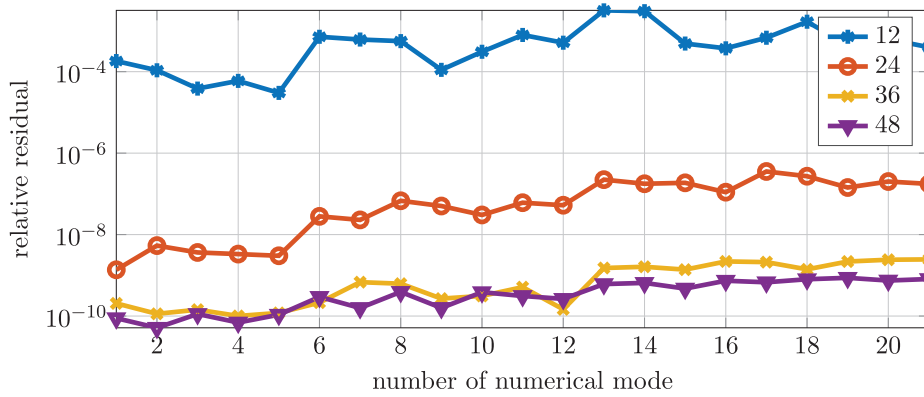


Fig. 12. Relative residuals for test case three ( $f_l = 35$  Hz,  $f_u = 100$  Hz, aspect ratio of 0.05,  $K = 5$ ,  $L = 16$ ), using 12, 24, 36 and 48 contour points, respectively.

Table 2. Computational time in computational time units [CTU] and sum over the relative residuals per test case — the subscript of  $C$  denotes the number of the case — presented for all four configurations of contour points (CPs).

Study 1	$t[\text{CTU}] (C_1)$	$t[\text{CTU}] (C_2)$	$t[\text{CTU}] (C_3)$	$\sum \epsilon_{\text{rel}} (C_1)$	$\sum \epsilon_{\text{rel}} (C_2)$	$\sum \epsilon_{\text{rel}} (C_3)$
12 CP	650	657	742	$1.452 \cdot 10^{-04}$	0.002	0.015
24 CP	1349	1303	1371	$2.451 \cdot 10^{-10}$	$7.147 \cdot 10^{-09}$	$2.172 \cdot 10^{-06}$
36 CP	1957	1965	2012	$1.368 \cdot 10^{-10}$	$1.545 \cdot 10^{-09}$	$2.070 \cdot 10^{-08}$
48 CP	2636	2616	2626	$1.216 \cdot 10^{-10}$	$5.609 \cdot 10^{-10}$	$8.759 \cdot 10^{-9}$

The results of study one in terms of the computational time and the sum over the relative residuals per test case and for all four configurations of contour points are shown in Table 2. Based on these results, all configurations with 12 contour points as well as test case three with 24 points turn out to be the least accurate. Particularly, test case three has the lowest accuracy but needs the most computational time. The second test case is a little less

accurate than the first one. Nevertheless, both need approximately the same computational time. In nearly every configuration, test case one turns out to be the best, since it achieves an accuracy of  $2.541 \cdot 10^{-10}$  at only 1349 CTU and 24 contour points, highlighted in Table 2. Thus, more accurate results are achieved, when the contour of the ellipse is minimized in its extent with respect to the sought eigenvalues.

Additionally, the relative error

$$e^i = \frac{|\bar{\omega}_a^i - \bar{\omega}^i|}{|\bar{\omega}_a^i|} \quad (3.4)$$

of the numerically obtained eigenvalues is defined as a function of the absolute values of the analytical eigenfrequencies and the computed ones. In Eq. (3.4),  $\bar{\omega}_a^i$  and  $\bar{\omega}^i$  denote the analytical and computed eigenfrequencies, respectively. The relative error for each eigenfrequency  $i$  is displayed in Fig. 13. The relative errors of all configurations of study one follow a similar pattern. The errors of the eigenfrequencies of the hexadecapole modes of  $\approx 1.28\%$  can be reduced by a mesh refinement. For comparison only, the errors of the eigenfrequencies of the octupole modes are  $\approx 0.17\%$ . For study one, a mesh with an outer radius of 15 m at six elements per wavelength is applied. The reason for the relatively high errors  $\approx 1.66\%$  of the first five eigenfrequencies is discussed later in this paper.

In a second study, the influence of the parameter  $K$  on the stability of the eigenfrequencies and on the relative residual are evaluated. Based on the results of the first study, the configuration of test case one with 24 contour points, as well as the same mesh is chosen here. The parameter  $K$  is varied from 2, 3, 4, ... to 10. Concerning the eigenfrequencies, all nine configurations lead to the exact same results. The relative residuals show a different behavior, though. As it can be seen in Fig. 14, the results for  $K = 2$  are about one order of magnitude larger than the others, which are all in a similar area. Hence, the choice of

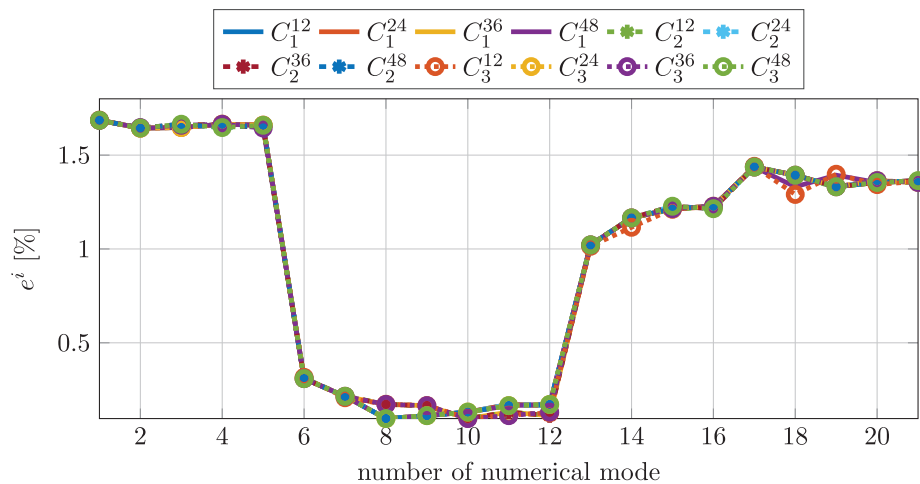


Fig. 13. The relative error of the individual eigenfrequencies with respect to the analytical solution is shown for all cases of study one. The subscript of  $C$  denotes the number of the test case of study one and the superscript stands for the number of contour points used.



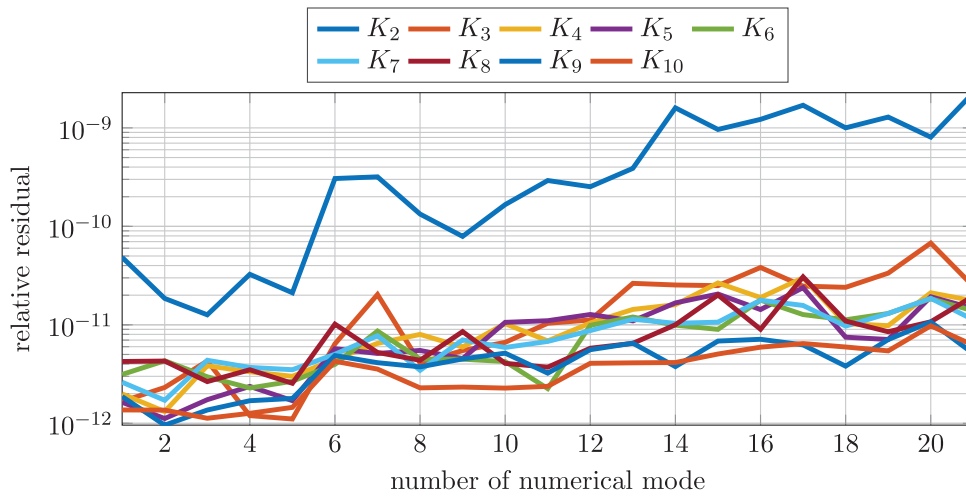


Fig. 14. Relative residuals for the second study with degree of moments  $K$  varying from  $K = 2$  to  $K = 10$ .

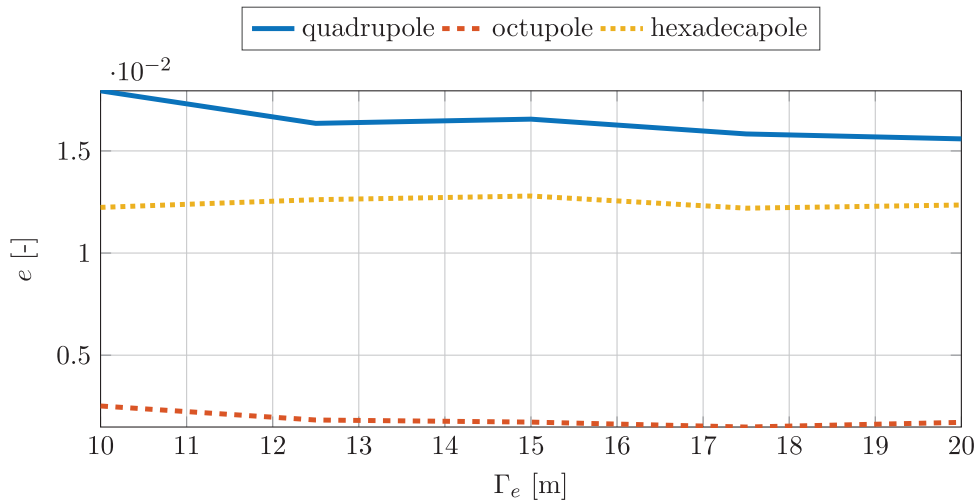


Fig. 15. (Color online) The average relative error of the quadrupole, the octupole and hexadecapole modes plotted as a function of the extent of the FE discretization in radial direction are depicted as a blue, red and yellow lines, respectively.

$K = 2$  is not recommended, whereas all other choices of  $K$  are suitable for this analysis. In a third study, the influence of the extent of the finite element discretization in radial direction on the accuracy of the solution is shown in Fig. 15. For this purpose, the average relative error is defined as

$$e = \frac{1}{N} \sum_{n=1}^N e^n, \tag{3.5}$$

where  $N$  are either the amount of quadrupole, octupole or hexadecapole modes. The average relative error for each group of modes is shown in Fig. 15. The average relative error associated to the hexadecapole modes remains unaffected by the extent of the finite element

fluid domain. The eigenfrequencies corresponding to the quadrupole and octupole modes exhibit convergence with an increasing radius of  $\Gamma_e$ .

In a final study, the performance of the CIM is compared to a second-order Krylov subspace method. The parameter configuration for the CIM is based on the results of the previous studies. For the reference solution via the second-order Krylov subspace method, a real-valued expansion point of 67 Hz is defined for the generation of the projection basis using the SOAR algorithm. The expansion point is chosen such that it lies within in the middle of the frequency range of sought eigenvalues. A reduced dimension of  $q = 320$  is chosen. At this order, all 21 eigenvalues can be found using *quadeig*. Any further increase in the reduced order does not lead to an improvement of the results.

Additionally, a reference solution using COMSOL Multiphysics is generated. COMSOL offers the computation of normal modes applying a perfectly matched layer at the outer boundary of the fluid domain. All three meshes for the finite element domains are identical. The radius of the fluid domain is set to 15 m. The finite element domain of the fluid is discretized using second-order Lagrange elements with a mesh size of 15 elements per wavelength. Eight-noded shell elements are selected for the discretization of the solid domain. The FEM-IFEM results in matrices with 311426 degrees of freedom. Examples of the mode shapes of the shell visualized via COMSOL are displayed in Fig. 16.

Furthermore, the eigenfrequencies and corresponding mode shapes of a steel shell surrounded by air are computed. Although, the real parts of the eigenfrequencies significantly increase, the imaginary parts of the quadrupole and octupole modes decrease, cf. Table 3. The mode shapes of the shell submerged in air are shown in Fig. 17. All three considered mode shapes do not change compared to the ones of the shell submerged in water.

The eigenfrequencies of the steel shell in a vacuum are discussed in the publication by Zheng *et al.*<sup>7</sup> The real parts of the vacuo eigenfrequencies of the sphere are similar to those in air. Hence, the air has a minor influence on the eigenfrequencies. The imaginary parts are solely existent for air but vanishing for vacuum. Based on the mode shapes remaining the same for air and water, it can be concluded that they are identical to the vacuo modes.

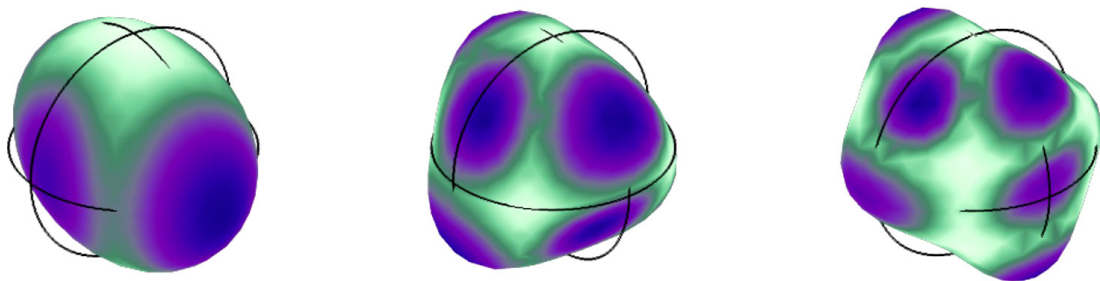


Fig. 16. A quadrupole mode is shown on the left, an octupole mode in the middle and a hexadecapole mode on the right. All three are visualized via COMSOL.

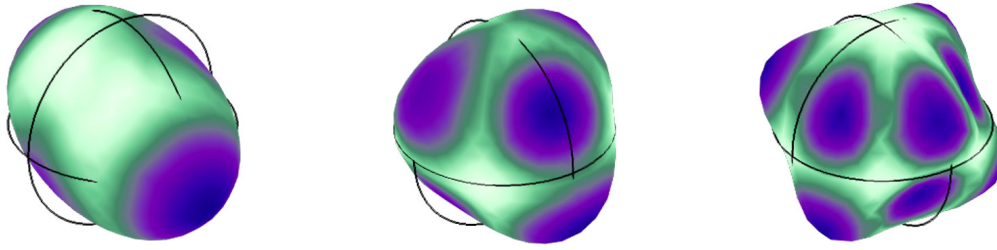


Fig. 17. A quadrupole mode is shown on the left, an octupole mode in the middle and a hexadecapole mode on the right. The fluid medium is changed from water to air, cf. Fig. 16. All three are visualized via COMSOL.

The analytical as well as the numerical eigenfrequencies are presented in Table 3. The different signs in the imaginary part of the FEM-IFEM formulation are due to the harmonic time dependency chosen.<sup>8</sup>

The relative errors of the eigenfrequencies computed using the CIM, the second-order Krylov subspace method and COMSOL are shown in Fig. 18.

Table 3. Analytical and numerical solutions of the quadratic EVP.

	Quadrupole	Octupole	Hexadecapole
Analytical	$56.0770 - 1.9267i$ [Hz]	$70.5598 - 0.2987i$ [Hz]	$80.5737 - 0.0294i$ [Hz]
CIM	$55.7423 + 1.1113i$ [Hz]	$70.2286 + 0.2639i$ [Hz]	$80.3822 + 0.0344i$ [Hz]
	$55.7111 + 1.1081i$ [Hz]	$70.2292 + 0.2663i$ [Hz]	$80.2849 + 0.0355i$ [Hz]
	$55.6851 + 1.1046i$ [Hz]	$70.2532 + 0.2744i$ [Hz]	$80.2998 + 0.0281i$ [Hz]
	$55.6528 + 1.0929i$ [Hz]	$70.2972 + 0.2752i$ [Hz]	$80.3143 + 0.0280i$ [Hz]
	$55.6636 + 1.0942i$ [Hz]	$70.2906 + 0.2761i$ [Hz]	$80.3359 + 0.0328i$ [Hz]
		$70.2835 + 0.2771i$ [Hz]	$80.3228 + 0.0352i$ [Hz]
		$70.2860 + 0.2749i$ [Hz]	$80.3288 + 0.0342i$ [Hz]
			$80.3281 + 0.0330i$ [Hz]
			$80.3261 + 0.0339i$ [Hz]
	Second Ord. Krylov	$55.6612 + 0.9055i$ [Hz]	$70.1376 + 0.1823i$ [Hz]
$55.5896 + 0.7343i$ [Hz]		$70.4211 + 0.1501i$ [Hz]	$80.4767 + 0.0286i$ [Hz]
$55.5125 + 0.9608i$ [Hz]		$70.4185 + 0.2091i$ [Hz]	$80.5730 + 0.0360i$ [Hz]
$55.3004 + 0.8779i$ [Hz]		$70.3142 + 0.1313i$ [Hz]	$80.5714 + 0.0090i$ [Hz]
$55.3183 + 0.8139i$ [Hz]		$70.2285 + 0.1515i$ [Hz]	$80.5241 + 0.0449i$ [Hz]
		$70.2335 + 0.1982i$ [Hz]	$80.5025 + 0.0187i$ [Hz]
		$70.2549 + 0.1884i$ [Hz]	$80.5440 + 0.0203i$ [Hz]
			$80.5156 + 0.0225i$ [Hz]
			$80.5335 + 0.0123i$ [Hz]
COMSOL PML		$56.3321 + 1.0755i$ [Hz]	$70.6765 + 0.2850i$ [Hz]
	$56.3353 + 1.0757i$ [Hz]	$70.6984 + 0.2855i$ [Hz]	$80.8659 + 0.0431i$ [Hz]
	$56.3369 + 1.0758i$ [Hz]	$70.7114 + 0.2858i$ [Hz]	$80.8685 + 0.0431i$ [Hz]
	$56.3375 + 1.0758i$ [Hz]	$70.7139 + 0.2858i$ [Hz]	$80.9061 + 0.0433i$ [Hz]
	$56.3423 + 1.0761i$ [Hz]	$70.7266 + 0.2861i$ [Hz]	$80.9180 + 0.0433i$ [Hz]
		$70.7294 + 0.2862i$ [Hz]	$80.9227 + 0.0433i$ [Hz]
		$70.7307 + 0.2862i$ [Hz]	$80.9326 + 0.0434i$ [Hz]
			$80.9479 + 0.0434i$ [Hz]
			$80.9555 + 0.0434i$ [Hz]

Table 3. (Continued)

	Quadrupole	Octupole	Hexadecapole
Peters <i>et al.</i>	55.84 – 1.18 <i>i</i> [Hz]	70.48 – 0.31 <i>i</i> [Hz]	80.59 – 0.042 <i>i</i> [Hz]
Air	120.8577 + 0.0576 <i>i</i> [Hz]	143.2180 + 0.1078 <i>i</i> [Hz]	152.2708 + 0.0631 <i>i</i> [Hz]
	120.8656 + 0.0507 <i>i</i> [Hz]	143.2224 + 0.0906 <i>i</i> [Hz]	152.3099 + 0.0708 <i>i</i> [Hz]
	120.8705 + 0.0528 <i>i</i> [Hz]	143.2969 + 0.0915 <i>i</i> [Hz]	152.3388 + 0.0685 <i>i</i> [Hz]
	120.8732 + 0.0512 <i>i</i> [Hz]	143.3150 + 0.1003 <i>i</i> [Hz]	152.3766 + 0.0651 <i>i</i> [Hz]
	120.8848 + 0.0529 <i>i</i> [Hz]	143.3431 + 0.0968 <i>i</i> [Hz]	152.3971 + 0.0625 <i>i</i> [Hz]
		143.3791 + 0.0924 <i>i</i> [Hz]	152.4851 + 0.0673 <i>i</i> [Hz]
		143.4104 + 0.0976 <i>i</i> [Hz]	152.5065 + 0.0632 <i>i</i> [Hz]
			152.5399 + 0.0664 <i>i</i> [Hz]
			152.6995 + 0.0648 <i>i</i> [Hz]

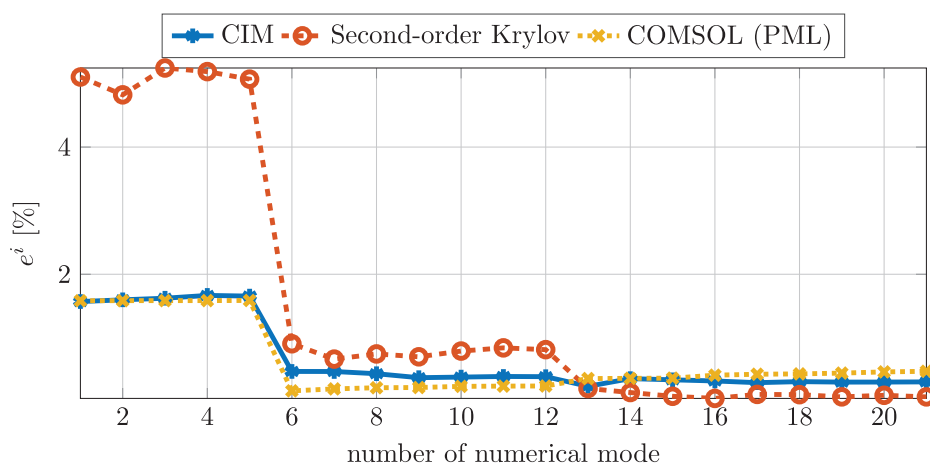


Fig. 18. Relative error of the individual eigenfrequencies computed employing the CIM, the second-order Krylov subspace method and COMSOL.

The performance of the CIM and COMSOL is about the same, with relative errors of maximum 0.47% for the eigenfrequencies of octupole and a maximum of 0.36% for those of the hexadecapole modes. The influence of the mesh refinement can be observed compared to Fig. 13 concerning the error decrease of the eigenfrequencies of the hexadecapole modes. However, the relative error associated with the second-order Krylov subspace method is higher for the eigenfrequencies of the octupole modes, with a maximum of 0.91%. The relative error of the hexadecapole modes is smallest, with a maximum of 0.2%, though. All eigenfrequencies show good accordance with respect to the analytical results, except for the imaginary parts of the complex eigenfrequencies belonging to the quadrupole modes. Particularly, the second-order Krylov subspace method gives results with a maximum error of  $\approx 5\%$ .

Additionally, a reference solution obtained by a coupled FEM-BEM simulation is presented to check, whether the FEM-BEM eigenfrequencies of the quadrupole modes also diverge from the analytical solution. The FEM-BEM reference solution was computed as

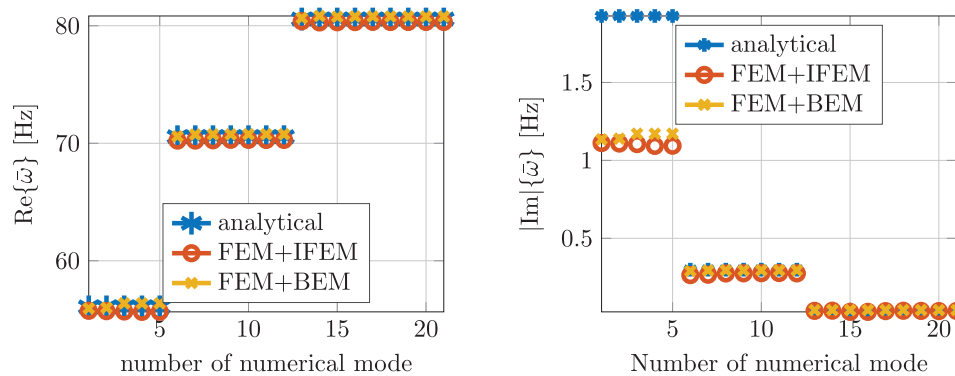


Fig. 19. (Color online) Real and imaginary parts of the complex eigenfrequencies  $\bar{\omega}$  obtained by the analytical expression (blue stars) as well as the results of the FEM-IFEM (red circles) and the FEM-BEM simulations (yellow crosses).

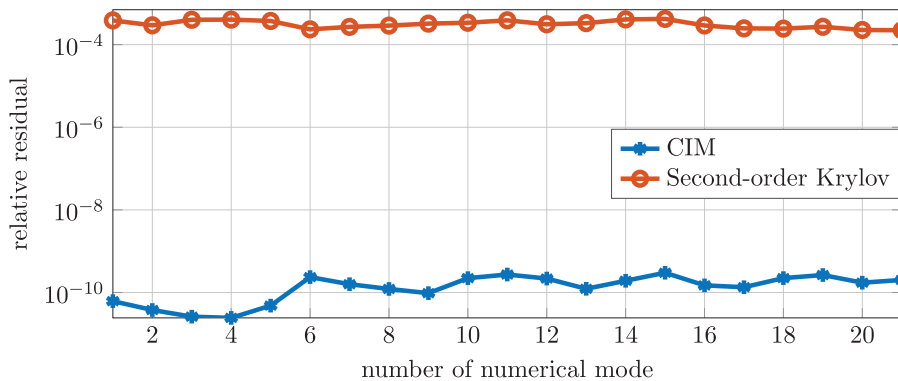


Fig. 20. (Color online) Relative residuals for results of the CIM (blue) and of the second-order Krylov subspace method (red).

described in the paper by Zheng *et al.*<sup>7</sup> Both the real and imaginary parts of the eigenfrequencies are shown in Fig. 19 for the analytical solutions as well as the solutions obtained by the CIM based on matrices generated by the FEM-IFEM and the FEM-BEM.

The FEM-BEM results show the same behavior as the FEM-IFEM ones, leading to a much lower imaginary part for quadrupole modes. Similar results are presented in the paper by Peters *et al.*,<sup>6</sup> also shown in Table 3. The presumed cause of the variances of the imaginary parts of the quadrupole modes is the use of eight-noded shell elements that introduce an error associated with the discretization of the sphere.

Figure 20 shows the relative residuals of the CIM and of the second-order Krylov subspace method. The former are in the order of magnitude of  $\approx 1 \cdot 10^{-10}$ , whereas the latter achieves a minimum of greater-than  $1 \cdot 10^{-4}$ .

#### 4. Conclusion and Outlook

A numerical framework based on a CIM and a FEM-IFEM formulation for modal analysis of acoustic-structure interaction has been presented and applied to a benchmark problem

of a submerged spherical shell. The accuracy of the proposed framework has been assessed based on relative errors in the eigenfrequencies with respect to an analytical expression as well as based on the relative residuals of the computed eigenpairs.

Extensive studies on the influence of the CIM parameters on the accuracy of the eigen-solution have been presented. While all eigenvalues of interest have been found regardless of the chosen parameters of CIM, an appropriate choice of the contour is crucial to obtain small relative residuals. In general, the elliptic contour should tightly enclose the eigenvalues of interest in order to enable an accurate projection with only a few contour points. The degree of resolvent moments should be large enough such that the dimension of the resulting subspace is larger than the number of expected eigenvalues. In our test cases, large values for the degree did not deteriorate the results. Finally, a sufficiently accurate discretization of the acoustic finite element domain in radial direction is crucial in order to capture the modes of interest. Furthermore, the accuracy of CIM has been compared to the solution of the same FEM-IFEM EVP by a Rayleigh Ritz procedure with second-order Krylov subspaces. While requiring a similar numerical effort, CIM achieves relative residuals that are several orders of magnitudes smaller. Finally, the eigenfrequencies obtained by FEM-IFEM were compared to those obtained by discretizations with FEM-BEM as well as FEM in conjunction with PML, showing good agreement throughout.

The advantage of CIMs lies in its capability to restrict the spectrum of the problem to a predefined region in the complex plane. Additionally, it admits parallelization of the problem at multiple levels: The evaluation of matrix vector products, the computations for each contour point, and even evaluations of several elliptic contours covering a large frequency range can be conducted in parallel. The CIM is a direct method which solves simultaneously for all eigenvalues of interest. In contrast to that, iterative schemes such as shift-and-invert methods typically only solve for a single eigenvalue at time, and hence, are executed sequentially in order to avoid repeated evaluation of the same eigenvalue.

Possible applications of modal analyses of fluid-loaded structures include the design of acoustic metamaterials, where the vibration of the structure affects the acoustic behavior. The performance of most metamaterials are connected to low damped eigenvalues leading to band gap-like behavior. The fluid-loaded structural modes of meta-atoms and finite meta-structures can be studied using the FEM-IFEM formulation. For infinite, periodic metamaterials, this paper approach can be extended by applying Floquet–Bloch boundary conditions.

## **Acknowledgments**

The contribution of S. K. Baydoun to this work was supported by the German Research Foundation (DFG) in the context of the priority program 1897 “Calm, Smooth and Smart — Novel Approaches for Influencing Vibrations by Means of Deliberately Introduced Dissipation.”

## References

1. U. Hetmaniuk, R. Tezaur and C. Farhat, Review and assessment of interpolatory model order reduction methods for frequency response structural dynamics and acoustics problems, *Int. J. Numer. Meth. Eng.* **90**(13) (2012) 1636–1662, <https://doi.org/10.1002/nme.4271>.
2. S. Van Ophem, E. Deckers and W. Desmet, Model based virtual intensity measurements for exterior vibro-acoustic radiation, *Mech. Syst. Signal Process.* **134** (2019) 106315, <https://doi.org/10.1016/j.ymssp.2019.106315>.
3. S. van Ophem, O. Atak, E. Deckers and W. Desmet, Stable model order reduction for time-domain exterior vibro-acoustic finite element simulations, *Comput. Methods Appl. Mech. Eng.* **325** (2017), <https://doi.org/10.1016/j.cma.2017.06.022>.
4. T. Liang, J. Wang, J. Xiao and L. Wen, Coupled BEFE based vibroacoustic modal analysis and frequency sweep using a generalized resolvent sampling method, *Comput. Methods Appl. Mech. Eng.* **345** (2019) 518–538, <https://doi.org/10.1016/j.cma.2018.09.038>.
5. S. K. Baydoun, M. Voigt, C. Jelic and S. Marburg, A greedy reduced basis scheme for multifrequency solution of structural acoustic systems, *Int. J. Numer. Meth. Eng.* **121**(2) (2020) 187–200, <https://doi.org/10.1002/nme.6205>.
6. H. Peters, N. Kessissoglou and S. Marburg, Modal decomposition of exterior acoustic-structure interaction, *J. Acoust. Soc. Am.* **133**(5) (2013) 2668–2677, <https://doi.org/10.1121/1.4796114>.
7. C.-J. Zheng, C.-X. Bi, C. Zhang, H.-F. Gao and H. Chen, Free vibration analysis of elastic structures submerged in an infinite or semi-infinite fluid domain by means of a coupled FE-BE solver, *J. Comput. Phys.* **359** (2018) 183–198, <https://doi.org/10.1016/j.jcp.2018.01.018>.
8. S. Marburg, F. Dienerowitz, T. Horst and S. Schneider, Normal modes in external acoustics. Part II: Eigenvalues and Eigenvectors in 2d, *Acta Acust. United Acust.* **92**(1) (2006) 97–111.
9. S. Marburg, Normal modes in external acoustics. Part III: Sound power evaluation based on frequency-independent superposition of modes, *Acta Acust. United Acust.* **92**(2) (2006) 296–311.
10. S. Fuß, S. C. Hawkins and S. Marburg, An eigenvalue search algorithm for modal analysis of a resonator in free space, *J. Comput. Acoust.* **19**(1) (2011) 95–109, <https://doi.org/10.1142/S0218396X11004304>.
11. L. Moheit and S. Marburg, Normal modes and modal reduction in exterior acoustics, *J. Theor. Comput. Acoust.* **26**(3) (2018) 1850029, <https://doi.org/10.1142/S2591728518500299>.
12. F. Tisseur and K. Meerbergen, The quadratic eigenvalue problem, *SIAM Rev.* **43**(2) (2001) 235–286, <https://doi.org/10.1137/S0036144500381988>.
13. Z. Bai and Y. Su, SOAR: A second-order arnoldi method for the solution of the quadratic eigenvalue problem, *SIAM J. Matrix Anal. Appl.* **26** (2005) 640–659, <https://doi.org/10.1137/S0895479803438523>.
14. S. Hammarling, C. Munro and F. Tisseur, An algorithm for the complete solution of quadratic eigenvalue problems, *ACM Trans. Math. Softw.* **39** (2013), <https://doi.org/10.1145/2450153.2450156>.
15. D. P. Elford, L. Chalmers, F. V. Kusmartsev and G. M. Swallowe, Matryoshka locally resonant sonic crystal, *J. Acoust. Soc. Am.* **130**(5) (2011) 2746–2755, <https://doi.org/10.1121/1.3643818>.
16. F. Maurin, C. Claeys, E. Deckers and W. Desmet, Probability that a band-gap extremum is located on the irreducible Brillouin-zone contour for the 17 different plane crystallographic lattices, *Int. J. Solids Struct.* **135** (2018) 26–36, <https://doi.org/10.1016/j.ijsolstr.2017.11.006>.
17. S. M. B. Fard, H. Peters, N. Kessissoglou and S. Marburg, Three-dimensional analysis of a noise barrier using a quasi-periodic boundary element method, *J. Acoust. Soc. Am.*, **137**(6) (2015) 3107–3114, <https://doi.org/10.1121/1.4921266>.

18. H. Ziegelwanger, P. Reiter and M. Conter, The three-dimensional quasi-periodic boundary element method: Implementation, evaluation, and use cases, *Int. J. Comput. Methods Exper. Measure.* **5**(3) (2017) 404–414, <http://doi.org/10.2495/CMEM-V5-N3-404-414>.
19. S. Schot, Eighty years of Sommerfeld's radiation condition, *Hist. Math.* **19**(4) (1992) 385–401, [https://doi.org/10.1016/0315-0860\(92\)90004-U](https://doi.org/10.1016/0315-0860(92)90004-U).
20. F. Ihlenburg, *Finite Element Analysis of Acoustic Scattering* (Springer-Verlag, New York, 1998), <https://doi.org/10.1007/b98828>.
21. M. Kaltenbacher, *Numerical Simulation of Mechatronic Sensors and Actuators* (Springer-Verlag, Berlin, Heidelberg, 2015), <https://doi.org/10.1007/978-3-540-71360-9>.
22. S. Marburg and B. Nolte, *Computational Acoustics of Noise Propagation in Fluids — Finite and Boundary Element Methods* (Springer-Verlag, Berlin, Heidelberg, Germany, 2008), <https://doi.org/10.1007/978-3-540-77448-8>.
23. J. J. Shirron and I. Babuka, A comparison of approximate boundary conditions and infinite element methods for exterior Helmholtz problems, *Comput. Methods Appl. Mech. Eng.* **164**(1–2) (1998) 121–139, [https://doi.org/10.1016/S0045-7825\(98\)00050-4](https://doi.org/10.1016/S0045-7825(98)00050-4).
24. R. J. Astley, Mapped spheroidal wave-envelope elements for unbounded wave problems, *Int. J. Numer. Meth. Eng.* **41** (1998) 1235–1254, [https://doi.org/10.1002/\(SICI\)1097-0207\(19980415\)41:7<1235::AID-NME331>3.0.CO;2-V](https://doi.org/10.1002/(SICI)1097-0207(19980415)41:7<1235::AID-NME331>3.0.CO;2-V).
25. R. J. Astley, G. J. Macaulay, J.-P. Coyette and L. Cremers, Three-dimensional wave-envelope elements of variable order for acoustic radiation and scattering. Part I. Formulation in the frequency domain, *J. Acoust. Soc. Am.* **103** (1998) 49–63, <https://doi.org/10.1121/1.421106>.
26. R. J. Astley, G. J. Macaulay and J. P. Coyette, Mapped wave envelope elements for acoustical radiation and scattering, *J. Sound Vib.* **170**(1) (1994) 97–118, <https://doi.org/10.1006/jsvi.1994.1048>.
27. L. Moheit, S. Anthis, J. Heinz, F. Kronowetter and S. Marburg, Analysis of scattering by finite sonic crystals in free field with infinite elements and normal modes, *J. Sound Vib.* (2020) 115291, <https://doi.org/10.1016/j.jsv.2020.115291>.
28. R. J. Astley, Infinite elements for wave problems: A review of current formulations and an assessment of accuracy, *Int. J. Numer. Meth. Eng.* **49** (2000) 951–976, [https://doi.org/10.1002/1097-0207\(20001110\)49:7<951::AID-NME989>3.0.CO;2-T](https://doi.org/10.1002/1097-0207(20001110)49:7<951::AID-NME989>3.0.CO;2-T).
29. C. H. Wilcox, A generalisation of theorems of Rellich and Atkinson, *Proc. Amer. Math. Soc.* **7** (1956) 271–276.
30. J. W. S. Rayleigh, *Theory of Sound (two volumes)* (Dover Publications, New York, 1945).
31. S. K. Baydoun and S. Marburg, Investigation of radiation damping in sandwich structures using finite and boundary element methods and a nonlinear eigensolver, *J. Acoust. Soc. Amer.* **147**(3) (2020) 2020–2034, <https://doi.org/10.1121/10.0000947>.
32. H. Peters, N. Kessissoglou and S. Marburg, Modal decomposition of exterior acoustic-structure interaction problems with model order reduction, *J. Acoust. Soc. Amer.* **135**(5) (2014) 2706–2717, <https://doi.org/10.1121/1.4869086>.
33. M. El-Guide, A. Miedlar and Y. Saad, A rational approximation method for solving acoustic nonlinear eigenvalue problems, *Eng. Anal. Bound. Elem.* **111** (2020) 44–54, <https://doi.org/10.1016/j.enganabound.2019.10.006>.
34. J. Asakura, T. Sakurai, H. Tadano, T. Ikegami and K. Kimura, A numerical method for nonlinear eigenvalue problems using contour integrals, *JSIAM Lett.* **1** (2009) 52–55, <https://doi.org/10.14495/jsiaml.1.52>.
35. S. Yokota and T. Sakurai, A projection method for nonlinear eigenvalue problems using contour integrals, *JSIAM Lett.* **5** (2013) 41–44, <https://doi.org/10.14495/jsiaml.5.41>.
36. W.-J. Beyn, An integral method for solving nonlinear eigenvalue problems, *Linear Algebra Appl.* **436**(10) (2012) 3839–3863, <https://doi.org/10.1016/j.laa.2011.03.030>.





37. T. Sakurai, Y. Futamura and H. Tadano, Efficient parameter estimation and implementation of a contour integral-based eigensolver, *J. Algorithms Comput. Technol.* **7**(3) (2013) 249–270, <https://doi.org/10.1260/1748-3018.7.3.249>.
38. Z. Bai and Y. Su, Dimension reduction of large-scale second-order dynamical systems via a second-order Arnoldi method, *SIAM J. Sci. Comput.* **26**(5) (2005) 1692–1709, <https://doi.org/10.1137/040605552>.
39. M. C. Junger and D. Feit, *Sound, Structures, and Their Interaction*, 2nd edn. (MIT Press, Cambridge, Massachusetts, London, England, 1986), <https://doi.org/10.1121/1.395243>.

### **5.3 Publication AP3**

AUGUST 11 2023

# Sound attenuation enhancement of acoustic meta-atoms via coupling

Felix Kronowetter ; Lisa Pretsch; Yan Kei Chiang; Anton Melnikov; Shahrokh Sepehrihnama; Sebastian Oberst; David A. Powell; Steffen Marburg 



*J. Acoust. Soc. Am.* 154, 842–851 (2023)

<https://doi.org/10.1121/10.0020570>



View  
Online



Export  
Citation

CrossMark

## Related Content

Measuring monopole and dipole polarizability of acoustic meta-atoms

*Appl. Phys. Lett.* (November 2018)

Geometry meta-optimization

*J. Chem. Phys.* (April 2022)

An effective theory for meta-mass and meta-material mechanical/electrical devices

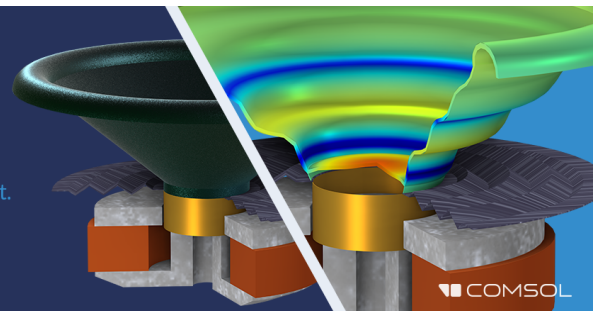
*J Acoust Soc Am* (November 2013)

11 September 2023 06:48:11

## Take the Lead in Acoustics



The ability to account for coupled physics phenomena lets you predict, optimize, and virtually test a design under real-world conditions – even before a first prototype is built.

» Learn more about COMSOL Multiphysics®



COMSOL

## Sound attenuation enhancement of acoustic meta-atoms via coupling<sup>a)</sup>

Felix Kronowetter,<sup>1,b)</sup>  Lisa Pretsch,<sup>2</sup> Yan Kei Chiang,<sup>3</sup> Anton Melnikov,<sup>4</sup> Shahrokh Sepehrihahnama,<sup>5</sup> Sebastian Oberst,<sup>5</sup> David A. Powell,<sup>3</sup> and Steffen Marburg<sup>1</sup> 

<sup>1</sup>Chair of Vibro-Acoustics of Vehicles and Machines, Department of Engineering Physics and Computation, Technical University of Munich, TUM School of Engineering and Design, Munich, Germany

<sup>2</sup>Associate Professorship of Computational Solid Mechanics, Department of Engineering Physics and Computation, Technical University of Munich, TUM School of Engineering and Design, Munich, Germany

<sup>3</sup>School of Engineering and Information Technology, University of New South Wales, Northcott Drive, Canberra, Australian Capital Territory 2600, Australia

<sup>4</sup>Bosch Sensortec, Dresden, Germany

<sup>5</sup>School of Mechanical and Mechatronic Engineering, Centre for Audio, Acoustics and Vibration, Faculty of Engineering and IT, University of Technology Sydney, Sydney, Australia

### ABSTRACT:

Arrangements of acoustic meta-atoms, better known as acoustic metamaterials, are commonly applied in acoustic cloaking, for the attenuation of acoustic fields or for acoustic focusing. A precise design of single meta-atoms is required for these purposes. Understanding the details of their interaction allows improvement of the collective performance of the meta-atoms as a system, for example, in sound attenuation. Destructive interference of their scattered fields, for example, can be mitigated by adjusting the coupling or tuning of individual meta-atoms. Comprehensive numerical studies of various configurations of a resonator pair show that the coupling can lead to degenerate modes at periodic distances between the resonators. We show how the resonators' separation and relative orientation influence the coupling and thereby tunes the sound attenuation. The simulation results are supported by experiments using a two-dimensional parallel-plate waveguide. It is shown that coupling parameters like distance, orientation, detuning, and radiation loss provide additional degrees of freedom for efficient acoustic meta-atom tuning to achieve unprecedented interactions with excellent sound attenuation properties.

© 2023 Author(s). All article content, except where otherwise noted, is licensed under a Creative Commons Attribution (CC BY) license (<http://creativecommons.org/licenses/by/4.0/>). <https://doi.org/10.1121/10.0020570>

(Received 17 March 2023; revised 5 June 2023; accepted 20 July 2023; published online 11 August 2023)

[Editor: Nicole Kessissoglou]

Pages: 842–851

### I. INTRODUCTION

Acoustic metamaterials are artificial structures consisting of an arrangement of meta-atoms that can be used to control or manipulate the propagation of sound and elastic waves due to their exotic behavior (Cummer *et al.*, 2016; Deymier, 2013; Ma and Sheng, 2016; Zangeneh-Nejad and Fleury, 2019). The operating principle of meta-atoms is mostly based on local resonances leading to, for example, a negative effective mass density (Milton and Willis, 2007; Yao *et al.*, 2008), negative bulk modulus (Fang *et al.*, 2006), or negative refractive index (Pendry, 2000). Since meta-atoms are typically arranged close to each other, i.e., less than their operating wavelength, interaction such as longitudinal near-field coupling (Wang and Laude, 2017) and transverse coupling (Fu *et al.*, 2011) occur. In the context of the acoustics of a lossless medium, there is only pressure coupling. Such coupling and associated parameters can provide

additional degrees of freedom to tune the system, e.g., to enhance sound transmission (Yang *et al.*, 2015).

Coupling effects have been applied for the tuning of electro-magnetic metamaterials (Pendry *et al.*, 2006; Schurig *et al.*, 2006; Valentine *et al.*, 2009). Keiser *et al.* (2013) employed near-field interaction phenomena in the design of electro-magnetic metamaterials. Coupling between electro-magnetic metamaterial elements can have a significant impact on the behavior of the material as a whole (Liu *et al.*, 2009a). Especially for very closely arranged elements, it is no longer adequate to solely consider the averaged effect of the uncoupled resonators. Instead of treating the metamaterial as a continuous effective medium, the near-field interaction phenomena have to be considered. These phenomena give rise to various applications, like frequency tunable and broad bandwidth metamaterials (Keiser *et al.*, 2013; Liu *et al.*, 2009a). Powell *et al.* (2010) investigated the near-field interaction between split-ring resonators (SRRs) as resonant structures of a metamaterial. They found that modifications of the structures' relative orientation and separation affected the near-field interaction. Thereby, the metamaterial response can be tuned. In a subsequent paper, Powell *et al.* (2011)

<sup>a)</sup>This paper is part of a special issue on wave phenomena in periodic, near-periodic, and locally resonant systems.

<sup>b)</sup>Electronic mail: felix.kronowetter@tum.de

examined the linear near-field interaction of a pair of SRRs on the same axis with varying relative angle and observed a crossing point between the symmetric and antisymmetric mode in the dispersion curve. The analysis of the (anti-)crossing behavior is based on the mode coupling model presented by [Yakovlev and Hanson \(2000\)](#). Studying a similar system, [Liu et al. \(2009b\)](#) found that with increasing twist angle the resonant modes converge, pass through an avoided crossing, and then diverge again. The acoustic counterpart to SRRs is Helmholtz resonators ([Movchan and Guenneau, 2004](#)).

Analogous coupling effects can be found in acoustics, more precisely, in the analysis of organ pipes. Existing studies on the interaction of organ pipes contribute useful findings that can be adapted to locally resonant structures. Two organ pipes sound in unison when close together, even if their natural frequencies differ slightly ([Strutt, 2011](#)). [Fischer et al. \(2016\)](#) investigated the mutual interaction of a pair of organ pipes experimentally and analytically. [Sawicki et al. \(2018\)](#) examined the effect of separation and frequency detuning of two coupled organ pipes on their synchronization behavior. [Pikovskiy et al. \(2001\)](#) give a summary of the nonlinear principle of synchronization with applications in diverse fields of science, like engineering, biology, and social behavior. Although synchronization is based on non-linear effects, analogies can be extracted to explain the degeneracy of modes. With the aim to understand the interaction between close organ pipes, [Johansson and Kleiner \(2001\)](#) investigated the coupling effects of two Helmholtz resonators. They argue that the coupling mechanisms of organ pipes and Helmholtz resonators resemble each other. Despite different working principles, simple Helmholtz resonators thus present a good approximation for more complex organ pipes. Two Helmholtz resonators can be coupled via the surrounding air by bringing them close together.

Various studies on coupling of acoustic resonators in waveguides ([Al Jahdali and Wu, 2018](#); [Herrero-Durá et al., 2020](#); [Wang and Laude, 2017](#); [Zhou et al., 2018](#)) have been reported. Recent publications ([Cavaliere et al., 2019](#); [Krasikova et al., 2022](#); [Lee and Iizuka, 2019](#)) apply coupling to acoustic metamaterials, whereby the interaction of local resonances within a unit cell—in a subwavelength region—is considered. [Cavaliere et al. \(2019\)](#) demonstrate that the combination of local resonators of different types combined with the periodicity of the system can lead to multiple coupled resonances to achieve broadband acoustic attenuation. The interaction of local resonances and Bragg scattering are investigated by [Lee and Iizuka \(2019\)](#). [Krasikova et al. \(2023\)](#) investigate the strong coupling between pairs of resonators within a unit cell and their influence on the dispersion curves and the transmission spectrum. Additionally, coupling is used for tuning acoustic lenses ([Yang et al., 2015](#)) and metagratings ([Dong et al., 2017](#)).

In this article, we investigate coupling of two C-shaped meta-atoms in a two-dimensional unbounded domain. Since almost all acoustic metamaterials can be thought of as arrayed coupled resonators, we refer to them as meta-atoms, even if

we consider only two of them ([Belacel et al., 2017](#); [Wu et al., 2017](#)). Coupling between meta-atoms affects the total performance of periodic structures shown by [Krasikova et al. \(2023\)](#). The modal behavior of the system for varying parameters, like distance, orientation, detuning, and radiation losses, is studied. Fundamental effects are explained for a better understanding of the coupling mechanisms. We demonstrate how the sound attenuation of meta-atoms can be improved and adjusted using orientation and positioning as tunable parameters. In addition, we detune the resonance frequency of one of the resonators and present how the detuning affects the modal behavior. Furthermore, we show how increased radiation losses can counteract detuning concerning the interaction of the eigenfrequencies of the system. The numerical results are validated by experiments. A two-dimensional parallel-plate waveguide ([Melnikov et al., 2019](#)) is used for the evaluation of sound pressure fields of the acoustic meta-atoms. We demonstrate how coupling affects the performance of local resonances in terms of sound attenuation and hence, can provide an improved design of acoustic metamaterials.

## II. NUMERICAL MODEL

Figure 1(a) shows the configuration of a pair of two-dimensional C-shaped Helmholtz resonators ([Chalmers et al., 2009](#); [Elford et al., 2011](#)), within a rectangular acoustic domain surrounded by a perfectly matched layer. The rectangular domain with absorbing boundaries is chosen such that it resembles the waveguide used for experiments hereinafter presented. We denote the C-shapes' inner radius  $r = 6$  mm, the aperture width  $w = 4$  mm, and the thickness  $t = 16$  mm. The choice of the geometric dimensions of the C-shape depends on the following factors: the walls of the C-shape must be thick enough to be considered sound hard. We choose a wall thickness of 16 mm based on our experience from previous measurements. Furthermore, the eigenfrequencies of our system are determined by the dimensions and thus, the measurable frequency range (1000–2400 Hz) of the waveguide used in our experimental setup. The chosen aperture width of 6 mm is large compared to the expected boundary layer thickness of  $\delta_\eta = \sqrt{2\eta/\rho_m\omega} \approx 0.05$  mm following the formulations in the book by [Dukhin and Goetz \(2002\)](#); nevertheless, we consider thermo-viscous losses in our simulations. Thermo-viscous boundary layer losses are significant for structures with narrow geometry features ([Jiang et al., 2017](#); [Jordaan et al., 2018](#)). The inter-resonator distance is denoted  $l$  and is measured from the exterior of each resonator. Initially, both apertures face  $\Gamma_i$  with  $\alpha = 90^\circ$ . All studies in this section are conducted as finite element simulations in COMSOL Multiphysics (COMSOL Inc., 2021), first in the form of modal analyses, then by the transmission response for harmonic excitation through a plane wave. The modal analysis of a single C-shape results in the complex individual eigenfrequency  $f_c = 1960 + 82i$  Hz. The real part of the complex eigenfrequencies  $f_c = f + i\gamma$  is the resonant frequency  $f$ ; the imaginary part  $\gamma$  characterizes the radiation loss ([Baydoun and Marburg, 2020](#);

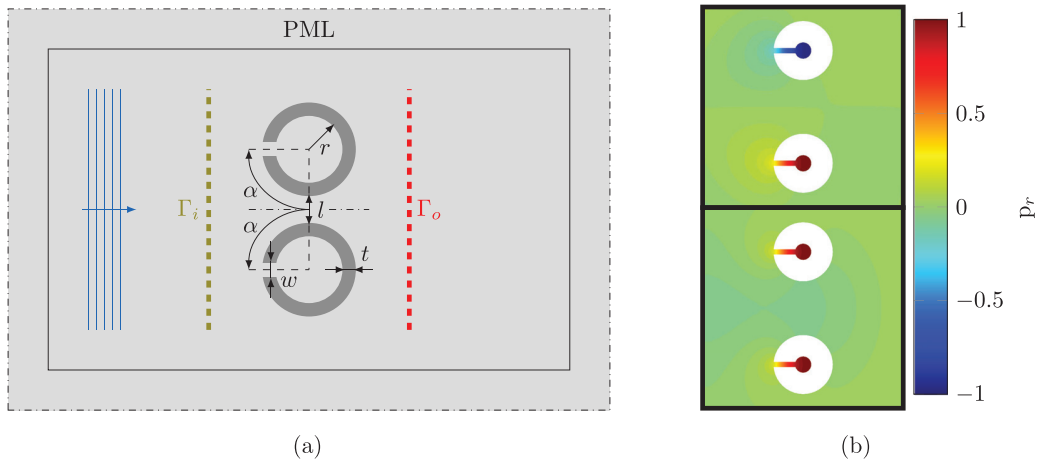


FIG. 1. (Color online) (a) Numerical setup. The schematic of the resonator pair geometry and dimensions, specified by inner radius  $r$ , aperture width  $w$ , wall thickness  $t$ , and inter-resonator distance  $l$  in a two-dimensional unbounded fluid domain are shown.  $\Gamma_i$  and  $\Gamma_o$  define the integration lines for calculating the transmitted sound power. (b) Cavity resonant modes. The symmetric mode (lower) termed as mode  $S$  and antisymmetric mode (upper) termed as mode  $AS$ , where  $p_r$  denotes the real part of the total pressure normalized to its maximum value.

Kronowetter *et al.*, 2020). Furthermore, the symmetric and antisymmetric cavity resonant modes, exhibiting in- and anti-phase oscillation of the two resonators, are depicted in Fig. 1(b). The cavity resonant modes are identified as the two modes with the highest quality factors ( $Q = f/2|\gamma|$ ). The corresponding cavity resonant frequencies will be discussed in the following section. In addition, we use the integration lines for the transmission response evaluation at  $\Gamma_i$  and  $\Gamma_o$ . Their positions are chosen such that they match the experimental microphone locations.

### III. RESULTS

#### A. Inter-resonator distance

The first influence parameter to be examined is the distance  $l$  between two identical resonators, varied from

$l = 2 \text{ mm}$  to  $l = 300 \text{ mm}$ . Figures 2(a) and 2(b) show the real and imaginary parts of the complex eigenfrequencies  $f_c$  associated with cavity resonance as a function of  $l$ . The real parts of the eigenfrequencies associated with cavity resonance oscillate around a reference frequency of  $f = 1960 \text{ Hz}$ . The oscillation period matches the resonant wavelength  $\lambda = 175 \text{ mm}$ , similar to the Fabry-Pérot interference observed by Hein *et al.* (2012) for duct-cavity systems. Thus, the two modes cross at periodic distances of  $\Delta l = \lambda/2$ . The crossing points of real parts [Fig. 2(a)] and imaginary parts [Fig. 2(b)] are shifted by about a quarter wavelength. Consequently, the imaginary parts split where the real parts cross and *vice versa*. The mode with the smaller imaginary part  $\gamma$  has increased lifetime and dominates the decay process in the time domain, whereas it leads to a higher sound attenuation in the frequency domain.

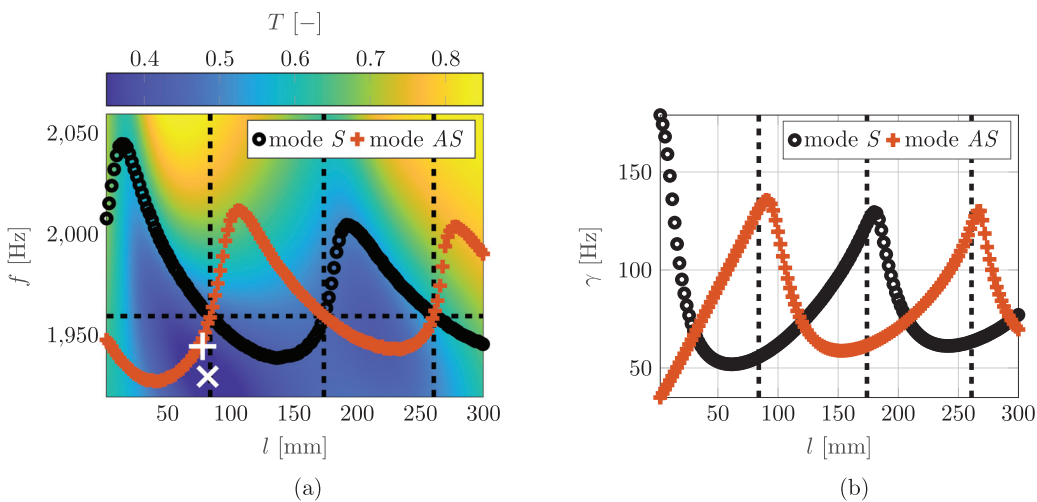


FIG. 2. (Color online) (a) Real and (b) imaginary parts of the complex eigenfrequencies  $f_c$  associated with cavity resonance as a function of the inter-resonator distance  $l$  (mm). The dashed black lines indicate the distances of the modal crossings and modal (anti-) crossings. The color bar represents the values of the transmission efficiency  $T$  (-). The white plus sign (lossless) and white cross (including thermo-viscous losses) mark the points where the transmission efficiencies reach their minima.

The phase difference between resonators is  $\Delta\Theta = \pm\pi$  for the antisymmetric mode and zero for the symmetric mode, independent of the inter-resonator distance.

Based on the modal analysis, the highest attenuation of an incident sound wave is expected at the crossing points of in- and anti-phase modes. On the one hand, the dominant mode—the mode with the lowest imaginary part—has the highest quality factor just below the degeneracy, which is the reason for the minimum in the transmission spectrum. On the other hand, detuning decreases the quality factor of the dominant mode. We can say that the modal degeneracy is a prerequisite for particularly high transmission minima and thus for increased local energy trapping. Figure 2(a) shows the transmission efficiency  $T = P_o/P_i$ —where  $P_o$  is the total transmitted sound power evaluated at  $\Gamma_o$  and  $P_i$  is the power of the incident wave evaluated at  $\Gamma_i$ —as a function of separation  $l$  and frequency  $f$  of the incident plane wave, including thermo-viscous losses.

The drops in the transmitted sound power are located around every second modal crossing point and extend along the frequency of the descending mode. This means that the attenuation reaches its maximum where the symmetric mode dominates. In the regions with dominating antisymmetric mode, transmitted sound power does not decrease. Sawicki *et al.* (2018) show in case of organ pipes that for zero detuning, the in-phase mode ( $\Delta\theta = 0$ ) corresponds to enhancement and the anti-phase mode ( $\Delta\theta = \pi$ ) corresponds to a cancellation of sound. We can see that the white plus sign in Fig. 2(a) is shifted from  $l = 78$  mm and  $f = 1945$  Hz to the white cross at  $l = 82$  mm and  $f = 1930$  Hz just by considering losses. Hence, losses lead to a frequency and distance shift of the minimum transmitted sound power and are considered in the following time harmonic studies.

The reason for the drop in the transmitted sound power at modal crossing points with the dominant symmetric mode is

the different coupling between the two modes and the incident plane wave. Modal degeneracy means that any superposition of the two interacting modes will have the same resonant dynamic behavior. In the present configuration, the symmetric mode dominates because both resonators are excited in phase by a plane wave that is normally incident on them. When the angle of incidence is changed by  $90^\circ$  with respect to the initial configuration in Fig. 1(a), there is a slight decrease in the transmitted sound power for the dominant antisymmetric mode. The coupled modes of the system are always linked. In particular, the minimum decay of the symmetric mode occurs near the degeneracy, and also near the maximum decay of the antisymmetric mode.

### B. Relative orientation

The second influence factor to be examined is the C-shapes' relative orientation. It is known to be relevant in electromagnetic metamaterials, as shown by the findings of Powell *et al.* (2011). In addition, earlier research results by Powell *et al.* (2010) and Hesmer *et al.* (2007) suggest that the relative orientation plays a major role for the coupling of SRRs. It may therefore also be of importance for the acoustic counterpart. Starting with facing apertures for zero twist angle  $\alpha = 0^\circ$ , the two C-shapes are rotated in opposite directions and reach the configuration in Fig. 1(a) for  $\alpha = 90^\circ$ . A maximum twist angle of  $\alpha = 180^\circ$  implies that the two apertures are pointing away from each other.

Figure 3(a) shows the absolute difference between the cavity resonant frequencies  $\Delta f = |f_1 - f_2|$  in the parameter plane of inter-resonator distance  $l$  and twist angle  $\alpha$ .

The dark blue regions indicate the course of the modal crossings (depicted by the red line) with  $\Delta f = 0$ . Regarding the coupling mechanism, the distance between the apertures is a relevant parameter. However, there has to be an

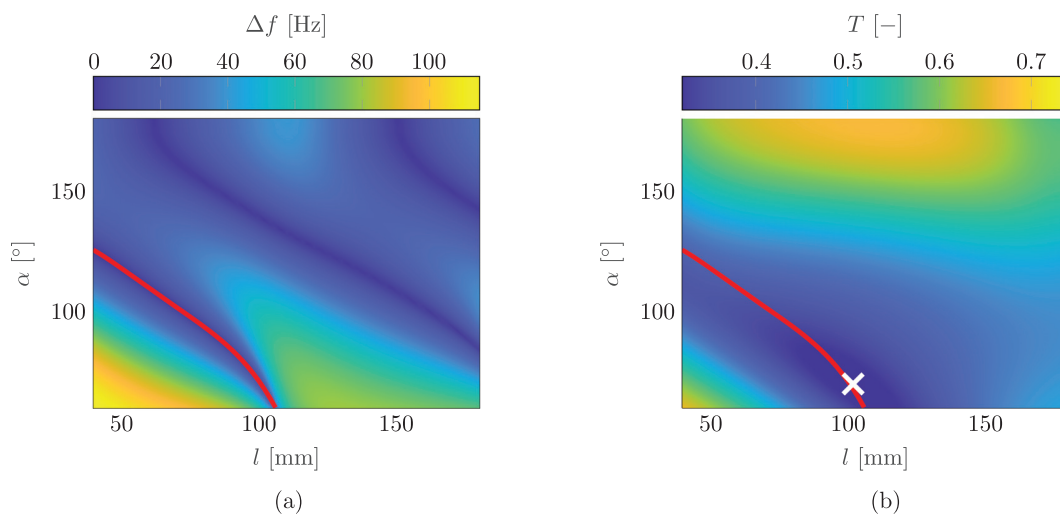


FIG. 3. (Color online) (a) Difference between the real parts of the cavity resonant frequencies  $\Delta f = |f_1 - f_2|$  of mode  $S$  and  $AS$  in the plane of inter-resonator distance  $l$  (mm) and angle  $\alpha$  ( $^\circ$ ). The modal crossings are represented by the dark blue lines with zero frequency difference  $\Delta f = 0$ . The black line indicates a constant inter-aperture distance  $l_a$  starting at the second crossing point for  $\alpha = 0^\circ$ . (b) Transmission efficiency  $T$  (-) for a plane wave with  $f = 1930$  Hz in the plane of inter-resonator distance  $l$  (mm) and angle  $\alpha$  ( $^\circ$ ). The minimum transmission efficiency is highlighted by the white cross. (a) and (b) For comparison, the first modal crossing is indicated by red lines in both figures.

additional effect besides the changing distance between the apertures. The C-shapes can be regarded as Helmholtz resonators embedded within a cylinder (Melnikov *et al.*, 2019). Thus, the background scattering of the cylinders also plays a major role. The impact of the scattering on the interaction between the resonators is negligible for facing apertures ( $\alpha = 0^\circ$ ) and grows with the twist angle, as the apertures move away from each other. A detailed analysis of the background scattering exceeds the scope of this work.

As observed in Fig. 2(a), the modal crossings provide the locations of possible transmission minima, that is attenuation maxima. The transmission efficiency  $T$  in the plane of inter-resonator distance  $l$  and twist angle  $\alpha$  is shown in Fig. 3(b). The incident wave has a frequency of  $f = 1930$  Hz, matching the frequency of the lowest transmission efficiency marked by the white cross in Fig. 2(a). As a result, transmission dips and modal crossings occur at the same distances and twist angles. For comparison, the first modal crossings are indicated by red lines in both plots in Fig. 3. Like in Fig. 2(a), the transmission dips only occur where the symmetric mode dominates, because of the relative orientation of resonators and incident wave.

The dark blue regions with  $\Delta f = 0$  in Fig. 3(a) cover all considered inter-resonator distances. This means that the modal crossings can be shifted to arbitrary resonator separations by varying the relative orientation of the two C-shapes. Independent of the orientation, the period is maintained. The transmission results show that the attenuation maxima follow the modal crossings. Thus, the combination of the two parameters, distance and orientation, offers the possibility of reaching attenuation maxima for a prescribed distance or lattice constant by adjusting the orientation and *vice versa*. Surprisingly, the attenuation maxima for this configuration is not found at  $\alpha = 90^\circ$  but at  $\alpha = 70^\circ$  and  $l = 102$  mm. Similar results are observed by additionally varying the frequency of the incoming wave.

### C. Frequency detuning and radiation losses

Another influencing factor is the frequency detuning  $\Delta = (f_B - f_A)/f_A$ . Therefore, we detune the resonance

frequency of one of the C-shaped resonators by adjusting the geometrical parameters ( $r$ ,  $w$ ,  $t$ ) before coupling them together. Often associated with synchronization theory (Pikovsky *et al.*, 2001), frequency detuning is a measure for the difference between the uncoupled natural frequencies of two oscillators  $A$  and  $B$ . In synchronization theory, non-linear effects can overcome detuning, but for our linear case, we can still observe degeneracy in certain cases. Detuning can arise due to fabrication imperfections, for example. In the following, it is set to  $\Delta = 3\%$ . Resonator  $A$  remains unchanged with a constant resonant frequency of  $f_A = 1960$  Hz and resonator  $B$  is scaled such that  $f_B = 2020$  Hz.

Like the case of zero detuning, the complex eigenfrequencies and the modal phase differences provide information about the coupling mechanism. The real and imaginary parts of the complex eigenfrequencies  $f_c$  associated with cavity resonance for variable resonator separation  $l$  are plotted in Figs. 4(a) and 4(b).

Except for the first crossing point of Fig. 2(a), the two modes no longer cross in the real part. The modal resonant frequencies still converge every half average wavelength  $\Delta l = \bar{\lambda}/2$  with  $\bar{\lambda} = (\lambda_A + \lambda_B)/2$ , like in the case of zero detuning in Fig. 2(a). However, they do not become identical, but pass through an avoided crossing and then diverge again. The resulting anti-crossing gap grows with increasing distance, that is, with decreasing coupling strength. In contrast, the imaginary parts of the eigenfrequencies exhibit an additional modal crossing at the distance of the anti-crossing in the real part. Thus, they cross every  $\Delta l = \bar{\lambda}/4$ .

The influence of a frequency mismatch on the occurrence of degenerate modes can be explained by varying the detuning at the points of degeneracy for zero detuning. More precisely, the detuning is varied from  $\Delta = \pm 15\%$  at the distances of the first two points of degeneracy for zero detuning, previously shown in Fig. 2(a), and furthermore, at the distance of the second crossing of the imaginary parts in Fig. 2(b). Figure 5 shows the real and imaginary parts of the complex eigenfrequencies  $f_c$  associated with cavity resonance as a function of the detuning  $\Delta$  at  $l = 84$ , 120, 174 mm, respectively.

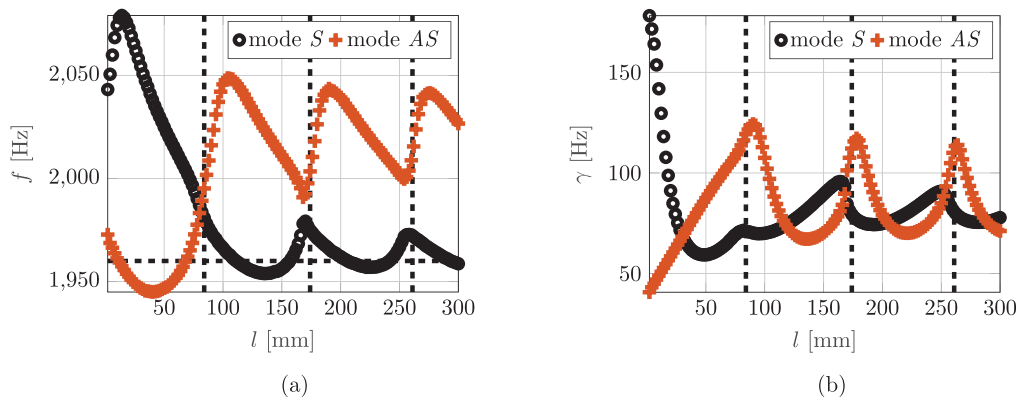


FIG. 4. (Color online) (a) Real and (b) imaginary parts of the complex eigenfrequencies  $f_c$  associated with cavity resonance as a function of the inter-resonator distance  $l$  (mm) with frequency detuning  $\Delta = 3\%$ . The dashed black lines indicate the distances of the modal crossings and modal (anti-) crossings extracted from Fig. 2(a).



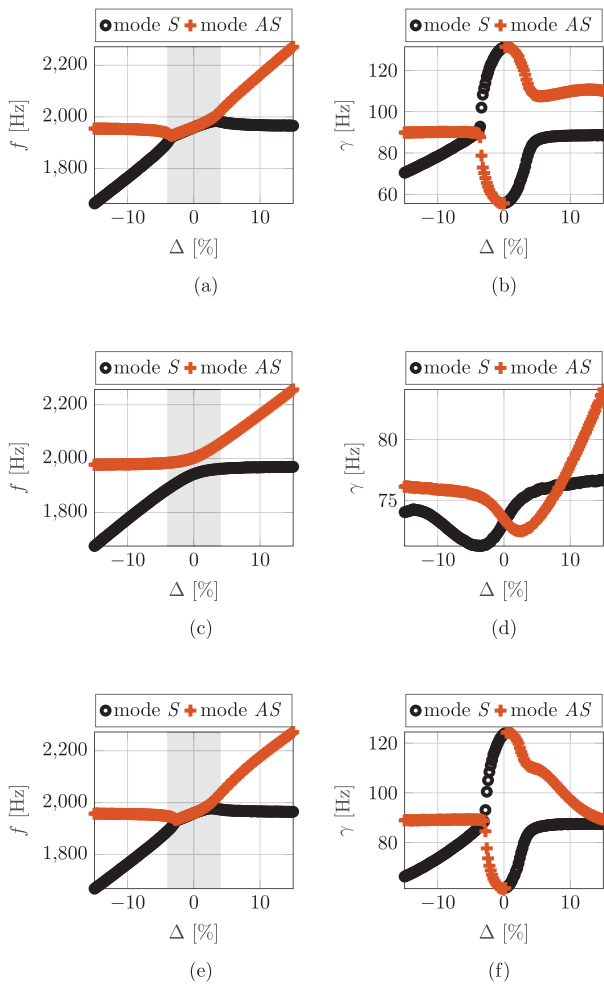


FIG. 5. (Color online) Real and imaginary parts of the complex eigenfrequencies  $f_c$  associated with cavity resonance as a function of the frequency detuning  $\Delta$  [%] at the first and second point of degeneracy obtained from Fig. 2(a) and at the second crossing point of the imaginary parts in Fig. 2(b). The gray area marks the range of  $\pm 3\%$  detuning. (a) real part,  $l = 84$  mm, (b) imaginary part,  $l = 84$  mm, (c) real part,  $l = 120$  mm, (d) imaginary part,  $l = 120$  mm, (e) real part,  $l = 174$  mm, and (f) imaginary part,  $l = 174$  mm.

Looking at the real parts in Figs. 5(a) and 5(e), the region of degeneracy with identical resonant frequencies is clearly visible. In this region, one can expect a destructive interference of the two degenerate modes, which can be observed, e.g., in the transmission spectrum. Figures 5(c) and 5(d) show an avoided crossing in the real parts of the eigenvalues and a point of degeneracy in the imaginary part. We can state that no degenerate modes can be found between crossing points in the real part, even for a detuned system. With decreasing coupling strength, that is, with increasing distance  $l$  from Figs. 5(a)–5(e), the region of degeneracy becomes smaller. This explains the previous results for  $\Delta = 3\%$  in Fig. 4(a). For very small distances, the coupling is still strong enough to overcome the frequency mismatch and thus cause degeneracy of the modes. As the separation increases, a detuning of  $\Delta = 3\%$  no longer lies in the region of degeneracy. The coupling is too weak to merge the two resonant frequencies, resulting in an

avoided crossing. The larger the inter-resonator distance, the larger the anti-crossing gap. As observed before, identical real parts of the eigenfrequencies cause the imaginary parts in Figs. 5(b) and 5(f) to move apart. The curves of the resonant frequencies in Figs. 5(a) and 5(e) agree with the typical curve based on synchronization theory (Pikovsky *et al.*, 2001), even if we do not consider non-linear effects. A similar behavior is observed in the experimental results for a pair of organ pipes by Fischer *et al.* (2016).

Having examined the influence parameters inter-resonator distance  $l$  and frequency detuning  $\Delta$  separately, the final step is their combination. Figure 6 shows the cavity resonant frequency difference  $\Delta f = |\Re(\bar{\omega}_1 - \bar{\omega}_2)|$  of mode S and AS as a function of the two variables and we call it the degeneracy pattern. In the resulting parameter plane, the frequency difference is approximately periodic in  $l$ -direction and nearly symmetric about  $\Delta = 0$ . The degeneracy of modes is represented by the dark blue regions (line-shaped regions in  $\Delta$ -direction) with zero frequency difference  $\Delta f = 0$ . These line-shaped regions of degeneracy are arranged periodically, with the period corresponding to half the average uncoupled wavelength  $\bar{\lambda}/2$ . This matches the period expected from the modal (anti-) crossings of the cavity resonant frequencies for varying separations in Figs. 2(a) and 4(a). The lines of degeneracy are slightly inclined towards smaller distances for positive frequency detuning due to smaller periods for smaller average resonant wavelengths. Since this effect accumulates over the distance, it becomes especially visible for larger separations. The first region of degeneracy extends over a wide range of detuning. For the second region, the range becomes smaller and decreases only weakly afterwards. This decrease in width with increasing separation, and thus weaker coupling, is in accordance with the regions of degeneracy in Fig. 5.

If the radiation losses are sufficiently increased for a fixed detuning, the modal crossing can be restored. In case of the C-shaped resonators, the radiation losses can be tuned by aperture width. This becomes obvious when comparing the results for the initial C-shape with  $w_A = 4$  mm and an increased aperture width of  $w_A = 4.25$  mm for  $\Delta = 3\%$  (see Fig. 7).

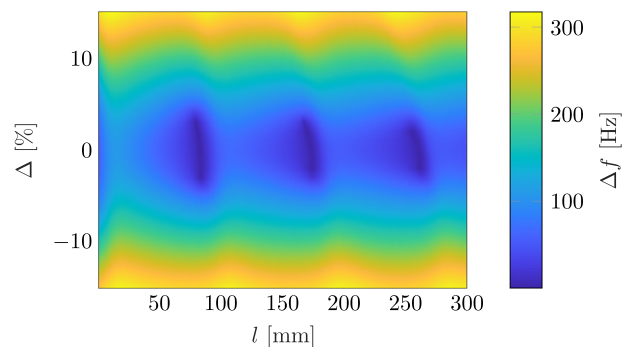


FIG. 6. (Color online) Difference between the real parts of the cavity resonant frequencies  $\Delta f = |\Re(\bar{\omega}_1 - \bar{\omega}_2)|$  [Hz] of mode S and AS in the plane of inter-resonator distance  $l$  (mm) and frequency detuning  $\Delta$  [%]. The degeneracy pattern shows the degeneracy of modes represented by the dark blue regions  $\Delta f = 0$ .

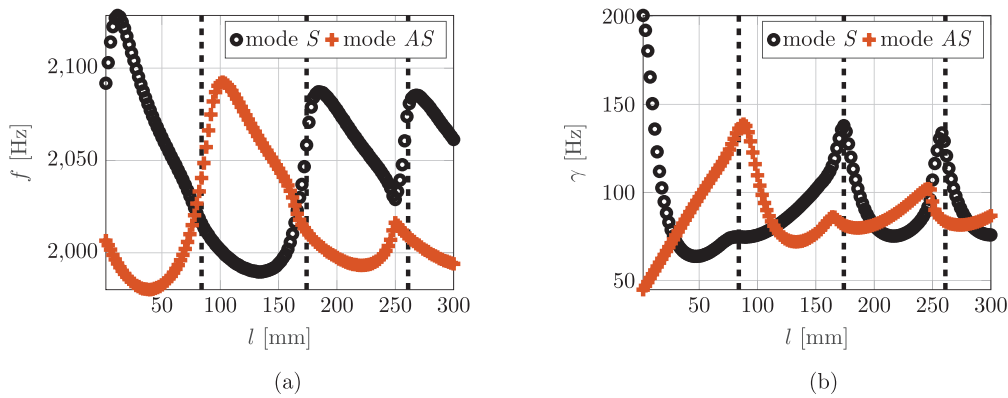


FIG. 7. (Color online) (a) Real and (b) imaginary parts of the complex eigenfrequencies  $f_c$  associated with cavity resonance as a function of the inter-resonator distance  $l$  (mm) with frequency detuning  $\Delta = 3\%$ , for a geometry with increased radiation losses increased aperture width  $w_A=4.25$  mm, initially  $w_A=4$  mm). The dashed black lines indicate the distances of the modal crossings and modal (anti-) crossings extracted from Fig. 2(a).

Figures 7(a) and 7(b) show the complex eigenfrequencies  $f$  as a function of the resonator separation  $l$  for the case with increased aperture width, that is, with increased  $\gamma$  of about 10%. Compared to Fig. 4(a), the modal crossings in the real parts are restored, while the imaginary parts approach each other without crossing at these distances, indicated by the dashed black lines. The further the losses are increased, the smoother are the curves in the vicinity of the crossing points.

An illustrative explanation for the counteracting effects can be given looking at the real parts of the cavity resonant frequencies in Figs. 2(a), 4(a) and 7(a). The frequency detuning opens a gap between the uncoupled and coupled resonant frequencies [see Fig. 4(a)]. However, this gap can be bridged by a sufficiently high increase in  $\gamma$  [see

Fig. 7(a)]. As the coupling increases with the radiation losses, it can be tuned by aperture width.

**D. Experimental validation**

To experimentally validate the acoustic performance of the coupled resonators, the transmission efficiency of two identical C-shaped meta-atoms was measured in a two-dimensional parallel-plate waveguide system as shown in Fig. 8(a).

The meta-atom samples are fabricated using additive manufacturing (3D printing) with polylactide (PLA). The two samples are shown in Fig. 8(b). We create an incident plane wave by using an array of eight loudspeakers. The

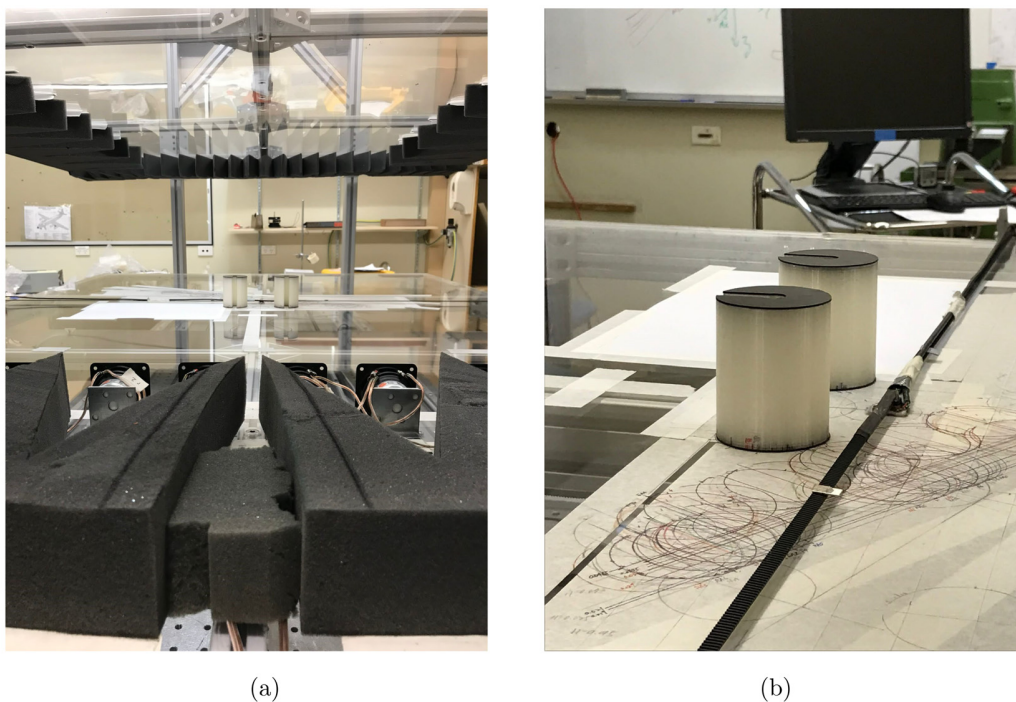


FIG. 8. (Color online) Experimental setup. (a) C-shaped meta-atoms placed in waveguide. (b) C-shaped meta-atoms.

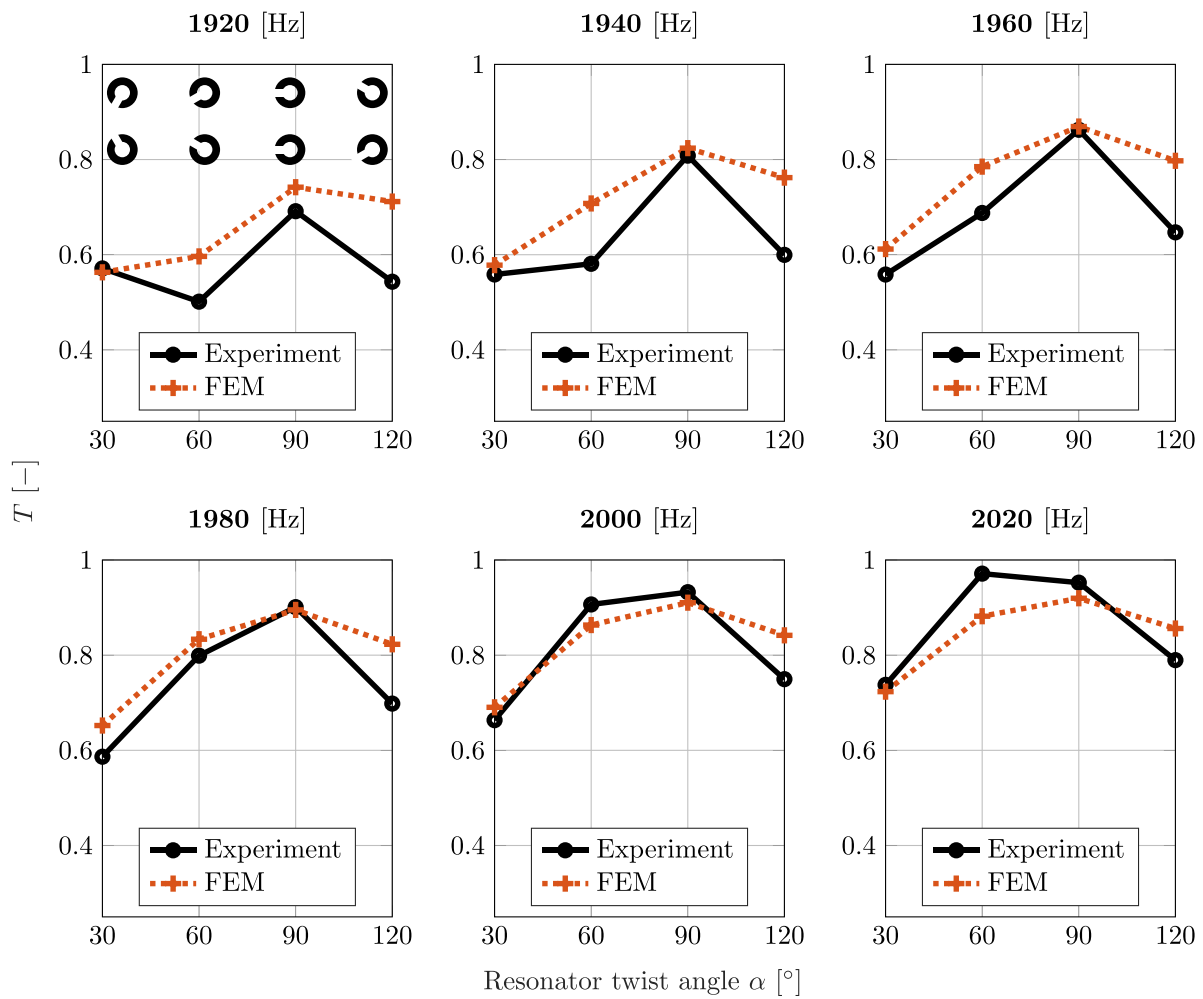


FIG. 9. (Color online) Experimental and numerical transmission efficiencies for six different frequencies evaluated at the twist angles of the resonators  $\alpha = 30^\circ, 60^\circ, 90^\circ,$  and  $120^\circ$  and an inter-resonator distance of 60 mm. The configurations of the C-shapes in dependence of the twist angles are presented on the top left.

incident and transmitted fields are measured along a vertical straight line by the microphone mounted on a belt system. The waveguide system is surrounded by absorbing foam to reduce unwanted reflection from the boundaries. We use four different orientations  $\alpha = 30^\circ, 60^\circ, 90^\circ,$  and  $120^\circ$  to experimentally demonstrate the sound attenuation of coupled meta-atoms. The sound reduction performance is examined by the transmission efficiency and compared with the numerical results (see Fig. 9).

The measured data match the trend of the simulated data quite well. The minor deviations in the transmission efficiency are due to inaccuracies in the setup, inaccuracies of modelling losses, and also modelling the acoustic source. Our model only covers the acoustic field, and no flow is considered. We also use a background pressure field in the COMSOL model, leading to plane wave excitation, while we use an array of loudspeakers mimicking a plane wave in the experimental setup. Since we are still able to reproduce the characteristic of the transmission efficiency in simulation and experiment, we consider the results as validated by experiment and hence, applicable in a real environment

including all kind of losses. Furthermore, we show that the transmission efficiency strongly depends on the twist angle of the C-shapes at a fixed distance  $l$ . The configurations of the C-shapes for the four measured twist angles are presented on the top left of Fig. 9. We control the level of sound attenuation of the coupled C-shapes, for instance, by changing the twist angle from  $90^\circ$ – $60^\circ$  at an excitation frequency of 1960 Hz. This leads to a decrease in the transmission efficiency from 0.86–0.69. As a result, the measurement results confirm the simulated data and hence, demonstrate the twist angle as parameter to control the level of sound attenuation of the coupled C-shapes.

#### IV. CONCLUSION

We show that degeneracy of modes for identical C-shaped Helmholtz resonators occurs at periodic distances with either the symmetric or antisymmetric mode dominating. By introducing detuning, we demonstrate that modal degeneracy depends on the level of detuning and on the coupling strength. Modal degeneracy can still occur for weak enough

detuning at certain specific distances between the resonators and, moreover, leads to the highest sound attenuation.

This region of degeneracy has similarities to Arnold tongues in non-linear synchronization theory. The degeneracy of modes holds within a certain range of frequency detuning—the region of degeneracy. Its scope narrows with increasing inter-resonator distance, that is, decreasing coupling strength. At the edge of the region of degeneracy, the phase differences converge to  $\Delta\Theta = \pm\pi/2$ . For varying distances, detuning values outside the degeneracy region lead to periodic avoided modal crossings of the real parts of the eigenfrequencies. The imaginary parts of the eigenfrequencies cross at the location of the avoided crossings of the real parts. At the distances of these (avoided) crossings, also the phase differences cross. This indicates an interchange in the nature of the two modes.

For C-shaped resonators, the radiation losses can be tuned by aperture width and counteract the effect of detuning. The combined effect of distance and detuning becomes visible in the degeneracy pattern. It consists of line-shaped regions of degeneracy, which are periodic in distance–direction and symmetric about zero detuning.

Furthermore, coupling induces the possibility of tuning via the resonators' relative arrangement, that is, distance and orientation. Starting with facing apertures, the two resonators were twisted in opposite directions. Thereby, the degeneracy of modes can be shifted to arbitrary distances, while the period is maintained. The location of the crossing points depends on the inter-aperture distance and is additionally influenced by background scattering effects. Moreover, the relative orientation affects the width of the regions of degeneracy. This means that the coupling strength depends on relative orientation and distance. Accordingly, these two influence parameters offer additional degrees of freedom for tuning the metamaterial response with unchanged components.

We also use coupled mode theory as an analytical approach to determine the coupling coefficient, but do not present it throughout the manuscript. The reason for this is that any asymmetry depends on the off diagonal terms, which makes the eigenvalue problem quite complicated. Determining the coupling coefficients using analytical models could be the subject of future research.

Experiments in a two-dimensional parallel-plate waveguide were conducted, showing good agreement and hence, validating the numerical results. In addition to their validation, the presented findings provide a base for further research, in particular, concerning the application to acoustic metamaterials.

The impact of the resonators' relative arrangement on the interaction and hence, the metamaterial response, provides additional degrees of freedom for the design of metamaterials. Since we can significantly manipulate the transmission efficiency of the coupled meta-atoms by changing the twist angle, our results offer new possibilities for more efficient and versatile metamaterials for noise control. In addition, our findings help drive progress in the design of advanced and high-performance metamaterials for a wide range of applications besides sound barriers.

- Al Jahdali, R., and Wu, Y. (2018). “Coupled resonators for sound trapping and absorption,” *Sci. Rep.* **8**, 13855.
- Baydoun, S. K., and Marburg, S. (2020). “Investigation of radiation damping in sandwich structures using finite and boundary element methods and a nonlinear eigensolver,” *J. Acoust. Soc. Am.* **147**(3), 2020–2034.
- Belacel, C., Todorov, Y., Barbieri, S., Gacemi, D., Favero, I., and Sirtori, C. (2017). “Optomechanical terahertz detection with single meta-atom resonator,” *Nat. Commun.* **8**, 1578.
- Cavaliere, T., Cebrecos, A., Groby, J.-P., Chaufour, C., and Romero-García, V. (2019). “Three-dimensional multiresonant lossy sonic crystal for broadband acoustic attenuation: Application to train noise reduction,” *Appl. Acoust.* **146**, 1–8.
- Chalmers, L., Elford, D. P., Kusmartsev, F. V., and Swallowe, G. M. (2009). “Acoustic band gap formation in two-dimensional locally resonant sonic crystals comprised of Helmholtz resonators,” *Int. J. Mod. Phys. B.* **23**(20-21), 4234–4243.
- COMSOL Inc. (2021). “COMSOL Multiphysics v5.6.”
- Cummer, S. A., Christensen, J., and Alù, A. (2016). “Controlling sound with acoustic metamaterials,” *Nat. Rev. Mater.* **1**(3), 16001.
- Deymier, P. A. (2013). *Acoustic Metamaterials and Phononic Crystals* (Springer, Heidelberg, Germany), available at <https://link.springer.com/book/10.1007/978-3-642-31232-8>.
- Dong, Y., Yu, G., Wang, X., Niu, X., Wu, K., and Wang, N. (2017). “Broadband and wide-angle blazed acoustic gratings using multiple coupled Helmholtz resonators,” *Appl. Phys. Express* **10**(9), 097201.
- Dukhin, A., and Goetz, P. (2002). *Ultrasound for Characterizing Colloids: Particle Sizing Zeta Potential Rheology*, 1st ed. (Elsevier, Boston).
- Elford, D. P., Chalmers, L., Kusmartsev, F. V., and Swallowe, G. M. (2011). “Matryoshka locally resonant sonic crystal,” *J. Acoust. Soc. Am.* **130**(5), 2746–2755.
- Fang, N., Xi, D., Xu, J., Ambati, M., Srituravanich, W., Sun, C., and Zhang, X. (2006). “Ultrasonic metamaterials with negative modulus,” *Nat. Mater.* **5**(6), 452–456.
- Fischer, J. L., Bader, R., and Abel, M. (2016). “Aeroacoustical coupling and synchronization of organ pipes,” *J. Acoust. Soc. Am.* **140**(4), 2344–2351.
- Fu, Y. H., Liu, A. Q., Zhu, W. M., Zhang, X. M., Tsai, D. P., Zhang, J. B., Mei, T., Tao, J. F., Guo, H. C., Zhang, X. H., Teng, J. H., Zheludev, N. I., Lo, G. Q., and Kwong, D. L. (2011). “A micromachined reconfigurable metamaterial via reconfiguration of asymmetric split-ring resonators,” *Adv. Funct. Mater.* **21**(18), 3589–3594.
- Hein, S., Koch, W., and Nannen, L. (2012). “Trapped modes and Fano resonances in two-dimensional acoustical duct-cavity systems,” *J. Fluid Mech.* **692**, 257–287.
- Herrero-Durá, I., Cebrecos, A., Picó, R., Romero-García, V., García-Raffi, L. M., and Sánchez-Morcillo, V. J. (2020). “Sound absorption and diffusion by 2D arrays of Helmholtz resonators,” *Appl. Sci.* **10**(5), 1690.
- Hesmer, F., Tatartschuk, E., Zhuromskyy, O., Radkovskaya, A., Shamonin, M., Hao, T., Stevens, C., Faulkner, G., Edwards, D., and Shamonina, E. (2007). “Coupling mechanisms for split ring resonators: Theory and experiment,” *Phys. Status Solidi B* **244**, 1170–1175.
- Jiang, X., Li, Y., and Zhang, L. (2017). “Thermoviscous effects on sound transmission through a metasurface of hybrid resonances,” *J. Acoust. Soc. Am.* **141**(4), EL363–EL368.
- Johansson, T. A., and Kleiner, M. (2001). “Theory and experiments on the coupling of two Helmholtz resonators,” *J. Acoust. Soc. Am.* **110**(3), 1315–1328.
- Jordaán, J., Punzet, S., Melnikov, A., Sanches, A., Oberst, S., Marburg, S., and Powell, D. A. (2018). “Measuring monopole and dipole polarizability of acoustic meta-atoms,” *Appl. Phys. Lett.* **113**(22), 224102.
- Keiser, G. R., Fan, K., Zhang, X., and Averitt, R. D. (2013). “Towards dynamic, tunable, nonlinear metamaterials via near field interactions: A review,” *J. Infrared. Millim. Terahertz Waves* **34**(11), 709–723.
- Krasikova, M., Krasikov, S., Melnikov, A., Baloshin, Y., Marburg, S., Powell, D. A., and Bogdanov, A. (2023). “Metahouse: Noise-insulating chamber based on periodic structures,” *Adv. Mater. Technol.* **8**, 2200711.
- Kronowetter, F., Baydoun, S. K., Eser, M., Moheit, L., and Marburg, S. (2020). “A benchmark study on eigenfrequencies of fluid-loaded structures,” *J. Theor. Comput. Acoust.* **28**(02), 2050013.
- Lee, T., and Iizuka, H. (2019). “Bragg scattering based acoustic topological transition controlled by local resonance,” *Phys. Rev. B* **99**, 064305.
- Liu, H., Liu, Y. M., Li, T., Wang, S. M., Zhu, S. N., and Zhang, X. (2009a). “Coupled magnetic plasmons in metamaterials,” *Phys. Status Solidi B* **246**(7), 1397–1406.

- Liu, N., Liu, H., Zhu, S., and Giessen, H. (2009b). "Stereometamaterials," *Nat. Photon.* **3**(3), 157–162.
- Ma, G., and Sheng, P. (2016). "Acoustic metamaterials: From local resonances to broad horizons," *Sci. Adv.* **2**(2), e1501595.
- Melnikov, A., Chiang, Y. K., Quan, L., Oberst, S., Alù, A., Marburg, S., and Powell, D. (2019). "Acoustic meta-atom with experimentally verified maximum Willis coupling," *Nat. Commun.* **10**(1), 3148.
- Milton, G. W., and Willis, J. R. (2007). "On modifications of Newton's second law and linear continuum elastodynamics," *Proc. R. Soc. A.* **463**(2079), 855–880.
- Movchan, A. B., and Guenneau, S. (2004). "Split-ring resonators and localized modes," *Phys. Rev. B* **70**(12), 125116.
- Pendry, J. B. (2000). "Negative refraction makes a perfect lens," *Phys. Rev. Lett.* **85**(18), 3966–3969.
- Pendry, J. B., Schurig, D., and Smith, D. R. (2006). "Controlling electromagnetic fields," *Science* **312**(5781), 1780–1782.
- Pikovskiy, A., Rosenblum, M., and Kurths, J. (2001). *Synchronization: A Universal Concept in Nonlinear Sciences*, Cambridge Nonlinear Science Series (Cambridge University Press, Cambridge, UK).
- Powell, D. A., Hannam, K., Shadrivov, I. V., and Kivshar, Y. S. (2011). "Near-field interaction of twisted split-ring resonators," *Phys. Rev. B* **83**(23), 235420.
- Powell, D. A., Lapine, M., Gorkunov, M. V., Shadrivov, I. V., and Kivshar, Y. S. (2010). "Metamaterial tuning by manipulation of near-field interaction," *Phys. Rev. B* **82**(15), 155128.
- Sawicki, J., Abel, M., and Schöll, E. (2018). "Synchronization of organ pipes," *Eur. Phys. J. B* **91**(2), 1–9.
- Schurig, D., Mock, J. J., Justice, B. J., Cummer, S. A., Pendry, J. B., Starr, A. F., and Smith, D. R. (2006). "Metamaterial electromagnetic cloak at microwave frequencies," *Science* **314**(5801), 977–980.
- Strutt, J. W. (2011). *The Theory of Sound*, Cambridge Library Collection - Physical Sciences (Cambridge University Press, Cambridge, UK).
- Valentine, J., Li, J., Zentgraf, T., Bartal, G., and Zhang, X. (2009). "An optical cloak made of dielectrics," *Nat. Mater.* **8**(7), 568–571.
- Wang, Y.-F., and Laude, V. (2017). "Longitudinal near-field coupling between acoustic resonators grafted onto a waveguide," *Crystals* **7**, 323.
- Wu, L., Xi, X., Li, B., and Zhou, J. (2017). "Dielectric meta-atom with tunable resonant frequency temperature coefficient," *Sci. Rep.* **7**, 2566.
- Yakovlev, A. B., and Hanson, G. (2000). "Mode-transformation and mode-continuation regimes on waveguiding structures," *IEEE Trans. Microw. Theory Techn.* **48**, 67–75.
- Yang, X., Yin, J., Yu, G., Peng, L., and Wang, N. (2015). "Acoustic superlens using Helmholtz-resonator-based metamaterials," *Appl. Phys. Lett.* **107**(19), 193505.
- Yao, S., Zhou, X., and Hu, G. (2008). "Experimental study on negative effective mass in a 1D mass-spring system," *New J. Phys.* **10**(4), 043020.
- Zangeneh-Nejad, F., and Fleury, R. (2019). "Active times for acoustic metamaterials," *Rev. Phys.* **4**, 100031.
- Zhou, Y., Fang, X., Li, D., Hao, T., and Li, Y. (2018). "Acoustic multiband double negativity from coupled single-negative resonators," *Phys. Rev. Appl.* **10**, 044006.

## 5.4 **Publication AP4**



Contents lists available at ScienceDirect

# Mechanical Systems and Signal Processing

journal homepage: [www.elsevier.com/locate/ymssp](http://www.elsevier.com/locate/ymssp)

## Novel compound material and metamaterial wheelhouse liners for tire noise reduction

Felix Kronowetter<sup>a,\*</sup>, Philipp Wagner<sup>b</sup>, Juri Kolodi<sup>c</sup>, Ines Brabandt<sup>b</sup>,  
Thomas Neumeyer<sup>c</sup>, Norbert Rümmler<sup>b</sup>, Steffen Marburg<sup>a</sup>

<sup>a</sup> Chair of Vibro-Acoustics of Vehicles and Machines, Department of Engineering Physics and Computation, TUM School of Engineering and Design, Technical University of Munich, Boltzmannstraße 15, Garching (near Munich), 85748, Germany

<sup>b</sup> AMITRONICS Angewandte Mikromechatronik GmbH, Waldmeisterstraße 99, Munich, 80935, Germany

<sup>c</sup> Neue Materialien Bayreuth GmbH, Gottlieb-Keim-Str. 60, Bayreuth, 95448, Germany

### ARTICLE INFO

Communicated by E. Fernandez-Grande

#### Keywords:

Acoustic metamaterials  
Passive noise control  
NVH  
Traffic noise

### ABSTRACT

Traffic noise has increased in recent years and hence the European Union has regulated the noise emission norm more strictly. New technologies have to be developed to reach the future regulations. Automotive lightweight construction deteriorate the noise, vibrations and harshness performance, though. The airborne and structure-borne noise emitted by tires contribute significantly to the entire noise spectrum of the vehicle. Our goal is to develop a new wheelhouse liner that improves the acoustic attenuation properties in the frequency range of 800 Hz to 4000 Hz. We pursue the strategy of adapting two different approaches. First, we design a compound material consisting of porous layers and a microperforated panel. This approach combines the effect of a porous absorber and local resonators. Thus, broadband noise attenuation is achieved. The starting frequency of the absorbing band is shifted towards lower frequencies than conventional porous absorbers due to the effect of local resonances. Second, we construct an acoustic metamaterial based on resonant cavities. In comparison to the first approach, the material does not produce broadband absorption but targets a particular frequency of interest. Both approaches are first simulated and then experimentally evaluated by impedance tube, Alpha Cabin and full vehicle measurements. The chosen design concepts are developed for mass production and hence a trade-off between being cost-efficient and manufacturable while improving the acoustic attenuation. We demonstrate two new types of wheelhouse liners for vehicles outperforming state-of-the-art solutions made from compressed nonwoven materials

### 1. Introduction

Increasing traffic in Europe and particularly on German roads comes hand in hand with increased noise exposure. Therefore, the European Union decided to counteract increasing noise exposure by tightening regulation No. 51 and No. 117 of the Economic Commission for Europe of the United Nations (UN/ECE), respectively. In the EU, four different power classes are described, which are distinguished by the power-to-mass ratio. From July 2026, a limit of 68 dB will apply to all new registrations in the lowest power

\* Corresponding author.

E-mail address: [felix.kronowetter@tum.de](mailto:felix.kronowetter@tum.de) (F. Kronowetter).

<https://doi.org/10.1016/j.ymssp.2023.110548>

Received 6 October 2022; Received in revised form 31 May 2023; Accepted 18 June 2023

Available online 1 July 2023

0888-3270/© 2023 Elsevier Ltd. All rights reserved.

class ( $\leq 120\text{ kW}/1000\text{ kg}$  – this is around 90% of all vehicles – current limit 72 dB), which means a reduction in pass-by noise of 4 dB (enormous feat).

Due to the electrification of the drive train, the noise emitted from the engine is reduced. Hence, the tires become a dominant sound source, contributing to the pass-by noise and also to the interior cabin noise via transmission path through the structure of the car. Tire noise is composed of texture impact, tread impact, air pumping, pipe resonance, Helmholtz resonance, horn effect, and tire cavity resonance [1]. The low frequency cavity resonances have intensively been investigated by the scientific community in recent years [2–8]. So is the total performance of the tire and its optimization as acoustic source [1,9–11]. Lafont et al. [12] investigate tire radiation numerically. They identify the contact patch as a principal contributor from 800 Hz to 2000 Hz.

Weight reduction of vehicles typically leads to impaired noise, vibration and harshness (NVH) performance. This is due to the fact, that the NVH performance is mainly dependent on mass and stiffness. To satisfy the demands of reduced pass-by noise and of reduced cabin noise, classic noise reduction techniques — relying on increased mass and stiffness — are not applicable, since they are contradictory to the lightweight construction of the vehicle. Particularly noise propagation in electric vehicles will be of increased future interest [13–15].

Installing sound absorbing materials is another well known approach to increase sound attenuation. Porous materials, for example, are great absorbers for higher frequencies. They can be modeled by semi-empirical models, e.g. the five-parameter Johnson–Champoux–Allard (JCA) model [16–18], that effectively describes the characteristics of acoustic propagation in porous materials. Furthermore, the application of microperforated panels (MPPs) is a basic procedure to reduce noise in room acoustics. The theory to predict the acoustic properties of MPPs was first proposed by Maa [19–21]. MPPs can be considered an assembly of periodically arranged Helmholtz resonators with thin apertures, that are connected by a cavity behind them. The advantage of MPPs is that they can be connected in various ways and hence are adaptable to a variety of acoustic problems [22–25]. However, MPPs are narrow-band absorbers limited by the dimensions of the aperture and the quarter-wavelength dependence of the cavity, necessary for maximum absorptions. A composite structure consisting of MPPs and porous materials can be chosen to overcome these limitations. Thereby, broadband absorption shifted towards a lower frequency range can be achieved, compared to conventional porous materials. Various composite structures have been intensively studied in recent years [26–31].

A novel approach called acoustic metamaterials (AMMs) is breaking the laws of classic noise reduction techniques, and hence the dependency on mass and stiffness [32–36]. AMMs mostly consist of periodically arranged meta-atoms [37] based on local resonances leading to, for example, a negative effective mass density [38–40], bulk modulus [41] or refractive index [42]. If we exemplarily consider structural metamaterials based on microslits [43] or more complex shaped meta-atoms [44], thermo-viscous losses play a major role due to small openings and narrow channels. Losses are intensively studied since they can significantly effect the metamaterial performance [45–47].

The transfer of AMMs to vehicles is latterly studied by multiple research groups. Sangiuliano et al. [48] apply AMMs for structural noise mitigation in vehicles. Therefore, they place 3D printed resonant structures onto the wheelhouse of a hatchback vehicle. They address the first acoustic tire resonance in the low-frequency domain at 230 Hz. In a recent work by Sangiuliano et al. [49], the authors investigate a resonant metamaterial tire solution and its influence on the low-frequency structure-borne tire-road noise. Liao et al. [50] target the low-frequency cabin noise at 20 Hz to 100 Hz with AMM plates placed in the tail door producing stop-bands at 35 Hz. Chang et al. [51] apply AMMs to suppress the noise transfer through vehicle body panels. They target a frequency range of 500 Hz to 900 Hz with periodic vibration damping unit cells. All of the above mentioned approaches use solid structures harvesting energy when they are activated in their natural frequencies.

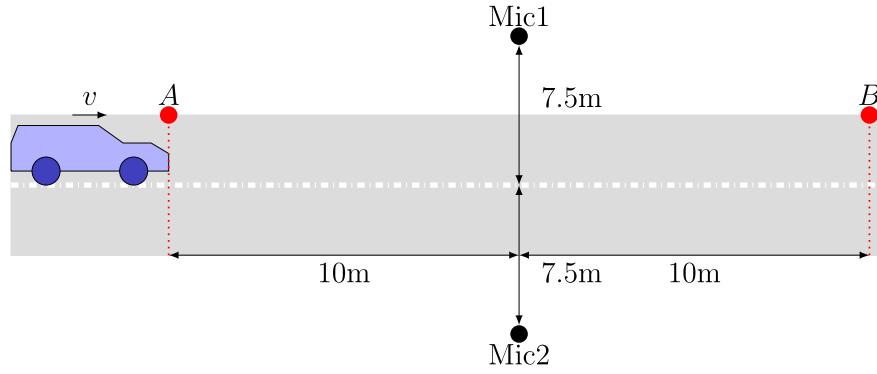
The wheelhouses of a vehicle offer large areas for the attachment of acoustically effective liners. State-of-the-art wheelhouse liners are made of compressed nonwoven materials or even plastic material. There is a huge potential to improve sound absorption at the material level and to utilize surfaces with untapped acoustic potential. We investigate the influence of a compound material wheelhouse liner consisting of porous layers and a microperforated panel as well as an acoustic metamaterial wheelhouse liner on the pass-by noise as well as on the cabin noise. The metamaterial approach differs from the aforementioned ones by relying on resonances in the fluid field and neglecting structural vibrations. Most metamaterials achieve outstanding sound attenuation properties in laboratory conditions. Here, we face complex wave fields, high influence of thermo-viscous losses due to the small dimensions and several restrictions given by production guidelines. The task is quite demanding, since the designs needed to be realizable, manufacturable, low-cost and the acoustic performance needs to be maintained in built-in condition. First, we present the baseline problem. In the second step, we introduce the modeling approaches in Section 3. In the third step, the material properties are studied and we explain the manufacturing process, in Section 4. We then discuss the results and evaluate the measurement data extracted from full vehicle measurements. Finally, we conclude the discussed results.

## 2. Baseline problem

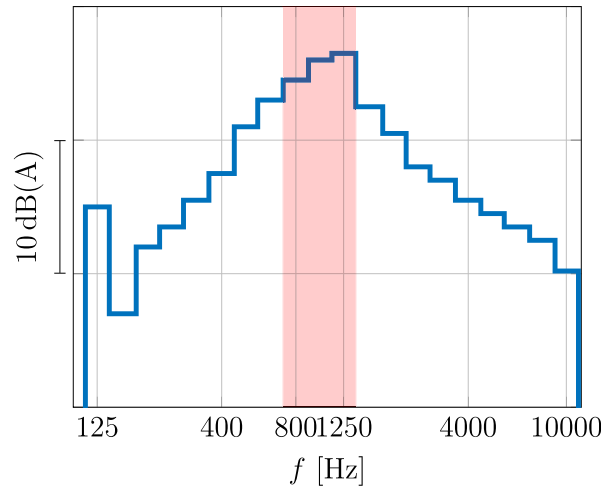
The pass-by noise of vehicles in Europe is governed by regulation No. 51 and No. 117 of the Economic Commission for Europe of the United Nations (UN/ECE). To get a better understanding of the baseline problem, we present the spectrum of the pass-by noise of an upper premium class hatchback vehicle. The vehicle is equipped with Continental ContiWinterContact 225/55 R17 tires. Fig. 1 displays the pass-by noise measurement set-up for outdoor measurements as well as the corresponding noise spectrum.

Fig. 1(a) shows the pass-by noise measurement set-up regarding to regulation No. 51 (UN/ECE). The vehicle is passing a measurement track of 20 m (from A to B) at a predefined speed  $v = 50\text{ km/h}$ . The microphones are positioned at 10 m distance from point A, at 7.5 m distance from the middle of the road and at a height of 1.2 m. Multiple outdoor measurements are conducted in different driving maneuvers. For that purpose, we increase the vehicle speed in 10 km/h steps from 40 to 80 km/h. Fig. 1(b) shows





(a) Measurement set-up.



(b) Noise spectrum.

Fig. 1. Measurement set-up regarding to regulation No. 51 (UN/ECE) and Pass-by noise of the vehicle over the frequency in third octave bands. The shaded regions colored red depict the third octave bands where the highest  $L_p$  is measured.

the averaged sound pressure level ( $L_p$ ) measured at two microphones — their position is defined by the pass-by norm — with respect to third octave bands from 125 Hz to 10 000 Hz. We can identify the frequency range around 800 Hz to 1250 Hz being the one with the highest  $L_p$  measured. Particularly, the  $L_p$  reaches its maximum around 1250 Hz and hence represents the most problematic noise. The goal of this work is to design a wheelhouse liner that reduces the pass-by noise of the vehicle. Therefore, the focus of our study is on the influence of the wheelhouse liners on the pass-by noise, besides we additionally investigate the influence on the cabin noise.

### 3. Theory

We investigate two approaches to enhance sound absorption of the wheelhouse liner. First, we combine a microperforated panel with a custom-built porous layer. This leads to broad-band wave attenuation. Second, a meta-structure is designed to target the dominant frequency.

#### 3.1. MPP

An MPP can be considered an assembly of small tubes connected to a cavity. Each perforation hole with enclosed air cavity acts as individual Helmholtz resonator. Under normal incidence, an MPP can be regarded as a large number of Helmholtz resonators with shared air volume. Due to thin necks, the thickness of the viscous boundary layer is approximately that of the hole orifices. This results in high viscous losses and hence high absorption. Representing the resonator as harmonic oscillator, the oscillating air in the neck acts as mass and the cavity as spring. The complex surface impedance of the MPP is given by Maa [19–21]

$$Z_{MPP} = r + i\omega m \quad (1)$$

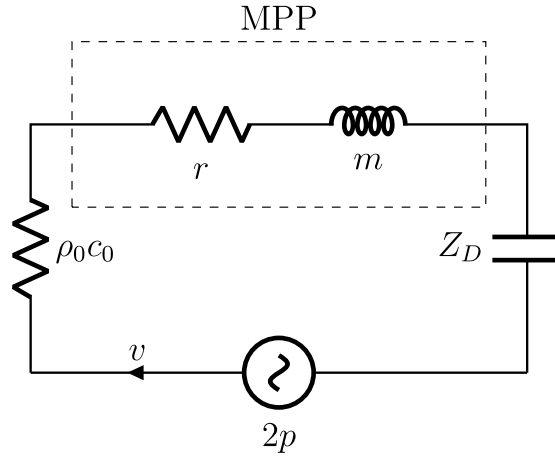


Fig. 2. Equivalent circuit for the MPP absorber with air layer.

with  $r$  being the acoustic resistance and  $m$  the acoustic mass reactance

$$r = \frac{32\eta t}{\sigma d^2} k_r, \quad k_r = \left(1 + \frac{k^2}{32}\right)^{\frac{1}{2}} + \frac{\sqrt{2}}{8} k \frac{d}{t}, \quad k = \frac{d}{2} \sqrt{\frac{\omega \rho}{\eta}} = \frac{d}{2} \sqrt{\frac{\omega}{\mu}} \tag{2}$$

$$m = \frac{t \rho k_m}{\sigma}, \quad k_m = 1 + \left(9 + \frac{k^2}{2}\right)^{-\frac{1}{2}} + 0.85 \frac{d}{t}.$$

and  $\eta, \sigma, \rho_0, \omega, d, t$  being the dynamic viscosity of air, percentage perforation, density of air, circular viscosity, diameter of the tube and thickness of the MPP layer, respectively. The acoustic impedance of the cavity of length  $x$  can be derived using the standing wave approach [52] as

$$Z_D = -i \rho_0 c_0 \cot(k_0 x) \tag{3}$$

with  $c_0$  being the speed of sound in air. The equivalent RLC series circuit shown in Fig. 2 gives the assembled impedance as

$$Z = Z_{MPP} + Z_D = r + i \omega m - i \rho_0 c_0 \cot(k_0 x). \tag{4}$$

The resonance frequency of the system can be extracted from the circuit formulation  $f = \frac{1}{\rho_0 c_0 \sqrt{L_{eff} C_{eff}}}$  and complies with  $x = \frac{\lambda}{4}$  inducing a maximum velocity at the MPP layer. The absorption of a single layer MPP backed by a cavity filled with air is dominated by its resonant frequency. Since we aim at broadband absorption we tune the system by filling the cavity with porous media. We develop our own porous material meeting the demands given by available space, weight, material safety data sheet, costs and absorption properties. The acoustic impedance is modeled by using the five parameter, semi-empirical Johnson–Champoux–Allard equivalent fluid model [16–18] leading to the equivalent dynamic density

$$\rho_p = \frac{\rho_0 \alpha_\infty}{\phi} \left(1 + \frac{\phi \sigma}{i \omega \rho_0 \alpha_\infty} \left(1 + i \frac{4 \omega \rho_0 \eta \alpha_\infty^2}{(\sigma \phi \Lambda)^2}\right)^{\frac{1}{2}}\right) \tag{5}$$

and the equivalent bulk modulus

$$K_p = \frac{\gamma p_0}{\phi} \left(\gamma - (\gamma - 1) \left(1 + \frac{8 \eta}{i \omega \text{Pr} \Lambda'^2 \rho_0} \left(1 + i \frac{\omega \text{Pr} \rho_0 \Lambda'^2}{16 \eta}\right)^{\frac{1}{2}}\right)^{-1}\right)^{-1}. \tag{6}$$

We denote  $\gamma, \phi, \alpha_\infty, \sigma, \text{Pr}, \Lambda, \Lambda',$  and  $p_0$  the specific heat ratio of air at room temperature, porosity, tortuosity, flow resistivity, Prandtl number, viscous characteristic length, the thermal characteristic length and the ambient pressure, respectively. The characteristic impedance and the wavenumber are calculated using the square root of the dynamic density and bulk modulus:

$$Z_c = \sqrt{\rho_p K_p}, \quad k_p = \omega \sqrt{\frac{\rho_p}{K_p}}. \tag{7}$$

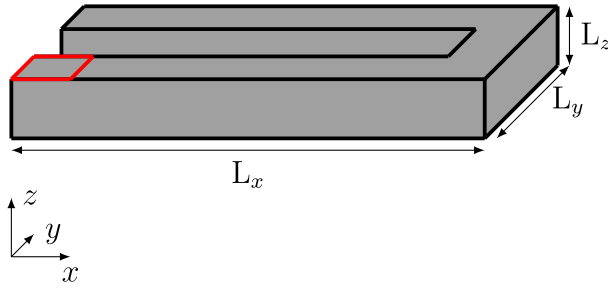
We obtain the surface impedance by using the transfer matrix method [53,54]

$$T_{MPP} = \begin{bmatrix} 1 & Z_{MPP} \\ 0 & 1 \end{bmatrix}, \quad T_P = \begin{bmatrix} \cos(k_p x_p) & i Z_c \sin(k_p x_p) \\ i \sin(k_p x_p) / Z_c & \cos(k_p x_p) \end{bmatrix} \tag{8}$$

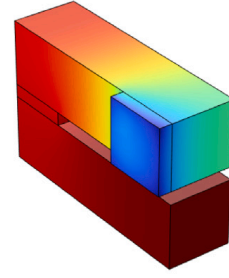
leading to

$$T = T_{MPP} T_P = \begin{bmatrix} T_{11} & T_{12} \\ T_{21} & T_{22} \end{bmatrix}, \quad \begin{bmatrix} p_s \\ v_s \end{bmatrix} = \begin{bmatrix} T_{11} & T_{12} \\ T_{21} & T_{22} \end{bmatrix} \begin{bmatrix} p_w \\ v_w \end{bmatrix} \tag{9}$$

$$Z_s = \frac{T_{11}}{T_{21}} = Z_{MPP} - i Z_c \cot(k_p x_p).$$



(a) Drawing of the final quarter-wave resonator.



(b) Sound pressure level inside the resonant cavity.

Fig. 3. Drawing of the resonant cavity and the visualized sound pressure level at 1250 Hz.

We denote  $x_p$  the thickness of the porous layer,  $p_s, u_s$  the pressure and velocity at the surface of the MPP and  $p_w, u_w = 0$  the pressure and velocity at the rigid wall behind the porous layer. The absorption coefficient is defined by the well-known formula

$$\alpha = \frac{4 \frac{\text{Re}(Z_s)}{\rho_0 c_0}}{\left(1 + \frac{\text{Re}(Z_s)}{\rho_0 c_0}\right)^2 + \left(\frac{\text{Im}(Z_s)}{\rho_0 c_0}\right)^2}. \quad (10)$$

### 3.2. Metamaterial

As a second concept we choose an acoustic metamaterial targeting one particular frequency of interest. Here, we choose a frequency of 1250 Hz regarding maximum  $L_p$  of Fig. 1(a). A more detailed explanation can be found subsequently in Section 5, where we additionally analyze the surface contribution. Due to the restricted space in the wheelhouse we need a subwavelength structure with good sound attenuation properties. This is realized by periodically arranged local resonators leading to band-gaps in the frequency spectrum. Therefore, we design a mixture of a Helmholtz resonator and quarter wave resonator. The goal is to achieve sound attenuation by absorption and not just changing the directivity. On these grounds, we build two different models. We use COMSOL Multiphysics to simulate the resonant cavity and hence predict its eigenfrequencies as well as the transmission spectrum. The first model analyzes the transmission coefficient of our cavity and the second one works like a digital twin of an impedance tube providing its reflection coefficient and absorption coefficient in the presence of thermo-viscous losses. We end up with designing a U-shaped quarter-wave resonator with a short neck and a large opening to increase the amount of affected fluid. To obtain metamaterial properties, we apply periodic boundary conditions. A schematic as well as the sound pressure level inside of the resonant cavity excited at 1250 Hz are shown in Fig. 3.

Fig. 3(a) displays the geometry of the resonant cavity. The dimensions  $L_x$ ,  $L_y$  and  $L_z$  are set to 50 mm, 22 mm and 10 mm, respectively. The neck of the cavity is highlighted by the red lines and has a thickness of 2 mm in  $y$ -direction. Fig. 3(b) shows the distribution of the sound pressure level inside the cavity at resonance. It is similar to the distribution of the total thermo-viscous power dissipation density. Hence, most energy gets dissipated in the last section of the cavity. We additionally computed the complex reflection factor with and without losses as well as the absorption coefficient from 1150 to 1350 Hz. This is presented in Fig. 4.

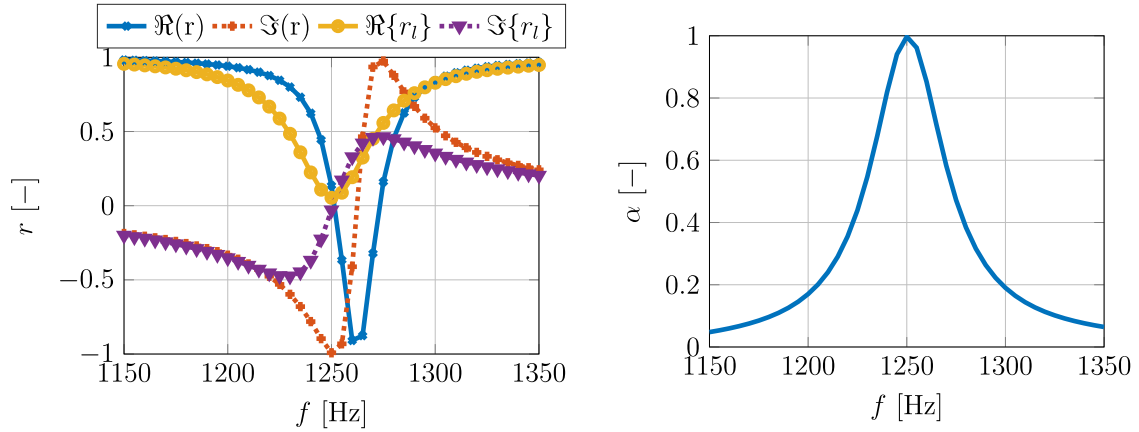
Fig. 4(a) shows the real and imaginary parts ( $\Re$  and  $\Im$ ) of the complex reflection factor. Here we differ two cases, one without losses ( $r$ ) and a second one in the presence of thermo-viscous losses ( $r_l$ ). We can see that including losses leads to a significant reduction of the dip in the real part and observe a smoothed course of the imaginary part over the frequency. Furthermore, the incorporation of losses leads to a downward shift regarding the resonance frequency. The real part of  $r_l$  is always positive and the imaginary part bounded by  $\pm 0.5$ . This leads to almost perfect absorption and is depicted in Fig. 4(b). Thus, we conclude that the sound energy is absorbed at the target frequency.

## 4. Development of a production process and analysis of the process structure property relationships

For the production of sound-absorbing nonwoven components, a process has been developed which is described in more detail in the following chapter. In addition, the dependence of the sound absorption coefficient of nonwoven materials on the processing method is explained.

### 4.1. Process structure property relationships

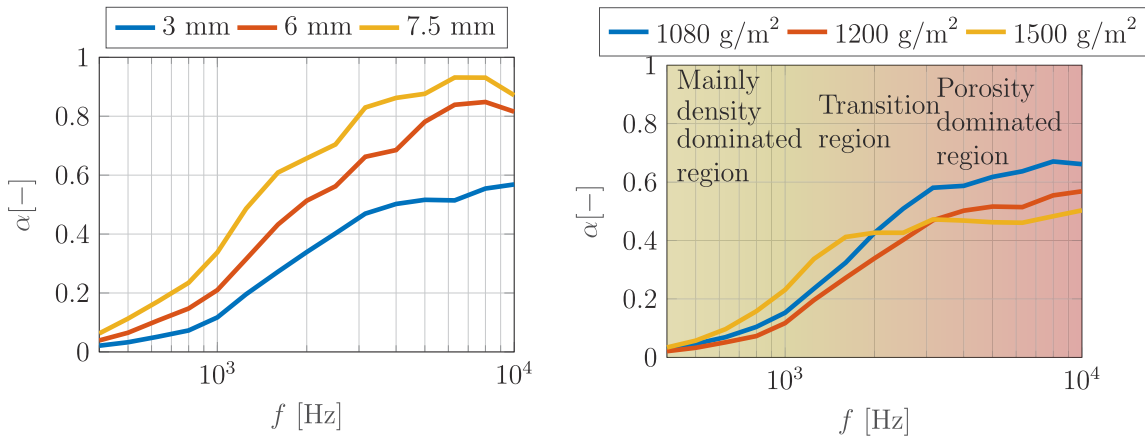
For the study of the sound absorption coefficient  $\alpha$ , the thickness of a fiberglass polyester (PES) bi-component (PES-bico/GF) nonwoven is varied between 3 mm, 6 mm and 7.5 mm. Furthermore, different mass per unit area configurations — 1080 g/m<sup>2</sup>, 1200 g/m<sup>2</sup> and 1500 g/m<sup>2</sup> — are investigated. This results in a test matrix of three thicknesses and basis weights. Fig. 5(a) shows the sound absorption properties as a function of frequency for three different thicknesses at a mass per unit area of 1200 g/m<sup>2</sup>.



(a) Simulated complex reflection factor with and without losses.

(b) Simulated absorption coefficient.

Fig. 4. Simulated complex reflection factors (with and without losses) and absorption coefficient from 1150 to 1350 Hz.



(a) PES-bico/GF nonwoven (1200 g/m<sup>2</sup>).

(b) PES-bico/GF nonwoven (3 mm).

Fig. 5. Absorption coefficient over frequency for varying thickness and mass per unit area.

With increasing thickness, the sound absorption almost doubles from 3 mm to 7.5 mm. This effect is particularly noticeable above a frequency of 1000 Hz. The explanation can be found by looking at the microstructure. For a better understanding, we investigated the nonwovens by using a scanning electron microscope (SEM). The corresponding pictures are presented in Fig. 6.

We can see that the fibers are tightly compressed and quite dense, regarding a thickness of 3 mm. Thus, the incoming sound wave is only slightly attenuated by the material. Increased thickness from 3 mm to 7.5 mm leads to increased porosity of the material by up to 80%. As a result, the surface area of the material also increases and thus allows sound to be trapped and dissipated in the structure.

The sound absorption coefficient as a function of frequency for varying mass per unit area at a constant thickness of 3 mm is shown in Fig. 5(b). It can be observed that the sound absorption coefficient does not increase in the same way over the entire frequency range as the mass per unit area increases. Basically, the sound absorption can be divided into two ranges. At low frequencies up to 1000 Hz to 3000 Hz, a mainly density-dominated region can be identified. In this region, the material with the highest mass per unit area usually comes along with the highest absorption coefficient. In the low frequency domain, sound absorption is dominated by high density and volume and hence mass. Here we face an exception to the rule, because the blue curve (1080 g/m<sup>2</sup>) has a higher absorption coefficient than the red curve (1200 g/m<sup>2</sup>), see Fig. 5(b). We assume that since we enforce higher density by compressing the nonwoven, we also change the porosity and other material properties. Above about 1000 Hz to 3000 Hz, high porosity becomes more and more advantageous for sound absorption. This region is called transition region, where the dominant parameter switches from density to porosity. At higher frequencies from 3000 Hz upwards, we observe a porosity-dominated region. Higher frequency sound waves with short wavelengths are strongly affected by dissipation inside porous materials with pore sizes in dimensions of μm to mm. Fig. 7 provides an explanation for the poor performance of the 1500 g/m<sup>2</sup> in the frequency region over 3000 Hz.

Due to the high degree of compression, the nonwoven only forms tiny pores and hence is quite dense. In the porosity-dominated region, a higher density has a negative effect on the absorption coefficient. This is exactly what we see in the red colored region in Fig. 5(b).

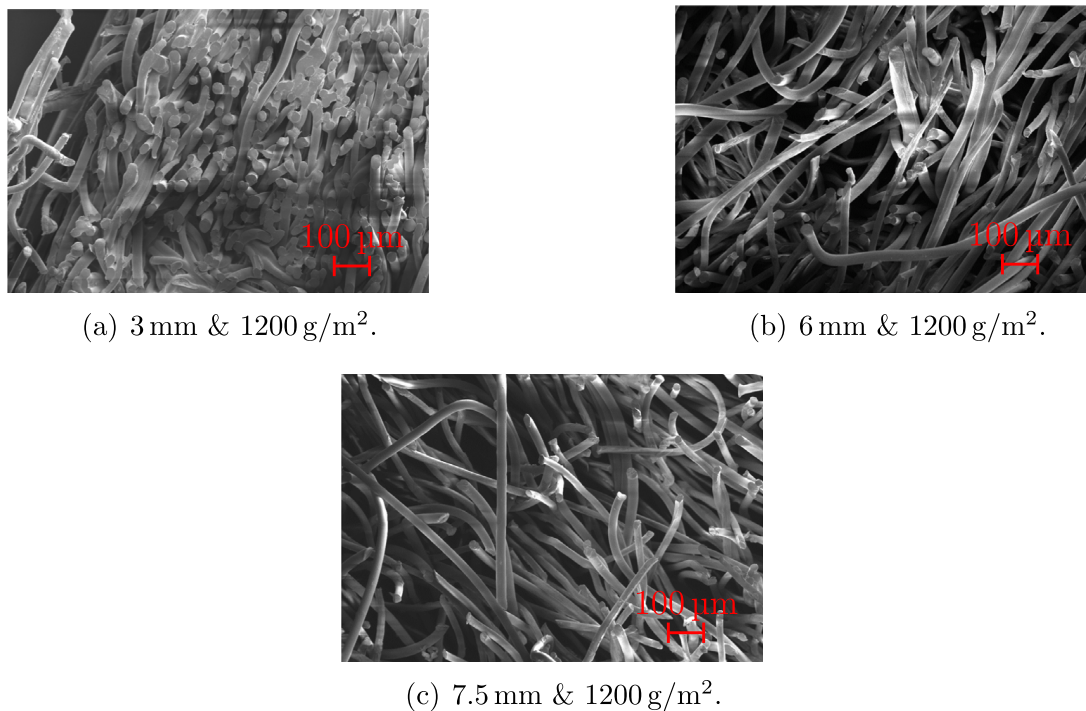


Fig. 6. SEM pictures of the nonwoven at different thicknesses and constant mass per unit area. The width of the frames are 1100 μm.

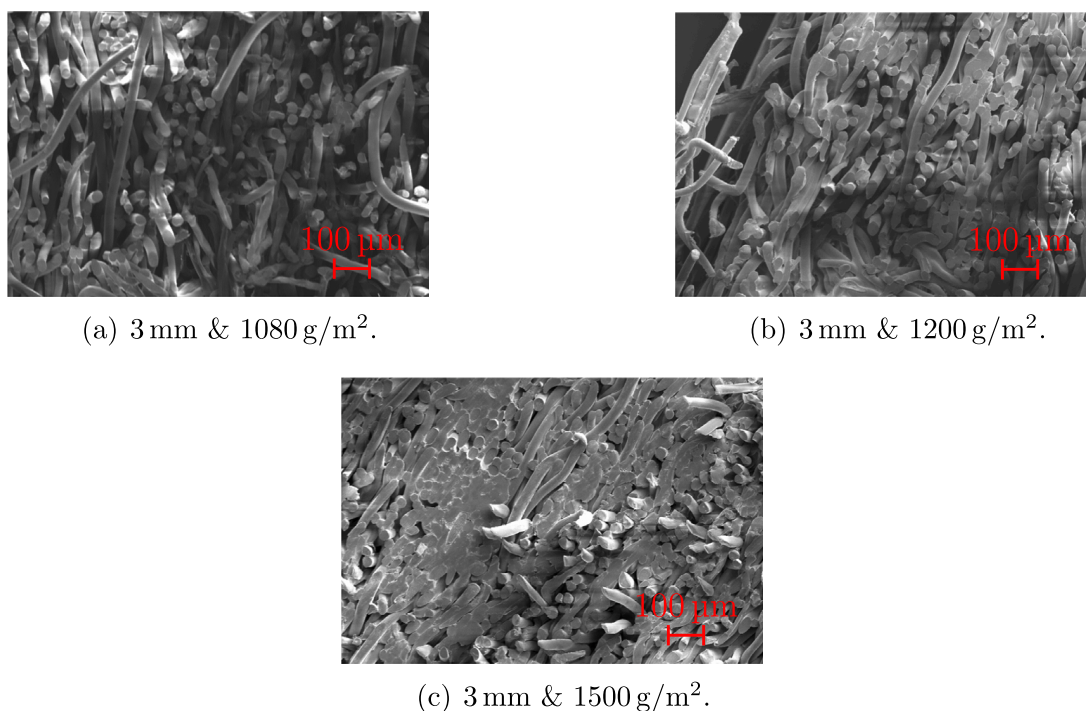


Fig. 7. SEM pictures of the nonwoven at different mass per unit area and at constant thickness 3 mm. The width of the frames are 1100 μm.

We now consider the sound absorption coefficient as a function of porosity and density. Fig. 8(a) shows this relationship at the third octave of 1000 Hz. It can be seen that there is a reciprocal influence of the two parameters. As the density increases from 0.2 g/cm<sup>3</sup> to 0.55 g/cm<sup>3</sup>, the sound absorption coefficient decreases from  $\approx 0.45$  to  $\approx 0.19$ . By increasing the porosity from  $55 \pm 3\%$  to  $86 \pm 1\%$ , the sound absorption coefficient doubles from  $\approx 0.23$  to  $\approx 0.45$ .

Fig. 8(b) shows the absorption coefficient over the density and porosity at the third octave band of 3150 Hz. We observe identical dependencies as in Fig. 8(a), but for higher values of the absorption coefficient. As the density increases from 0.2 g/cm<sup>3</sup> to 0.55 g/cm<sup>3</sup>,

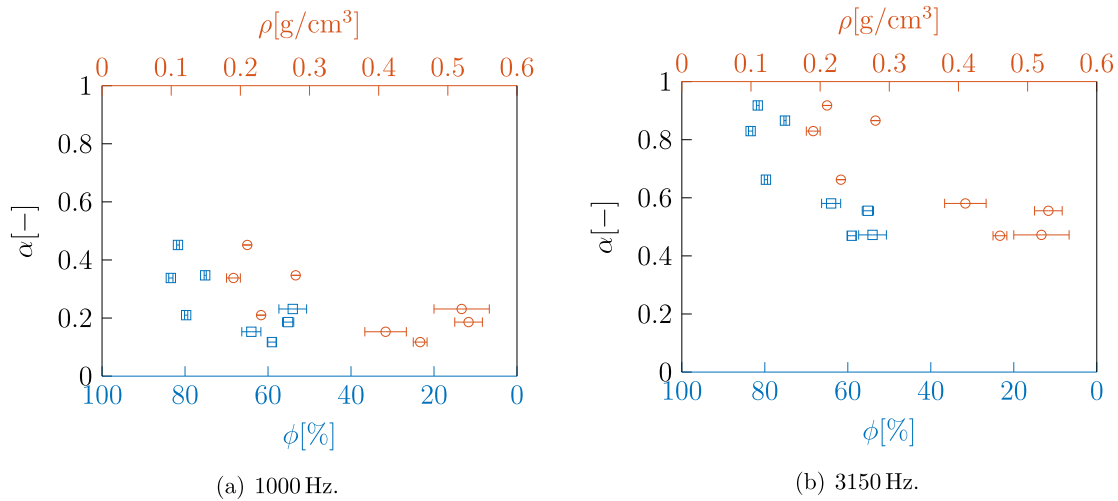


Fig. 8. Absorption coefficient over density and porosity for a frequency of 1000 Hz 8(a) and 3150 Hz 8(b).

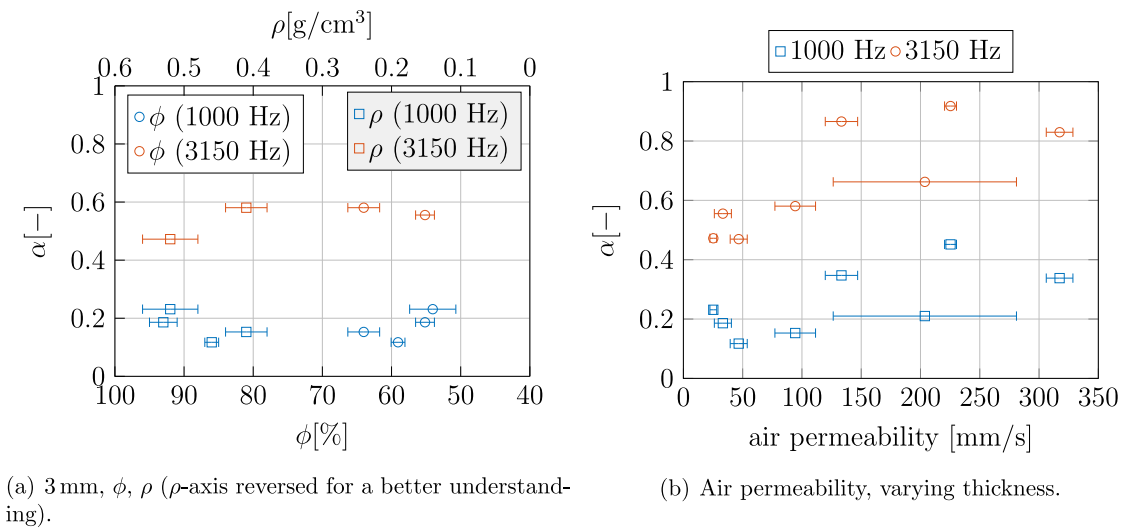


Fig. 9. Absorption coefficient over density and porosity for a frequency of 1000 Hz and 3150 Hz and constant thickness of 3 mm in Fig. 9(a). Absorption coefficient over air permeability in Fig. 9(b).

the sound absorption coefficient decreases from  $\approx 0.92$  to  $\approx 0.5$ . By increasing the porosity from  $55 \pm 3 \%$  to  $86 \pm 1 \%$ , the sound absorption coefficient doubles again from  $\approx 0.47$  to  $\approx 0.92$ .

For a better understanding of the results, we vary the density over constant thickness. This is displayed in Fig. 9(a).

It can be seen that the density exhibits different influence on the sound absorption coefficient for the two third octave bands studied, 1000 Hz and 3150 Hz. For the former band, increased density leads to increased absorption and increased porosity to decreased absorption. Regarding the latter third octave, both parameters behave in a reciprocal way. Hence, increased density leads to decreased absorption and increased porosity to increased absorption. Those findings conform with the graphs and colored regions in Fig. 5(b).

The air permeability (Fig. 9(b)) has a maximum sound absorption coefficient at around  $250 \text{ mm s}^{-1}$  to  $300 \text{ mm s}^{-1}$  for both frequencies considered. Above an air permeability of  $300 \text{ mm s}^{-1}$ , transmission dominates and hence leads to reduced sound absorption.

#### 4.2. Processing

We develop a manufacturing process for the production of a sound absorbing nonwoven material with an integrated MPP layer. The process has to fulfill financial, economical and ecological requirements specified by the car manufacturer and safety regulations. Additional specifications for the wheelhouse liner include a maximum weight of  $\approx 5 \text{ kg}$  (dependent on the model of the vehicle) and a maximum cost of  $\text{€}15$  per liner. We hence decide to use cost-effective processes such as thermal pressing and thermal forming, which are suitable for high volume production. Besides, we use a low-cost base material, such as the standard

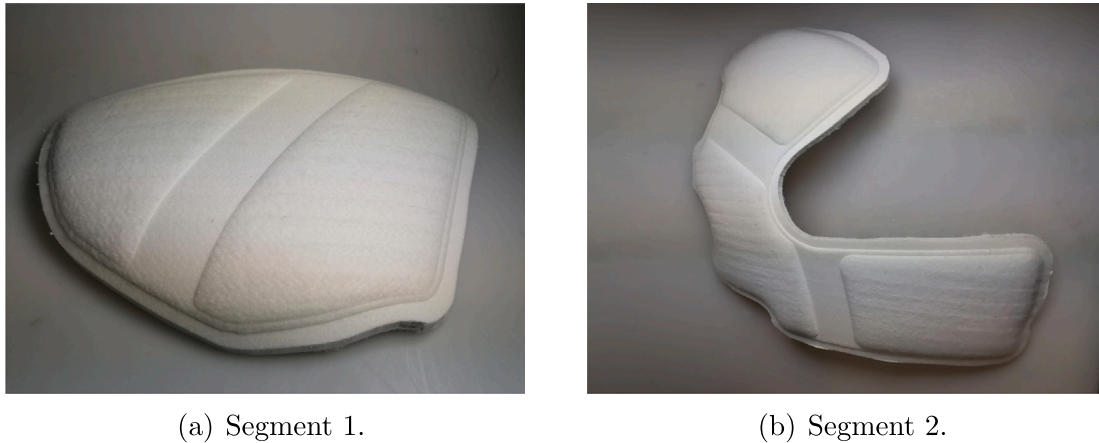


Fig. 10. Segments of the CM wheelhouse liner.

thermoplastic PES with low processing temperatures, to even further reduce costs. In a first step, we manufacture the MPP layer. We cut a polyester/polypropylene (PES/PP) nonwoven to the target dimensions. Then, the scrim is thermally consolidated at 180 °C in a double belt press to form a foil of  $1 \pm 0.04$  mm thickness. In this process, the PP fiber melts due to its low melting point and forms a compact matrix around the PES fibers. In the another pass through the double belt press, a bipolar compound film is laminated onto the surface of the PES/PP film at 140 °C to assure adhesion needed in the second step of the process. The material is perforated by a CO<sub>2</sub> laser, cutting thin holes (diameter <1 mm) to obtain the MPP layer. In a second step, we assemble the MPP and the PES-bico/GF nonwoven. The MPP and the PES-bico/GF nonwoven are arranged in form of the computed assembly and pre-tempered for further processing.

The semi-finished product is preheated for 10 min in a convection oven at 180 °C, hence the PES-bico-fiber and the two-pole compound film are above their melting temperature of 110 °C. At this point, the material is placed in the isotherm heated mold and pressed to the target thickness of 15 mm. As soon as the formed part has cooled down to the mold temperature, the mold is opened and the consolidated part is demolded.

Segments of the fiberglass PES-bico wheelhouse liner with built-in MPP layer (CM) are presented in Fig. 10.

Each wheelhouse liner consists of multiple segments (see Figs. 10(a) and 10(b)), such that the available space is maximally covered.

## 5. Validation and design modifications

In this section, the manufactured prototypes are measured and compared to the simulated data. We conduct Alpha Cabin measurements as well as full vehicle measurements. The wheelhouse liners are placed in an Alpha Cabin (<https://www.autoneum.com/de/alpha-cabin-ii/>) and excited by a sound source emitting white noise. We measure the sound pressures at four microphones in the diffuse wave field and average the acquired data. Since we know the acoustic characteristics of the empty cabin, the absorption coefficient can be determined by calculating the difference of the measurement data with and without liners. The subsequent measurements are conducted in an indoor measuring facility on a chassis dynamometer. Therefore, we are able to eliminate the influence of wind-induced noise at higher speeds. The focus of our study is on the influence of the wheelhouse liners on the pass-by noise, besides we additionally investigate the noise inside the cabin. Thus, we measure at the driver's seat, the rear seat and a microphone positioned at 7.5 m distance and 1.2 m height, regarding to regulation No. 51 (UN/ECE). Since winter tires lead to a more intensive rolling noise compared to summer tires, we use that feature to increase the significance of the measurements. Therefore, we equip the vehicle with Continental ContiWinterContact 225/55 R17 tires.

### 5.1. Fiberglass PES-bico material with MPP

In a first step the fiberglass PES-bico material with built-in MPP layer (CM) is measured in the Alpha Cabin. The design and its layers are optimized in multiple iteration steps to reach maximum absorption over a wide frequency range starting at the lowest frequency of interest, i.e. 800 Hz. We use an in-house code based on the theory by Maa and the five-parameter JCA model to compute the absorption coefficient of the CM. With the parameters being known, we set-up a COMSOL model to extract the complex surface impedance of our material. We assume infinite periodicity to reduce the computational costs. In order to find the best set-up of the CM within the restrictions set by the limited space, we run an optimization loop. Therefore, we apply a gradient-based method to find the minimum of our objective function, which is defined by Eq. (10). We hence solve a nonlinear optimization problem with upper and lower bounds for the design variables, i.e. the thickness of the arrangement of the layers. For this purpose, we use the MATLAB based function *fmincon*. The result of the optimized configuration is shown in Fig. 11. The solid blue curve indicates the measurement data, the dashed red curve the simulated one and the dotted black curve the target line to be beaten. It can be

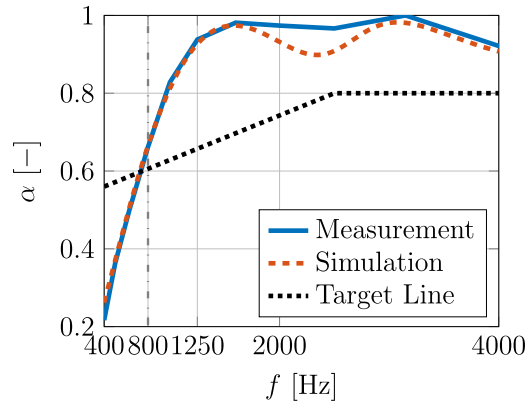


Fig. 11. Absorption coefficient of the CM.

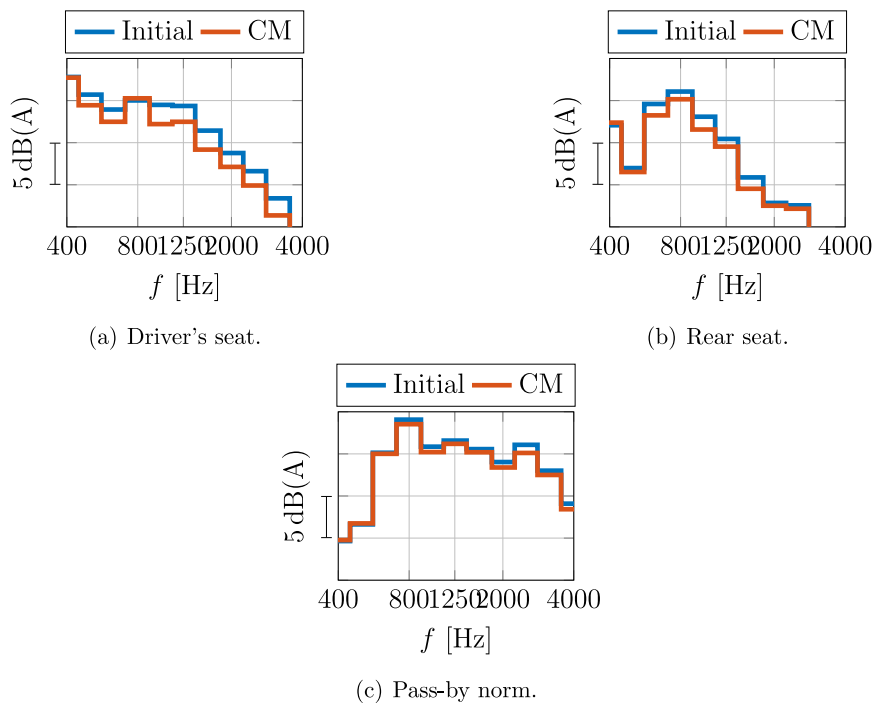


Fig. 12.  $L_p$  of the full vehicle measurements with the initial wheelhouse liner (blue) and the CM liner (red) over the frequency in third octave bands.

seen, that the absorption coefficient reaches a value of  $\alpha \approx 0.6$  at 800 Hz, complying with the defined specifications. The absorption coefficient increases with higher frequencies reaching a level of  $\alpha \approx 1$ . Therefore, it is really close to the ideal value.

In a next step, the prototypes are placed in the wheelhouses and mounted to a car. Multiple measurements are conducted in different driving maneuvers. The analysis of the pass-by measurement is based on the ISO 362-3:2016 standard. In addition to that, we use the UN ECE R51.03 supplement number 4 for indoor measurements of the pass-by noise. The effect of the modified wheelhouse liners is evaluated via simulated pass-by measurements at constant driving speeds from 40 up to 80 km/h. The position of the microphones is 7.5 m distance and 1.2 m height, which is required by the pass-by norm. The results of the spectra at the driver's seat, at the rear seat and at the pass-by norm microphones are shown with respect to third octave bands in Fig. 12.

We can see an improvement of the sound attenuation of the CM liner compared to the initial one. Particularly the cabin noise is reduced (Figs. 12(a) and 12(b)), whereas the pass-by noise seems to be less affected by the new liner Fig. 12(c). To have a clearer impression of the noise reduction, we plot the difference between the sound pressure levels of the CM liner and the initial liner in Fig. 13.

We achieve an improvement of the sound attenuation up to 3 dB compared to the initial liner. It can be seen, that the CM liner is most effective with regard to the driver's seat. A slightly lower noise reduction of up to 1.5 dB is measured at the rear seat. The pass-by noise is reduced up to 1 dB. Hence, we deduce that the wheelhouse liner mainly affects the interior cabin noise. The third octave bands colored red show the frequency bands, where the CM liner does not outperform the initial liner.



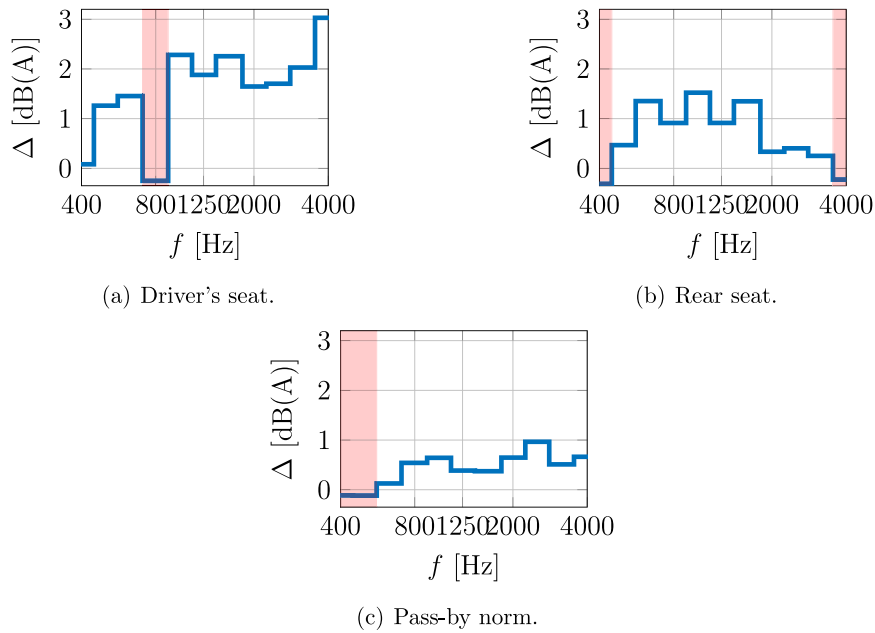


Fig. 13. Difference  $\Delta$  in dB(A) of the full vehicle measurements with the initial wheelhouse liner and the CM liner over the frequency in third octave bands. The shaded regions colored red depict the third octave bands where the CM liner does not outperform the initial liner.



Fig. 14. Schematic of the volume source and its position in the measurement set-up.

As a consequence, frequency response measurements with special volume sources are performed to investigate the impact of the liners in more detail. Fig. 14 depicts a schematic of the acoustic source in form of a dodecahedron and how it is positioned.

The contribution surfaces are characterized using a modified dodecahedron with integrated loudspeakers [55,56]. Furthermore, each single loudspeaker (marked by the colored faces) can be controlled separately or grouped to investigate the influence of each contribution surface. We use a white noise as excitation signal. To achieve as accurate results as possible, we position the dodecahedron at the wheel hub position. The different contribution surfaces are characterized based on measurements of the frequency response functions (FRFs) — grouped excitation from loudspeakers to different microphone positions —, shown in Fig. 15.

Fig. 15 shows, regarding to the microphone in 7.5 m distance, that the contact area and the tread are the surfaces with main contribution. This results are consistent with the observations made by Lafont et al. [12]. Nevertheless, the goal of our work is to design and investigate the influence of the wheelhouse liner. According to that, we focus on the curve marked by the thick blue line, which is mainly influenced by the wheelhouse liner. We can see that the contribution of the inner side of the wheel mostly gets lost in the shuffle. Except for two frequency ranges around 800 Hz and 1250 Hz, where the inner side of the wheel has a greater effect. Besides, we beforehand identified these two frequency bands as most dominant in the pass-by noise spectrum shown in Fig. 1(b). We now focus on the two dominant frequency bands in the following sections.

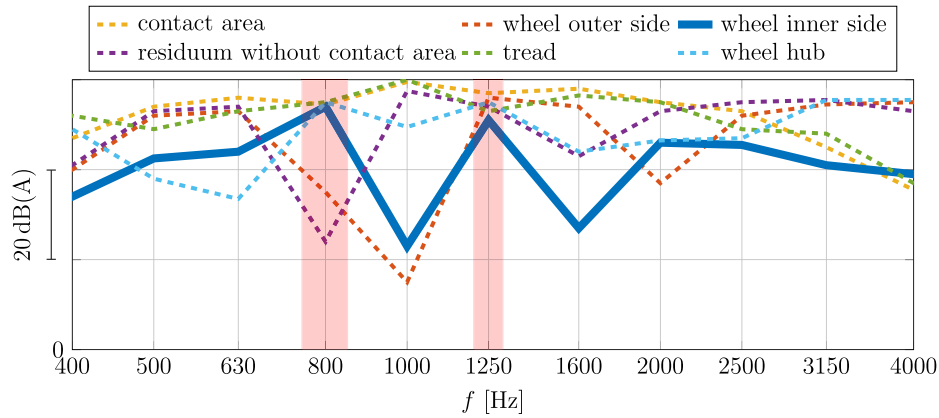


Fig. 15. Sound pressure level ( $L_p$ ) contributed by different surfaces.

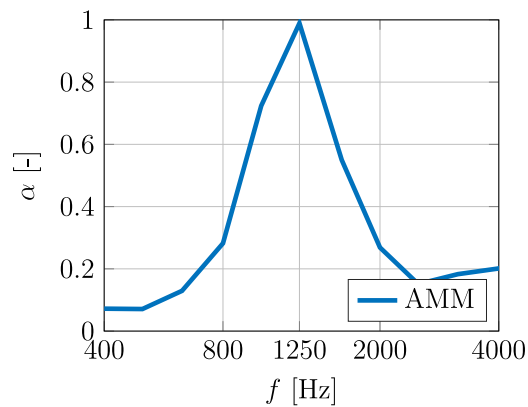


Fig. 16. Absorption coefficient of the optimized AMM.

## 5.2. Acoustic metamaterial

Based on the previous findings of the panel contributions, we develop a new design incorporating the AMM mentioned earlier in Section 3.2. The new AMM prototype is realized via additive manufacturing (fused deposition modeling). We design the AMM to achieve maximum absorption at the higher frequency of 1250 Hz, where space is limited and a larger number of resonant structures can be mounted. Impedance tube as well as Alpha Cabin measurements yield ideal absorption of the AMM at the target frequency of 1250 Hz. This is shown in Fig. 16.

The entire wheelhouse liner is too big compared to the available construction space of the printer. Therefore, we designed AMM plates that are in the dimension of the cross-section of the printer. Hence, we assemble the plates and attach them to the wheelhouse. The AMM wheelhouse liners (front-front and rear part) are displayed in Fig. 17.

Fig. 18 shows the resulting absorption coefficients for the front and rear wheelhouse liners.

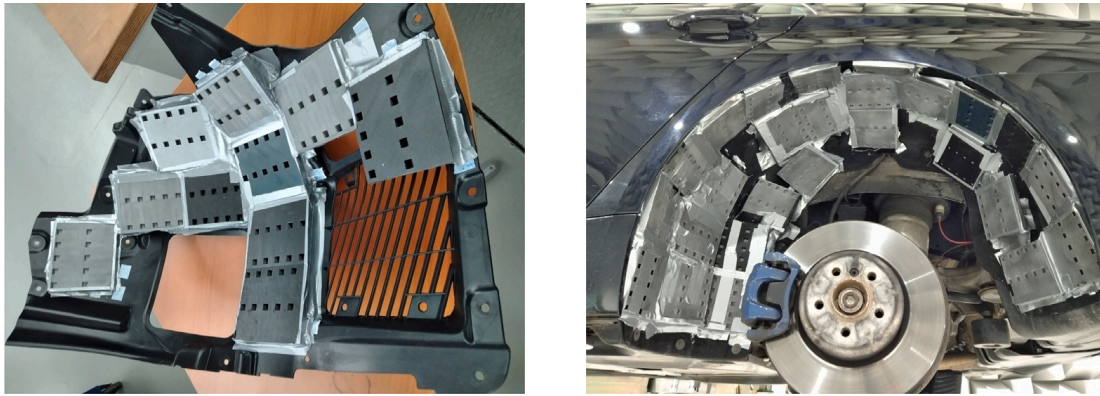
The front housing consist of two parts — denoted front-front part and rear-front part — to include the damper and the kinematics of the front axle. It can be seen that the absorption coefficient of the front part of the front liner has more than doubled compared to the initial state, regarding the frequency band from 630 to 1400 Hz. The rear part of the front liner also almost doubled its absorption coefficient in the frequency band from 800 to 1250 Hz. In addition, the rear wheelhouse liner has much better absorption values ( $\alpha_{max} \approx 0.5$ ) than the front parts ( $\alpha_{max} \approx 0.3$ ). This is due to the fact, that the front wheelhouse liner consists of two parts and has less space to install AMM plates, i.e. see Fig. 17(a).

In a last step, the AMM wheelhouse liner is evaluated via full-vehicle measurements. Fig. 19 shows the pressure difference  $\Delta$  in dB(A) of the FRFs regarding to the CM wheelhouse liner.

The AMM liner outperforms the CM liner by up to 2 dB. Particularly in the lower frequencies up to 1400 Hz for the difference between the sound pressure levels to the driver's seat and the rear seat, see Figs. 19(a) and 19(b). The influence on the pass-by noise is more or less constant up to 2800 Hz and leads to a reduction of the sound pressure level of  $\approx 0.8$  dB.

## 6. Conclusion

We show that two different design concepts of wheelhouse liners can reduce the cabin noise as well as the pass-by noise of vehicles. Both concepts are compared to the current state of the art wheelhouse liner (initial wheelhouse liner) on the market.



(a) AMM front wheelhouse liner - front part. (b) Rear AMM wheelhouse liner - mounted.

Fig. 17. The AMM liner at the front axle is made up of two parts denoted front-front and front-rear. The front-front AMM liner is shown in Fig. 17(a). The AMM liner at the rear axle consists of a single part. Fig. 17(b) displays the rear wheelhouse liner mounted to the car.

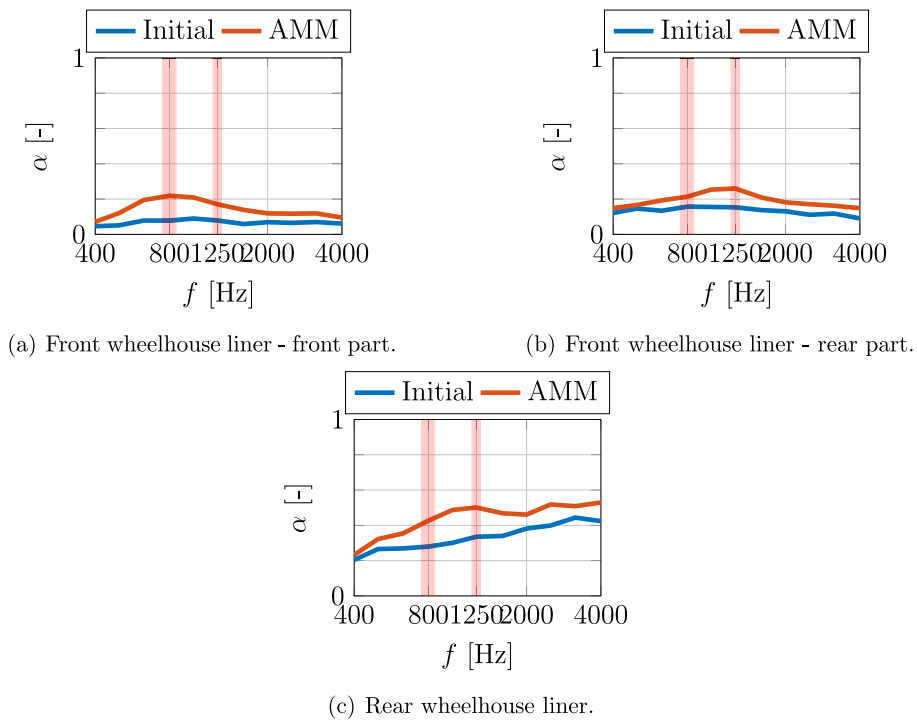


Fig. 18. Absorption coefficients of the initial wheelhouse liner and the AMM one.

We first develop a fiberglass PES bi-component material with built-in MPP layer wheelhouse liner to achieve broadband attenuation. Alpha Cabin measurements result in an absorption coefficient of  $\approx 0.6$  at 800 Hz and  $\approx 1$  from 1500 Hz upwards. Although the measured absorption coefficients are quite high and promising, we did not achieve the desired reduction of the sounds pressure level in full vehicle measurements. Nevertheless, we achieve to outperform the initial wheelhouse liner by up to 3 dB. Therefore, we conduct further measurements to identify the main contribution surfaces. Two frequency bands are determined, where the contribution of the inner side of the wheel exhibits a maximum.

Our second concept is based on an AMM that targets one of the two frequency bands of interest. The AMM prototype is realized via additive manufacturing and placed in the wheelhouse. Alpha cabin measurements show an absorption coefficient of 1 at the target frequency. Furthermore, the AMM liner outperforms the CM liner by up to 2 dB in full vehicle measurements.

The AMM wheelhouse liner showed great performance in terms of sound attenuation although the design has a sound hard surface. Thus, a more advanced wheelhouse liner can be designed by combining our AMM design and porous materials.

Another finding is discovered by analyzing the contribution of different sound sources. The effect of the wheelhouse liner with regard to the total noise of the car is of minor importance. Nevertheless, we identify two frequency ranges where the wheelhouse

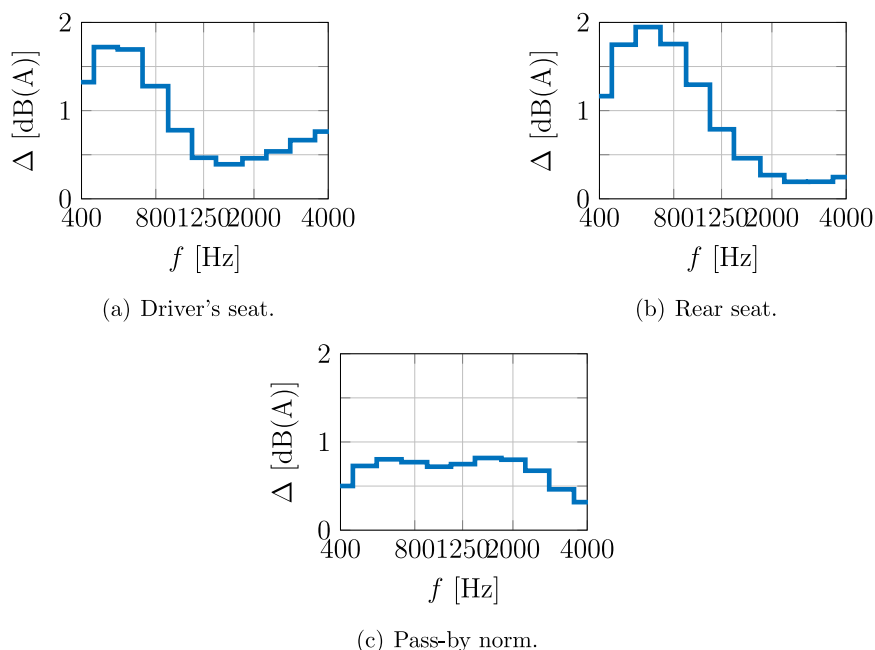


Fig. 19. Difference  $\Delta$  in dB(A) of the full vehicle measurements with the CM wheelhouse liner and the AMM liner over the frequency in third octave bands.

liner makes a substantial contribution to the pass-by noise as well as the cabin noise of the car. This is due to the contribution ratio and the absorption properties of the liners. Therefore, the application of AMMs to different areas of the car would be more effective considering sound attenuation.

The fiberglass PES bi-component material with built-in MPP layer wheelhouse liner is designed such that it retains its sound absorbing properties despite rain and dirt. However, the AMM liner is subject to dirt leading to reduced sound attenuation. This could be counteracted by applying a protective membrane layer on top of the AMM. Another approach would be to add a layer of non-woven material that covers the AMM so that its acoustic properties are also immune to rain and dirt.

We develop a concept for mass production (CM liner) that can be manufactured in the same way as today's state-of-the-art wheelhouse liners, so that the assembly of the product and its application to the wheelhouse remain unaffected. The AMM liner is purely a concept study to outline the acoustic performance and potential of acoustic metamaterials for use in wheelhouse liners. However, AMM structures could be incorporated into nonwovens by injection molding, making them suitable for mass production.

We demonstrate that the pass-by noise as well as the cabin noise is significantly affected by an AMM liner. Thus, AMMs based elements are an option for improvement of the NVH performance of vehicles and other machines. The future goal is to develop an economically advantageous manufacturing process.

#### Declaration of competing interest

The authors declare that they have no known competing financial interests or personal relationships that could have appeared to influence the work reported in this paper.

#### Data availability

The data that has been used is confidential.

#### Acknowledgments

The contribution of F. Kronowetter to this work was supported by the German Central Innovation Program for small and medium-sized enterprises (ZIM) in the context of "Development of an innovative wheelhouse liner made of metamaterial to improve sound absorption".

#### References

- [1] S. Mohammadi, A. Ohadi, A novel approach to design quiet tires, based on multi-objective minimization of generated noise, *Appl. Acoust.* 175 (2021) 107825, <http://dx.doi.org/10.1016/j.apacoust.2020.107825>, URL <https://www.sciencedirect.com/science/article/pii/S0003682X20309300>.
- [2] X. Hu, X. Liu, X. Wan, Y. Shan, J. Yi, Experimental analysis of sound field in the tire cavity arising from the acoustic cavity resonance, *Appl. Acoust.* 161 (2020) 107172, <http://dx.doi.org/10.1016/j.apacoust.2019.107172>, URL <https://www.sciencedirect.com/science/article/pii/S0003682X19300234>.

- [3] X. Hu, X. Liu, Y. Shan, T. He, Simulation and experimental validation of sound field in a rotating tire cavity arising from acoustic cavity resonance, *Appl. Sci.* 11 (3) (2021) <http://dx.doi.org/10.3390/app11031121>, URL <https://www.mdpi.com/2076-3417/11/3/1121>.
- [4] C. Wan, C.-J. Zheng, C.-X. Bi, Y.-B. Zhang, An approach for assessing the effects of porous materials on controlling the tire cavity resonance noise, *Eng. Anal. Bound. Elem.* 143 (2022) 418–427, <http://dx.doi.org/10.1016/j.enganabound.2022.06.016>, URL <https://www.sciencedirect.com/science/article/pii/S0955799722002132>.
- [5] J. Yi, X. Liu, Y. Shan, H. Dong, Characteristics of sound pressure in the tire cavity arising from acoustic cavity resonance excited by road roughness, *Appl. Acoust.* 146 (2019) 218–226, <http://dx.doi.org/10.1016/j.apacoust.2018.11.025>, URL <https://www.sciencedirect.com/science/article/pii/S0003682X18308417>.
- [6] Z. Mohamed, X. Wang, A study of tyre cavity resonance and noise reduction using inner trim, *Mech. Syst. Signal Process.* 50–51 (2015) 498–509, <http://dx.doi.org/10.1016/j.ymsp.2014.05.044>, URL <https://www.sciencedirect.com/science/article/pii/S0888327014002209>.
- [7] Z. Mohamed, X. Wang, R. Jazar, Structural-acoustic coupling study of tyre-cavity resonance, *J. Vib. Control* 22 (2) (2016) 513–529, <http://dx.doi.org/10.1177/1077546314533585>.
- [8] T. Sakata, H. Morimura, H. Ide, Effects of tire cavity resonance on vehicle road noise, *Tire Sci. Technol.* 18 (2) (1990) 68–79, <http://dx.doi.org/10.2346/1.2141695>, [arXiv:https://meridian.allenpress.com/tst/article-pdf/18/2/68/1975049/1\\_2141695.pdf](https://meridian.allenpress.com/tst/article-pdf/18/2/68/1975049/1_2141695.pdf).
- [9] D. de Klerk, A. Ossipov, Operational transfer path analysis: Theory, guidelines and tire noise application, *Mech. Syst. Signal Process.* 24 (7) (2010) 1950–1962, <http://dx.doi.org/10.1016/j.ymsp.2010.05.009>, URL <https://www.sciencedirect.com/science/article/pii/S0888327010001524> Special Issue: ISMA 2010.
- [10] D. Wang, J. Guo, X. Xiao, X. Sheng, CSA-based acoustic beamforming for the contribution analysis of air-borne tyre noise, *Mech. Syst. Signal Process.* 166 (2022) 108409, <http://dx.doi.org/10.1016/j.ymsp.2021.108409>, URL <https://www.sciencedirect.com/science/article/pii/S0888327021007597>.
- [11] H. Huang, X. Huang, W. Ding, M. Yang, D. Fan, J. Pang, Uncertainty optimization of pure electric vehicle interior tire/road noise comfort based on data-driven, *Mech. Syst. Signal Process.* 165 (2022) 108300, <http://dx.doi.org/10.1016/j.ymsp.2021.108300>, URL <https://www.sciencedirect.com/science/article/pii/S0888327021006646>.
- [12] T. Lafont, R. Stelzer, R. D'Amico, W. Kropp, C. Bertolini, Modelling tyre noise in finite element simulations for pass-by noise predictions, *Proc. Inst. Mech. Eng. C* 233 (18) (2019) 6398–6408, <http://dx.doi.org/10.1177/0954406219832908>.
- [13] H.B. Huang, J.H. Wu, X.R. Huang, M.L. Yang, W.P. Ding, The development of a deep neural network and its application to evaluating the interior sound quality of pure electric vehicles, *Mech. Syst. Signal Process.* 120 (2019) 98–116, <http://dx.doi.org/10.1016/j.ymsp.2018.09.035>, URL <https://www.sciencedirect.com/science/article/pii/S0888327018306538>.
- [14] H.B. Huang, J.H. Wu, X.R. Huang, W.P. Ding, M.L. Yang, A novel interval analysis method to identify and reduce pure electric vehicle structure-borne noise, *J. Sound Vib.* 475 (2020) 115258, <http://dx.doi.org/10.1016/j.jsv.2020.115258>, URL <https://www.sciencedirect.com/science/article/pii/S0022460X20300894>.
- [15] Y. Qin, X. Tang, T. Jia, Z. Duan, J. Zhang, Y. Li, L. Zheng, Noise and vibration suppression in hybrid electric vehicles: State of the art and challenges, *Renew. Sustain. Energy Rev.* 124 (2020) 109782, <http://dx.doi.org/10.1016/j.rser.2020.109782>, URL <https://www.sciencedirect.com/science/article/pii/S1364032120300782>.
- [16] J. Allard, Y. Champoux, New empirical equations for sound propagation in rigid frame fibrous materials, *J. Acoust. Soc. Am.* 91 (6) (1992) 3346–3353, <http://dx.doi.org/10.1121/1.402824>.
- [17] Y. Champoux, J. Allard, Dynamic tortuosity and bulk modulus in air-saturated porous media, *J. Appl. Phys.* 70 (4) (1991) 1975–1979, <http://dx.doi.org/10.1063/1.349482>.
- [18] D.L. Johnson, J. Koplik, R. Dashen, Theory of dynamic permeability and tortuosity in fluid-saturated porous media, *J. Fluid Mech.* 176 (1987) 379–402, <http://dx.doi.org/10.1017/S0022112087000727>.
- [19] D.-Y. Maa, Theory and design of microperforated panel sound-absorbing constructions, 1975.
- [20] D.-Y. Maa, Microperforated-panel wideband absorbers, *Noise Control Eng. J.* 29 (3) (1987) 77–84, <http://dx.doi.org/10.3397/1.2827694>.
- [21] D.-Y. Maa, Potential of microperforated panel absorber, *J. Acoust. Soc. Am.* 104 (5) (1998) 2861–2866, <http://dx.doi.org/10.1121/1.423870>.
- [22] X. Zhao, X. Fan, Enhancing low frequency sound absorption of micro-perforated panel absorbers by using mechanical impedance plates, *Appl. Acoust.* 88 (2015) 123–128, <http://dx.doi.org/10.1016/j.apacoust.2014.08.015>, URL <https://www.sciencedirect.com/science/article/pii/S0003682X14002229>.
- [23] A. Mosa, A. Putra, R. Ramlan, E. Al-Ameri, Micro-perforated panel absorber arrangement technique: A review, *J. Adv. Res. Dyn. Control Syst.* 10 (2018) 372–381.
- [24] Y. Qian, K. Cui, S.M. Liu, Z.B. Li, D.S. Shao, D.Y. Kong, S.M. Sun, Optimization of multi-size micro-perforated panel absorbers using multi-population genetic algorithm, *Noise Control Eng. J.* 62 (2014) <http://dx.doi.org/10.3397/1/376204>.
- [25] B. Dong, D. Xie, F. He, L. Huang, Noise attenuation and performance study of a small-sized contra-rotating fan with microperforated casing treatments, *Mech. Syst. Signal Process.* 147 (2021) 107086, <http://dx.doi.org/10.1016/j.ymsp.2020.107086>, URL <https://www.sciencedirect.com/science/article/pii/S0888327020304726>.
- [26] W. Sun, B. Pan, X. Song, H. Xiao, J. Zhou, D. Sui, A novel sound absorber design of nanofibrous composite porous material, *Mater. Des.* 214 (2022) 110418, <http://dx.doi.org/10.1016/j.matdes.2022.110418>, URL <https://www.sciencedirect.com/science/article/pii/S0264127522000399>.
- [27] N. Atalla, F. Sgard, Modeling of perforated plates and screens using rigid frame porous models, *J. Sound Vib.* 303 (2007) 195–208, <http://dx.doi.org/10.1016/j.jsv.2007.01.012>.
- [28] P. Bai, X. Yang, X. Shen, X. Zhang, Z. Li, Q. Yin, G. Jiang, F. Yang, Sound absorption performance of the acoustic absorber fabricated by compression and microperforation of the porous metal, *Mater. Des.* 167 (2019) 107637, <http://dx.doi.org/10.1016/j.matdes.2019.107637>.
- [29] Q. Zhang, Sound transmission through micro-perforated double-walled cylindrical shells lined with porous material, *J. Sound Vib.* 485 (2020) 115539, <http://dx.doi.org/10.1016/j.jsv.2020.115539>, URL <https://www.sciencedirect.com/science/article/pii/S0022460X20303710>.
- [30] Z. Liu, J. Zhan, M. Fard, J.L. Davy, Acoustic measurement of a 3D printed micro-perforated panel combined with a porous material, *Measurement* 104 (2017) 233–236, <http://dx.doi.org/10.1016/j.measurement.2017.03.032>, URL <https://www.sciencedirect.com/science/article/pii/S0263224117302002>.
- [31] K. Sakagami, S. Kobatake, K. Kano, M. Morimoto, M. Yairi, Sound absorption characteristics of a single microperforated panel absorber backed by a porous absorbent layer, *Acoust. Aust.* 39 (2011).
- [32] S. Cummer, J. Christensen, A. Alù, Controlling sound with acoustic metamaterials, *Nat. Rev. Mater.* 1 (2016) 16001, <http://dx.doi.org/10.1038/natrevmats.2016.1>.
- [33] J.J. Wu, F. Ma, S. Zhang, L. Shen, Application of acoustic metamaterials in low-frequency vibration and noise reduction, *J. Mech. Eng.* 52 (2016) 68–78, <http://dx.doi.org/10.3901/JME.2016.13.068>.
- [34] P.A. Deymier, *Acoustic Metamaterials and Phononic Crystals*, Springer, 2013, <http://dx.doi.org/10.1007/978-3-642-31232-8>.
- [35] G. Ma, P. Sheng, Acoustic metamaterials: From local resonances to broad horizons, *Sci. Adv.* 2 (2) (2016) <http://dx.doi.org/10.1126/sciadv.1501595>.
- [36] F. Zangeneh-Nejad, R. Fleury, Active times for acoustic metamaterials, *Rev. Phys.* 4 (2019) 100031, <http://dx.doi.org/10.1016/j.revip.2019.100031>.
- [37] A. Melnikov, Y.K. Chiang, L. Quan, S. Oberst, A. Alù, S. Marburg, D.A. Powell, Acoustic meta-atom with experimentally verified maximum Willis coupling, *Nature Commun.* 10 (1) (2019) 3148, <http://dx.doi.org/10.1038/s41467-019-10915-5>.
- [38] G.W. Milton, J.R. Willis, On modifications of Newton's second law and linear continuum elastodynamics, *Proc. R. Soc. A: Math. Phys. Eng. Sci.* 463 (2079) (2007) 855–880, <http://dx.doi.org/10.1098/rspa.2006.1795>.

- [39] S. Yao, X. Zhou, G. Hu, Experimental study on negative effective mass in a 1D mass–spring system, *New J. Phys.* 10 (4) (2008) 43020, <http://dx.doi.org/10.1088/1367-2630/10/4/043020>.
- [40] Z. Liu, X. Zhang, Y. Mao, Y.Y. Zhu, Z. Yang, C.T. Chan, P. Sheng, Locally resonant sonic materials, *Science* 289 (5485) (2000) 1734 LP – 1736, <http://dx.doi.org/10.1126/science.289.5485.1734>.
- [41] N. Fang, D. Xi, J. Xu, M. Ambati, W. Srituravanich, C. Sun, X. Zhang, Ultrasonic metamaterials with negative modulus, *Nature Mater.* 5 (6) (2006) 452–456, <http://dx.doi.org/10.1038/nmat1644>.
- [42] J.B. Pendry, Negative refraction makes a perfect lens, *Phys. Rev. Lett.* 85 (18) (2000) 3966–3969, <http://dx.doi.org/10.1103/PhysRevLett.85.3966>.
- [43] H. Ruiz, C.C. Claeys, E. Deckers, W. Desmet, Numerical and experimental study of the effect of microslits on the normal absorption of structural metamaterials, *Mech. Syst. Signal Process.* 70–71 (2016) 904–918, <http://dx.doi.org/10.1016/j.ymssp.2015.09.028>, URL <https://www.sciencedirect.com/science/article/pii/S0888327015004409>.
- [44] L. Quan, Y. Ra’di, D.L. Sounas, A. Alù, Maximum Willis coupling in acoustic scatterers, *Phys. Rev. Lett.* 120 (2018) 254301, <http://dx.doi.org/10.1103/PhysRevLett.120.254301>, URL <https://link.aps.org/doi/10.1103/PhysRevLett.120.254301>.
- [45] Y.K. Chiang, S. Oberst, A. Melnikov, L. Quan, S. Marburg, A. Alù, D.A. Powell, Reconfigurable acoustic metagrating for high-efficiency anomalous reflection, *Phys. Rev. A* 13 (2020) 064067, <http://dx.doi.org/10.1103/PhysRevApplied.13.064067>.
- [46] V.C. Henriquez, P.R. Andersen, J.S. Jensen, P.M. Juhl, J. Sánchez-Dehesa, A numerical model of an acoustic metamaterial using the boundary element method including viscous and thermal losses, *J. Comput. Acoust.* 25 (04) (2017) 1750006, <http://dx.doi.org/10.1142/S0218396X17500060>.
- [47] V.C. Henriquez, V.M. García-Chocano, J. Sánchez-Dehesa, Viscothermal losses in double-negative acoustic metamaterials, *Phys. Rev. Appl.* 8 (2017) 014029, <http://dx.doi.org/10.1103/PhysRevApplied.8.014029>, URL <https://link.aps.org/doi/10.1103/PhysRevApplied.8.014029>.
- [48] L. Sangiuliano, B. Reff, J. Palandri, F. Wolf-Monheim, B. Pluymers, E. Deckers, W. Desmet, C.C. Claeys, Low frequency tyre noise mitigation in a vehicle using metal 3D printed resonant metamaterials, *Mech. Syst. Signal Process.* 179 (2022) 109335, <http://dx.doi.org/10.1016/j.ymssp.2022.109335>, URL <https://www.sciencedirect.com/science/article/pii/S0888327022004708>.
- [49] L. Sangiuliano, R. Boukadia, E. Deckers, W. Desmet, C. Claeys, Reduction of structure-Borne tyre/road noise through rubber resonant metamaterials in tyres, in: 12th International Styrian Noise, Vibration & Harshness Congress: the European Automotive Noise Conference, SAE International, 2022, <http://dx.doi.org/10.4271/2022-01-0954>.
- [50] Y. Liao, H. Huang, G. Chang, D. Luo, C. Xu, Y. Wu, J. Tang, Research on low-frequency noise control of automobiles based on acoustic metamaterial, *Materials* 15 (9) (2022) <http://dx.doi.org/10.3390/ma15093261>, URL <https://www.mdpi.com/1996-1944/15/9/3261>.
- [51] K.-J. Chang, J. Jung, H.-G. Kim, D. Choi, S. Wang, An application of acoustic metamaterial for reducing noise transfer through car body panels, *SAE Tech. Pap.* (2018) <http://dx.doi.org/10.4271/2018-01-1566>.
- [52] M. Möser, *Technische Akustik*, 2015, p. 545, <http://dx.doi.org/10.1007/978-3-662-47704-5>.
- [53] B.H. Song, J.S. Bolton, A transfer-matrix approach for estimating the characteristic impedance and wave numbers of limp and rigid porous materials, *J. Acoust. Soc. Am.* 107 (3) (2000) 1131–1152, <http://dx.doi.org/10.1121/1.428404>.
- [54] L. Sun, H. Hou, L.-Y. Dong, F.-R. Wan, Measurement of characteristic impedance and wave number of porous material using pulse-tube and transfer-matrix methods, *J. Acoust. Soc. Am.* 126 (6) (2009) 3049–3056, <http://dx.doi.org/10.1121/1.3242354>.
- [55] J. Putner, M. Lohrmann, H. Fastl, *Analysis of the contributions from vehicle cabin surfaces to the interior noise*, 2013.
- [56] N.M. Papadakis, G.E. Stavroulakis, Review of acoustic sources alternatives to a dodecahedron speaker, *Appl. Sci.* 9 (18) (2019) <http://dx.doi.org/10.3390/app9183705>, URL <https://www.mdpi.com/2076-3417/9/18/3705>.

## 5.5 Publication AP5

# Realistic prediction and engineering of high-Q modes to implement stable Fano resonances in acoustic devices

Received: 25 November 2022

Accepted: 17 October 2023

Published online: 27 October 2023

 Check for updates

Felix Kronowetter<sup>1,2,3</sup>✉, Marcus Maeder<sup>1</sup>, Yan Kei Chiang<sup>2</sup>, Lujun Huang<sup>2</sup>, Johannes D. Schmid<sup>1</sup>, Sebastian Oberst<sup>3</sup>, David A. Powell<sup>2</sup> & Steffen Marburg<sup>1</sup>

Quasi-bound states in the continuum (QBICs) coupling into the propagating spectrum manifest themselves as high-quality factor (Q) modes susceptible to perturbations. This poses a challenge in predicting stable Fano resonances for realistic applications. Besides, where and when the maximum field enhancement occurs in real acoustic devices remains elusive. In this work, we theoretically predict and experimentally demonstrate the existence of a Friedrich-Wintgen BIC in an open acoustic cavity. We provide direct evidence for a QBIC by mapping the pressure field inside the cavity using a Laser Doppler Vibrometer (LDV), which provides the missing field enhancement data. Furthermore, we design a symmetry-reduced BIC and achieve field enhancement by a factor of about three compared to the original cavity. LDV measurements are a promising technique for obtaining high-Q modes' missing field enhancement data. The presented results facilitate the future applications of BICs in acoustics as high-intensity sound sources, filters, and sensors.

Bound states in the continuum were first established by Neumann and Wigner<sup>1</sup> in the context of an electron that remains in its orbit, although it has enough energy to overcome the attractive forces and propagate to infinity. The transfer to acoustics was made by Ursell<sup>2</sup> followed by seminal works on symmetry-protected BICs<sup>3–6</sup>, Fabry–Pérot BICs<sup>7–9</sup>, and Friedrich–Wintgen BICs<sup>8,10–12</sup>.

In linear acoustics, the continuous spectrum of an open system is spanned by propagating waves that radiate to infinity, i.e., the solutions corresponding to complex eigenfrequencies greater than or equal to the cut-off frequency of the system. Propagating waves can also be described as extended states with an outgoing energy flux. Apart from the continuum or several continua, the total frequency spectrum of the open system includes localized solutions corresponding to discrete eigenvalues. Localized solutions corresponding to discrete eigenvalues outside the continuous spectrum are called bound states. Bound states are perfectly confined waves

since they are completely decoupled from open propagation channels and carry no outgoing energy flux, hence they can't radiate away. In contrast, localized solutions in the continuum generally couple to open propagation channels, becoming leaky resonances. The eigenfrequency of the highly localized quasi-trapped modes is complex, in which the real part denotes the resonance frequency, and the imaginary part characterizes the radiation loss<sup>13,14</sup>. For a particular configuration of the geometric parameters, the radiation loss vanishes and the resonances become confined states. These localized solutions to discrete eigenvalues coexisting with propagating waves are known as embedded trapped modes or, more commonly BICs. From the mathematical point of view, the discrete eigenvalues of BICs can be described by purely real eigenfrequencies. Since BICs are localized solutions, they are invisible to extended states in the first propagation channel, hence they cannot be excited by them.

<sup>1</sup>Chair of Vibro-Acoustics of Vehicles and Machines, Department of Engineering Physics and Computation, TUM School of Engineering and Design, Technical University of Munich, Bavaria, Germany. <sup>2</sup>School of Engineering and Information Technology, University of New South Wales, Northcott Drive, Canberra, ACT 2600, Australia. <sup>3</sup>School of Mechanical and Mechatronic Engineering, Centre for Audio, Acoustics and Vibration, Faculty of Engineering and IT, University of Technology Sydney, Sydney, Australia. ✉e-mail: [felix.kronowetter@tum.de](mailto:felix.kronowetter@tum.de)



In recent years, extensive theoretical studies on numerous BIC configurations and BIC tuning have been conducted<sup>15–23</sup>. Additionally, geometrical phase engineering of BICs extending Fano resonances beyond their conventional limits is investigated<sup>17</sup>. Furthermore, the theoretical and experimental demonstration of BIC-induced high Q-factors<sup>24,25</sup> can be applied to the design of novel, high-performance acoustics sensors. Huang et al.<sup>26</sup> demonstrate a Friedrich–Wintgen quasi-BIC leading to emission enhancement of a sound source by nearly two orders of magnitude. Recent studies have suggested that acoustodynamic devices can be used for quantum computing<sup>27–30</sup>, where the application of mechanical BIC-induced high-Q Fano resonances (e.g., Yu et al.<sup>31</sup>) could be of further interest. A comprehensive review of BICs can be found in Hsu et al.<sup>32</sup>, Pagneux<sup>33</sup>, Joseph<sup>34</sup>, and Sadreev<sup>35</sup>.

All aforementioned studies lack information on the exact sound pressure field inside the resonant cavity leading to BIC formation under realistic conditions. Here, we demonstrate a BIC induced by mode interference or Friedrich–Wintgen BIC. The specific design of the resonator geometry and measurement technique allows us to measure the transmission spectrum and map the sound pressure field inside the cavity using laser Doppler vibrometry. This technique leads to the first visual proof of an acoustic BIC and, most notably, provides direct access to the pressure distribution inside the cavity. Thus, it is possible to run a detailed analysis of the sound pressure field and its contribution to the reflection or transmission spectrum. Our findings lead to a new type of Friedrich–Wintgen BIC relying on reduced symmetry and the principle of mirror sources resulting in a high-Q mode without exciting unwanted resonances. We further present the first direct visualization of a Friedrich–Wintgen BIC using laser Doppler vibrometry as a pressure field mapping technique. We use laser Doppler vibrometry measurements to obtain a complete mapping of the sound pressure field to better understand BIC formation in the presence of realistic losses. The reflection and transmission spectra are obtained using microphones but do not provide information about the exact pressure enhancement inside the cavity. The pressure distribution inside the cavity is needed to develop high-performance acoustic devices based on BICs, such as acoustic sources and sound lasers. Because BICs are extremely sensitive, any perturbation of the high-Q mode, energy extraction, or backscattering from microphones will degrade the BIC, so we use this technique to avoid any perturbation of

the pressure field. By mapping the sound pressure field of the BIC, we have direct access to the actual pressure values and thus to the critical information of when and where the pressure magnitude reaches a maximum. The interaction between the localized thermo-viscous losses and the concentrated high-intensity fields of the BIC is the key to determining the achievable Q-factor and pressure field enhancement. We facilitate the accurate analysis of high-Q modes in the presence of realistic losses, determine the configuration with maximum pressure enhancement, and enable the future application of high-Q Fano resonances to acoustic devices.

## Results

Here, we consider a BIC associated with the Friedrich–Wintgen full destructive interference of degenerate modes of the same symmetry. Friedrich and Wintgen<sup>10</sup> demonstrated the formation of BICs due to the interference of resonances belonging to different channels. In contrast to symmetry-protected BICs in waveguides, Friedrich–Wintgen BICs occur above the cut-off frequency of the first duct cross-mode (antisymmetric about the duct axis) and close to the point of modal degeneracy of the closed system. Friedrich–Wintgen BICs have the special feature that BICs still form, even if the symmetry of the system is broken<sup>8</sup>. An open system with a non-Hermitian Hamiltonian is a prerequisite for the observation of BICs since they are forbidden in compact systems<sup>36,37</sup>. We use coupled-mode theory<sup>15,23,35,38</sup> to predict the point of modal degeneracy for a closed cavity. See Supplementary Information Section 1 for a complete theoretical analysis. By coupling the cavity to an acoustic waveguide, the localized solutions of the closed cavity turn into leaky resonances. Hence, we investigate the complex eigenfrequencies and corresponding modes of a resonant cavity with open ends. By variation of the geometrical parameters, the relevant eigenfrequencies and modes are identified, forming a BIC. The existence of a Friedrich–Wintgen BIC is numerically shown for a non-rotationally symmetric duct-cavity structure with open ends, i.e., a rectangular cavity placed in a tubular waveguide. A schematic illustration of the structure is displayed in Fig. 1a.

We chose this structure since the formed BIC is stable against asymmetry and isolated in the studied frequency range, i.e., the BIC is robust even in the presence of manufacturing imperfections and no further resonance peaks are found. Embedded trapped modes can only be found for a particular configuration of the geometric

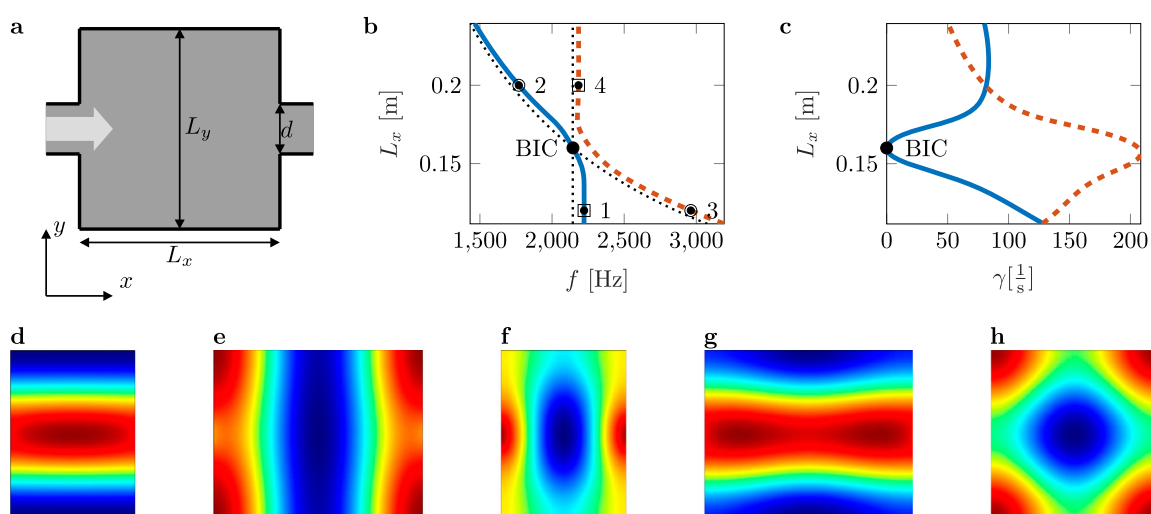


**Fig. 1 | BIC in an open acoustic resonator.** **a** Schematic of a resonant cavity coupled to an acoustic waveguide. The  $z$ -axis is perpendicular to the  $xy$ -plane. The length  $L_y$  is set to 160 mm and the diameter  $d$  of the pipe to 40 mm. **b** Avoided crossing of the real parts of high-Q and low-Q modes for varying length  $L_x$  of the resonant cavity. **c** Vanishing imaginary part of the BIC, where the BIC mode

dominates the decay process. **d–h** Interacting modes of different configurations of  $L_x$  (**d**  $M_{131}$  (at point 1 in **(b)**), **e**  $M_{311}$  (at point 2 in **(b)**), **f**  $M_{311}$  (at point 3 in **(b)**), **g**  $M_{131}$  (at point 4 in **(b)**)), as well as the mode shape of the BIC (**h**  $M_{331}$ ), are shown, corresponding to the points marked in **(b)**.

parameters of the system and are a result of modal coupling via a common continuum, i.e., the interaction of modes of the same symmetry. As a consequence of the interaction, avoided crossings are observed, where the real parts of the eigenfrequencies cross with modal interchange and a weakly damped resonance dominates the decay process. This is also called resonance trapping<sup>39,40</sup> and is shown by the blue and orange lines in Fig. 1b, c. The exact mechanism of BIC formation as well as the complex eigenfrequencies are presented in Supplementary Information Sections 2 and 3. The thin black dotted lines are the results of the coupled mode theory for a closed cavity. Consequently, the crossing point of the black lines is the point of modal degeneracy and exactly predicts the BIC. We solve a numerical problem, including thermo-viscous losses, to take dissipation in the boundary layer into account, leading to a reduced Q-factor (shown in Supplementary Information Section 4). Referring to Lyapina et al.<sup>15</sup>, the leaky modes are denoted by  $M_{pqr}$ , with  $p$ ,  $q$ , and  $r$  being the number of maxima in the pressure field along the  $x$ -,  $y$ -, and  $z$ -axis, respectively. The distance  $L_x$  is varied with the resulting modal interchange depicted regarding mode  $M_{131}$  in Fig. 1d, becoming mode  $M_{311}$  in Fig. 1e and mode  $M_{311}$  in Fig. 1f, turning into mode  $M_{131}$  in Fig. 1g, respectively. Additionally, the BIC mode  $M_{331}$  is shown in Fig. 1h. The BIC is observed at a frequency of  $f=2145$  Hz with a cavity length of  $L_x=160$  mm. Excellent agreement is found between the numerically computed eigenfield profile of the Friedrich–Wintgen BIC and the eigenfield profile predicted by the analytical solution, see Supplementary Information Section 1.

### Experimental verification of BIC

To experimentally demonstrate the existence of the predicted BIC, we manufacture three samples of the resonant cavity with varying dimensions  $L_x$  shown in Fig. 2a.

The samples are fabricated using selective laser sintering to keep manufacturing tolerances small and avoid asymmetry in our geometry. Furthermore, the walls are designed to be thick enough to suppress structural resonances in the frequency range of interest. In experiments, we use an impedance tube to obtain the transmission spectrum. The measurement setup is depicted in Fig. 2b, where the sample is integrated into the tube. The diameter of the tube, as well as the

height and depth of the cavity, are kept constant at  $d=40$  mm,  $L_y=160$  mm, and  $L_z=d=40$  mm, cf. Fig. 1a. The length of the cavity  $L_x$  is set to 160, 165, and 170 mm (left to right in Fig. 2a), respectively. Hence, we realize a parameter variation in the vicinity of the BIC configuration.

BICs couple into extended states and become QBICs if the BIC configuration of the system is disturbed. QBICs are slightly damped complex resonances that radiate energy and reveal themselves in the form of Fano resonances. Fano resonances are a well-studied phenomenon in many different fields of physics, e.g., see the detailed review by Miroshnichenko et al.<sup>41</sup>. Therefore, the second and third samples are designed such that QBICs can be measured. Due to the destructive interference of bound states and continua, the typical resonance and antiresonance features of the asymmetric Fano resonances can be observed, in the sound transmission spectrum, see Fig. 2c. In contrast to the BIC, we identify Fano peaks of finite height and increased width.

The Fano peak widens and a frequency shift toward lower frequencies is observed due to the increased cavity volume as  $L_x$  is increased from the BIC configuration. We can see that the numerical results coincide with the experimental ones and also show the expected behavior. Additionally, the transmission loss (TL) of the system is plotted over the frequency for all three configurations. The Fano peak of the transmission spectrum leads to a high amplitude in the TL. Similar to the previously mentioned behavior of the Fano peaks, the TL peaks broaden and lessen with increasing  $L_x$ . Nevertheless, the TL peak of  $L_x=165$  mm seems to be lower than the one of  $L_x=170$  mm shown in Fig. 2d. Thermo-viscous losses affect the amplitude of the TL more strongly the closer we get to the BIC configuration. The measured Q-factors for  $L_x=165$  mm and  $L_x=170$  mm are 328 and 302, respectively. In the case of the BIC configuration being restored, the Fano resonances collapse. This state is described as the ghost of the Fano resonance by Ladron de Guevara et al.<sup>42</sup> and can be identified in Fig. 2c, d regarding the blue lines, i.e., no Fano peak is present.

### Visualization of QBIC

Three continua exist in our duct-cavity structure. The first continuum is symmetric to the duct axis, with a lower limit defined by the cut-off

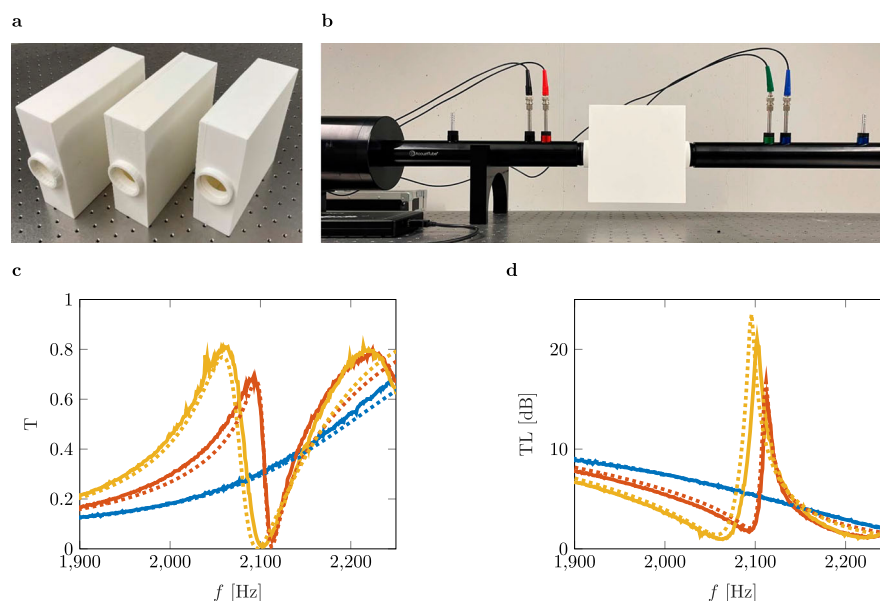


**Fig. 2 | Transmission spectra of cavities of varying lengths.** **a** Images of three manufactured samples with different dimensions  $L_x$ . **b** Transmission measurement set-up. **c, d** Transmission coefficient as well as the transmission loss in the frequency range 1900–2250 Hz. The blue lines represent the results of the

measurement and the numerical simulation of the BIC configuration ( $L_x=160$  mm), respectively. The orange lines represent the results of  $L_x=165$  mm, and the yellow lines are the ones of  $L_x=170$  mm.

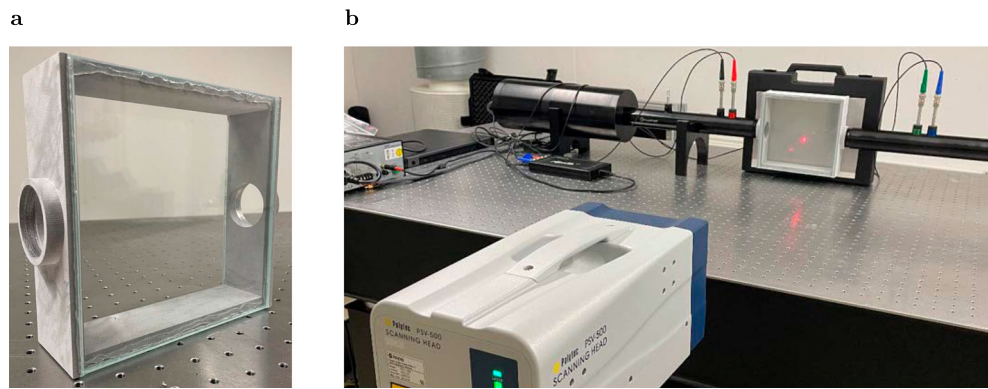


**Fig. 3 | Experimental set-up for the visualization of the sound pressure field.** **a** Printed sample with high-transmission glass mounted as side walls. **b** Experimental set-up for the refracto-vibrometry measurements.

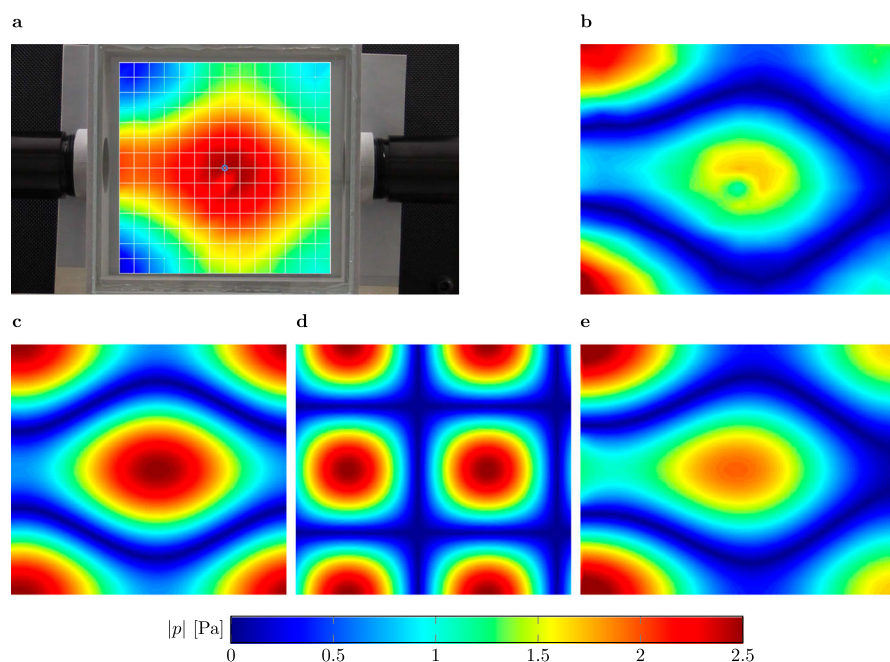


**Fig. 4 | Sound pressure field visualization.** **a** Visualization of the real part of the sound pressure field inside the cavity. The red color indicates a pressure maximum and the blue color a minimum, respectively. **b** Absolute value of the measured pressure field. **c** Superposition of the four most dominant modes (modes with the

highest FFT coefficients). **d** Superposition of the next four modes with high coefficients. **e** Simulation results. The colored scales display the absolute values of the pressure in Pa, with the pressure being normalized to the incident pressure field.

frequency of the duct. The second and third continua have lower limits defined by the cut-off frequencies of the first duct cross-mode and the first cavity cross-mode (symmetric to the  $y$ -axis), respectively. The shortest side of the cavity is chosen such that it matches the diameter of the pipe. Therefore, we expect unitary pressure distribution in this direction. This enables experiments applying refracto-vibrometry to visualize the sound pressure field of the QBIC. A new sample is manufactured, allowing a laser to pass through the structure. To do so, two side walls are replaced by high-transmission glass, as shown in Fig. 3a.

We chose the  $L_x = 170$  mm configuration of the previous measurements for the new sample since the Fano peak is the widest. This is crucial for the measurement, in which we have a single excitation frequency matching the frequency of the QBIC. Due to the sensitivity of the QBIC, the gradient of the Fano peak should be as low as possible to ensure that we find the QBIC. The sample is placed in the impedance tube set-up.

To conduct the refracto-vibrometry, a laser Doppler scanning vibrometer PSV-500 from Polytec (Polytec GmbH, Waldbronn,

Germany) is used to measure the changes of the refractive index of the fluid, which is proportional to the acoustic pressure variation within the cavity<sup>43–46</sup>:

$$v(\omega) = \omega \frac{1}{\gamma p_0} \frac{n_0 - 1}{n_0} \int_L p(l, \omega) dl \quad (1)$$

where  $\omega$  is the angular frequency,  $v$  is the LDV velocity,  $p$  is the sound pressure,  $n_0$  is the refractive index of air at standard atmospheric pressure,  $p_0$  is the static atmospheric pressure, and  $\gamma$  is the specific heat capacity ratio of air. The basic principle of the LDV is based on the well-known Doppler shift. The pressure waves inside the cavity slightly shift the phase of the emitted monochromatic laser light. The superimposition of the reflected and emitted laser light produces a speckle pattern on the photodetector, which allows the measurement of the corresponding frequency of the pressure waves and the change in the refractive index. The latter is proportional to the sound pressure inside the cavity. This makes it possible to visualize the corresponding

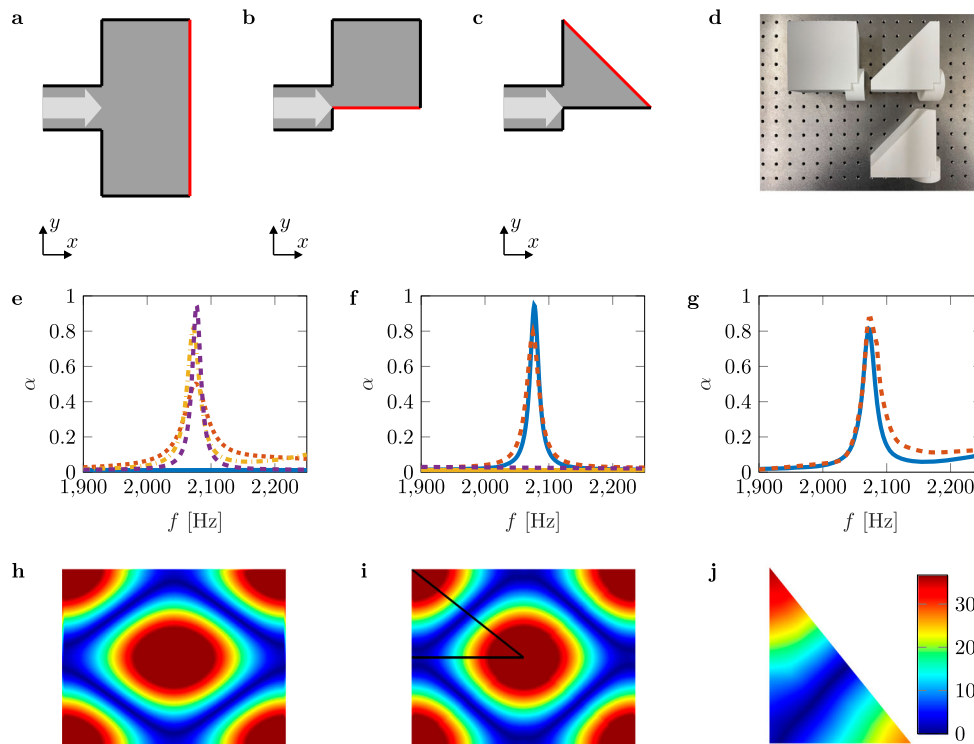


**Fig. 5 | Experimental verification of symmetry-reduced BICs.** **a** Schematic of a resonant cavity similar to that shown in Fig. 1a. The  $z$ -axis is perpendicular to the  $xy$ -plane. The length  $L_y$  is set to 160 mm, and the diameter  $d$  of the pipe to 40 mm. We halve the cavity at the axis of symmetry (highlighted in red) based on the principle of mirror sources and thus obtain a cavity length of  $L_x = 85$  mm, which corresponds to half the length of the configuration with  $L_x = 170$  mm. **b** Further reduction of the configuration in a using the principle of mirror sources once again. **c** Fully reduced configuration. **d** Manufactured samples for configurations **b** ( $L_x = 85$  mm) and **c** ( $L_x = 85$  mm for the top sample and  $L_x = 77$  mm for the bottom sample). **e** Absorption coefficient  $\alpha$  in the frequency range 1900–2250 Hz. The blue line represents the result of the numerical simulation of the BIC configuration of **c** with  $L_x = 77$  mm. The orange dotted line, the yellow dash-dotted line, and the purple dashed line represent the numerical results of  $L_x = 85$  mm for the configurations

(**a–c**), respectively. **f** Absorption coefficient  $\alpha$  in the frequency range 1900–2250 Hz. The blue and yellow lines represent the results of the numerical simulation of the BIC configuration of **c** with  $L_x = 85$  mm and  $L_x = 77$  mm, respectively. The orange and the purple dashed lines represent the measurement results of configuration **c** with  $L_x = 85$  mm and  $L_x = 77$  mm. **g** The computed and measured absorption coefficients for configuration **b** are represented by the blue and orange dashed lines, respectively. **h** Sound pressure field of the BIC mode inside the cavity with  $L_x = 170$  mm. **i** Sound pressure field of the BIC mode inside the fully reduced cavity with  $L_x = 85$  mm for configuration (**c**), framed by the black lines and extrapolated to the rectangular cavity. **j** Measured absolute sound pressure inside the fully reduced cavity with  $L_x = 67$  mm excited at 2315 Hz. The color scale represents the absolute pressure in Pa.

pressure distribution. The measured pressure distribution of the QBIC is displayed together with the results of the corresponding finite element simulations in Fig. 4.

The visualized sound pressure field of the QBIC within the experimental set-up is presented in Fig. 4a. In addition, we show a mapping of the absolute values of the pure measurement data in Fig. 4b for better comparison with the numerical data displayed in Fig. 4e. We observe that the measurement is in good agreement with the numerical prediction. As expected, the pressure maxima are located at both the edges and the center of the cavity. Minor inaccuracies within the numerical prediction are due to real losses and uncertainties within the experiments, i.e., imprecise alignment of the parts or imperfect plane wave excitation. We note only a slight pressure fluctuation in the center, just below the marked node in Fig. 4a. The position of the LDV for this measurement point is normal incidence to the glass. This results in a lower signal-to-noise ratio, which leads to higher measurement errors. We obtain a stable image of the QBIC that is in good agreement with the simulated sound pressure field. Thus, we present the visual evidence of a QBIC.

The visualized field allows us to further analyze the pressure field. For this purpose, we apply a fast Fourier transform (FFT) on the BIC mode, which is the same as applying an overlap integral with modes of the closed cavity. The values of the Fourier coefficients indicate the contribution of the modes. We take the first four dominant modes that are degenerate with the (0,1) mode (for mode indexing, see

Supplementary Information Section 5). Thus, we consequently reassemble the modes by conducting an inverse FFT. The result is depicted in Fig. 4c. By further analyzing the FFT coefficients, we identify the modes being excited alongside the BIC mode. The modes with the next higher FFT coefficients are the modes that are degenerate with the (1,1) mode. Figure 4d shows the result of their modal superposition. This mode is slightly shifted due to the incoming waves from the sound source and can also be found by conducting a modal analysis. We observe this mode due to an anti-symmetric excitation because we place our sound source on one side of the cavity. We, therefore, deduce, being consistent with the coupled mode theory<sup>15,23,35,38</sup>, that we can create a perfect BIC mode by eliminating the contribution of other modes. This is done by applying the principle of mirror sources, where we retain the properties of the full cavity but suppress all anti-symmetric modes, as shown in Fig. 5.

Figure 5a–c shows three schematics of the previously studied resonant cavities reduced in size by applying the principle of mirror sources. We cut the geometry in half at a particular axis of symmetry (marked by the red lines in the schematics mentioned above). The axis of symmetry has to be chosen with care since the BIC mode needs to be sustained, and all anti-symmetric modes with respect to this axis need to be suppressed. Figure 5c depicts the schematic of the fully reduced geometry. We manufacture three additional samples for impedance tube measurements, shown in Fig. 5d. Figure 5e shows the numerically obtained absorption coefficients of the configurations in Fig 5a–c with

$L_x = 85$  mm and also of the BIC configuration in Fig. 5c determined at  $L_x = 77$  mm. The more we reduce the geometry, the more unwanted modes are removed. Accordingly, we observe a clear peak in the absorption spectrum. We perform impedance tube measurements to validate our observations. The measured absorption coefficients are presented in Fig. 5f for the fully reduced configuration, see Fig. 5c, and in Fig. 5g for the configuration shown in Fig. 5b. The measurement results agree with our prediction. We observe the collapse of the Fano resonance (yellow and dashed purple lines in Fig. 5f), the sharp peak of the Fano resonance with no further absorption in the spectrum shown (blue and dashed red lines), and thus prove the existence of a Friedrich-Wintgen BIC based on the concept of fully reduced symmetry without exciting unwanted modes. Figure 5h shows the unexcited QBIC mode for a rectangular cavity with  $L_x = 170$  mm. The sound pressure field of the fully reduced geometry framed by the black lines is depicted in Fig. 5i. For comparison, we extrapolate the reduced sound pressure field onto the rectangular cavity. We infer from comparing Fig. 5h, i that identical sound pressure distributions are obtained. Finally, we manage to preserve the BIC mode although the geometry is reduced significantly and thus present a new type of fully reduced high-Q mode without exciting unwanted modes.

### Pressure enhancement

Impedance tube studies allow us to extract values for reflection spectra and absorption but not for cavity pressure enhancement. The missing cavity pressure information is provided by the LDV. The numerical and experimental procedure to determine the maximum pressure is presented in detail in Supplementary Information Section 6. Figure 5j shows the measured absolute pressure field inside the fully reduced cavity with  $L_x = 67$  mm excited at 2315 Hz. This configuration leads to the maximum pressure enhancement possible for this structure with a measured peak value of 36.74 Pa. We additionally measure the sound pressure fields of the fully reduced cavity with  $L_x = 64$  mm and  $L_x = 70$  mm to prove the existence of a pressure peak. The measurements show peak pressures of 26.08 Pa and 32.26 Pa, respectively. To demonstrate the magnitude of the pressure enhancement, we measure the pressure field inside the full cavity with  $L_x = 170$  mm for several frequencies. The maximum pressure is 12.61 Pa. Thus, the fully reduced cavity leads to the highest pressure enhancement of the investigated Friedrich-Wintgen BIC by a factor of about three compared to the full cavity.

Finally, we extract the sound pressure field of a QBIC mode. The sound pressure field inside the cavity gives us accurate information about the influence of losses and hence the stability and confinement of the mode. We also show that LDV measurements are a powerful tool for predicting the maximum pressure enhancement of high-Q modes, can resolve even small deviations from numerical predictions, and thus provide seminal guidance for the application of QBICs. Thus, we present the realistic sound pressure field of a stable high-Q mode, enabling further analysis and its application to acoustic devices.

### Discussion

We report the theoretical design, computation, experimental verification, and visualization of an acoustic Friedrich-Wintgen BIC in an open rectangular cavity. This is not only the first visual proof of an acoustic BIC but, above all, enables direct access to the pressure values inside the cavity. An exact analysis of stable high-Q modes facilitates its application to acoustic devices.

For this purpose, we design and manufacture three versions of the cavity with varying lengths. One to match the BIC configuration and two more to broaden and stabilize the Fano peak in the transmission spectrum. For an accurate prediction of the BIC, thermo-viscous losses are taken into account, leading to reduced peaks in the sound transmission spectrum. We find that the numerical results match the experimental ones accurately.

Furthermore, we manufacture a sample with high-transmission glass side walls to facilitate experiments applying refracto-vibrometry, and pioneer the direct visualization of an acoustic QBIC. Consequently, we have direct access to the pressure information of the high-Q modes inside the cavity. Exact mapping of the pressure field gives us a better understanding of real QBICs, including losses of all kinds, and hence enables further analyses of the excited modes.

We decompose the pressure field and identify higher-order modes excited simultaneously with the BIC mode. In addition, we further adapt the concept of designing BICs proposed by Huang et al.<sup>23</sup> and thus reduce the resonant cavity to the smallest possible size. As a result, we design a new type of BIC relying on fully reduced symmetry. Hence, we only excite the QBIC mode and suppress all unwanted modes. We verify our predictions by impedance tube measurements. Finally, we determine the configuration with maximum pressure enhancement by mapping the pressure fields of the fully reduced cavity with varying lengths. The fully reduced cavity leads to the highest pressure enhancement of the investigated Friedrich-Wintgen BIC by a factor of about three compared to the full cavity.

Our findings are a fundamental contribution to the study of BICs and open up entirely new opportunities in this field of research. Recent studies demonstrate an emission enhancement based on acoustic BICs. Nevertheless, prior to this work, it has not been shown when the large field enhancement happens if thermo-viscous losses are considered in real acoustic devices. Mapping the pressure field of the BIC is a promising technique to obtain the missing data and hence facilitates the application of BICs to high-intensity sound sources, acoustic devices, and nonlinear acoustics.

### Methods

#### Analytical model

The eigenfield profile of the Friedrich-Wintgen BIC can be predicted from the following equation

$$\psi_{BIC}(x,y) \approx \cos \theta \psi_{31}(x,y) + \sin \theta \psi_{13}(x,y) \quad (2)$$

where

$$\cos \theta = \frac{A}{\sqrt{A^2 + B^2}}, \quad \sin \theta = \frac{B}{\sqrt{A^2 + B^2}}, \quad (3)$$

$$A = -\sqrt{\frac{L_y}{2\pi^2 L_x}} \left[ \sin\left(\frac{\pi(Ly+1)}{L_y}\right) - \sin\left(\frac{\pi(Ly-1)}{L_y}\right) \right], \quad (4)$$

$$B = \sqrt{\frac{2}{L_x L_y}}. \quad (5)$$

The corresponding modes  $\psi$  are defined by

$$\psi_{m,n} = \sqrt{\frac{(2 - \delta_m^1)(2 - \delta_n^1)}{L_x L_y}} \cos\left(\frac{\pi(m-1)(2x+L_x)}{2L_x}\right) \cos\left(\frac{\pi(n-1)(2y+L_y)}{2L_y}\right) \quad (6)$$

with  $\delta_n^1$  and  $\delta_m^1$  being the Kronecker delta. See Supplementary Information Section 1 for a complete theoretical analysis.

#### Numerical simulations

All Simulations in this article are performed with the commercial software COMSOL Multiphysics (Acoustics Module). The speed of sound and the air density is  $c_0 = 343$  m/s and  $\rho_0 = 1.2$  kg/m<sup>3</sup>, respectively. We consider the walls of the cavity as well as the walls of the

waveguide to be rigid and hence apply sound hard boundary conditions. Additionally, we consider thermo-viscous losses in our system. We apply the no-slip condition for the velocity field and an isothermal condition for the temperature at the walls of the cavity. To ensure non-reflective boundary conditions at the ends of the waveguide, we apply perfectly matched layers. We perform modal analyses to compute the eigenvalues and corresponding modes and time-harmonic studies to predict the transmission or reflection spectrum.

### Device fabrication

The ten experimental samples are fabricated by additive manufacturing (3D-printing) using selective laser sintering with a manufacturing precision of  $\pm 0.2$  mm. The material of choice is polyamide (PA 2200 from EOS). We manufacture four samples with high-transmission glass side walls to facilitate experiments using refracto-vibrometry. The glass is bonded to the sample and the sample is hermetically sealed.

### Measurement

The complex transmission (and reflection) coefficients of the samples are measured using an AED 1200—AcoustiTube transmission tube with a diameter of 40 mm. The transmission coefficient and the transmission loss are calculated by applying the two-load method with four microphones according to the transfer matrix method. The absorption coefficients of the symmetry-reduced cavities are measured using an AED 1000—AcoustiTube impedance tube with a diameter of 40 mm.

### Visualization

We use refracto-vibrometry to visualize the sound pressure field inside the cavity. A laser Doppler scanning vibrometer PSV-500 from Polytec is used to measure the changes in the refraction index of the fluid, which is proportional to the acoustic pressure variation within the cavity. Overall, 225 measurement points were sequentially recorded with a sampling frequency of 50 kHz for a duration of 2 ms, while the measurements were triggered by the sinusoidal sound generator. To ensure an optimal signal-to-noise ratio, a highly reflective sheet was placed against the rigid surface behind the sample to improve diffuse light reflection. Note that LDV is usually used for surface normal vibration measurements of structures but captures the pressure wave-induced variation in the refraction index when measured against a rigid surface. In the case of a low-vibration surface, the velocity measurement from the LDV is dominated by the dynamic phase caused by the sound pressure fluctuations and the changed refractive index of the acoustic medium along the traveling path of the light. To ensure the required rigidity, a single point LDV (Polytec PDV-100) measured the surface vibration of the rigid surface from the opposite direction. The surface velocities were found to be orders of magnitude smaller than the signal of the scanning PSV500, confirming that the acoustic pressure dominates the measured results. As the LDV works up to frequencies of 1 MHz, the frequency range is not a limiting factor for pressure field mapping. The size of the structure can be much smaller than those presented in this article and is only limited by the focal point of the laser (25  $\mu$ m). We use such large structures here because we need to measure the transmission/reflection spectra using an impedance tube with a diameter of 40 mm. Since the Helmholtz equation is linearly scalable, our results can be transferred to different frequency ranges.

### Data availability

The data used in this study are available in the figshare database under [<https://doi.org/10.6084/m9.figshare.24211515>].

### Code availability

The codes used in this study are available in the figshare database under [<https://doi.org/10.6084/m9.figshare.24211515>]. Additionally, we host a COMSOL server, where we provide free access to vibro-

acoustic applications: <https://apps.vib.ed.tum.de:2037/app-lib>. We particularly created an application to give people an understanding of BICs and their influence on sound attenuation: [https://apps.vib.ed.tum.de:2037/app/BIC\\_TL\\_EF\\_App\\_V02\\_mph?id=0012](https://apps.vib.ed.tum.de:2037/app/BIC_TL_EF_App_V02_mph?id=0012).

### References

1. von Neumann, J. & Wigner, E. P. *Über Merkwürdige Diskrete Eigenwerte*, 291–293 (Springer Berlin Heidelberg, Berlin, Heidelberg, 1993). [https://doi.org/10.1007/978-3-662-02781-3\\_19](https://doi.org/10.1007/978-3-662-02781-3_19).
2. Ursell, F. Trapping modes in the theory of surface waves. *Math. Proc. Camb. Philos. Soc.* **47**, 347–358 (1951).
3. Evans, D. & Linton, C. Trapped modes in open channels. *J. Fluid Mech.* **225**, 153–175 (1991).
4. Evans, D. V., Levitin, M. & Vassiliev, D. Existence theorems for trapped modes. *J. Fluid Mech.* **261**, 21–31 (1994).
5. Hein, S. & Koch, W. Acoustic resonances and trapped modes in pipes and tunnels. *J. Fluid Mech.* **605**, 401–428 (2008).
6. Hein, S., Koch, W. & Nannen, L. Fano resonances in acoustics. *J. Fluid Mech.* **664**, 238–264 (2010).
7. Boudouti, E. H. E. et al. Transmission gaps and fano resonances in an acoustic waveguide: analytical model. *J. Phys.* **20**, 255212 (2008).
8. Hein, S., Koch, W. & Nannen, L. Trapped modes and fano resonances in two-dimensional acoustical duct-cavity systems. *J. Fluid Mech.* **692**, 257–287 (2012).
9. Huang, L. et al. Topological supercavity resonances in the finite system. *Adv. Sci.* **9**, 2200257 (2022).
10. Friedrich, H. & Wintgen, D. Interfering resonances and bound states in the continuum. *Phys. Rev. A* **32**, 3231–3242 (1985).
11. Linton, C. M. & McIver, P. Embedded trapped modes in water waves and acoustics. *Wave Motion* **45**, 16–29 (2007).
12. Duan, Y., Koch, W., Linton, C. M. & McIver, M. Complex resonances and trapped modes in ducted domains. *J. Fluid Mech.* **571**, 119–147 (2007).
13. Baydoun, S. K. & Marburg, S. Investigation of radiation damping in sandwich structures using finite and boundary element methods and a nonlinear eigensolver. *J. Acoust. Soc. Am.* **147**, 2020–2034 (2020).
14. Kronowetter, F., Baydoun, S. K., Eser, M., Moheit, L. & Marburg, S. A benchmark study on eigenfrequencies of fluid-loaded structures. *J. Theor. Comput. Acoust.* **28**, 2050013 (2020).
15. Lyapina, A. A., Maksimov, D., Pilipchuk, A. & Sadreev, A. Bound states in the continuum in open acoustic resonators. *J. Fluid Mech.* <https://doi.org/10.1017/jfm.2015.480> (2015).
16. Lyapina, A. A., Pilipchuk, A. & Sadreev, A. Bound states with orbital angular momentum in the continuum of cylindrical non-axisymmetric waveguide. *Ann. Phys.* <https://doi.org/10.1016/j.aop.2018.05.020> (2018).
17. Lyapina, A. A., Pilipchuk, A. & Sadreev, A. Trapped modes in a non-axisymmetric cylindrical waveguide. *J. Sound Vib.* **421**, 48–60 (2018).
18. Xiong, L., Bi, W. & Aurégan, Y. Fano resonance scatterings in waveguides with impedance boundary conditions. *J. Acoust. Soc. Am.* **139**, 764–772 (2016).
19. Maznev, A. A. & Every, A. G. Bound acoustic modes in the radiation continuum in isotropic layered systems without periodic structures. *Phys. Rev. B* **97**, 014108 (2018).
20. Peng, Y.-G., Geng, Z.-G. & Zhu, X.-F. Topologically protected bound states in one-dimensional floquet acoustic waveguide systems. *J. Appl. Phys.* **123**, 091716 (2018).
21. Chen, Z.-G., Xu, C., Al Jahdali, R., Mei, J. & Wu, Y. Corner states in a second-order acoustic topological insulator as bound states in the continuum. *Phys. Rev. B* **100**, 075120 (2019).
22. Deriy, I., Toftul, I., Petrov, M. & Bogdanov, A. Bound states in the continuum in compact acoustic resonators. *Phys. Rev. Lett.* **128**, 084301 (2022).

23. Huang, L. et al. General framework of bound states in the continuum in an open acoustic resonator. *Phys. Rev. Appl.* **18**, 054021 (2022).
24. Huang, S. et al. Extreme sound confinement from quasibound states in the continuum. *Phys. Rev. Appl.* <https://doi.org/10.1103/PhysRevApplied.14.021001>.
25. Huang, L. et al. Sound trapping in an open resonator. *Nat. Commun.* <https://doi.org/10.1038/s41467-021-25130-4> (2021).
26. Huang, S. et al. Acoustic purcell effect induced by quasibound state in the continuum. *Fundam. Res.* <https://doi.org/10.1016/j.fmre.2022.06.009>. <https://www.sciencedirect.com/science/article/pii/S2667325822002783> (2022).
27. Manenti, R. et al. Circuit quantum acoustodynamics with surface acoustic waves. *Nat. Commun.* <https://doi.org/10.1038/s41467-017-01063-9> (2017).
28. von Lüpke, U. et al. Parity measurement in the strong dispersive regime of circuit quantum acoustodynamics. *Nat. Phys.* **18**, 1–6 (2022).
29. Navarathna, A. & Bowen, W. Good vibrations for quantum computing. *Nat. Phys.* **18**, 1–2 (2022).
30. Wollack, E. A. et al. Quantum state preparation and tomography of entangled mechanical resonators. *Nature* **604**, 463–467 (2022).
31. Yu, Y., Xi, X. & Sun, X. Observation of mechanical bound states in the continuum in an optomechanical microresonator. *Light* **11**, 328 (2022).
32. Hsu, C. W., Zhen, B., Stone, A. D., Joannopoulos, J. & Soljačić, M. Bound states in the continuum. *Nat. Rev. Mater.* **1**, 16048 (2016).
33. Pagneux, V. *Trapped Modes and Edge Resonances in Acoustics and Elasticity*, 181–223 (Springer Vienna, Vienna, 2013). [https://doi.org/10.1007/978-3-7091-1619-7\\_5](https://doi.org/10.1007/978-3-7091-1619-7_5).
34. Joseph, S., Pandey, S., Sarkar, S. & Joseph, J. Bound states in the continuum in resonant nanostructures: an overview of engineered materials for tailored applications. *Nanophotonics* **10**, 4175–4207 (2021).
35. Sadreev, A. Interference traps waves in open system: bound states in the continuum. *Rep. Progr. Phys.* <https://doi.org/10.1088/1361-6633/abefb9> (2021).
36. Dittes, F.-M. The decay of quantum systems with a small number of open channels. *Phys. Rep.* **339**, 215–316 (2000).
37. Silveirinha, M. Trapping light in open plasmonic nanostructures. *Phys. Rev.* <https://doi.org/10.1103/PhysRevA.89.023813> (2014).
38. Maksimov, D., Sadreev, A., Lyapina, A. A. & Pilipchuk, A. Coupled mode theory for acoustic resonators. *Wave Motion* **56**, 52–66 (2015).
39. Persson, E., Rotter, I., Stockmann, H.-J. & Barth, M. Observation of resonance trapping in an open microwave cavity. *Phys. Rev. Lett.* **85**, 2478–81 (2000).
40. Okolowicz, J., Płoszajczak, M. & Rotter, I. Dynamics of quantum systems embedded in a continuum. *Phys. Rep.* **374**, 271–383 (2003).
41. Miroshnichenko, A. E., Flach, S. & Kivshar, Y. S. Fano resonances in nanoscale structures. *Rev. Mod. Phys.* **82**, 2257–2298 (2010).
42. Ladrón de Guevara, M., Claro, F. & Orellana, P. Ghost fano resonance in a double quantum dot molecule attached to leads. *Phys. Rev. B* <https://doi.org/10.1103/PhysRevB.67.195335> (2003).
43. Mbailassem, F., Leclère, Q., Redon, E. & Gourdon, E. Experimental analysis of acoustical properties of irregular cavities using laser refracto-vibrometry. *Appl. Acoust.* **130**, 177–187 (2018).
44. Malkin, R., Todd, T. & Robert, D. A simple method for quantitative imaging of 2d acoustic fields using refracto-vibrometry. *J. Sound Vib.* **333**, 4473–4482 (2014).
45. Jackett, R., Piper, B. & Hughes, R. J. Characterization of acoustic diffusion using refracto-vibrometry. *J. Sound Vib.* **392**, 70–76 (2017).
46. Dong, H., Yu, Z., Kenneth, G., Sun, T. & Li, T. Acoustic standing wave field measurement using a laser doppler vibrometer based on the hankel Fourier algorithm. *IEEE Access PP*, 1–1 (2019).

## Author contributions

F.K., S.M., S.O., and D.A.P. conceived the project. F.K., Y.K.C., L.H., and D.A.P. designed the geometry and modeled the physics behind it. F.K. and M.M. made samples and performed measurements to obtain the transmission spectra and the visualization of the BIC. D.A.P. and Y.K.C. advised the modeling and experimental process. J.D.S. implemented and uploaded the BIC APP. All authors discussed the results. F.K. prepared the paper with contributions from all authors. M.M., S.M., S.O., and D.A.P. edited the paper.

## Funding

Open Access funding enabled and organized by Projekt DEAL.

## Competing interests

The authors declare no competing interests.

## Additional information

**Supplementary information** The online version contains supplementary material available at <https://doi.org/10.1038/s41467-023-42621-8>.

**Correspondence** and requests for materials should be addressed to Felix Kronowetter.

**Peer review information** *Nature Communications* thanks Xin-Ye Zou and the other anonymous reviewer(s) for their contribution to the peer review of this work. A peer review file is available.

**Reprints and permissions information** is available at <http://www.nature.com/reprints>

**Publisher's note** Springer Nature remains neutral with regard to jurisdictional claims in published maps and institutional affiliations.

**Open Access** This article is licensed under a Creative Commons Attribution 4.0 International License, which permits use, sharing, adaptation, distribution and reproduction in any medium or format, as long as you give appropriate credit to the original author(s) and the source, provide a link to the Creative Commons licence, and indicate if changes were made. The images or other third party material in this article are included in the article's Creative Commons licence, unless indicated otherwise in a credit line to the material. If material is not included in the article's Creative Commons licence and your intended use is not permitted by statutory regulation or exceeds the permitted use, you will need to obtain permission directly from the copyright holder. To view a copy of this licence, visit <http://creativecommons.org/licenses/by/4.0/>.

© The Author(s) 2023

# Realistic prediction and engineering of high-Q modes for the implementation of stable Fano resonances to acoustic devices

## — Supplementary Information —

Felix Kronowetter<sup>1,2,3</sup>, Marcus Maeder<sup>1</sup>, Yan Kei Chiang<sup>2</sup>, Lujun Huang<sup>2</sup>, Johannes D. Schmid<sup>1</sup>, Sebastian Oberst<sup>3</sup>, David A. Powell<sup>2</sup>, and Steffen Marburg<sup>1</sup>

<sup>1</sup>*Chair of Vibro-Acoustics of Vehicles and Machines, Department of Engineering Physics and Computation, Technical University of Munich, TUM School of Engineering and Design*

<sup>2</sup>*School of Engineering and Information Technology, University of New South Wales, Northcott Drive, Canberra, ACT 2600, Australia*

<sup>3</sup>*School of Mechanical and Mechatronic Engineering, Centre for Audio, Acoustics and Vibration, Faculty of Engineering and IT, University of Technology Sydney, Sydney, Australia*

## S 1 Coupled mode theory

We use coupled mode theory [1, 2, 3] to predict the location of the BIC. For simplicity, we consider a reduced two-dimensional coupled rectangular waveguide-resonator system shown in Fig. S 1.

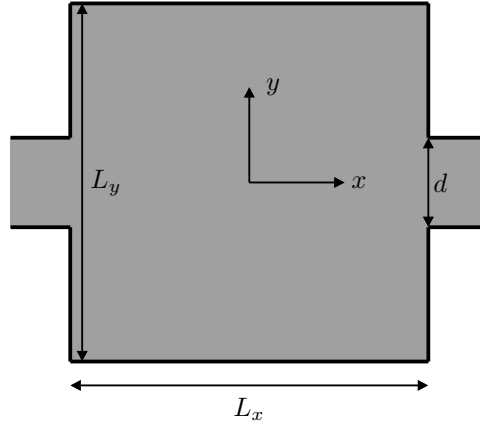


**Fig. S 1. Schematic drawing of a coupled two-dimensional waveguide-resonator system.**

To make the conclusion as general as possible, we set the width of the waveguide  $d = 1$  (unitless), and the width and height of the resonator are  $L_x$  and  $L_y$ , respectively. Also, the center of the resonator is set as the origin, and the left and right waveguides are attached along the  $x$ -axis. Thus, the waveguide spans from  $y = -1/2$  to  $y = +1/2$ . The first step is to compute the eigenfrequencies and eigenmodes of a closed resonator. They eigenfrequencies can be solved analytically with Neumann boundary conditions as follows

$$\frac{\nu_{m,n}^2}{\omega_0^2} = \left( \frac{(m-1)}{L_x} \right)^2 + \left( \frac{(n-1)}{L_y} \right)^2, \quad n, m = 1, 2, 3, \dots \quad (1)$$

where  $\nu_{m,n}$  is the resonant frequency and  $\omega_0 = \pi c/d$ ,  $c$  is the speed of sound in air. We obtain the corresponding modes  $\psi$  by

$$\psi_{m,n} = \sqrt{\frac{(2 - \delta_m^1)(2 - \delta_n^1)}{L_x L_y}} \cos\left(\frac{\pi(m-1)(2x + L_x)}{2L_x}\right) \cos\left(\frac{\pi(n-1)(2y + L_y)}{2L_y}\right) \quad (2)$$



with  $\delta_n^1$  and  $\delta_m^1$  being the Kronecker delta. The propagating wave numbers in the waveguide are given by

$$\frac{\nu^2}{\omega_0^2} = \frac{k_p^2}{\pi^2} + (p-1)^2 \quad (3)$$

with  $k_p$  being the wavenumber of the  $p$ th channel of the waveguide. We obtain the corresponding modes  $\phi$  by

$$\phi_p = \sqrt{(2 - \delta_p^1)} \cos\left(\frac{\pi(p-1)(2y+1)}{2}\right) e^{ik_p x}. \quad (4)$$

Then the coupling matrix elements between eigenmodes of closed resonator and  $p$ th propagation channels of the left/right waveguide can be obtained by

$$W_{m,n;p} = \int_{-\frac{1}{2}}^{\frac{1}{2}} \psi_{m,n}(x = -\frac{L_x}{2}, y) \phi_p(x = -\frac{L_x}{2}, y) dy. \quad (5)$$

After obtaining the coupling matrix, we compute the complex eigenvalues of the effective Hamiltonian [4, 5, 6, 7], where the real parts correspond to the resonance frequencies and the imaginary parts to the half resonance linewidth. Thus, the search for BICs amounts to finding the zero imaginary part of the eigenvalues. In general, the eigenfunction of any BIC can be decomposed as

$$\phi_{BIC} = \sum_{m,n} a_{m,n} \psi_{m,n}(x, y). \quad (6)$$

Since the BIC is perfectly decoupled from the continuum, its eigenfunction must be given by

$$\int_{-\frac{1}{2}}^{\frac{1}{2}} \phi_{BIC}(x = -\frac{L_x}{2}, y) dy = 0. \quad (7)$$

When two resonant states approach each other as a function of a certain continuous parameter, interference causes an avoided crossing of the two states in their energy positions. At the same time, one of the resonance line widths vanishes exactly at a certain value of the parameter and the other one is boosted to maximum. This is known as Friedrich-Wintgen BIC [8]. Typically, a pair of eigenmodes  $M_{mn}$  and  $M_{m+2, n-2}$  (or  $M_{mn}$  and  $M_{m-2, n+2}$ ) is often used to construct Friedrich-Wintgen BICs. The essence of finding Friedrich-Wintgen BICs is to find two degenerate resonances in a closed resonator with a certain size ratio.

In the present work, we consider the Friedrich-Wintgen BIC in a rectangular resonator embedded in the first channel  $p = 1$ , provided that other channels are closed for  $\nu < 1$ . There are numerous degeneracies in a closed rectangular resonator

$$\frac{m^2}{L_x^2} + \frac{n^2}{L_y^2} = \frac{m'^2}{L_x^2} + \frac{n'^2}{L_y^2}. \quad (8)$$

The lowest case corresponds to  $m, n = 1, 3$  and  $m', n' = 3, 1$  for a square resonator  $L_x = L_y$ .

After the introduction of the left and right waveguides, these two modes  $M_{13}$  and  $M_{31}$  are strongly coupled to each other, giving rise to an increase in the destructive interference at a given size ratio. Thus, the resonance frequencies of two modes experience avoided crossing. At the same time, one of the imaginary parts is suppressed to zero while the other is boosted to maximum. Therefore, the formation of such a BIC can be mainly attributed to the destructive interference of modes  $M_{13}$  and  $M_{31}$  in a closed resonator. We can approximate the eigenfunction of this Friedrich-Wintgen BIC as a superposition of the two eigenmodes of the closed resonator, and its coefficients  $A$  and  $B$  can be rigorously calculated by

$$\psi_{BIC}(x, y) \approx A\psi_{31}(x, y) + B\psi_{13}(x, y). \quad (9)$$

Substituting Eq. (9) in Eq. (7) gives us

$$A = -W_{1,3;p=1} = -\frac{1}{2\pi} \sqrt{\frac{2L_y}{L_x}} \left[ \sin\left(\frac{\pi(Ly+1)}{L_y}\right) - \sin\left(\frac{\pi(Ly-1)}{L_y}\right) \right], \quad (10)$$

$$B = W_{3,1;p=1} = \sqrt{\frac{2}{L_x L_y}}. \quad (11)$$

We can rewrite Eq. (9) as

$$\psi_{BIC}(x, y) \approx \cos \theta \psi_{31}(x, y) + \sin \theta \psi_{13}(x, y), \quad (12)$$

$$\cos \theta = \frac{A}{\sqrt{A^2 + B^2}} \quad , \quad \sin \theta = \frac{B}{\sqrt{A^2 + B^2}} \quad (13)$$

Excellent agreement is found between the eigenfield profile predicted from Eqs.(8-9) and the numerically calculated eigenfield profile of Friedrich-Wintgen BIC, see Fig. S 2.

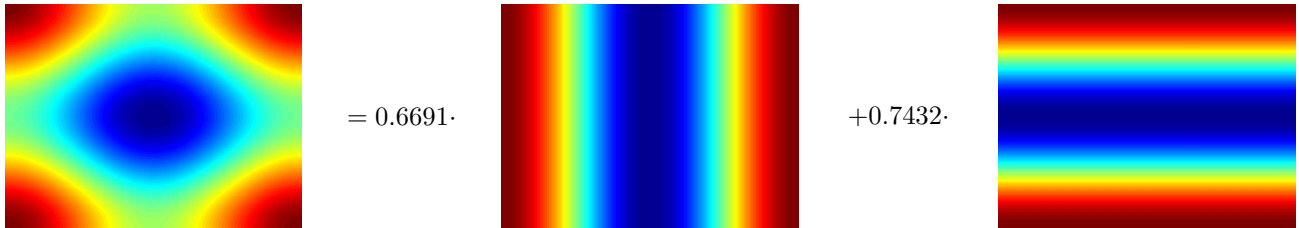
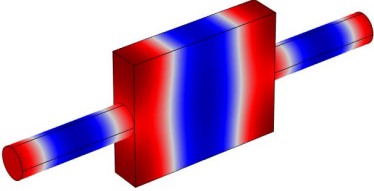


**Fig. S 2. Eigenfield profile.** Decomposition of Friedrich-Wintgen BIC into eigenmodes  $M_{31}$  and  $M_{13}$ .

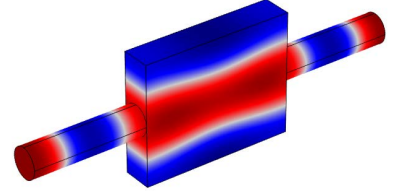
## S 2 BIC formation

We investigate a Friedrich-Wintgen BIC induced by mode interference. Therefore, two modes of the same symmetry interact, which results in a highly damped mode and one of increased lifetime. In our configuration, two Friedrich-Wintgen BICs form in a frequency spectrum up to 2300 Hz. The first one at  $\approx 2145$  Hz named BIC 1 and the second one at  $\approx 2277$  Hz named BIC 2. Both BICs and the corresponding interacting modes are displayed in Figs. S S 3 and S 4.

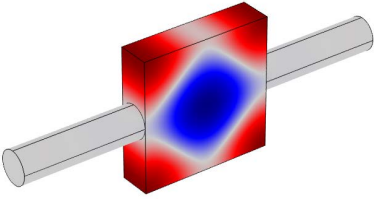
a



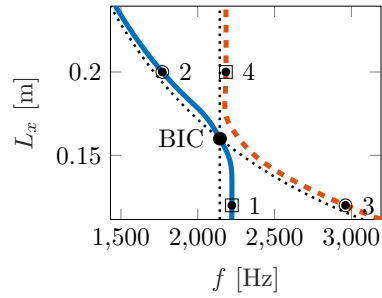
b



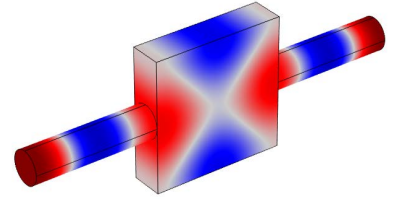
c



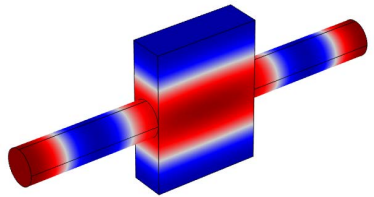
d



e



f



g

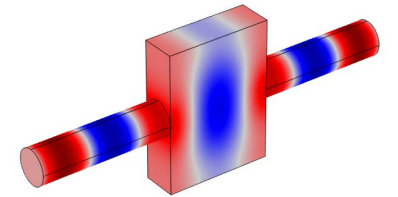


**Fig. S 3. Formation BIC 1.** a,b,f,g Interacting modes (2,4,1,3) of the same symmetry for different  $L_x$ . c Mode shape of the BIC. e Mode shape of the highly damped mode. d Avoided crossing of the eigenfrequencies (real parts) of the interacting modes.

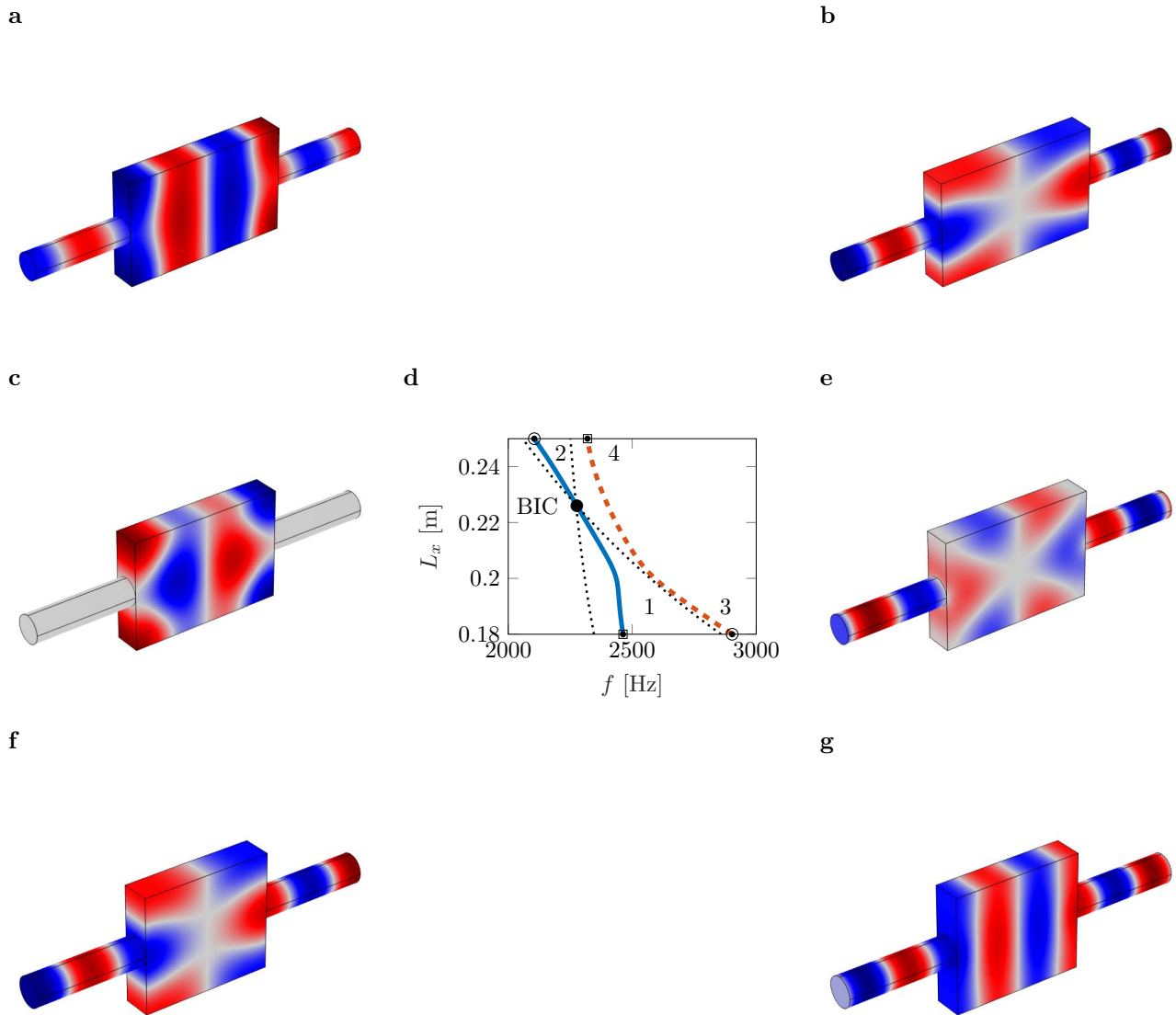


**Fig. S 4. Formation BIC 2.** **a,b,f,g** Interacting modes (2,4,1,3) of the same symmetry for different  $L_x$ . **c** Mode shape of the BIC. **e** Mode shape of the highly damped mode. **d** Avoided crossing of the eigenfrequencies (real parts) of the interacting modes.

### S 3 Complex Eigenfrequencies

The solutions to a waveguide symmetric with respect to the duct axis can be composed of symmetric and antisymmetric solutions [9]. Hence, we can also split the continuum to symmetric and antisymmetric parts. If we excite the waveguide, e.g., by using a background pressure field in the numerical simulations, the symmetric modes can be activated. That means, they couple into the propagating spectrum. The eigenvalues for varying cavity length  $L_x$  are shown in Fig. S 5.

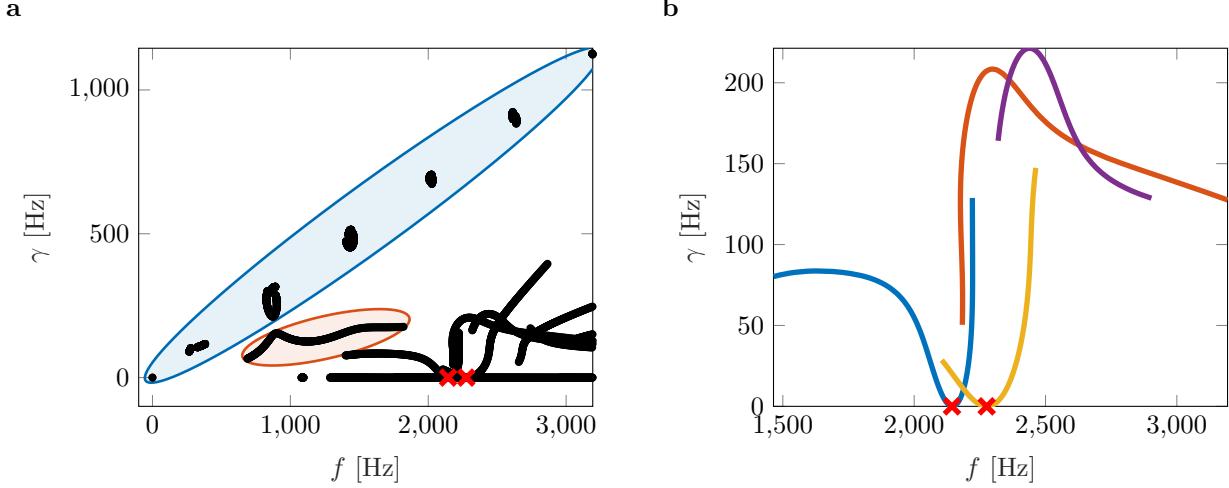


**Fig. S 5. Complex eigenfrequencies for varying  $L_x$ .** **a** The spectrum of propagating waves dominated by the pipe is marked by the region colored blue. Cavity resonances are highlighted by the region colored red. BIC 1 and BIC 2 are marked by the red crosses. **b** Evolution over  $L_x$  of the interacting modes that form BIC 1 & 2.

The blue area is the spectrum of propagating waves dominated by the tube and characterized by high radiation loss. An example of propagating symmetric modes corresponding to cavity resonances are outlined by the red area. Other propagating modes are highlighted by colored curves. Increasing the cavity length results in a lower real part of the eigenfrequencies. Antisymmetric modes cannot radiate away and are therefore localized or trapped modes. They are purely real eigenfrequencies on the  $x$ -axis in Fig. S 5. By varying the distance  $L_x$ , certain modes interact and their eigenfrequencies pass through an avoided crossing. Therefore, one of the eigenfrequencies has a decreasing imaginary part, becomes purely real and thus a BIC. This is highlighted by the red crosses for BIC 1 and BIC 2.

## S 4 Thermo-viscous losses

BICs have a theoretically infinite quality factor. In reality, thermo-viscous losses limit the quality factor to a finite value. We consider losses in our computations. This is done by describing the acoustic boundary layer as a combination of the viscous and thermal boundary layers. Viscous losses occur due to gradients in the velocity field, whereas thermal losses are based on a temperature gradient. We apply the no-slip condition for the velocity field and an isothermal condition for the temperature at the walls of the cavity. Furthermore, we compare the lossless case to the one with losses. The decrease of the Q-factor is displayed in Fig. S 6.

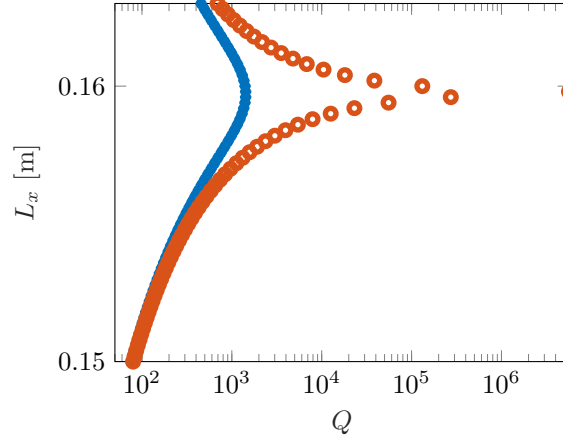


**Fig. S 6. Q-factor.** Q-factor of the system with (blue line) and without (orange circles) thermo-viscous losses.

We can see a significant reduction of the Q-factor of the lossless case (blue line) compared to one including thermo-viscous losses (orange circles). The effect of thermo-viscous losses on the Fano peaks in the transmission spectra is shown in Fig. S 7.

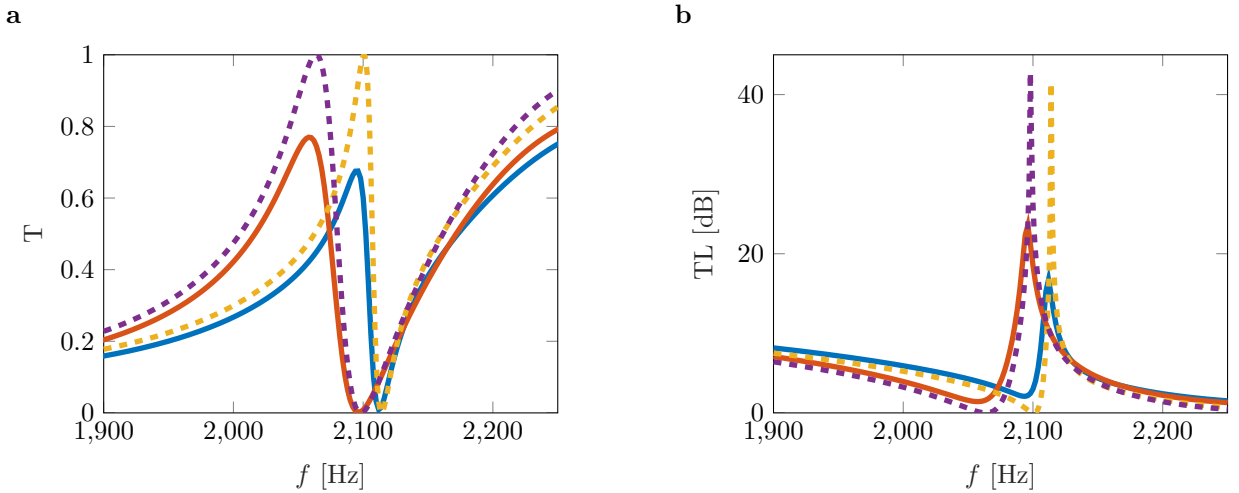


**Fig. S 7. Transmission spectra with and without losses.** **a** Transmission coefficient in the 1900 - 2250 Hz frequency range. The solid blue and dashed yellow lines represent the results of  $L_x = 165$  mm with and without thermo-viscous losses, respectively. The results of  $L_x = 170$  mm are shown by the red and purple lines. **b** Transmission loss of  $L_x = 165$  mm and  $L_x = 170$  mm with and without losses. The coloring of the lines is identical to Fig. S 7a.

Thermo-viscous losses significantly reduce the transmission coefficient due to increased absorption. Nevertheless, the transmission goes to zero at the frequency of the QBIC, see Fig. S 7a. The maxima of the Fano peaks in the TL also decrease including the losses. We observe a reduction from  $\approx 42$  dB to  $\approx 17$  dB ( $L_x = 165$  mm) and from  $\approx 43$  dB to  $\approx 24$  dB ( $L_x = 170$  mm). The losses have a more significant effect on the amplitude of the

Fano peak of the TL the closer we are to the BIC configuration. In addition, due to thermo-viscous losses, the Fano peaks are shifted to lower frequencies by about 2 Hz. To illustrate the effect of losses on pressure field enhancement, the maximum absolute sound pressure is plotted against cavity length and frequency in Fig. S 8.

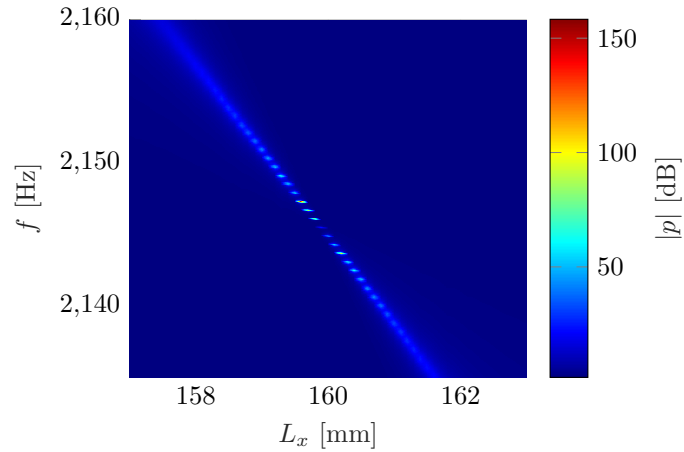
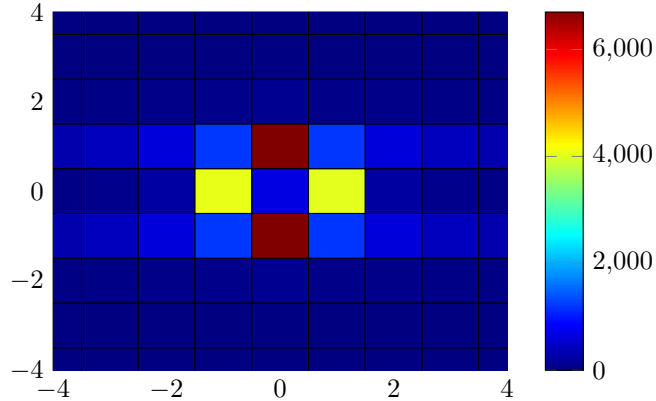


**Fig. S 8. Pressure mapping (without losses).** Maximum absolute sound pressure inside the rectangular cavity shown in Fig. S 1. The cavity length is varied from  $L_x = 157 - 163$  mm in 0.1 Hz steps in the frequency range 2135 - 2160 Hz.

We observe amplified sound pressure up to 160 dB when excited at 1 Pa and narrow Fano peaks near the BIC. Figs. S 6 to S 8 illustrate the importance of considering thermo-viscous losses in our simulations.

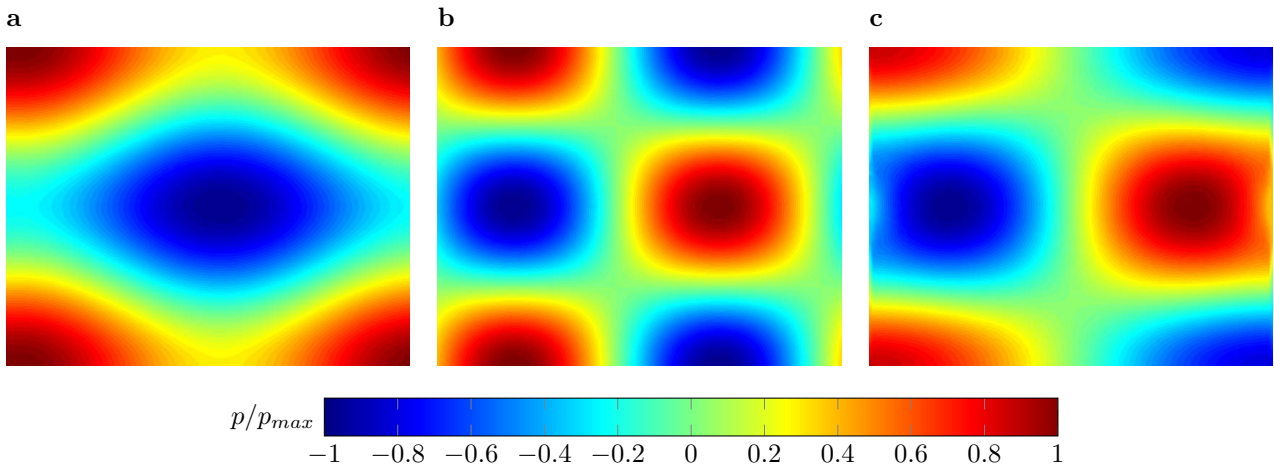
## S 5 Analysis of the measured sound pressure field

We use an FFT to further analyze the sound pressure field inside the cavity and thereby obtain the modal coefficients shown in Fig. S 9.



**Fig. S 9. FFT coefficients.** Coefficients of the fast Fourier transformation corresponding to modes. The indices of the abscissa and the ordinate stand for the modal index in  $x$ - and  $y$ -direction, respectively. The mode with the indices  $(0, 0)$  represents the plane wave.

The four modes with the most dominant Fourier coefficients are the ones that are degenerate with the  $(0, 1)$  mode. Hence, the modes with corresponding mode indices  $(0, -1), (1, 0), (-1, 0)$ . In other terms, referring to Lyapina et al. [2], we denote the modes  $(0, 1), (0, -1)$   $M_{211}$  and the modes  $(1, 0), (-1, 0)$   $M_{121}$ . A modal superposition by an inverse FFT gives us the sound pressure field of the BIC mode depicted in Fig. S 10a.



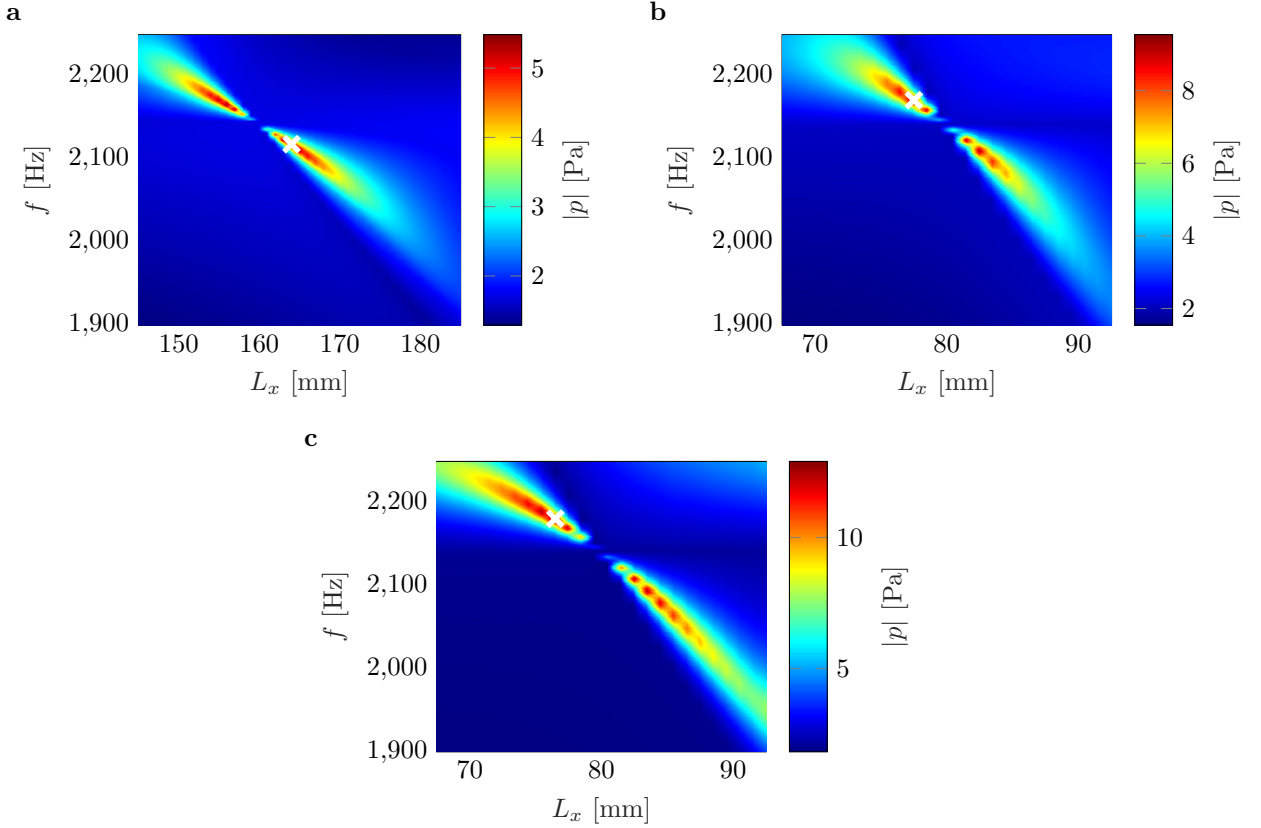
**Fig. S 10. Sound pressure fields from modes.** **a** Superposition of the four most dominant modes (modes with the highest FFT coefficients). **b** Superposition of the next four modes with high coefficients. **c** Identical mode to the one shown in **b** obtained from modal analysis. The colored scales display the nondimensionalized pressure, with the pressure being normalized to the maximum pressure of the experiment and the simulation, respectively.

Fig. S 10b shows the sound pressure field of the superposition of the modes that are degenerate with the  $(1, 1)$  mode, i.e. the  $(1, -1), (-1, 1), (-1, -1)$  modes. The modal analysis of the unexcited system gives us a mode similar to the one in Fig. S 10b, see Fig. S 10c. Therefore, we identify one additional contributing mode excited by the plane wave.



## S 6 Pressure enhancement

The configuration with the highest pressure field enhancement is determined by parameter studies. Therefore, we vary the cavity lengths of the configurations depicted in Fig. 1a, Fig. 5a and Fig. 5b. The corresponding plots are shown in Fig. S 11.



**Fig. S 11. Simulated pressure mappings.** **a** Maximum absolute sound pressure inside the rectangular cavity shown in Fig. 1a. The cavity length is varied from  $L_x = 145 - 185$  mm in 1 mm and 1 Hz steps in the frequency range 1900 - 2250 Hz. **b** Maximum absolute sound pressure inside the reduced cavity presented in Fig. 5a with cavity length  $L_x = 67.5 - 92.5$  mm in the same frequency range. **c** Maximum absolute sound pressure inside the further reduced cavity (Fig. 5b). The white crosses indicate the maxima.

Pressure enhancement can be observed in certain regions around the BIC configurations. We can also see that the maximum pressure enhancement does not occur directly adjacent to the BIC as it would without losses, i.e., see Fig. S 8. Thermo-viscous losses shift the maximum enhancement away from the BIC configuration. The pressure peaks are 5.50 Pa, 9.54 Pa, and 12.89 Pa. It can be said that the more the geometry is reduced and thus the antisymmetric modes are suppressed, the higher the pressure enhancement. The visualized pressure fields for the full cavity are shown in Fig. S 12.

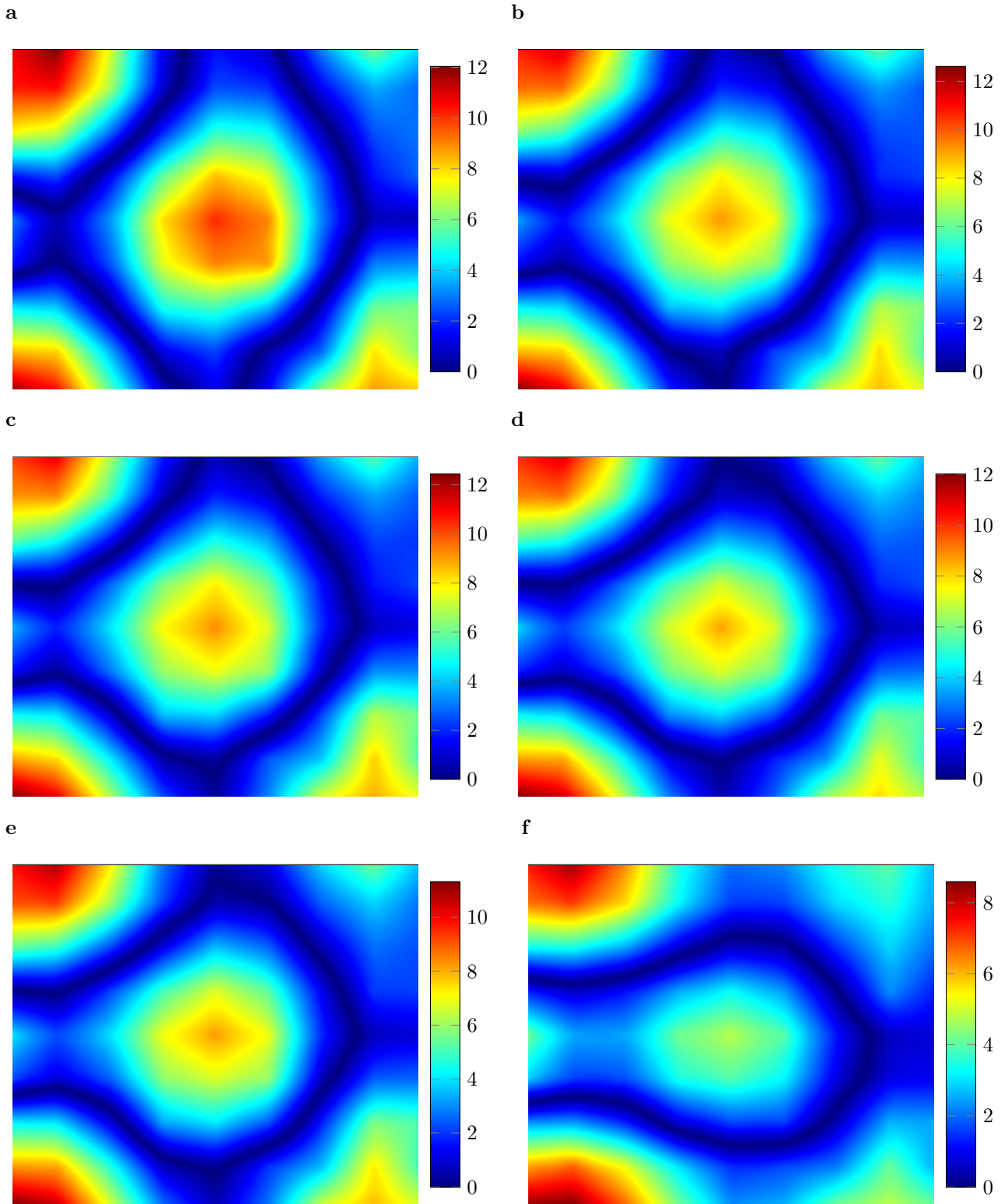


**Fig. S 12. Visualized pressure fields of the full cavity.** a - f Absolute sound pressure inside the rectangular cavity shown in Fig. 1a. with  $L_x = 170$  mm excited at 2070 Hz, 2075 Hz, 2077 Hz, 2079 Hz, 2081 Hz, and 2094 Hz, respectively. All color scales represent the absolute pressure in Pa.

The corresponding maximum pressure values in Figs. S 12a to 12f are 12.04 Pa, 12.61 Pa, 12.44 Pa, 12.02 Pa, 11.32 Pa, and 8.59 Pa, respectively. Therefore, we can say that the maximum pressure enhancement occurs at 2075 Hz. The evolution of the modal field is also demonstrated. The dark blue line representing the pressure

nodes extends in the  $y$ -direction, the more the configuration deviates from the BIC configuration.

We numerically determine the configuration with the highest pressure gain by plotting the maximum absolute sound pressure inside the cavity as the cavity length is varied in the 1900 - 2400 Hz frequency range and excited by a plane wave of 1 Pa. This is shown in Fig. S 13 for the fully reduced cavity presented in Fig. 5c.

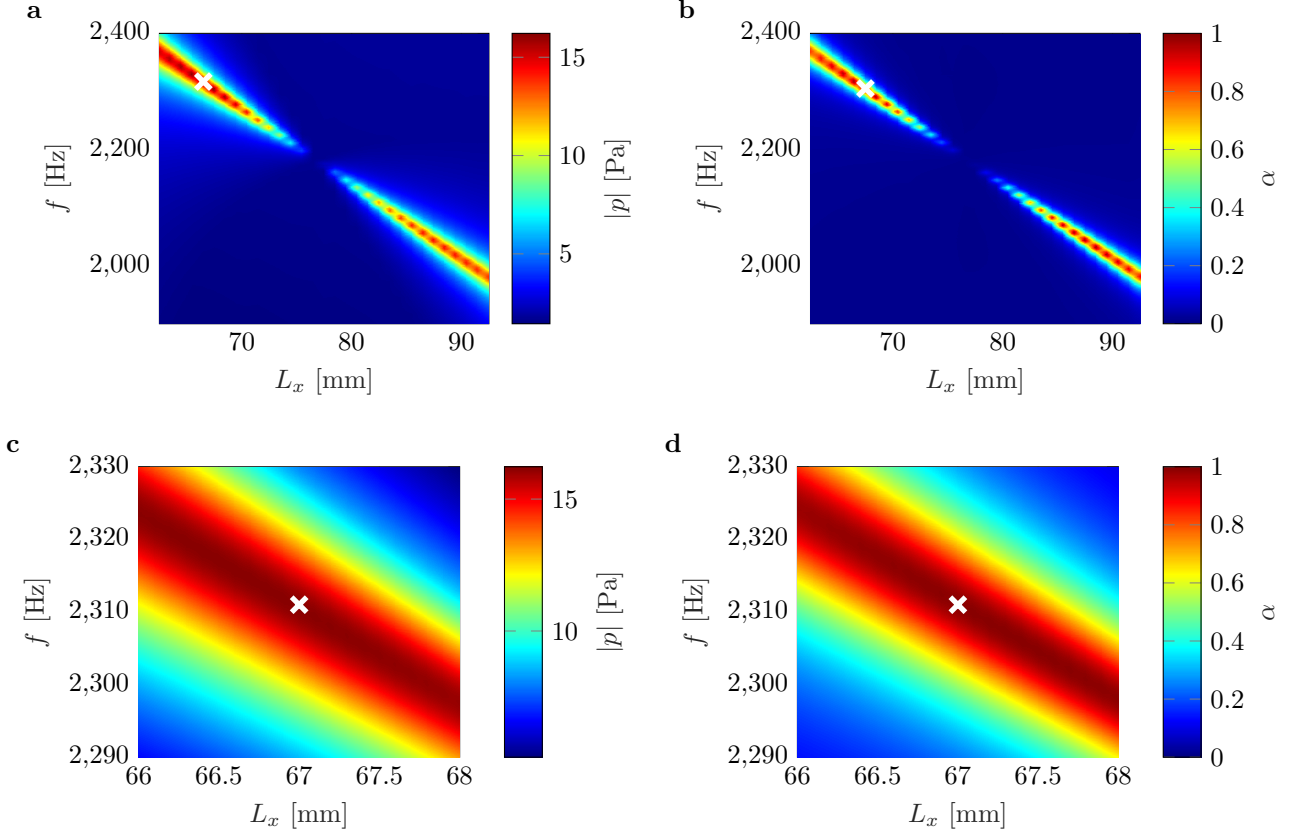


**Fig. S 13. Simulated pressure mappings.** **a,b** Maximum absolute sound pressure and absorption inside the cavity shown in Fig. 5c. The cavity length is varied from  $L_x = 67.5 - 92.5$  mm in 1 mm and 1 Hz steps in the frequency range 1900 - 2400 Hz. **c,d** Maximum absolute sound pressure and absorption at finer resolution. The cavity length is varied from  $L_x = 66 - 68$  mm in 0.1 mm and 0.1 Hz steps in the frequency range 2290 - 2330 Hz. The white crosses indicate the maxima.

The BIC is visible as the dark blue dot in the center of the red lines in Figs. S 13a and 13b. Pressure enhancement can be observed in certain regions around the BIC configurations. The smaller the cavity length, the higher the frequency of the enhancement and vice versa. It can be seen that the maximum pressure enhancement and absorption occurs at a cavity length of  $L_x = 67$  mm. We fabricate three additional samples of the fully reduced cavity ( $L_x = 64, 67,$  and  $70$  mm) to experimentally validate our numerical predictions, see Fig. S 14.

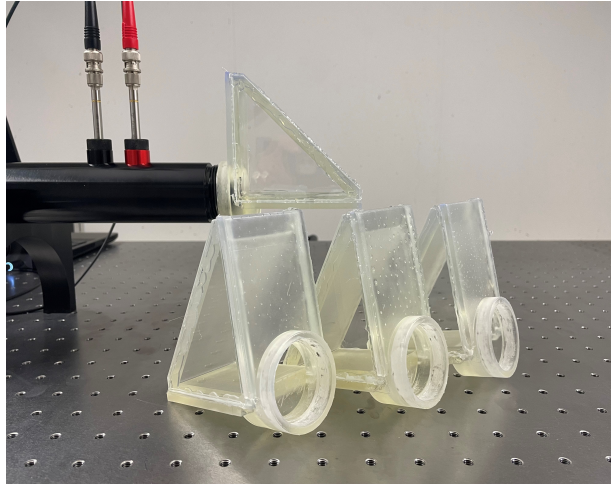


**Fig. S 14. LDV samples.** Printed samples of the fully reduced cavity with high-transmission glass mounted as side panels.

We then measure the sound pressure field inside the cavity for several frequencies to determine the configuration (frequency and cavity length) where the maximum absolute sound pressure is found. The visualized pressure fields for the fully reduced cavity with  $L_x = 64$  mm,  $L_x = 67$  mm, and  $L_x = 70$  mm are shown in Fig. S 15.

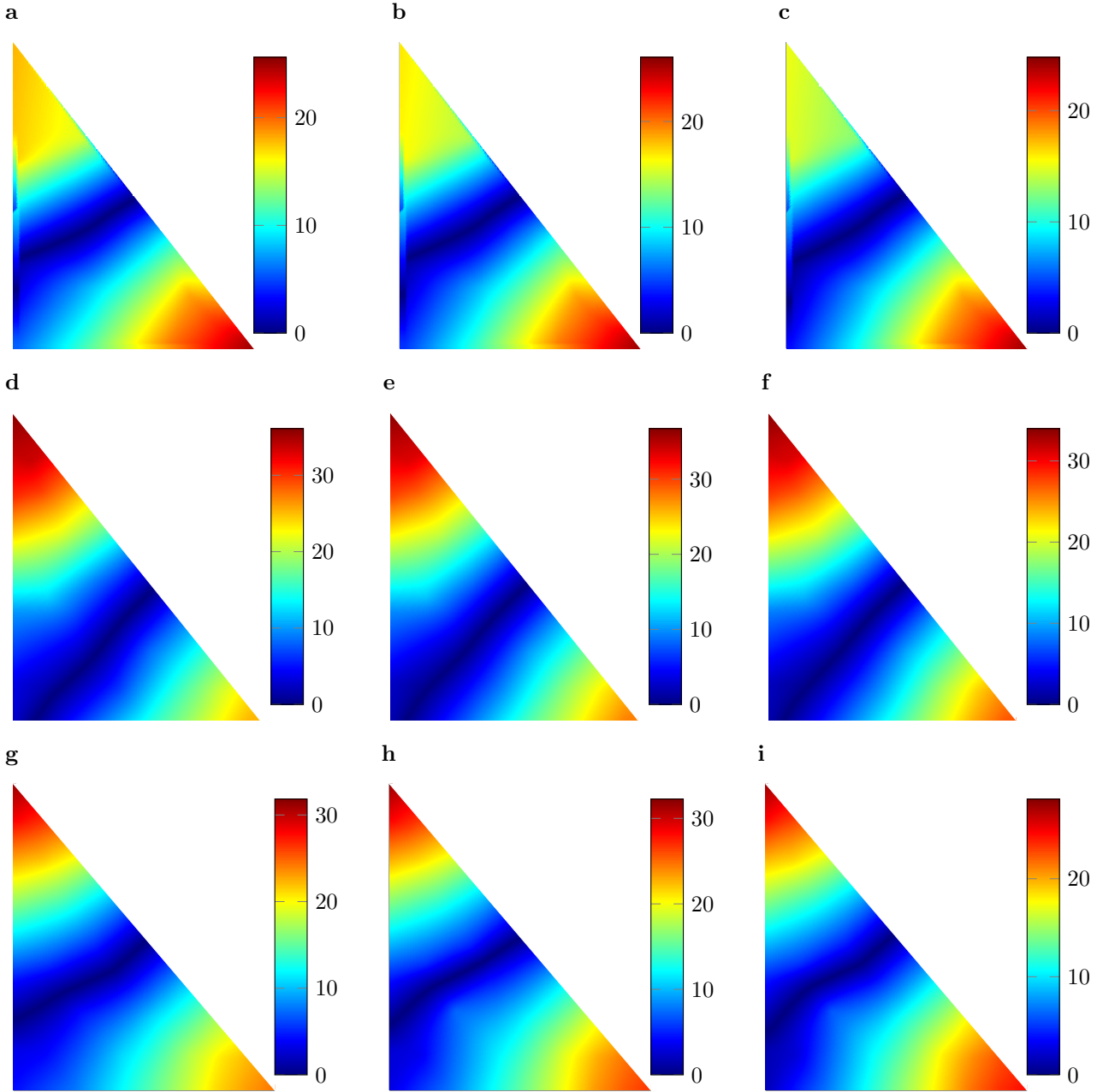


**Fig. S 15. Visualized pressure fields of the fully reduced cavity.** **a - c** Absolute sound pressure inside the fully reduced cavity shown in Fig. 5c with  $L_x = 64$  mm excited at 2335 Hz, 2345 Hz, and 2353 Hz. **d - f** Absolute sound pressure inside the fully reduced cavity with  $L_x = 67$  mm excited at 2310 Hz, 2315 Hz, and 2319 Hz. **g - i** Absolute sound pressure inside the fully reduced cavity with  $L_x = 70$  mm excited at 2267 Hz, 2272 Hz, and 2277 Hz. All color scales represent the absolute pressure in Pa.

The data are not normalized to the incident pressure field, but the actual pressure values are shown. The corresponding maximum pressure values in Figs. S 15a to 15i are 25.61 Pa, 26.07 Pa, 24.80 Pa, 36.11 Pa, 36.74 Pa, 33.98 Pa, 31.83 Pa, 32.26 Pa, and 28.12 Pa, respectively. Therefore, we can say that the maximum pressure enhancement for the cavity with  $L_x = 64$  mm occurs at 2345 Hz and for the cavity with  $L_x = 70$  mm at 2272 Hz. The maximum pressure enhancement occurs at  $L_x = 67$  mm at 2315 Hz and reaches 36.74 Pa. This is similar to the results shown in Fig. S 13c.

We compare this maximum pressure value to the sound pressure fields of the fully reduced cavity with  $L_x = 64$  mm and  $L_x = 70$  mm to prove the existence of a pressure peak. The measurements show peak pressures of 26.07 and 32.26 Pa, respectively. To demonstrate the magnitude of the pressure enhancement, we

also compare it to the pressure field inside the full cavity with  $L_x = 170$  mm for several frequencies. The maximum pressure of the full cavity is 12.61 Pa. Thus, the fully reduced cavity leads to the highest pressure enhancement of the investigated Friedrich-Wintgen BIC by a factor of about three.

## References

- [1] D. Maksimov, A. Sadreev, A. A. Lyapina, and A. Pilipchuk. “Coupled mode theory for acoustic resonators”. In: *Wave Motion* 56 (Feb. 2015). DOI: 10.1016/j.wavemoti.2015.02.003.
- [2] A. A. Lyapina, D. Maksimov, A. Pilipchuk, and A. Sadreev. “Bound states in the continuum in open acoustic resonators”. In: *Journal of Fluid Mechanics* 780 (June 2015). DOI: 10.1017/jfm.2015.480.
- [3] L. Huang et al. “General Framework of Bound States in the Continuum in an Open Acoustic Resonator”. In: *Phys. Rev. Applied* 18 (5 Nov. 2022), p. 054021. DOI: 10.1103/PhysRevApplied.18.054021. URL: <https://link.aps.org/doi/10.1103/PhysRevApplied.18.054021>.
- [4] A. Sadreev. “Interference traps waves in open system: Bound states in the continuum”. In: *Reports on Progress in Physics* 84 (Mar. 2021). DOI: 10.1088/1361-6633/abefb9.
- [5] H. Feshbach. “Unified theory of nuclear reactions”. In: *Annals of Physics* 5.4 (1958), pp. 357–390. ISSN: 0003-4916. DOI: [https://doi.org/10.1016/0003-4916\(58\)90007-1](https://doi.org/10.1016/0003-4916(58)90007-1). URL: <https://www.sciencedirect.com/science/article/pii/0003491658900071>.
- [6] F.-M. Dittes. “The decay of quantum systems with a small number of open channels”. In: *Physics Reports* 339 (Dec. 2000), pp. 215–316. DOI: 10.1016/S0370-1573(00)00065-X.
- [7] J. Okolowicz, M. Płoszajczak, and I. Rotter. “Dynamics of quantum systems embedded in a continuum”. In: *Physics Reports* 374 (Feb. 2003), pp. 271–383. DOI: 10.1016/S0370-1573(02)00366-6.
- [8] H. Friedrich and D. Wintgen. “Interfering resonances and bound states in the continuum”. In: *Phys. Rev. A* 32 (6 Dec. 1985), pp. 3231–3242. DOI: 10.1103/PhysRevA.32.3231. URL: <https://link.aps.org/doi/10.1103/PhysRevA.32.3231>.
- [9] V. Pagneux. “Trapped Modes and Edge Resonances in Acoustics and Elasticity”. In: *Dynamic Localization Phenomena in Elasticity, Acoustics and Electromagnetism*. Ed. by R. V. Craster and J. Kaplunov. Vienna: Springer Vienna, 2013, pp. 181–223. ISBN: 978-3-7091-1619-7. DOI: 10.1007/978-3-7091-1619-7\_5. URL: [https://doi.org/10.1007/978-3-7091-1619-7\\_5](https://doi.org/10.1007/978-3-7091-1619-7_5).